

1 LEVERAGING MULTI-MESSENGER ASTROPHYSICS FOR DARK MATTER SEARCHES

By

Daniel Nicholas Salazar-Gallegos

A DISSERTATION

Submitted to
Michigan State University
in partial fulfillment of the requirements
for the degree of

Physics—Doctor of Philosophy
Computational Mathematics in Science and Engineering—Dual Major

Today

ABSTRACT

3 I did Dark Matter with HAWC and IceCube. I also used Graph Neural Networks

⁴ Copyright by

⁵ DANIEL NICHOLAS SALAZAR-GALLEGOS

⁶ Today

ACKNOWLEDGMENTS

8 I love my friends. Thanks to everyone that helped me figure this out. Amazing thanks to the people
9 at LANL who supported me. Eames, etc Dinner Parties Jenny and her child Kaydince Kirsten, Pat,
10 Andrea Family. You're so far but so critical to my formation. Unconditional love. Roommate

TABLE OF CONTENTS

12	LIST OF TABLES	vii
13	LIST OF FIGURES	ix
14	LIST OF ABBREVIATIONS	xx
15	CHAPTER 1 INTRODUCTION	1
16	CHAPTER 2 DARK MATTER IN THE COSMOS	2
17	2.1 Introduction	2
18	2.2 Dark Matter Basics	3
19	2.3 Evidence for Dark Matter	4
20	2.4 Searching for Dark Matter: Particle DM	11
21	2.5 Sources for Indirect Dark Matter Searches	16
22	2.6 Multi-Messenger Dark Matter	18
23	CHAPTER 3 HIGH ALTITUDE WATER CHERENKOV (HAWC) OBSERVATORY	21
24	3.1 The Detector	21
25	3.2 Event Reconstruction	26
26	3.3 Background Estimation: Direct Integration	34
27	CHAPTER 4 ICECUBE NEUTRINO OBSERVATORY	36
28	4.1 The Detector	36
29	4.2 Events Reconstruction and Data Acquisition	36
30	4.3 Northern Test Site	36
31	CHAPTER 5 GLORY DUCK: MULTI-WAVELENGTH SEARCH FOR DARK MATTER ANNIHILATION TOWARDS DWARF SPHEROIDAL GALAXIES	37
32	5.1 Introduction	37
33	5.2 Dataset and Background	39
34	5.3 Analysis	41
35	5.4 Likelihood Methods	45
36	5.5 HAWC Results	52
37	5.6 Glory Duck Combined Results	54
38	5.7 HAWC Systematics	59
39	5.8 J -factor distributions	61
40	5.9 Discussion and Conclusions	67
43	CHAPTER 6 MULTITHREADING HAWC ANALYSES FOR DARK MATTER SEARCHES	71
44	6.1 Introduction	71
45	6.2 Dataset and Background	71
46	6.3 Analysis	73

48	6.4	Likelihood Methods	77
49	6.5	Computational Methods: Multithreading	77
50	6.6	Analysis Results	83
51	6.7	Systematics	88
52	6.8	Conclusion and Discussion	88
53	CHAPTER 7	HEAVY DARK MATTER ANNIHILATION SEARCH WITH ICE-CUBE'S NORTH SKY TRACK DATA	90
54	7.1	Introduction	90
55	7.2	Dataset and Background	90
56	7.3	Analysis	92
57	7.4	Likelihood Methods	101
58	7.5	Background Simulation	101
59	7.6	Signal Recovery	119
60	7.7	Systematics	122
61	7.8	Conclusions	125
63	CHAPTER 8	NU DUCK: CONCLUSIONS AND FUTURE DIRECTIONS	127
64	8.1	Conclusions	127
65	8.2	Future Directions: Multi-Messenger Dark Matter Search	128
66	APPENDIX A	MULTI-EXPERIMENT SUPPLEMENTARY FIGURES	130
67	APPENDIX B	MULTITHREADING DARK MATTER ANALYSES SUPPLEMENTARY MATERIAL	131
68	B.1	Remaining Spectral Models	131
69	B.2	<code>mpu_analysis.py</code>	132
70	B.3	Comparison with Glory Duck	141
72	APPENDIX C	ICECUBE HEAVY DARK MATTER ANALYSIS SUPPLEMENTARY MATERIAL	144
73	C.1	Docker Image for Oscillating Neutrino Spectra	144
74	C.2	Spline Fitting Statuses	147
75	C.3	Neutrino Composite Spectra	148
76	C.4	Segue 1 And Ursa Major II Signal Recovery	149
77	C.5	n_s Sensitivities	155
79	BIBLIOGRAPHY		157

LIST OF TABLES

<p>81 Table 3.1 Definitions of f_{hit} energy estimator bins. Bins are defined by the fraction of 82 available PMTs that are triggered during an air shower event. The angular 83 resolution, Θ_{68}, is the bin containing 68% of events [34].</p> <p>84 Table 5.1 Summary of the relevant properties of the dSphs used in the present work. 85 Column 1 lists the dSphs. Columns 2 and 3 present their heliocentric distance 86 and galactic coordinates, respectively. Columns 4 and 5 report the J-factors of 87 each source given from the \mathcal{GS} and \mathcal{B} independent studies and their estimated 88 $\pm 1\sigma$ uncertainties. The values $\log_{10} J$ (\mathcal{GS} set) [59] correspond to the mean 89 J-factor values for a source extension truncated at the outermost observed star. 90 The values $\log_{10} J$ (\mathcal{B} set) [63] are provided for a source extension at the tidal 91 radius of each dSph. Bolded sources are within HAWC's field of view and 92 provided to the Glory Duck analysis.</p> <p>93 Table 5.2 Summary of dSph observations by each experiment used in this work. A 94 ‘-’ indicates the experiment did not observe the dSph for this study. For 95 Fermi-LAT, the exposure at 1 GeV is given. For HAWC, $\Delta\theta$ is the absolute 96 difference between the source declination and HAWC latitude. HAWC is more 97 sensitive to sources with smaller $\Delta\theta$. For IACTs, we show the zenith angle 98 range, the total exposure, the energy range, the angular radius θ of the signal or 99 ON region, the ratio of exposures between the background-control (OFF) and 100 signal (ON) regions (τ), and the significance of gamma-ray excess in standard 101 deviations, σ.</p> <p>102 Table 6.1 Summary of the relevant properties of the dSphs used in the present work. 103 Column 1 lists the dSphs. Columns 2 and 3 present their heliocentric distance 104 and galactic coordinates, respectively. Column 4 reports the J-factors of each 105 source given from the \mathcal{LS} studies and estimated $\pm 1\sigma$ uncertainties. The 106 values $\log_{10} J$ (\mathcal{LS} set) [80] correspond to the mean J-factor values for a 107 source extension truncated at 0.5°.</p> <p>108 Table 6.2 Timing summaries for analyses for serial and multithreaded processes. M 109 tasks is the number of functional-parallel tasks ran for the computation. $T_{p,c}$ 110 is a single run time in hours:minutes:seconds for runs utilizing p nodes and 111 c threads. Runs are run interactively on the same computer to maximize 112 consistency. Empty entries are indicated with ‘-’. (·) entries are estimated 113 entries extrapolated from data earlier in the column.</p> <p>114 Table 6.3 Speed up summaries for analyses for serial and multithreaded processes. M 115 tasks is the number of functional-parallel tasks ran for the computation. $S_{p,c}$ 116 is a single speedup comparison for runs utilizing p nodes and c threads. [·] 117 are the estimated speedups calculated from Tab. 6.2, Eq. (6.7), and Eq. (6.4). 118 Empty entries are indicated with ‘-’.</p>	<p>31</p> <p>46</p> <p>47</p> <p>77</p> <p>81</p> <p>83</p>
---	---

119	Table 7.1	Spline err tolerances used for input in particle physics component to Eq. (5.1).	
120		Column 1 is the DM annihilation channel being fit. Columns 2, 3, and 4	
121		are the tolerances for "GOOD" (pass), "OK" requires inspection, and "FAIL"	
122		(tune and refit) respectively. Column 5 has the X ranges over which the error	
123		is evaluated. MAX/MIN $[\cdot, \cdot]$ takes the maximum or minimum of the two	
124		enclosed values.	98
125	Proof I know how to include		

LIST OF FIGURES

127	Figure 2.1	Rotation curve fit to NGC 6503 from [7]. Dashed line is the contribution 128 from visible matter. Dotted curves are from gas. Dash-dot curves are from 129 dark matter (DM). Solid line is the composite contribution from all matter 130 and DM sources. Data are indicated with bold dots with error bars. Data 131 agree strongly with a matter + DM composite prediction.	5
132	Figure 2.2	Light from distant galaxy is bent in unique ways depending on the distribution 133 of mass between the galaxy and Earth. Yellow dashed lines indicate where 134 the light would have gone if the matter were not present [8].	7
135	Figure 2.3	(left) Optical image of galactic cluster 1E0657-558. (right) X-ray image of the 136 cluster with redder meaning hotter and higher baryon density. (both) Green 137 contours are reconstruction of gravity contours from weak lensing. White 138 rings are the best fit mass maxima at 68.3%, 95.5%, and 99.7% confidence. 139 The matter maxima of the clusters are clearly separated from x-ray maxima. [9]	8
140	Figure 2.4	Plank CMB sky. Sky map features small variations in temperature in primor- 141 dial light. These anisotropies are used to make inferences about the universe's 142 energy budget and developmental history. [10]	9
143	Figure 2.5	Observed Cosmic Microwave Background power spectrum as a function of 144 multipole moment from Plank [10]. Blue line is best fit model from Λ CDM. 145 Red points and lines are data and error, respectively.	10
146	Figure 2.6	Predicted power spectra of CMB for different $\Omega_m h^2$ values for fixed baryon 147 density from [11]. (left) Low $\Omega_m h^2$ increases the prominence of first and 148 second peaks. (middle) $\Omega_m h^2$ is most similar to the observed power spectrum. 149 The second and third peaks are similar in height. (right) $\Omega_m h^2$ is large which 150 suppresses the first peak and raises the prominence of the third peak.	10
151	Figure 2.7	The Standard Model (SM) of particle physics. Figure taken from http://www.quantumdiaries.org/2014/03/14/the-standard-model-a-beautiful-but-flawed-theory/	12
154	Figure 2.8	Simplified Feynman diagram demonstrating with different ways DM can 155 interact with SM particles. The 'X's refer to the DM particles whereas the 156 SM refer to fundamental particles in the SM. The large circle in the center 157 indicates the vertex of interaction and is purposely left vague. The colored 158 arrows refer to different directions of time as well as their respective labels. 159 The arrows indicate the initial and final state of the DM -SM interaction in time.	13

160	Figure 2.9 A single jet event in ATLAS detector from 2017 [16]. Jet momentum was 161 observed to be 1.9 TeV. Missing transverse momentum was observed to be 162 1.9 TeV compared to the initial transverse momentum of the event was 0. 163 Implied MET is traced by a red dashed line in event display.	14
164	Figure 2.10 More detailed pseudo-Feynman diagram of particle cascade from dark matter 165 annihilation into 2 quarks. The quarks hadronize and down to stable particles 166 like γ or the anti-proton (p^-). Diagram pulled from ICRC 2021 presentation 167 on DM annihilation search [17].	15
168	Figure 2.11 Dark Matter (DM) decay spectrum for $b\bar{b}$ initial state and γ final state. Redder 169 spectra are for larger DM masses. Bluer spectra are light DM masses. x is a 170 unitless factor defined as the ratio of the mass of DM, m_χ , and the final state 171 particle energy E_γ . Figure from [19].	17
172	Figure 2.12 Different dark matter density profiles compared. Some models produce ex- 173 ceptionally large densities at small r [20].	18
174	Figure 2.13 The Milky Way Galaxy in photons (γ) and neutrinos (ν) [22]. The Galactic 175 center is at $l=0^\circ$ and is the brightest region in all panels. (top) An Optical 176 color image of the Milky Way galaxy seen from Earth. Clouds of gas and dust 177 obscure some light from stars. (2nd down) Integrated flux of γ -rays observed 178 by the Fermi-LAT telescope [23]. (middle) Expected neutrino emission 179 that corresponds with Fermi-LAT observations. (2nd up) Expected neutrino 180 emission profile after considering detector systematics of IceCube. (bottom) 181 Observed neutrino emission from region of the galactic plane. Substantial 182 neutrino emission was detected.	19
183	Figure 2.14 Dark Matter annihilation spectra for different final state particle and standard 184 model annihilation channels [24]. Photons (red), e^\pm (green), \bar{p} (blue), ν (black).	20
185	Figure 3.1 Photo of the HAWC detector that I took on May 17, 2023. Main array is 186 centered in the photo and comprised of the larger tanks. Outriggers are the 187 smaller tanks around the main array.	21
188	Figure 3.2 A particle physics illustration of high energy particle showers. Left shower is 189 an electromagnetic shower from a high energy gamma-ray. Most particles in 190 the shower will be a combination of photons and charged leptons, in this case 191 electrons (e). Right figure shows a cosmic ray particle shower. The cosmic 192 ray will produce many more types of particles including pions (π), neutrinos, 193 and charged leptons. Figure pulled from [26].	22
194	Figure 3.3 The WCDs. Left image features several WCDs looking from within the main 195 array of HAWC. Right image shows a schematic of a WCD pulled from [25].	23

196	Figure 3.4	Overview of HAWC control and data electronics. The LoToT and HiToT threshold signals are discussed in Section 3.1.2. Figure from [28]	24
198	Figure 3.5	Schematic of data flow in HAWC data acquisition and online processing system. Pulled from [29].	24
200	Figure 3.6	How HAWC FEB intially processes analog PMT signals. Signals are split through an amplifier and discriminator circuit. Each path is designated for ei- ther the HIGH or LOW threshold for the signal. The 2-edge event corresponds to LOW, while the 4 edge corresponds to HIGH.	25
204	Figure 3.7	An particle shower incident on WCDs. Secondary particles of an air shower travel in a cone centered on primary incident particle. Reconstruction of the initial angle is possible with arrival time of hits in PMTs inside WCDs. Figure from [33].	27
208	Figure 3.8	Charge deposition in each PMT for a reconstructed gamma-ray event. WCDs are outlined in black surrounding the 4 smaller circles that represent PMTs. The color scale indicates the charge deposition in each PMT. The best shower core fit from SFCF is noted with a red star in the center of the dashed circle [34].	28
212	Figure 3.9	Simulated normalized energy distribution of each f_{hit} bin defined in Tab. 3.1. Monte Carlo simulation of gamma-rays with $E^{-2.63}$ spectral shape and sim- ulated source at 20° declination. Figure from [34].	30
215	Figure 3.10	Neural Network energy estimator performance compared to true energy. The dotted line is the identity line where the estimator and injection agree. Gam- ma/hadron separation cuts were applied with the energy estimation. Figure pulled from [37]	32
219	Figure 3.11	Lateral distribution functions (LDFs) for cosmic ray (left) and a photon can- didate from the Crab Nebula (right). Cosmic ray LDF has clearly isolated hits far from the reconstructed shower core. Gamma-ray shower shows a more cuspy event [34].	33

223	Figure 5.1 Sensitivities of five gamma-ray experiments compared to percentages of the 224 Crab nebula's emission and dark matter annihilation. Solid lines present 225 estimated sensitivities to power law spectra [FACT CHECK THIS]for each 226 experiment. Green lines are Fermi-LAT sensitivities where lighter green is 227 the sensitivity to the galactic center and dark green is its sensitivity to higher 228 declinations. Orange, red, and purple solid lines represent the MAGIC, HESS, 229 and VERITAS 50 hour sensitivities respectively. The maroon and brown lines 230 are the HAWC 1 year and 5 year sensitivities. Across four decades of gamma- 231 ray energy, these experiments have similar sensitivities on the order 10^{-12} 232 erg cm $^{-2}$ s $^{-1}$. The dotted lines are estimated dark matter fluxes assuming 233 $m_\chi = 5$ TeV DM annihilating to bottom quarks (red), tau leptons (blue), 234 and W bosons (green). Faded gray lines outline percentage flux of the Crab 235 nebula. Figure is an augmented version of [40]	38
236	Figure 5.2 Effect of Electroweak (EW) corrections on expected DM annihilation spec- 237 trum for $\chi\chi \rightarrow W^-W^+$. Solid lines are spectral models that consider EW 238 corrections. Dash-dot lines are spectral models without EW corrections. Red 239 lines are models for $M_\chi = 1$ TeV. Blue lines represent models for $M_\chi = 100$ 240 TeV. All models are sourced from the PPPC4DMID [58].	42
241	Figure 5.3 $\frac{dJ}{d\Omega}$ maps for Segue1 (top) and Coma Berenices (bottom). Origin is centered 242 on the specific dwarf spheroidal galaxies (dSph). X and Y axes are the angular 243 separation from the center of the dwarf. Profile is truncated at the scale radius. 244 Plots of the remaining 11 dSph HAWC studied are linked in Fig. A.1.	44
245	Figure 5.4 Illustration of the combination technique showing a comparison between 246 $-2 \ln \lambda$ provided by four instruments (colored lines) from the observation 247 of the same dSph without any J nuisance and their sum, <i>i.e.</i> the resulting 248 combined likelihood (thin black line). According to the test statistics of 249 Equation (5.7), the intersection of the likelihood profiles with the line $-2 \ln \lambda$ 250 = 2.71 indicates the 95% C.L. upper limit on $\langle \sigma v \rangle$. The combined likelihood 251 (thin black line) shows a smaller value of upper limit on $\langle \sigma v \rangle$ than those 252 derived by individual instruments. We also show how the uncertainties on 253 the J factor effects the combined likelihood and degrade the upper limit on 254 $\langle \sigma v \rangle$ (thick black line). All likelihood profiles are normalized so that the global 255 minimum $\widehat{\langle \sigma v \rangle}$ is 0. We note that each profile depends on the observational 256 conditions in which a target object was observed. The sensitivity of a given 257 instrument can be degraded and the upper limits less constraining if the 258 observations are performed in non-optimal conditions such as a high zenith 259 angle or a short exposure time.	50
260	Figure 5.5	53

261	Figure 5.6 HAWC TS values for best fit $\langle\sigma v\rangle$ versus m_χ for seven SM annihilation channels with J factors from \mathcal{GS} . The solid black line shows the combined best fit TS values. The colored, dashed lines are the TS values for each of the 13 sources HAWC studied.	54
265	Figure 5.7 HAWC Brazil bands at 95% confidence level on $\langle\sigma v\rangle$ versus DM mass for seven annihilation channels with J -factors from \mathcal{GS} [69]. The solid line represents the combined limit from 13 dSphs. The dashed line is the expected limit. The green band is the 68% containment. The yellow band is the 95% containment.	55
270	Figure 5.8 Upper limits at 95% confidence level on $\langle\sigma v\rangle$ in function of the DM mass for eight annihilation channels, using the set of J factors from Ref. [69] (\mathcal{GS} set in Table 5.1). The black solid line represents the observed combined limit, the black dashed line is the median of the null hypothesis corresponding to the expected limit, while the green and yellow bands show the 68% and 95% containment bands. Combined upper limits for each individual detector are also indicated as solid, colored lines. The value of the thermal relic cross-section in function of the DM mass is given as the red dotted-dashed line [70].	56
279	Figure 5.9 Same as Fig. 5.8, using the set of J factors from Ref. [63, 71] (\mathcal{B} set in Table 5.1).	57
280	Figure 5.10 Comparisons of the combined limits at 95% confidence level for each of the eight annihilation channels when using the J factors from Ref. [69] (\mathcal{GS} set in Table 5.1), plain lines, and the J factor from Ref. [63, 71] (\mathcal{B} set in Table 5.1), dashed lines. The cross-section given by the thermal relic is also indicated [70].	59
284	Figure 5.11 Comparisons of the combined limits at 95% confidence level for a point source analysis and extended source using [69] \mathcal{GS} J-factor distributions and PPPC [58] annihilation spectra. Shown are the limits for Segue1 which will have the most significant impact on the combined limit. 6 of the 7 DM annihilation channels are shown. Solid lines are extended source studies. Dashed lines are point source studies. Overall, the extended source analysis improves the limit by a factor of 2.	61
291	Figure 5.12 Same as Fig. 5.11 on Coma Berenices. This dSph also contributes significantly to the limit. The limits are identical in this case.	62
293	Figure 5.13 Comparison of combined limits when correcting for HAWC's pointing systematic. All DM annihilation channels are shown. The solid black line is the ratio between published limit to the declination corrected limit. The blue solid line or "Combined_og" represented the limits computed for Glory Duck. The solid orange line or "Combined_ad" represented the limits computed after correcting for the pointing systematic.	63

299	Figure 5.14 Differential map of dJ/Ω from model built in Section 5.8.1 and profiles 300 provided directly from authors. (Top) Differential from Segue1. (bottom) 301 Differential from Coma Berenices. Note that their scales are not the same. 302 Segue1 shows the deepest discrepancies which is congruent with its large 303 uncertainties. Both models show anuli where unique models become apparent.	64
304	Figure 5.15 HAWC limits for Coma Berenices (top) and Segue1 (bottom) for two different 305 map sets. Blue lines are limits calculated on maps with poor model repre- 306 sentation. Orange lines are limits calculated on spatial profiles provided by 307 the authors of [59]. Black line is the ratio of the poor spatial model limits to 308 the corrected spatial models. The left y-axis measures $\langle\sigma v\rangle$ for the blue and 309 orange lines. The right y-axis measures the ratio and is unitless.	65
310	Figure 5.16 Comparisons between the J -factors versus the angular radius for the com- 311 putation of J factors from Ref. [69] (\mathcal{GS} set in Table 5.1) in blue and for 312 the computation from Ref. [63, 71] (\mathcal{B} set in Tab. 5.1) in orange. The solid 313 lines represent the central value of the J -factors while the shaded regions 314 correspond to the 1σ standard deviation.	67
315	Figure 5.17 Comparisons between the J -factors versus the angular radius for the com- 316 putation of J factors from Ref. [69] (\mathcal{GS} set in Tab. 5.1) in blue and for the 317 computation from Ref. [63, 71] (\mathcal{B} set in Tab. 5.1) in orange. The solid 318 lines represent the central value of the J -factors while the shaded regions 319 correspond to the 1σ standard deviation.	68
320	Figure 6.1 Spectral hypotheses from PPPC [58] and HDM [79] for DM annihilation: $\chi\chi \rightarrow W^-W^+$. Solid lines are spectral models with EW corrections from the 321 PPPC. Dash-dot lines are spectral models from HDM. Red lines are models 322 for $M_\chi = 1$ TeV. Blue lines represent models for $M_\chi = 100$ TeV.	73
324	Figure 6.2 Photon spectra for $\chi\chi \rightarrow \gamma\gamma$ (left) and $\chi\chi \rightarrow ZZ$ (right) after Gaussian 325 convolution of line features. Both spectra have δ -features at photon energies 326 equal to the DM mass. Bluer lines are annihilation spectra with lower DM 327 mass. Redder lines are spectra from larger DM mass. All spectral models are 328 sourced from the Heavy Dark Matter models [79]. Axes are drawn roughly 329 according to the energy sensitivity of HAWC.	74
330	Figure 6.3 $\frac{dJ}{d\Omega}$ maps for Coma Berenices, Draco, Segue1, and Sextans. Columns are 331 divided for the $\pm 1\sigma$ uncertainties in $dJ/d\Omega$ around the mean value from \mathcal{LS} 332 [80]. Origin is centered on the specific dwarf spheroidal galaxies (dSph). θ 333 and ϕ axes are the angular separation from the center of the dwarf. Profiles 334 are truncated at 1° and flattened beyond.	76

335	Figure 6.4	Infographic on how jobs and DM computation was organized in Section 5.3. Jobs were built for each permutation of CHANS and SOURCES shown by the left block in the figure. Each job, which took on the order 2 hrs to compute, had the following work flow: 1. Import HAWC analysis software, 2 min to run. 2. Load HAWC count maps, 5 min to run. 3. Load HAWC energy and spatial resolutions, 4 min. 5. Load DM spatial source templates and spectral models, less than 1 s. 6. Perform likelihood fit on data and model, about 8 min per DM mass. 7. Write results to file, less than 1s.	78
343	Figure 6.5	Graphic of Gustafson parallel coding pattern. f_s is the fraction of a program, in time, spent on serial computation. f_p is the fraction of computing time that is parallelizable. T_p is the total time for a parallel program to run. T_1 is the total time for a parallel program to run if only 1 processor is allocated. P_N is the N -th processor where it's row is the computation the processor performs. The Gustafson pattern is most similar to what is implemented for this analysis. Figure is pulled from [82].	79
350	Figure 6.6	Task chart for one multithreaded job developed for this project. Green blocks indicate a shared resource across the threads AND computation performed serially. Red blocks indicate functional parallel processing within each thread. 3 threads are represented here, yet many more can be employed during the full analysis. Jobs are defined by the SOURCE as these require unique maps to be loaded into the likelihood estimator. The m_χ , CHAN, and $\langle\sigma v\rangle$ variables are entered into the thread pool and allocated as evenly as possible across the threads.	81
358	Figure 6.7	HAWC upper limits at 95% confidence level on $\langle\sigma v\rangle$ versus m_χ for $\chi\chi \rightarrow b\bar{b}$, $t\bar{t}$, $u\bar{u}$, $d\bar{d}$, $s\bar{s}$, $c\bar{c}$, gg , W^+W^- , and hh . Limits are with \mathcal{LS} J -factors [80]. The solid line represents the observed combined limit. Dashed lines represent limits from individual dSphs.	84
362	Figure 6.8	HAWC upper limits at 95% confidence level on $\langle\sigma v\rangle$ versus m_χ for $\chi\chi \rightarrow \nu_e\bar{\nu}_e$, $\nu_\mu\bar{\nu}_\mu$, $\nu_\tau\bar{\nu}_\tau$, $e\bar{e}$, $\mu\bar{\mu}$, $\tau\bar{\tau}$, $\gamma\gamma$ and ZZ . Limits use \mathcal{LS} J -factors [80]. The solid line represents the observed combined limit. Dashed lines represent limits from individual dSphs.	85
366	Figure 6.9	HAWC TS values for best fit $\langle\sigma v\rangle$ versus m_χ for SM annihilation channels: $\chi\chi \rightarrow b\bar{b}$, $t\bar{t}$, $u\bar{u}$, $d\bar{d}$, $s\bar{s}$, $c\bar{c}$, gg , W^+W^- , and hh . Limits use \mathcal{LS} J -factors. The solid black line shows the combined best fit TS values. The colored, dashed lines are the TS values from each dSph.	86
370	Figure 6.10	HAWC TS values for best fit $\langle\sigma v\rangle$ versus m_χ for SM annihilation channels: $\chi\chi \rightarrow \nu_e\bar{\nu}_e$, $\nu_\mu\bar{\nu}_\mu$, $\nu_\tau\bar{\nu}_\tau$, $e\bar{e}$, $\mu\bar{\mu}$, $\tau\bar{\tau}$, $\gamma\gamma$ and ZZ . Limits use \mathcal{LS} J -factors. The solid black line shows the combined best fit TS values. The colored, dashed lines are the TS values from each dSph.	87

374	Figure 6.11 Comparison of HAWC limits from this analysis to Glory Duck (Fig. 5.5) for 3 dSphs and 3 DM annihilation channels: $b\bar{b}$, $\tau\bar{\tau}$, and $e\bar{e}$. Each sector shows the 95% confidence limit from Glory Duck (blue line) and this analysis (orange line) in the top plot. The lower plot features the ratio in log scale of Glory Duck to this analysis in a red solid line. Horizontal dashed lines are for ratios of 1.0 (black) and $\sqrt{2}$ (blue). Ratios larger than 1.0 are for limits smaller, or stricter, than Glory Duck. Ratios larger than $\sqrt{2}$ indicates limits are stricter than a simple doubling of the Glory Duck data.	89
382	Figure 7.1 Neutrino spectra at production (left panels) and after oscillation at Earth (right panels). Blue, orange, and green lines are the ν_e , ν_μ , and ν_τ spectra respectively. Top panels show the spectra in $\frac{dN}{dE}$. Lower panels plot the flavor ratio to $\nu_e + \nu_\mu + \nu_\tau$. SM annihilation channels $b\bar{b}$, $\tau\bar{\tau}$, and $\nu_\mu\bar{\nu}_\mu$ are shown for $M_\chi = 1$ PeV, TeV, and EeV.	94
387	Figure 7.2 Signal recovery for 100 TeV DM annihilation into $\nu_\mu\bar{\nu}_\mu$ for a source at Dec = 16.06° . n_{inj} is the number of injected signal events in simulation. n_s is the number of reconstructed signal events from the simulation data. Although the uncertainties are small and tight, the reconstructed n_s are systematically underestimated.	95
392	Figure 7.3 Left panel shows the two kernels overlaying the original spectrum from χ arony after propagation to Earth [85]. The vertical red line indicates where the original neutrino line is maximized. Blue line is the output from χ aroy. Green line is the spectrum after convolution with a flat kernel. Orange line is the spectrum after Gaussian convolution. Right panel shows the signal recovery of the spectral model using the Gaussian kernel with parameters enumerated above.	96
399	Figure 7.4 Example spline that failed the fit. Failed splined are corrected on a case by case basis unless the SM channel has a systematic problem fitting the splines. In this case, I made a bookkeeping error and loaded the incorrect spectral model	98
402	Figure 7.5 Summary of input spectral models that were smoothed with Gaussian kernels. Spectral models are for $\chi\chi \rightarrow e\bar{e}, \mu\bar{\mu}, \tau\bar{\tau}, \nu_e\bar{\nu}_e, \nu_\mu\bar{\nu}_\mu$, and $\nu_\tau\bar{\nu}_\tau$. These spectra are the composite ($\nu_\mu + \nu_\tau$) of neutrino flavors. Every spectral model used for this analysis is featured as a colored solid line. Bluer lines are for low m_χ models. m_χ ranges from 681 GeV to 100 PeV. HDM [79], χ aroy [85], and Photospline [89] are used to generate these spectra. Energy (x-axis) was chosen to roughly represent the energy sensitivity of NST.	99

409	Figure 7.6 Test statistic (TS) distributions for Segue 1 and $\chi\chi \rightarrow b\bar{b}$. Each subplot, 410 except the final, is the TS distribution for a specific DM mass listed in the 411 subplot. Orange dashed lines are the traces for a χ^2 distribution with 1 degree 412 of freedom. $\epsilon[\cdot]$ is the fraction of trials smaller than the bracketed value. The 413 final subplot features the all DM spectral models, similar to Fig. 7.5, used as 414 input for the TS distributions.	102
415	Figure 7.7 Same as Fig. 7.6 for Segue 1 $\chi\chi \rightarrow \tau\bar{\tau}$	103
416	Figure 7.8 Same as Fig. 7.6 for Segue 1 $\chi\chi \rightarrow \nu_\mu\bar{\nu}_\mu$	104
417	Figure 7.9 Same as Fig. 7.6 for Ursa Major II 1 $\chi\chi \rightarrow b\bar{b}$	105
418	Figure 7.10 Same as Fig. 7.6 for Ursa Major II 1 $\chi\chi \rightarrow \tau\bar{\tau}$	106
419	Figure 7.11 Same as Fig. 7.6 for Ursa Major II 1 $\chi\chi \rightarrow \nu_\mu\bar{\nu}_\mu$	107
420	Figure 7.12 Same as Fig. 7.6 for 15, GS J-factor, stacked sources and $\chi\chi \rightarrow b\bar{b}$	108
421	Figure 7.13 Same as Fig. 7.6 for 15, GS J-factor, stacked sources and $\chi\chi \rightarrow t\bar{t}$	109
422	Figure 7.14 Same as Fig. 7.6 for 15, GS J-factor, stacked sources and $\chi\chi \rightarrow u\bar{u}$	110
423	Figure 7.15 Same as Fig. 7.6 for 15, GS J-factor, stacked sources and $\chi\chi \rightarrow d\bar{d}$	111
424	Figure 7.16 Same as Fig. 7.6 for 15, GS J-factor, stacked sources and $\chi\chi \rightarrow e\bar{e}$	112
425	Figure 7.17 Same as Fig. 7.6 for 15, GS J-factor, stacked sources and $\chi\chi \rightarrow \mu\bar{\mu}$	113
426	Figure 7.18 Same as Fig. 7.6 for 15, GS J-factor, stacked sources and $\chi\chi \rightarrow \tau\bar{\tau}$	114
427	Figure 7.19 Same as Fig. 7.6 for 15, GS J-factor, stacked sources and $\chi\chi \rightarrow W^+W^-$	115
428	Figure 7.20 Same as Fig. 7.6 for 15, GS J-factor, stacked sources and $\chi\chi \rightarrow ZZ$	116
429	Figure 7.21 Same as Fig. 7.6 for 15, GS J-factor, stacked sources and $\chi\chi \rightarrow \nu_e\bar{\nu}_e$	117
430	Figure 7.22 Same as Fig. 7.6 for 15, GS J-factor, stacked sources and $\chi\chi \rightarrow \nu_\mu\bar{\nu}_\mu$	118

431	Figure 7.23 Signal Recovery study for an analysis with 15 stacked sources using the \mathcal{GS}	120
432	J -factors [59]. Above shows 14 studies for DM mass ranging between 1	
433	TeV and 20 PeV for $\chi\chi \rightarrow \mu_\mu\overline{\mu_\mu}$. The bottom right subplot features every	
434	spectral model used as input for the remaining subplots. The remaining	
435	subplots show n_{inj} as the number of signal events injected into background	
436	simulation. Whereas, n_s is the number of signal events recovered from	
437	analyzing the injected simulation. Blue line represents the median values of	
438	100 simulations. Light blue bands show the 1σ statistical uncertainty around	
439	the median.	
440	Figure 7.24 Same as Fig. 7.23 but for $\chi\chi \rightarrow t\bar{t}$ (top) and $b\bar{b}$ (bottom).	121
441	Figure 7.25 IceCube North Sky Track Sensitivities. Each panel shows sensitivity curves	
442	for various DM annihilation channels. Sensitivities are for the velocity-	
443	weighted cross-section $\langle\sigma v\rangle$ versus m_χ . Dotted, colored lines are sensitivities	
444	for individual sources. Solid white lines are for the combined sensitivity of	
445	all 15 \mathcal{GS} sources used in this study.	123
446	Figure 7.26 Same as Fig. 7.25 for three additional DM annihilation channels.	124
447	Figure 7.27 Panel A: Neutrino's from the Northern sky and incident on the IceCube	
448	detector will travel through the Earth. How much of the Earth these neutrinos	
449	travels is a function of zenith from the vertical axis. Panel B: SM prediction of	
450	neutrino transmission probabilities for neutrinos arriving at $90^\circ - 180^\circ$ zenith	
451	and with 100 GeV to 100 PeV energies. High-energy neutrinos traversing	
452	the whole Earth are completely absorbed, whereas low-energy neutrinos pass	
453	through unimpeded. Neutrinos coming from above the horizon will arrive	
454	unimpeded for all neutrino energies. Figure pulled from [92].	125
455	Figure 7.28 $\langle\sigma v\rangle$ sensitivities for 5 imaginary sources with $\log_{10} J = 19.42 \log_{10}(\text{GeV}^2\text{cm}^{-5})$.	
456	Each imaginary source shares a declination with a source in Tab. 5.1	126
457	Figure 8.1 The prompt electron neutrino and photon spectrum resulting from the decay	
458	of a 2EeV DM particle to $\nu_e\overline{\nu}_e$, as currently being searched for at IceCube	
459	[5]. Solid curves represent the results of this work, and predict orders of	
460	magnitude more flux at certain energies than the dashed results of Pythia 8.2,	
461	one of the only existing methods to generate spectra at these masses. In both	
462	cases energy conservation is satisfied: there is a considerable contribution to	
463	a δ -function at $x = 1$, associated with events where an initial W or Z was never	
464	emitted and thus no subsequent shower developed. Large disagreements are	
465	generically observed at these masses for electroweak dominated channels,	
466	while the agreement is better for colored initial SM states.	128
467	Figure 8.2 TODO: neutrino and bb plot with nu Sensitivities[NEEDS A SOURCE][FACT	
468	CHECK THIS]	129

469	Figure A.1 Sister figure to Figure 5.3. Sources in the first row from left to right: Bootes I, Canes Venatici I, II. In second row: Draco, Hercules, Leo I. In the first row: Leo II, Leo IV, Sextans. In the final row: Ursa Major I, Ursa Major II.	130
472	Figure B.1 Sister figure to Figure 6.2 for remaining SM primary annihilation channels studied for this thesis. These did not require any post generation smoothing and so are directly pulled from [79] with a binning scheme most helpful for a HAWC analysis.	131
476	Figure B.2 Comparison of HAWC limits from this analysis to Glory Duck (Fig. 5.5) for Coma Berenices and 7 DM annihilation channels.	141
478	Figure B.3 Same as Fig. B.2 but for Segue 1.	142
479	Figure B.4 Same as Fig. B.2 but for Sextans.	143
480	Figure C.1 Current status of spline tables according to constraints defined by Tab. 7.1. Green splines are splines that passed under the GOOD tolerance. Yellow are splines that are OK. Red are splines that FAIL. All yellow splines were inspected individually before running the analysis. Splines were made for the μ (PID 14; top panel) flavor and τ (PID 16; bottom panel) neutrino flavors.	147
485	Figure C.2 Sister figure to Fig. 7.5 for annihilation channels that did not require kernel smoothing. These spectra are the composite ($\nu_\mu + \nu_\tau$) of neutrino flavors. Every spectral model used for this analysis is featured as a colored solid line. Bluer lines are for lower DM mass spectral models. DM masses range from 681 GeV to 100 PeV.	148
490	Figure C.3 Same as Fig. 7.23 but for Segue 1 and $\chi\chi \rightarrow b\bar{b}$	149
491	Figure C.4 Same as Fig. 7.23 but for Segue 1 and $\chi\chi \rightarrow t\bar{t}$	150
492	Figure C.5 Same as Fig. 7.23 but for Segue 1 and $\chi\chi \rightarrow \nu_\mu\bar{\nu}_\mu$	151
493	Figure C.6 Same as Fig. 7.23 but for Ursa Major II and $\chi\chi \rightarrow b\bar{b}$	152
494	Figure C.7 Same as Fig. 7.23 but for Ursa Major II and $\chi\chi \rightarrow t\bar{t}$	153
495	Figure C.8 Same as Fig. 7.23 but for Ursa Major II and $\chi\chi \rightarrow \nu_\mu\bar{\nu}_\mu$	154
496	Figure C.9 IceCube North Sky Track Sensitivities for $n_s/\langle N \rangle$. n_s values are the counts fed into Eq. (7.8) to produce Fig. 7.26 and Fig. 7.25.	155
498	Figure C.10 Same as Fig. C.9 for three additional DM annihilation channels.	156

LIST OF ABBREVIATIONS

- 500 **MSU** Michigan State University
501 **LANL** Los Alamos National Laboratory
502 **DM** Dark Matter
503 **SM** Standard Model
504 **HAWC** High Altitude Water Cherenkov Observatory
505 **dSph** Dwarf Spheroidal Galaxy

506

CHAPTER 1

INTRODUCTION

507 Is the text not rendering right? Ah ok it knows im basically drafting the doc still

CHAPTER 2

508

DARK MATTER IN THE COSMOS

509 **2.1 Introduction**

510 The dark matter problem can be summarized in part by the following thought experiment.

511 Let us say you are the teacher for an elementary school classroom. You take them on a field
512 trip to your local science museum and among the exhibits is one for mass and weight. The exhibit
513 has a gigantic scale, and you come up with a fun problem for your class.

514 You ask your class, "What is the total weight of the classroom? Give your best estimation to
515 me in 30 minutes, and then we'll check your guess on the scale. If your guess is within 10% of the
516 right answer, we will stop for ice cream on the way back."

517 The students are ecstatic to hear this, and they get to work. The solution is some variation of
518 the following strategy. The students should give each other their weight or best guess if they do
519 not know. Then, all they must do is add each student's weight and get a grand total for the class.
520 The measurement on the giant scale should show the true weight of the class. When comparing
521 the measured weight to your estimation, multiply the measurement by 1.0 ± 0.1 to get the $\pm 10\%$
522 tolerances for your estimation.

523 Two of your students, Sandra and Mario, return to you with a solution.

524 They say, "We weren't sure of everyone's weight. We used 65 lbs. for the people we didn't
525 know and added everyone who does know. There are 30 of us, and we got 2,000 lbs.! That's a ton!"

526 You estimated 1,900 lbs. assuming the average weight of a student in your class was 60 lbs.
527 So, you are pleased with Sandra's and Mario's answer. You instruct your students to all gather on
528 the giant scale and read off the weight together. To all your surprise, the scale reads *10,000 lbs.*!
529 10,000 is significantly more than a 10% error from 2,000. In fact, it is approximately 5 times more
530 massive than either your or your students' estimates. You think to yourself and conclude there
531 must be something wrong with the scale. You ask an employee to check the scale and verify it is
532 well calibrated. They confirm that the scale is in working order. You weigh a couple of students
533 individually to assess that the scale is well calibrated. Sandra weighs 59 lbs., and Mario weighs

534 62 lbs., typical weights for their age. You then weigh each student individually and see that their
535 weights individually do not deviate greatly from 60 lbs. So, where does all the extra weight come
536 from?

537 This thought experiment serves as an analogy to the Dark Matter problem. The important
538 substitution to make however is to replace the students with stars and the classroom with a galaxy,
539 say the Milky Way. Individually the mass of stars is well measured and defined with the Sun as our
540 nearest test case. However, when we set out to measure the mass of a collection of stars as large as
541 galaxies, our well-motivated estimation is wildly incorrect. There simply is no way to account for
542 this discrepancy except without some unseen, or dark, contribution to mass and matter in galaxies.
543 I set out in my thesis to narrow the possibilities of what this Dark Matter could be.

544 This chapter is organized like the following... **TODO: Text should look like ... Chapter x has**
545 **blah blah blah.**

546 2.2 Dark Matter Basics

547 Presently, a more compelling theory of cosmology that includes Dark Matter (DM) in order
548 to explain a variety of observations is Λ Cold Dark Matter, or Λ CDM. I present the evidence
549 supporting Λ CDM in Section 2.3 yet discuss the conclusions of the Λ CDM model here. According
550 to Λ CDM fit to observations on the Cosmic Microwave Background (CMB), DM is 26.8% of the
551 universe's current energy budget. Baryonic matter, stuff like atoms, gas, and stars, contributes to
552 4.9% of the universe's current energy budget [1, 2, 3].

553 DM is dark; it does not interact readily with light at any wavelength. DM also does not interact
554 noticeably with the other standard model forces (Strong and Weak) at a rate that is readily observed
555 [3]. DM is cold, which is to say that the average velocity of DM is below relativistic speeds [1].
556 'Hot' DM would not likely manifest the dense structures we observe like galaxies, and instead
557 would produce much more diffuse galaxies than what is observed [3, 1]. DM is old; it played a
558 critical role in the formation of the universe and the structures within it [1, 2].

559 Observations of DM have so far been only gravitational. The parameter space available to what
560 DM could be therefore is extremely broad. The broad DM parameter space is iteratively tested in

561 DM searches by supposing a hypothesis that has not yet been ruled out and performing observations
562 to test them. When the observations yield a null result, the parameter space is constrained further.
563 I present some approaches for DM searches in Section 2.4.

564 **2.3 Evidence for Dark Matter**

565 Dark Matter (DM) has been a looming problem in physics for almost 100 years. Anomalies
566 have been observed by astrophysicists in galactic dynamics as early as 1933 when Fritz Zwicky
567 noticed unusually large velocity dispersion in the Coma cluster. Zwicky's measurement was the
568 first recorded to use the Virial theorem to measure the mass fraction of visible and invisible matter
569 in celestial bodies [4]. From Zwicky in [5], "*If this would be confirmed, we would get the surprising*
570 *result that dark matter is present in much greater amount than luminous matter.*" Zwicky's and
571 others' observation did not instigate a crisis in astrophysics because the measurements did not
572 entirely conflict with their understanding of galaxies [4]. In 1978, Rubin, Ford, and Norbert
573 measured rotation curves for ten spiral galaxies [6]. Rubin et al.'s 1978 publication presented a
574 major challenge to the conventional understanding of galaxies that could no longer be dismissed by
575 measurement uncertainties. Evidence has been mounting ever since for this exotic form of matter.
576 The following subsections provide three compelling pieces of evidence in support of the existence
577 of DM.

578 **2.3.1 First Clues: Stellar Velocities**

579 Zwicky, and later Rubin, measured the stellar velocities of various galaxies to estimate their
580 virial mass. The Virial Theorem upon which these observations are interpreted is written as

$$2T + V = 0. \quad (2.1)$$

581 Where T is the kinetic energy and V is the potential energy in a self-gravitating system. The
582 classical Newton's law of gravity from stars and gas was used for gravitational potential modeled in
583 the observed galaxies:

$$V = -\frac{1}{2} \sum_i \sum_{j \neq i} \frac{m_i m_j}{r_{ij}}. \quad (2.2)$$

584 Zwicky et al. measured just the velocities of stars apparent in optical wavelengths [5]. Rubin et al.
 585 added by measuring the velocity of the hydrogen gas via the 21 cm emission line of Hydrogen [6].
 586 The velocities of the stars and gas are used to infer the total mass of galaxies and galaxy clusters
 587 via Equation (2.1). An inferred mass is obtained from the luminosity of the selected sources. The
 588 two inferences are compared to each other as a luminosity to mass ratio which typically yielded [1]

$$\frac{M}{L} \sim 400 \frac{M_{\odot}}{L_{\odot}} \quad (2.3)$$

589 M_{\odot} and L_{\odot} referring to stellar mass and stellar luminosity, respectively. These ratios clearly indicate
 590 a discrepancy in apparent light and mass from stars and gas and their velocities.

591 Rubin et al. [6] demonstrated that the discrepancy was unlikely to be an underestimation of
 592 the mass of the stars and gas. The inferred "dark" mass was up to 5 times more than the luminous
 593 mass. This dark mass also needed to extend well beyond the extent of the luminous matter.

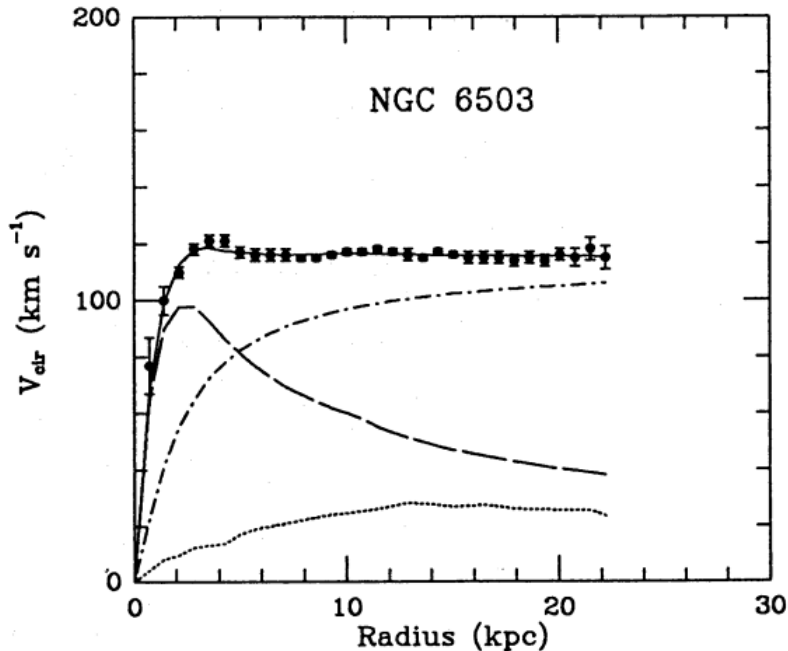


Figure 2.1 Rotation curve fit to NGC 6503 from [7]. Dashed line is the contribution from visible matter. Dotted curves are from gas. Dash-dot curves are from dark matter (DM). Solid line is the composite contribution from all matter and DM sources. Data are indicated with bold dots with error bars. Data agree strongly with a matter + DM composite prediction.

594 Figure 2.1 features one of many rotation curves plotted from the stellar velocities within galaxies.

595 The measured rotation curves mostly feature a flattening of velocities at higher radius which is not
596 expected if the gravity was only coming from gas and luminous matter. The extension of the
597 flat velocity region also indicates that the DM is distributed far from the center of the galaxy.
598 Modern velocity measurements include significantly larger objects, galactic clusters, and smaller
599 objects, dwarf galaxies. Yet, measurements along this regime are leveraging the Virial theorem
600 with Newtonian potential energies. We know Newtonian gravity is not a comprehensive description
601 of gravity. New observational techniques have been developed since 1978, and those are discussed
602 in the following sections.

603 **2.3.2 Evidence for Dark Matter: Gravitational Lensing**

604 Modern evidence for dark matter comes from new avenues beyond stellar velocities. Grav-
605 itational lensing from DM is a new channel from general relativity. General relativity predicts
606 aberrations in light caused by massive objects. In recent decades we have been able to measure the
607 lensing effects from compact objects and DM halos. Figure 2.2 shows how different massive ob-
608 jects change the final image of a faraway galaxy resulting from gravitational lensing. Gravitational
609 lensing developed our understanding of dark matter in two important ways.

610 Gravitational lensing provides additional compelling evidence for DM. The observation of two
611 merging galactic clusters in 2006, shown in Figure 2.3, provided a compelling argument for DM
612 outside the Standard Model. These clusters merged recently in astrophysical time scales. Galaxies
613 and star cluster have mostly passed by each other as the likelihood of their collision is low. Therefore,
614 these massive objects will mostly track the highest mass, dark and/or baryonic, density. Yet, the
615 intergalactic gas is responsible for the majority of the baryonic mass in the systems [4]. These gas
616 bodies will not phase through and will heat up as they collide together. The hot gas is located via
617 x-ray emission from the cluster. Two observations of the clusters were performed independently of
618 each other.

619 The first was the lensing of light around the galaxies due to their gravitational influences.
620 When celestial bodies are large enough, the gravity they exert bends space and time itself. The
621 warped space-time lenses light and will deflect in an analogous way to how glass lenses will bend

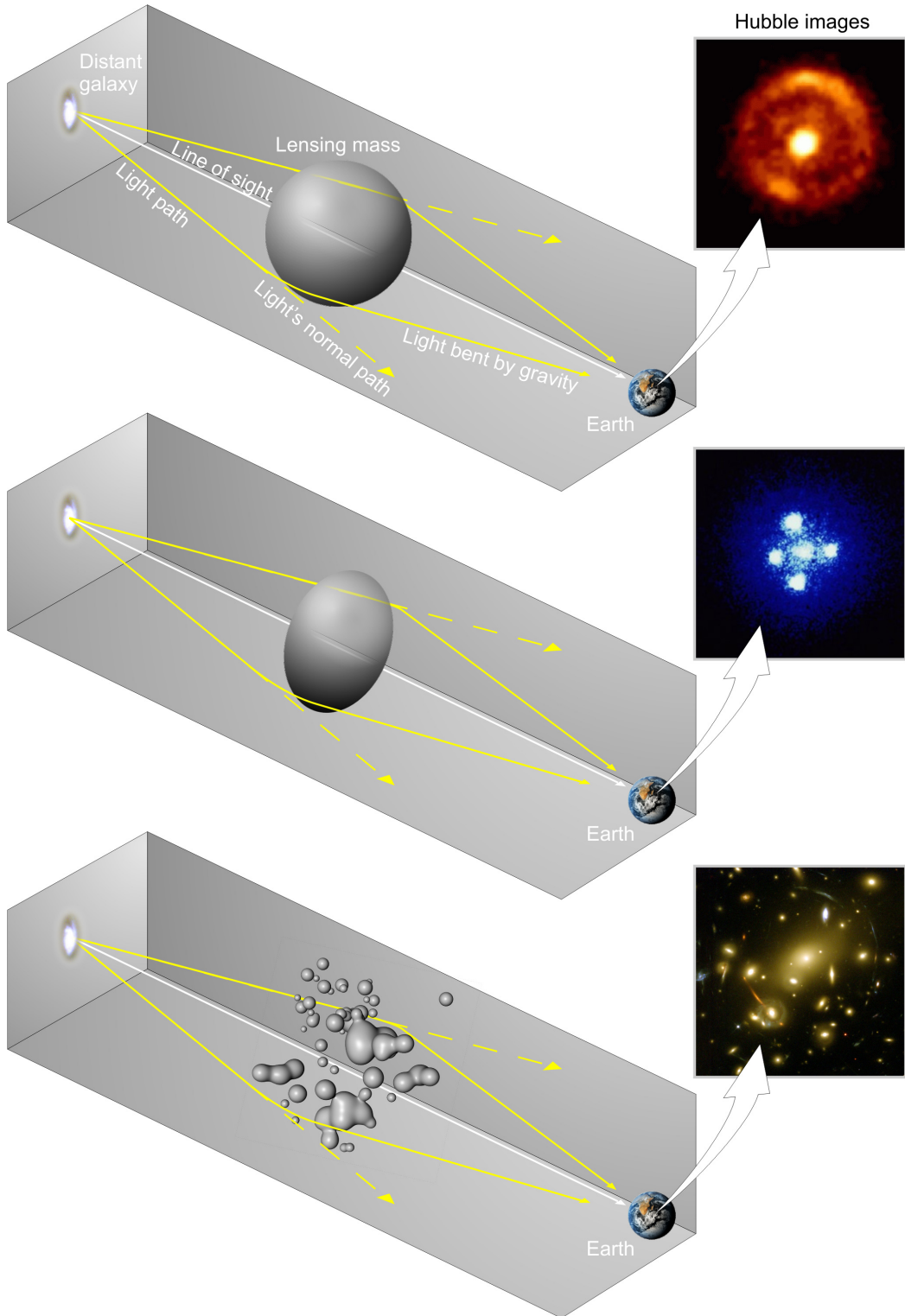


Figure 2.2 Light from distant galaxy is bent in unique ways depending on the distribution of mass between the galaxy and Earth. Yellow dashed lines indicate where the light would have gone if the matter were not present [8].

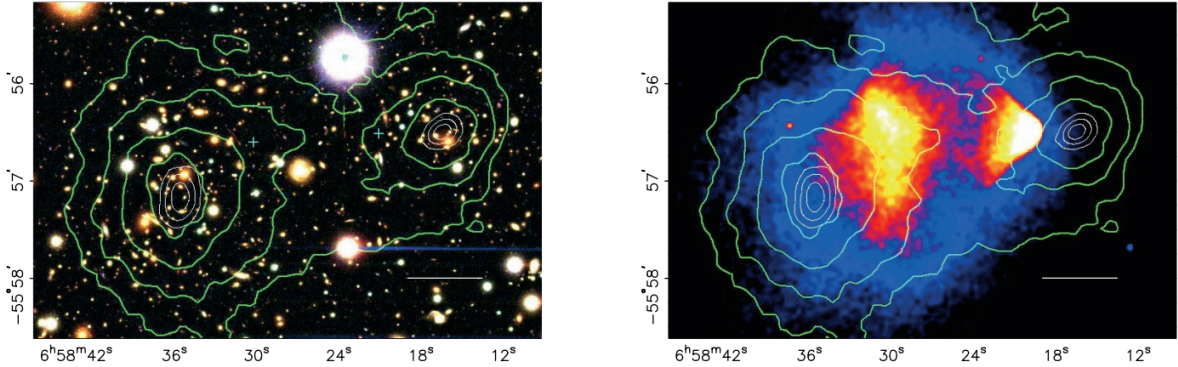


Figure 2.3 (left) Optical image of galactic cluster 1E0657-558. (right) X-ray image of the cluster with redder meaning hotter and higher baryon density. (both) Green contours are reconstruction of gravity contours from weak lensing. White rings are the best fit mass maxima at 68.3%, 95.5%, and 99.7% confidence. The matter maxima of the clusters are clearly separated from x-ray maxima. [9]

622 light, see Figure 2.2. With a sufficient understanding of light sources behind a massive object, we
 623 can reconstruct the contours of the gravitational lenses. The gradient of the contours shown in
 624 Figure 2.3 then indicates how dense the matter is and where it is.

625 The x-ray emission can then be observed from the clusters. Since these galaxies are mostly gas
 626 and are merging, then the gas should be getting hotter. If they are merging, the x-ray emissions
 627 should be the strongest where the gas is mostly moving through each other. Hence, X-ray emission
 628 maps out where the gas is in the merging galaxy cluster.

629 The lensing and x-ray observations were done on the Bullet cluster featured on Figure 2.3.
 630 The x-ray emissions do not align with the gravitational contours from lensing. The incongruence
 631 in mass density and baryon density suggests that there is a lot of matter somewhere that does
 632 not interact with light. Moreover, this dark matter cannot be baryonic [9]. The Bullet Cluster
 633 measurement did not really tell us what DM is exactly, but it did give the clue that DM also does
 634 not interact with itself very strongly. If DM did interact strongly with itself, then it would have been
 635 more aligned with the x-ray emission [9]. There have been follow-up studies of galaxy clusters with
 636 similar results. The Bullet Cluster and others like it provide a persuasive case against something
 637 possibly amiss in our gravitational theories.

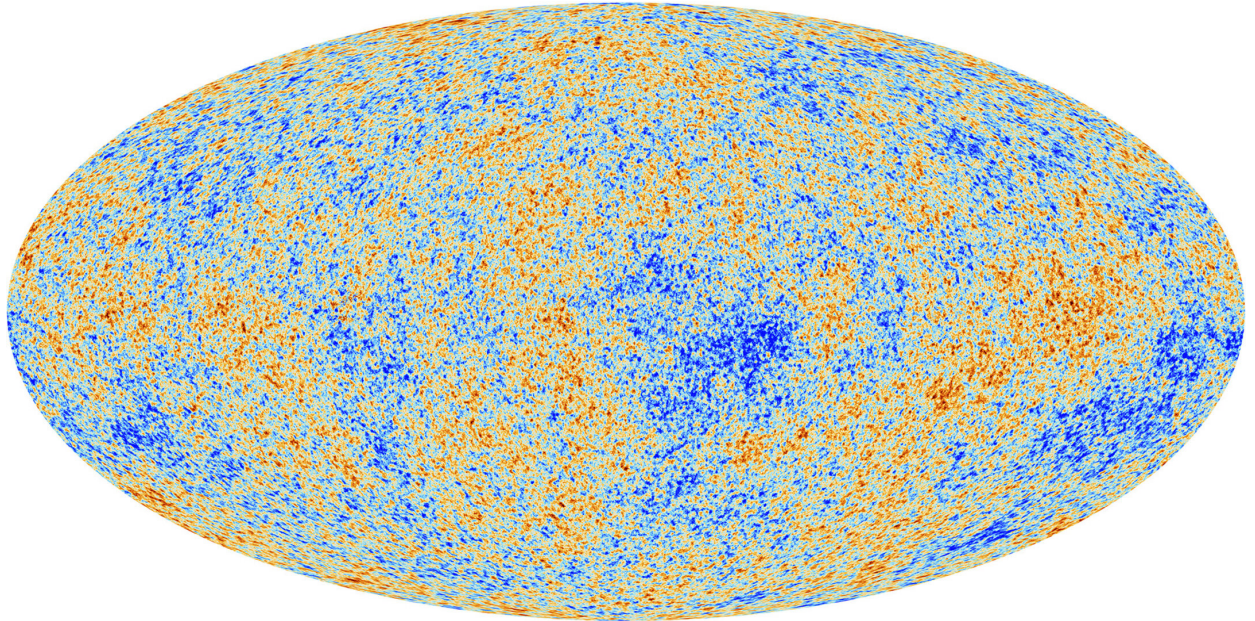


Figure 2.4 Plank CMB sky. Sky map features small variations in temperature in primordial light. These anisotropies are used to make inferences about the universe's energy budget and developmental history. [10]

638 **2.3.3 Evidence for Dark Matter: Cosmic Microwave Background**

639 The Cosmic Microwave Background (CMB) is the primordial light from the early universe
640 when Hydrogen atoms formed from the free electron and proton soup in the early universe. The
641 CMB is the earliest light we can observe; released when the universe was about 380,000 years old.
642 Then we look at how the simulated universes look like compared to what we see. Figure 2.4 is the
643 most recent CMB image from the Plank satellite after subtracting the average value and masking the
644 galactic plane [10]. Redder regions indicate a slightly hotter region in the CMB, and blue indicates
645 colder. The intensity variations are on the order of 1 in 1000 with respect to the average value.

646 The Cosmic Microwave Background shows that the universe had DM in it from an incredibly
647 early stage. To measure the DM, Dark Energy, and matter fractions of the universe from the CMB,
648 the image is analyzed into a power spectrum, which shows the amplitude of the fluctuations as
649 a function of spherical multipole moments. Λ CDM provides the best fit to the power spectra of
650 the CMB as shown in Figure 2.5. The CMB power spectrum is quite sensitive to the fraction
651 of each energy contribution in the early universe. Low l modes are dominated by variations
652 in gravitational potential. Intermediate l emerge from oscillations in photon-baryon fluid from

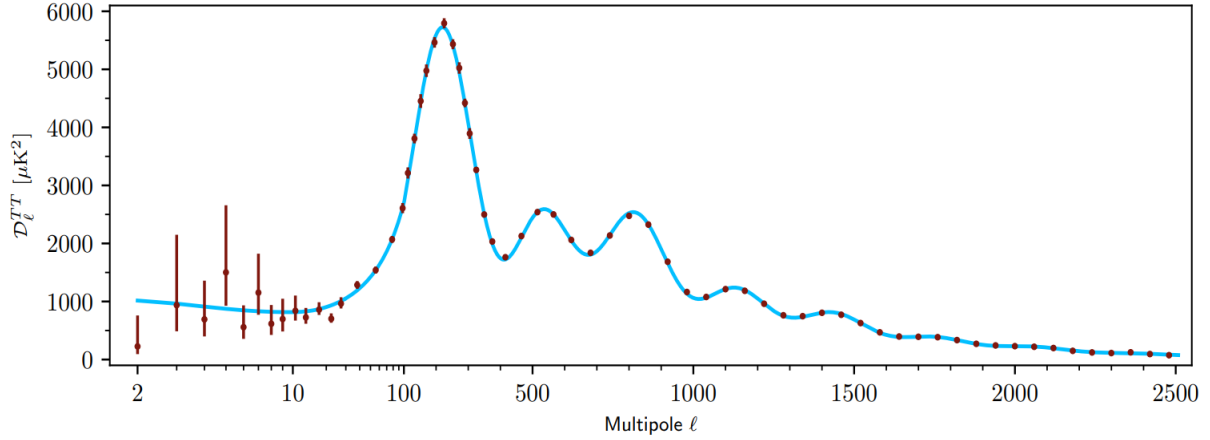


Figure 2.5 Observed Cosmic Microwave Background power spectrum as a function of multipole moment from Plank [10]. Blue line is best fit model from Λ CDM. Red points and lines are data and error, respectively.

653 competing baryon pressures and gravity. High l is a damped region from the diffusion of photons
 654 during electron-proton recombination. [1]

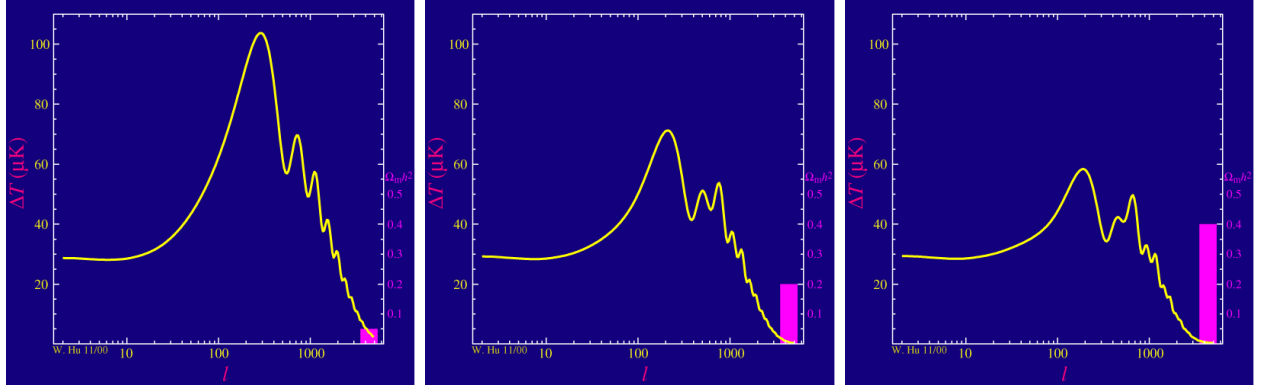


Figure 2.6 Predicted power spectra of CMB for different $\Omega_m h^2$ values for fixed baryon density from [11]. (left) Low $\Omega_m h^2$ increases the prominence of first and second peaks. (middle) $\Omega_m h^2$ is most similar to the observed power spectrum. The second and third peaks are similar in height. (right) $\Omega_m h^2$ is large which suppresses the first peak and raises the prominence of the third peak.

655 The harmonics would look quite different for a universe with less DM. Figure 2.6 demonstrates
 656 the effect $\Omega_m h^2$ has on the expected power spectrum for fixed baryon matter density. [11] Sweeping
 657 $\Omega_m h^2$ in this way clearly shows the effect dark matter has on the CMB power spectrum. The
 658 observations fit well with the Λ CDM model, and the derived fractions are as follows. The matter
 659 fraction: $\Omega_m = 0.3153$; and the baryon fraction: $\Omega_b = 0.04936$ [10]. Plank's observations also
 660 provide a measure of the Hubble constant, H_0 . H_0 especially has seen a growing tension in the

661 past decade that continues to deepened with observations from instruments like the James Webb
662 Telescope [12, 13]. As Hubble tensions deepen, we may find that perhaps Λ **CDM**, despite its
663 successes, is missing some critical physics.

664 Overall, the Newtonian motion of stars in galaxies, weak lensing from galactic clusters, and
665 power spectra from primordial light form a compelling body of research in favor of dark matter.
666 It takes another leap of theory and experimentation to make observations of DM that are non-
667 gravitational in nature. In Section 2.3, the evidence for DM implies strongly that the DM is matter
668 and not a lost parameter in the gravitational fields between massive objects. Finally, if we take one
669 axiom: that this matter has quantum behavior, such as being described by some Bohr wavelength
670 and abiding by some fermion or boson statistics; then we arrive at particle dark matter. One particle
671 DM hypothesis is the Weakly Interacting Massive Particle (WIMP). This DM candidate theory is
672 discussed further in the next section and is the focus of this thesis.

673 **2.4 Searching for Dark Matter: Particle DM**

674 Section 2.4 shows the Standard Model of particle physics and is currently the most accurate
675 model for the dynamics of fundamental particles like electrons and photons. The current status
676 of the SM does not have a viable DM candidate. When looking at the standard model, we can
677 immediately exclude any charged particle because charged particles interact strongly with light.
678 Specifically, this will rule out the following charged, fundamental particles: $e, \mu, \tau, W, u, d, s, c, t, b$
679 and their corresponding antiparticles. Recalling from Section 2.2 that DM must be long-lived and
680 stable over the age of the universe which excludes all SM particles with decay half-lives at or shorter
681 than the age of the universe. The lifetime constraint additionally eliminates the Z and H bosons.
682 Finally, the candidate DM needs to be somewhat massive. Recall from Section 2.2 that DM is cold
683 or not relativistic through the universe. This eliminates the remaining SM particles: $\nu_{e,\mu,\tau}, g, \gamma$ as
684 DM candidates. Because there are no DM candidates within the SM, the DM problem strongly
685 hints to physics beyond the SM (BSM).

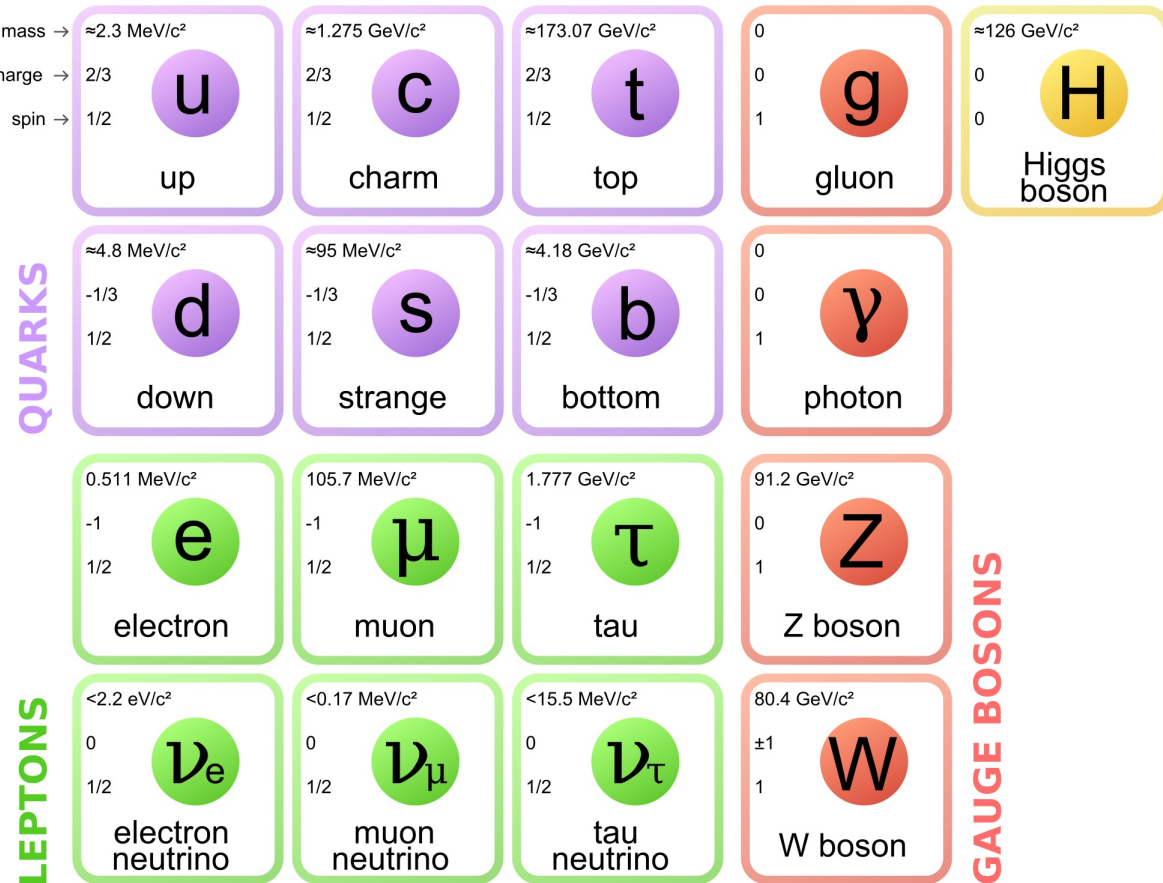


Figure 2.7 The Standard Model (SM) of particle physics. Figure taken from <http://www.quantumdiaries.org/2014/03/14/the-standard-model-a-beautiful-but-flawed-theory/>

686 2.4.1 Shake it, Break it, Make it

687 When considering DM that couples in some way with the SM, the interactions are roughly
 688 demonstrated by interaction demonstrated in Figure 2.8. The figure is a simplified Feynman
 689 diagram where the arrow of time represents the interaction modes of: **Shake it, Break it, Make it**.

690 **Shake it** refers to the direct detection of dark matter. Direct detection interactions start with
 691 a free DM particle and an SM particle. The DM and SM interact via elastic or inelastic collision
 692 and recoil away from each other. The DM remains in the dark sector and imparts some momentum
 693 onto the SM particle. The hope is that the momentum imparted onto the SM particle is sufficiently
 694 high enough to pick up with extremely sensitive instruments. Because we cannot create the DM in
 695 the lab, a direct detection experiment must wait until DM is incident on the detector. Most direct
 696 detection experiments are therefore placed in low-background environments with inert detection

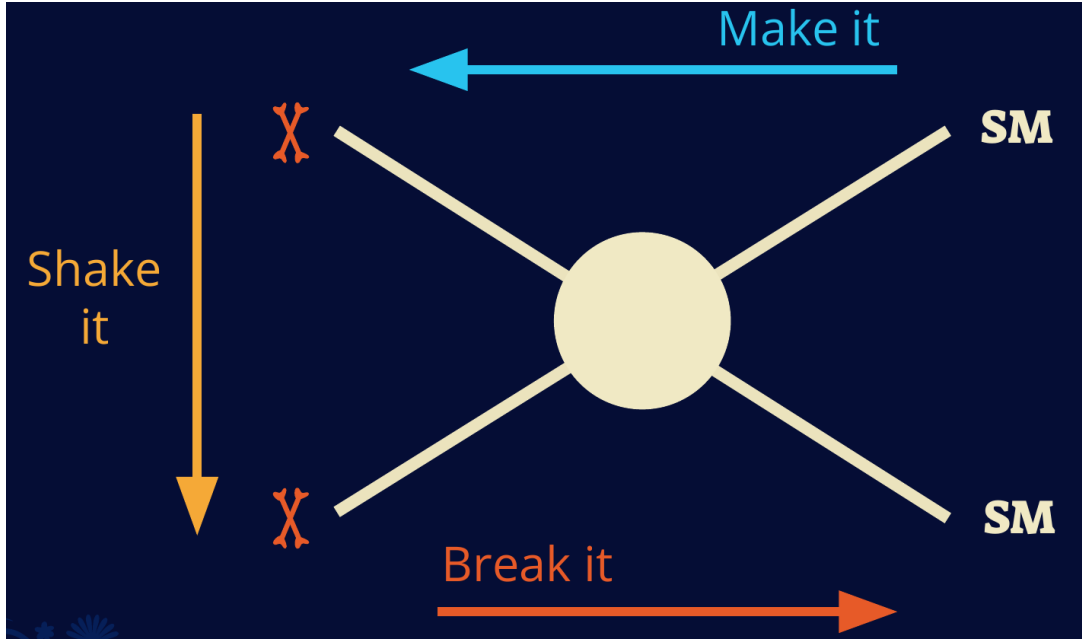


Figure 2.8 Simplified Feynman diagram demonstrating different ways DM can interact with SM particles. The 'X's refer to the DM particles whereas the SM refer to fundamental particles in the SM. The large circle in the center indicates the vertex of interaction and is purposely left vague. The colored arrows refer to different directions of time as well as their respective labels. The arrows indicate the initial and final state of the DM -SM interaction in time.

697 media like the noble gas Xenon. [14]

698 **Make it** refers to the production of DM from SM initial states. The experiment starts with
 699 particles in the SM. These SM particles are accelerated to incredibly high energies and then collide
 700 with each other. In the confluence of energy, DM hopefully emerges as a byproduct of the SM
 701 annihilation. Often it is the collider experiments that are energetic enough to hypothetically produce
 702 DM. These experiments include the world-wide collaborations ATLAS and CMS at CERN where
 703 proton collide together at extreme energies. The DM searches, however, are complex. DM likely
 704 does not interact with the detectors and lives long enough to escape the detection apparatus of
 705 CERN's colliders. This means any DM production experiment searches for an excess of events
 706 with missing momentum or energy in the events. An example event with missing transverse
 707 momentum is shown in Figure 2.9. The missing momentum with no particle tracks implies a
 708 neutral particle carried the energy out of the detector. However, there are other neutral particles
 709 in the SM, like neutrons or neutrinos, so any analysis has to account for SM signatures of missing

710 momentum. [15]

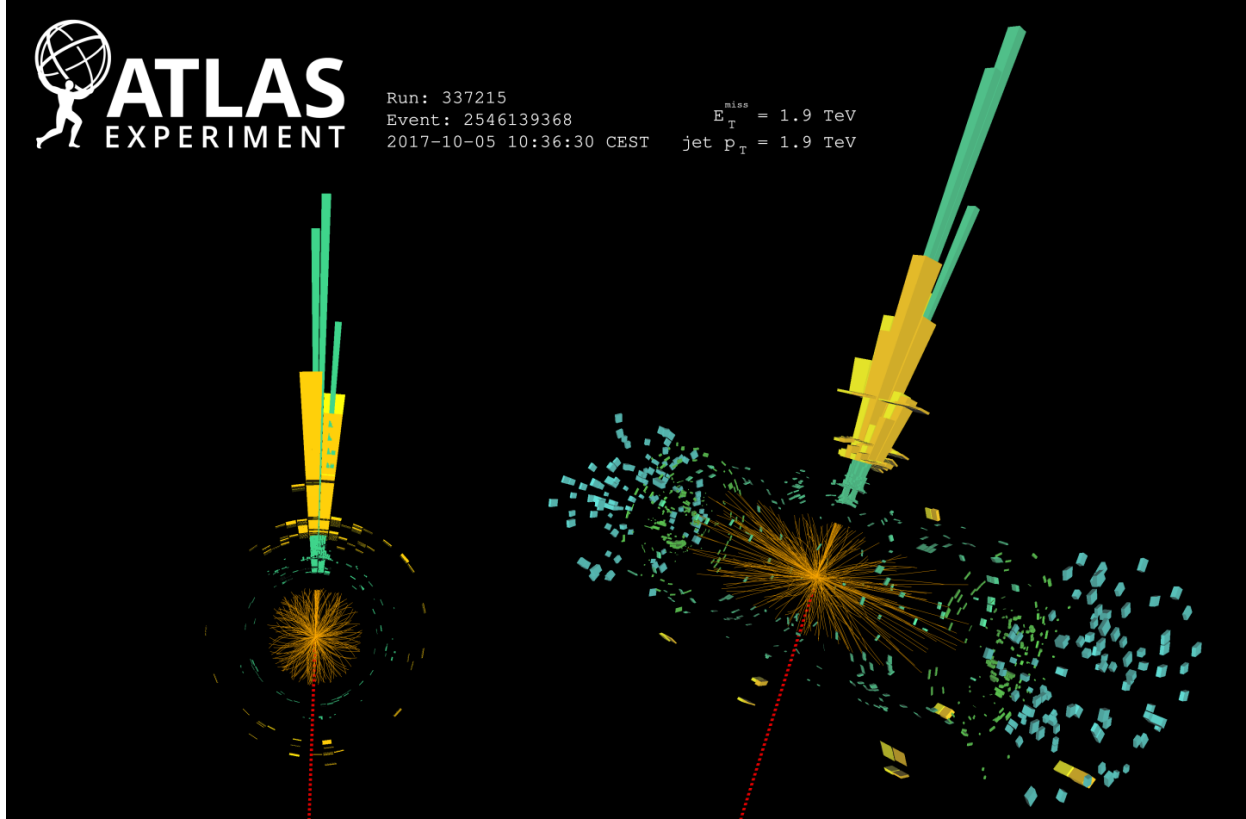


Figure 2.9 A single jet event in ATLAS detector from 2017 [16]. Jet momentum was observed to be 1.9 TeV. Missing transverse momentum was observed to be 1.9 TeV compared to the initial transverse momentum of the event was 0. Implied MET is traced by a red dashed line in event display.

711 **2.4.2 Break it: Standard Model Signatures of Dark Matter through Indirect Searches**

712 **Break it** refers to the creation of SM particles from the dark sector, and it is the primary focus
713 of this thesis. The interaction begins with DM or in the dark sector. The hypothesis is that this
714 DM will either annihilate with itself or decay and produce an SM byproduct. This method is
715 often referred to as the Indirect Detection of DM because we have no lab to directly control or
716 manipulate the DM. Therefore, most indirect DM searches are performed using observations of
717 known DM densities among the astrophysical sources. The strength is that we have the whole of the
718 universe and its 13.6-billion-year lifespan to use as a detector and particle accelerator. Additionally,
719 locations of dark matter are well cataloged since it was astrophysical observations that presented

720 the problem of DM in the first place.

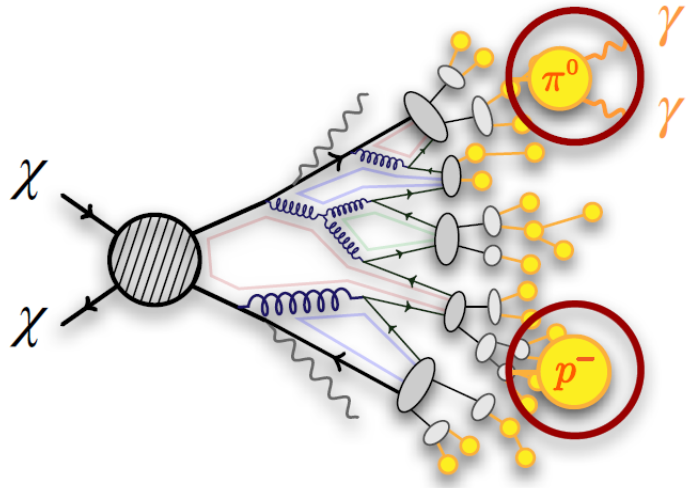


Figure 2.10 More detailed pseudo-Feynman diagram of particle cascade from dark matter annihilation into 2 quarks. The quarks hadronize and down to stable particles like γ or the anti-proton (p^-). Diagram pulled from ICRC 2021 presentation on DM annihilation search [17].

721 However, anything can happen in the universe. There are many difficult to deconvolve back-
722 grounds when searching for DM. One prominent example is the galactic center. We know the
723 galactic center has a large DM content because of stellar kinematics in our Milky Way and DM halo
724 simulations. Yet, any signal from the galactic center is challenging to parse apart from the extreme
725 environment of our supermassive black hole, unresolved sources, and diffuse emission from the
726 interstellar medium [18]. Despite the challenges, any DM model that yields evidence in the other
727 two observation methods, **Shake it or Make it** must be corroborated with indirect observations of
728 the known DM sources. Without corroborating evidence, DM observation in the lab is hard-pressed
729 to demonstrate that it is the model contributing to the DM seen at the universal scale.

730 In the case of WIMP DM, signals are described in terms of primary SM particles produced
731 from DM decay or annihilation. The SM initial state particles are then simulated down to stable
732 final states such as the γ , ν , p , or e which can traverse galactic lengths to reach Earth.

733 Figure 2.10 shows the quagmire of SM particles that emerges from SM initial states that are not
734 stable [17]. There are many SM particles with varying energies that can be produced in such an

735 interaction. For any arbitrary DM source and stable SM particle, the SM flux from DM annihilating
 736 to a neutral particle in the SM, ϕ , from a region in the sky is described by the following.

$$\frac{d\Phi_\gamma}{dE_\gamma} = \frac{\langle\sigma v\rangle}{8\pi m_\chi^2} \frac{dN_\gamma}{dE_\gamma} \times \int_{\text{source}} d\Omega \int_{l.o.s} \rho_\chi^2 dl(r, \theta') \quad (2.4)$$

737 In Equation (5.1), $\langle\sigma v\rangle$ is the velocity-weighted annihilation cross-section of DM to the SM. m_χ
 738 refers to the mass of DM, noted with Greek letter χ . $\frac{dN_\phi}{dE_\phi}$ is the N particle flux weighted by the
 739 particle energy. An example is provided in Figure 2.11 for the γ final state. The integrated terms
 740 are performed over the solid angle, $d\Omega$, and line of sight, l.o.s. ρ is the density of DM for a
 741 location (r, θ') in the sky. The terms left of the '×' are often referred to as the particle physics
 742 component. The terms on the right are referred to as the astrophysical component. For decaying
 743 DM, the equation changes to...

$$\frac{d\Phi_\phi}{dE_\phi} = \frac{1}{4\pi\tau m_\chi} \frac{dN_\phi}{dE_\phi} \times \int_{\text{source}} d\Omega \int_{l.o.s} \rho_\chi dl(r, \theta') \quad (2.5)$$

744 In Equation (2.5), τ is the decay lifetime of the DM. Just as in Equation (5.1), the left and right
 745 terms are the particle physics and the astrophysical components respectively. The integrated
 746 astrophysical component of Equation (5.1) is often called the J-Factor. Whereas the integrated
 747 astrophysical component of Equation (2.5) is often called the D-Factor.

748 Exact DM $\text{DM} \rightarrow \text{SM SM}$ branching ratios are not known, so it is usually assumed to go 100%
 749 into an SM particle/anti-particle. Additionally, when a DM annihilation or decay produces one of
 750 the neutral, long-lived SM particles (ν or γ), the particle is traced back to a DM source. For DM
 751 above GeV energies, there are very few SM processes that can produce particles with such a high
 752 energy. Seeing such a signal would almost certainly be an indication of the presence of dark matter.
 753 Fortunately, the universe provides us with the largest volume and lifetime ever for a particle physics
 754 experiment.

755 2.5 Sources for Indirect Dark Matter Searches

756 The first detection of DM relied on optical observations. Since then, we have developed new
 757 techniques to find DM dense regions. As described in Section 2.3.1, many DM dense regions were
 758 through observing galactic rotation curves. Our Milky Way galaxy is among DM dense regions

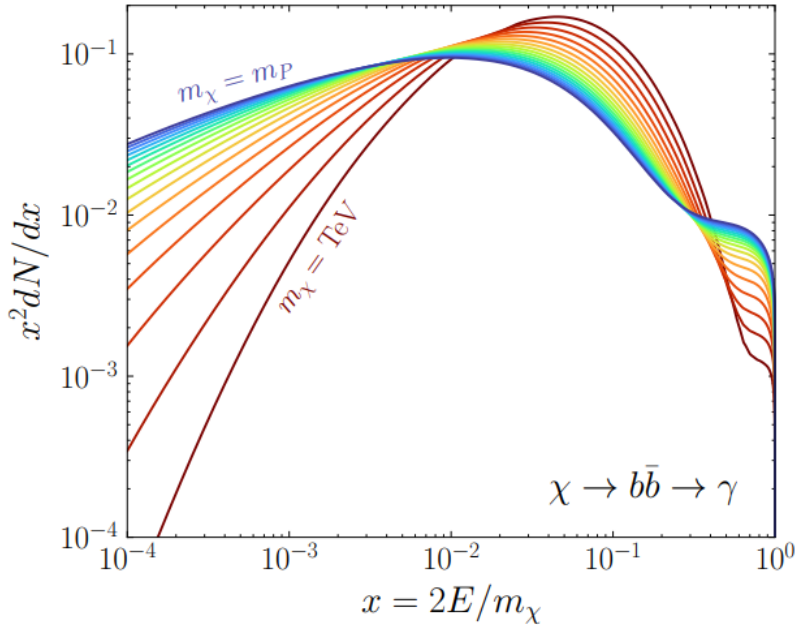


Figure 2.11 Dark Matter (DM) decay spectrum for $b\bar{b}$ initial state and γ final state. Redder spectra are for larger DM masses. Bluer spectra are light DM masses. x is a unitless factor defined as the ratio of the mass of DM, m_χ , and the final state particle energy E_γ . Figure from [19].

discovered, and it is the largest nearby DM dense region to look at. Additionally, the DM halo surrounding the Milky Way is clumpy [18]. There are regions in the DM halo of the Milky Way that have more DM than others that have captured gas over time. These sub-halos were dense enough to collapse gas and form stars. These apparent sub galaxies are known as dwarf spheroidal galaxies and are the main sources studied in this thesis. Each source type comes with different trade-offs. Galactic Center studies will be very sensitive to the assumed distribution of DM. The central DM density can vary substantially as demonstrated in Figure 2.12. At distances close to the center of the galaxy, or small r , the differences in DM densities can be 3-4 orders of magnitude. Searches toward the galactic center will therefore be quite sensitive to the assumed DM distribution.

Searches toward Dwarf Spheroidal Galaxies (dSph's) suffer from uncertainties in the DM density less than the galactic center studies. This is mostly from their diminutive size being smaller than the angular resolution of most γ -ray observatories [18]. The DM content dSph's are typically determined with the Virial theorem, Equation (2.1), and are usually majority DM [18] in mass. DSph's tend to be ideal sources to look at for DM searches. Their environments are quiet with little

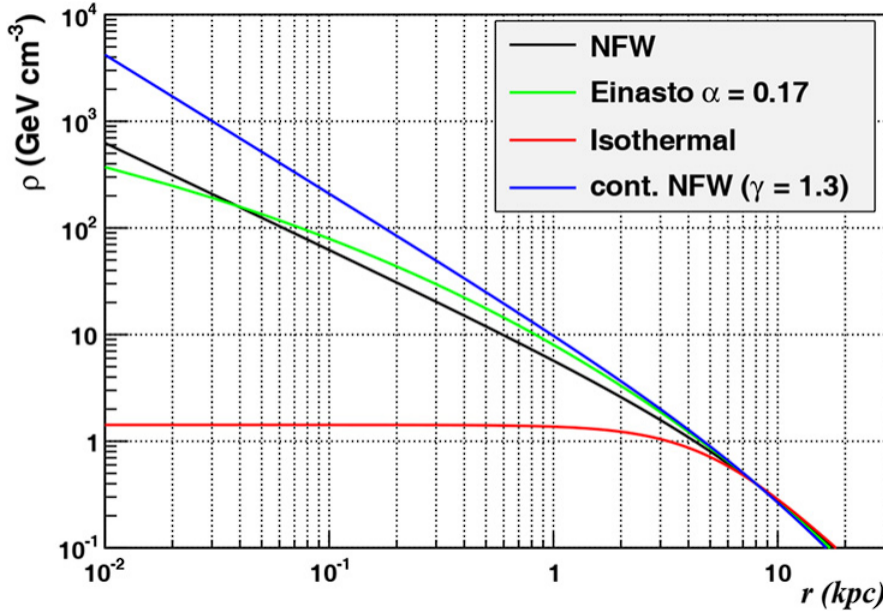


Figure 2.12 Different dark matter density profiles compared. Some models produce exceptionally large densities at small r [20].

773 astrophysical background. Unlike the galactic center, the most active components of dSph's are the
 774 stars within them versus a violent accretion disc around a black hole. All this together means that
 775 dSph's are among the best sources to look at for indirect DM searches. dSph's are the targets of
 776 focus for this thesis.

777 2.6 Multi-Messenger Dark Matter

778 Astrophysics entered a new phase in the past few decades that leverages our increasing sensitivity
 779 to SM channels and general relativity (GR). Up until the 21st century, astrophysical observations
 780 were performed with photons (γ) only. Astrophysics with this 'messenger' is fairly mature now.
 781 Novel observations of the universe have since only adjusted the sensitivity of the wavelength of
 782 light that is observed except at MeV energies. Gems like the CMB [10], and more have ultimately
 783 been observations of different wavelengths of light. Multi-messenger astrophysics proposes using
 784 other SM particles such the p^{+-} , or ν or gravitation waves predicted by general relativity.

785 The experiment LIGO had a revolutionary discovery in 2016 with the first detection of a binary
 786 black hole merger [21]. This opened the collective imagination to observing the universe through
 787 gravitational waves. There has also been a surge of interest in the neutrino (ν) sector. IceCube

788 demonstrated that we are sensitive to neutrinos in regions that correlate with significant photon
 789 emission like the galactic plane [22]. Neutrinos, like gravitational waves and light, travel mostly
 790 unimpeded from their source to our observatories. This makes pointing to the originating source
 791 of these messengers much easier than it is for cosmic rays which are deflected from their source by
 792 magnetic fields.

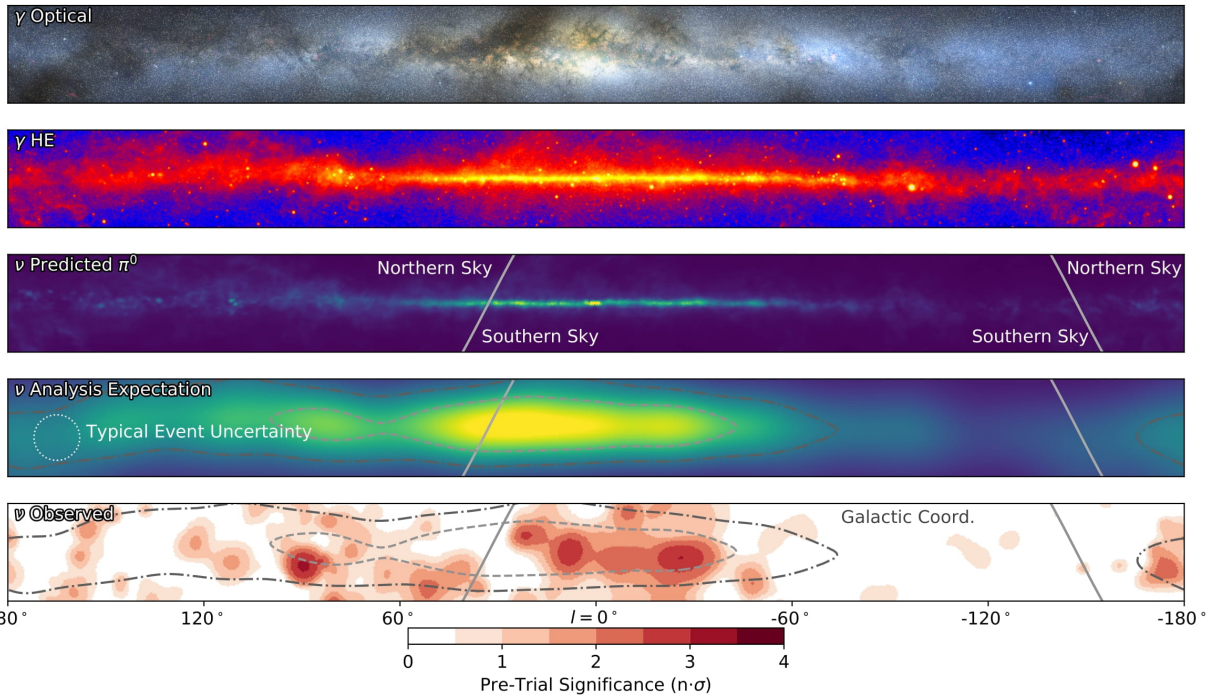


Figure 2.13 The Milky Way Galaxy in photons (γ) and neutrinos (ν) [22]. The Galactic center is at $l=0^\circ$ and is the brightest region in all panels. (top) An Optical color image of the Milky Way galaxy seen from Earth. Clouds of gas and dust obscure some light from stars. (2nd down) Integrated flux of γ -rays observed by the Fermi-LAT telescope [23]. (middle) Expected neutrino emission that corresponds with Fermi-LAT observations. (2nd up) Expected neutrino emission profile after considering detector systematics of IceCube. (bottom) Observed neutrino emission from region of the galactic plane. Substantial neutrino emission was detected.

793 The IceCube collaboration recently published a groundbreaking result of the Milky Way in
 794 neutrinos. The recent result from IceCube, shown in Figure 2.13, proves that we can make
 795 observations under different messenger regimes. The top two panels show the appearance of the
 796 galactic plane to different wavelengths of light. Some sources are more apparent in some panels,
 797 while others are not. This new channel is powerful because neutrinos are readily able to penetrate
 798 through gas and dust in the Milky Way. This new image also refines our understanding of how high

799 energy particles are produced. For example, the fit to IceCube data prefers neutrino production
 800 from the decay of π^0 [22].

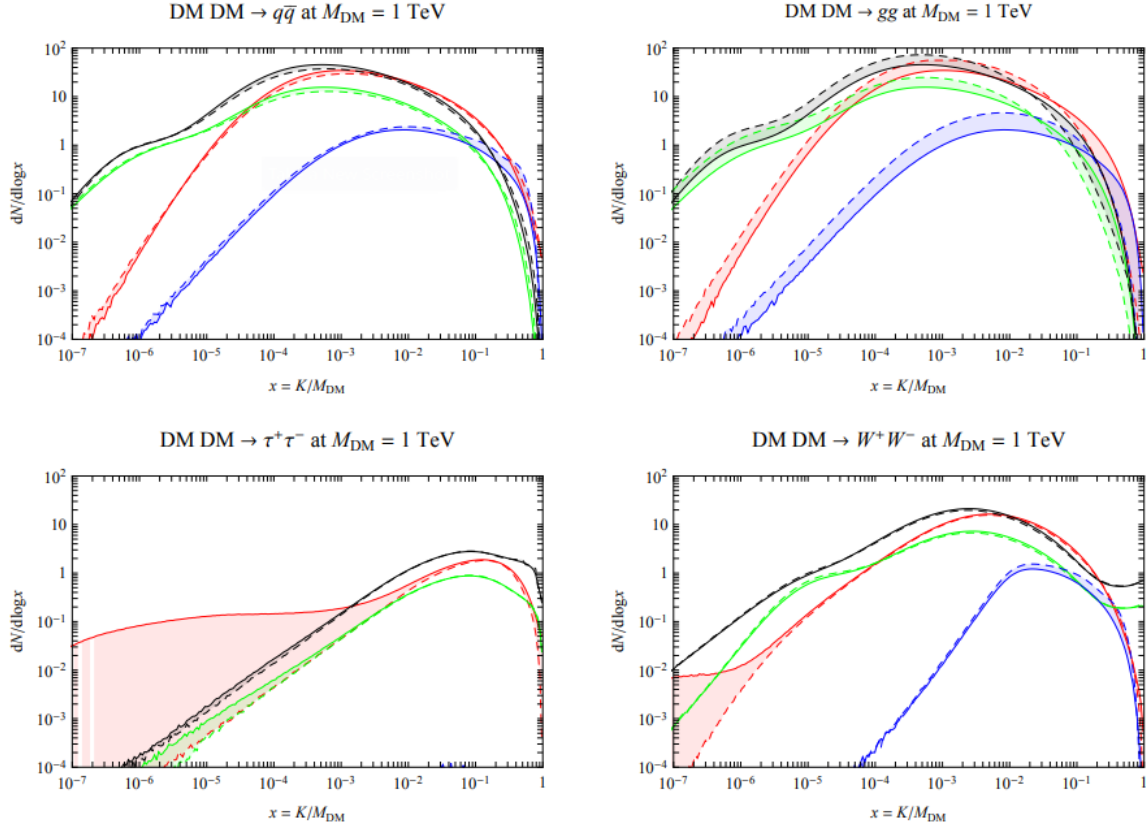


Figure 2.14 Dark Matter annihilation spectra for different final state particle and standard model annihilation channels [24]. Photons (red), e^\pm (green), \bar{p} (blue), ν (black).

801 Exposing our observations to more cosmic messengers greatly increases our sensitivity to
 802 rare processes. In the case of DM, Figure 2.14, there are many SM particles produced in DM
 803 annihilation. Among the final state fluxes are gammas and neutrinos. Charged particles are also
 804 produced however they would not likely make it to Earth since they will be deflected by magnetic
 805 fields between the source and Earth. This means observatories that can see the neutral messengers
 806 are especially good for DM searches and for combining data for a multi-messenger DM search.

CHAPTER 3

807

HIGH ALTITUDE WATER CHERENKOV (HAWC) OBSERVATORY

808



Figure 3.1 Photo of the HAWC detector that I took on May 17, 2023. Main array is centered in the photo and comprised of the larger tanks. Outriggers are the smaller tanks around the main array.

809

The High Altitude Water Cherenkov (HAWC) Observatory is a specialized instrument designed

810

for the observation of high energy gamma-rays and cosmic rays [25]. Located on the Sierra

811

Negra volcano in Mexico, HAWC observes gamma rays and cosmic rays in the energy range of

812

approximately 100 GeV to 100'ss of TeV. HAWC is strategically situated to maximize observational

813

efficiency due to its high altitude. At an elevation of 4,100 meters, it monitors about two-thirds of

814

the sky every day with an uptime above 90%. This capability is essential for studying high-energy

815

astronomical phenomena.

816

HAWC comprises of 300 water Cherenkov detectors (WCDs) spread over 22,000 square meters.

817

Each main array detector is filled with purified water and equipped with four, upward-facing

818

photomultiplier tubes (PMTs). These PMTs detect Cherenkov radiation from charged particles

819

passing through the tanks. These charged particles are generated when a high energy gamma or

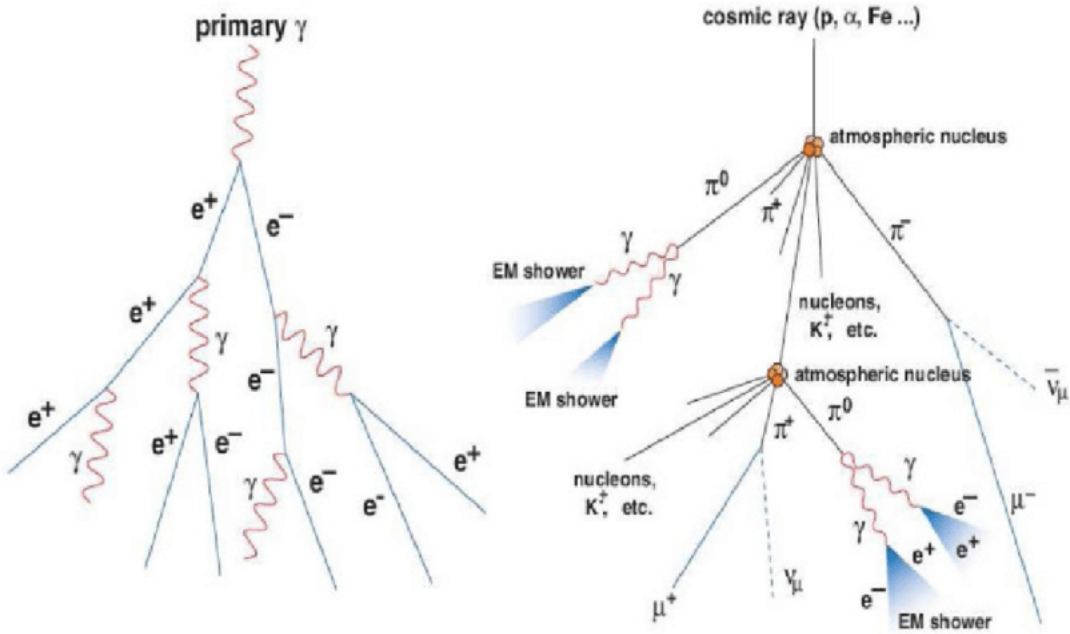


Figure 3.2 A particle physics illustration of high energy particle showers. Left shower is an electromagnetic shower from a high energy gamma-ray. Most particles in the shower will be a combination of photons and charged leptons, in this case electrons (e). Right figure shows a cosmic ray particle shower. The cosmic ray will produce many more types of particles including pions (π), neutrinos, and charged leptons. Figured pulled from [26].

820 cosmic ray collides with gas in the atmosphere to create a charged particle shower, see Fig. 3.2.
 821 The observatory includes a separate tank configuration which are referred to as the outriggers. They
 822 are a secondary array of 345 smaller WCD's. Surrounding the main array, each outrigger tank
 823 measures 1.55 meters in diameter and height and contain a single upward-facing eight-inch PMT.
 824 This expansion increases the instrumented footprint fourfold. It improves the reconstruction of
 825 showers extending beyond the main array, especially for events above 10 TeV. However, at the time
 826 of writing this thesis, the outriggers have not been fully integrated into HAWC's reconstruction
 827 software.

828 3.1.1 Construction and Hardware

829 Each main array WCD is a cylindrical tank with dimensions of 7.3 m in diameter and 5.4 m
 830 in height and filled with 180,000 liters of water [25]. The metal shell of these tanks is made from
 831 bolted together, corrugated, galvanized steel panels. The tanks are placed into 0.6 m deep trenches

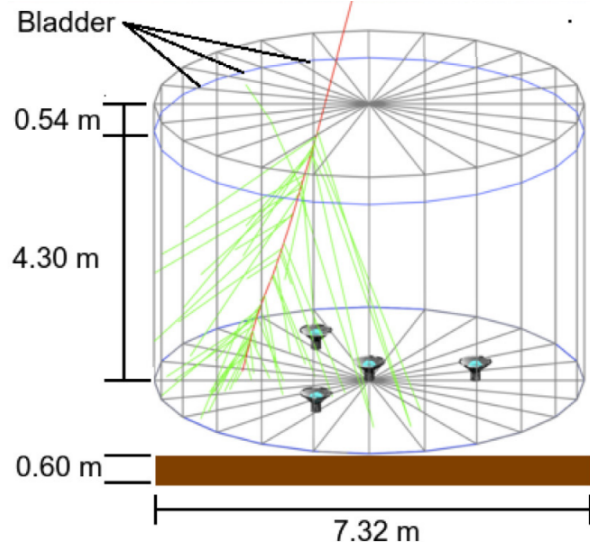


Figure 3.3 The WCDs. Left image features several WCDs looking from within the main array of HAWC. Right image shows a schematic of a WCD pulled from [25].

832 filled with rammed earth to secure it against seismic activity. The interior of each tank is lined
 833 with a black, low-density polyethylene bladder, designed to be impermeable to external light and
 834 to prevent reflection of Cherenkov light within the tank. This bladder is approximately 0.4 mm
 835 thick and composed of two layers of three-substrate film. To further minimize light penetration, a
 836 black agricultural foil covers the bladder. The ground and walls inside the tank are protected with
 837 felt and sand to safeguard against punctures. The tanks are filled 4.5 m deep of purified water,
 838 achieving a photon attenuation length for Cherenkov photons that exceeds the tank's dimensions.
 839 This purification level ensures the optimal detection environment for the photons generated by
 840 traversing charged particles.

841 At the base of each tank, four photomultiplier tubes (PMTs) are installed to detect the Cherenkov
 842 radiation emitted by charged particles. Three 8-inch diameter PMTs surround a larger 10 inch
 843 PMT from Hamamatsu [27]. The variation in PMT response is carefully accounted for in event
 844 reconstruction algorithms. Signals from the PMTs travel 610 ft cables to the counting house,
 845 where they are processed by Front-End Boards (FEBs). These FEBs, along with Time to Digital
 846 Converters (TDCs), digitize the signals and manage the high voltage supply to the PMTs.

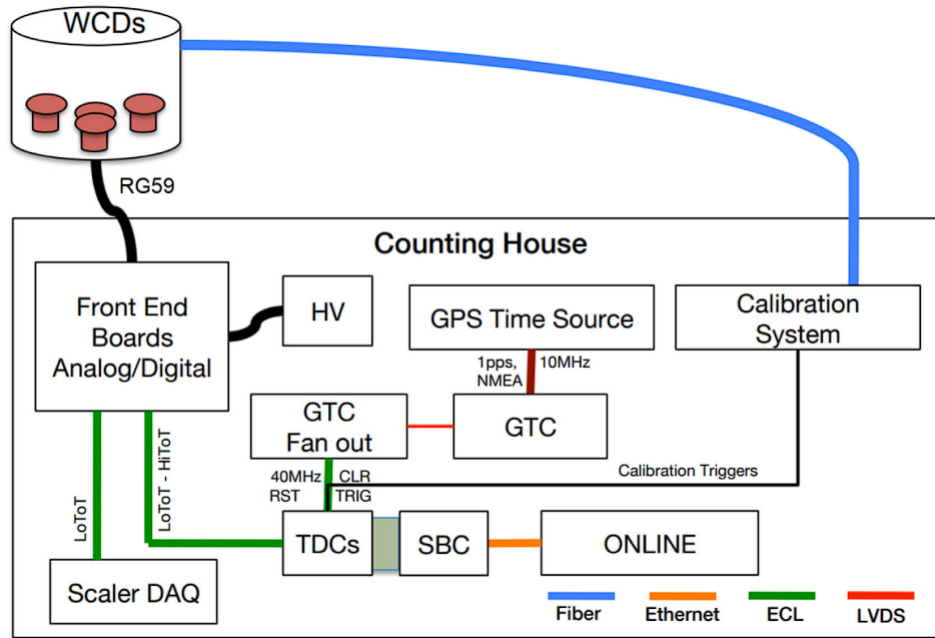


Figure 3.4 Overview of HAWC control and data electronics. The LoToT and HiToT threshold signals are discussed in Section 3.1.2. Figure from [28]

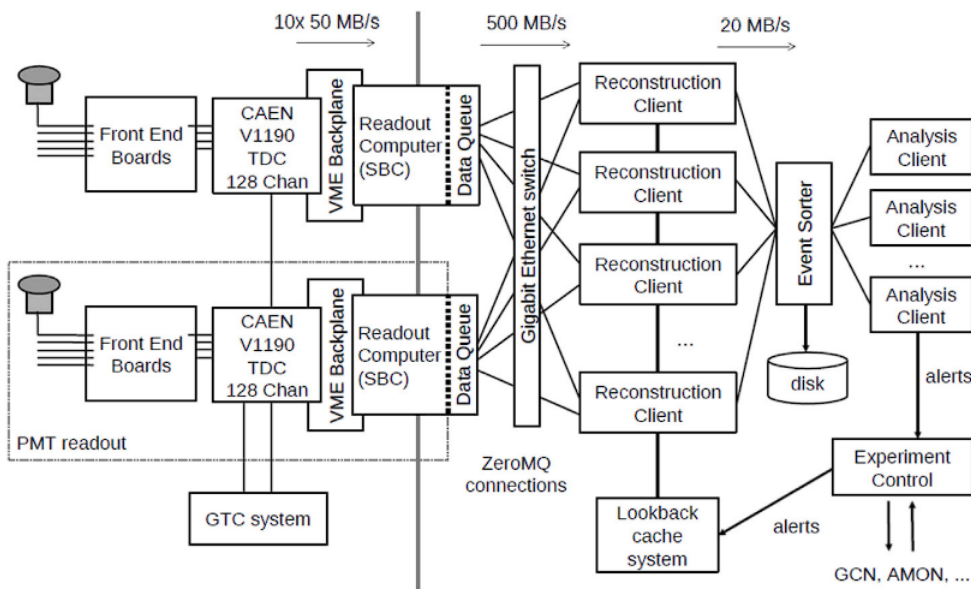


Figure 3.5 Schematic of data flow in HAWC data acquisition and online processing system. Pulled from [29].

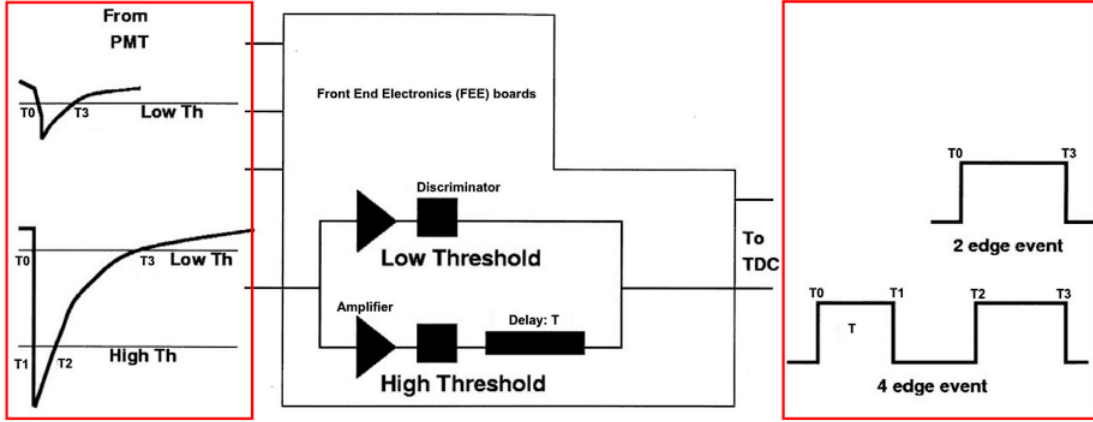


Figure 3.6 How HAWC FEB initially processes analog PMT signals. Signals are split through an amplifier and discriminator circuit. Each path is designated for either the HIGH or LOW threshold for the signal. The 2-edge event corresponds to LOW, while the 4 edge corresponds to HIGH.

847 3.1.2 Data Acquisition and Signal Processing

848 The HAWC data acquisition (DAQ) and signal processing systems convert the physical detection
 849 of particles into analyzable data. This process involves a series of steps from initial signal detection
 850 by PMTs to digital conversion and preliminary analysis, see Fig. 3.4 and Fig. 3.5.

851 Once the signal from the PMTs arrive at the counting house, they enter the Front-End Boards
 852 (FEBs). The FEBs are responsible for the initial processing of these signals, which includes
 853 amplification and integration [30]. Each PMT signal is compared against preset LOW/HIGH
 854 voltage thresholds in the FEBs Fig. 3.6, identifying signals that correspond to about 1/4 and
 855 4 photoelectrons, respectively. This differentiation allows the system to gauge the strength of
 856 the detected Cherenkov radiation. The processed signals are then digitized by Time to Digital
 857 Converters (TDCs). These converters measure the time over threshold (ToT) for each signal, a
 858 parameter that reflects both the duration and amplitude of the signal. This digitization facilitates
 859 reconstruction of the original event for translating the physical interactions within the detectors into
 860 data [28, 29, 30].

861 Synchronization across the HAWC observatory is maintained by a central GPS Timing and
 862 Control (GTC) system, which achieves a timing resolution of 98 ps. This high-resolution timing
 863 is vital for accurately reconstructing the timing and location of air showers initiated by cosmic

864 and gamma rays. The GTC system ensures that all components of the DAQ operate in unison to
865 preserve the temporal integrity of the detected events [28, 31].

866 Once digitized, the data are transferred to an online event reconstruction system. This system
867 runs the Reconstruction Client, which utilizes the raw PMT data to reconstruct the characteristics
868 of the air showers, such as their direction and energy [29]. The capacity for real-time analysis
869 allows HAWC to promptly respond to astrophysical phenomena like Gamma Ray Bursts (GRBs)
870 and to participate in multi-messenger astronomy by following up on alerts from other observatories.
871 This real-time processing system is designed to handle high data throughput, using ZeroMQ [32]
872 for efficient data transfer between software components. Analysis Clients perform specific online
873 analyses that require immediate data, including monitoring for GRBs, solar flare activity, and
874 participation in global efforts to track gravitational waves and neutrinos [28].

875 The DAQ system is overseen by an Experiment Control system and crew that manage the
876 operational aspects of data collection. This includes initiating and terminating data collection
877 runs and monitoring the experiment for errors. In the event of a system crash, often caused by
878 environmental factors such as lightning, the Experiment Control system is designed to automatically
879 restart the experiment and minimize downtime [28, 29].

880 **3.2 Event Reconstruction**

881 Event reconstruction at the HAWC Observatory is a critical procedure that converts the raw data
882 from the observatory’s WCDs into a coherent framework for understanding cosmic and gamma-
883 ray events. This process includes several distinct steps. Core Fitting determines the geometric
884 center of the air shower on the detector plane. Angle Reconstruction assesses the trajectory of the
885 incoming particle, revealing its origin in the sky. Energy Estimation is performed using both *f*-hit
886 and Neural Network (NN) methods to quantify the energy of the detected events. Gamma-hadron
887 (\tilde{G}) discrimination differentiates between gamma-ray and hadronic cosmic ray initiated showers,
888 a vital step for astrophysical interpretations. Each of these steps is integral to the observatory’s
889 objective of investigating the high-energy universe and enable the transformation of signals into
890 detailed insights about high energy cosmic phenomena.

891 **3.2.1 Core Fitting**

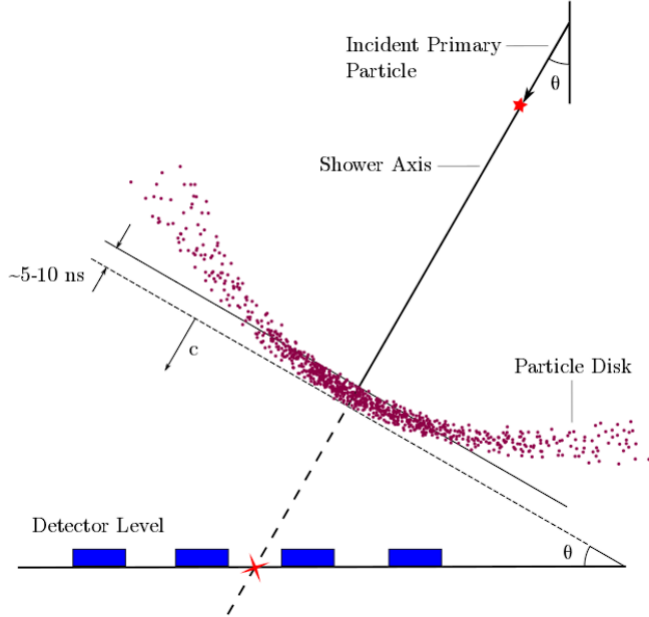


Figure 3.7 An air shower incident on WCDs. Secondary particles of an air shower travel in a cone centered on primary incident particle. Reconstruction of the initial angle is possible with arrival time of hits in PMTs inside WCDs. Figure from [33].

892 In the study of air showers, accurately determining the location of the air shower core on the
 893 ground is crucial for reconstructing the direction of the originating primary particle. An illustration
 894 of this can be seen in a HAWC event plot, where the lateral charge distribution across the array is
 895 displayed. The core is identified and marked with a red star, reconstructed using a predetermined
 896 functional form.

897 The signal S_i from the i th PMT is given by the following equation:

$$S_i = S(A, \tilde{x}, \tilde{x}_i) = A \left(\frac{1}{2\pi\sigma^2} e^{-\frac{|\vec{x}_i - \vec{x}|^2}{2\sigma^2}} + \frac{N}{(0.5 + |\vec{x}_i - \vec{x}|/R_m)^3} \right) \quad (3.1)$$

898 In this model, \tilde{x} represents the core location and \tilde{x}_i is the position of the i th PMT. R_m stands for
 899 the Molière radius, which is approximately 120 meters at the altitude of HAWC, while σ , is the
 900 standard deviation of the Gaussian distribution. The equation incorporates fixed values of $\sigma = 10$
 901 m and $N = 5.10^{-5}$. N is the normalization factor for the tail of the distribution. This leaves the
 902 core location and overall amplitude A as the free parameters to be determined during fitting.

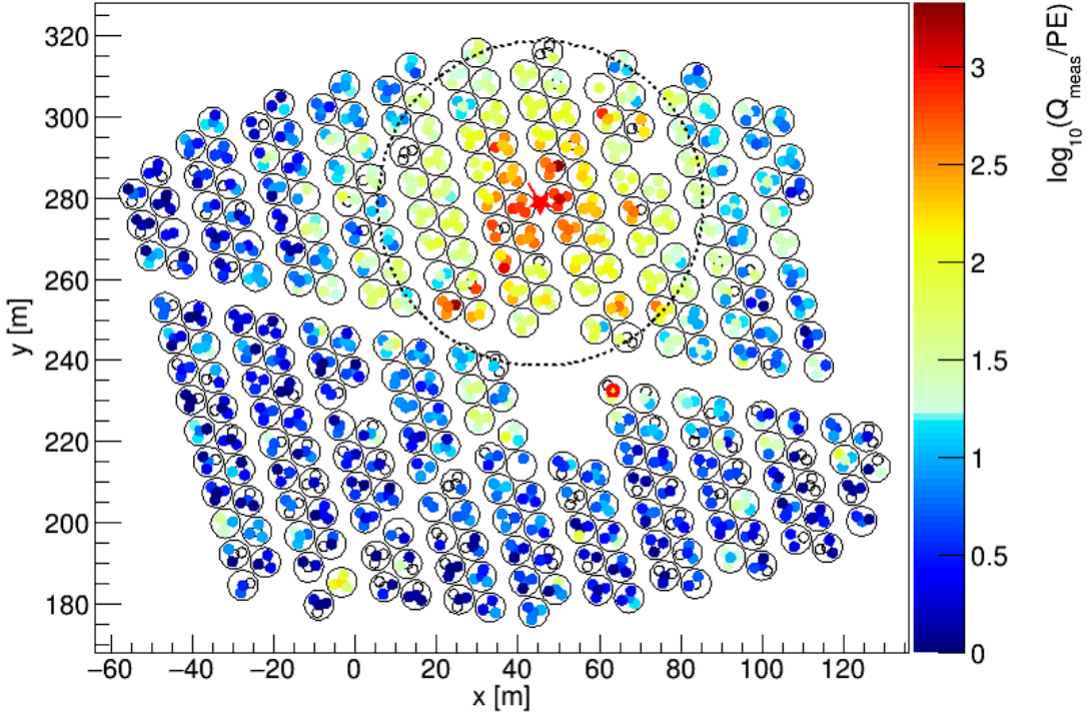


Figure 3.8 Charge deposition in each PMT for a reconstructed gamma-ray event. WCDs are outlined in black surrounding the 4 smaller circles that represent PMTs. The color scale indicates the charge deposition in each PMT. The best shower core fit from SFCF is noted with a red star in the center of the dashed circle [34].

903 The chosen functional form for the Super Fast Core Fit (SFCF) algorithm is a simplified version
 904 of a modified Nishimura-Kamata-Greisen (NKG) function [35], selected for its computational
 905 efficiency which is essential for rapid fitting of air shower cores. The SFCF form allows numerical
 906 minimization to converge more quickly due to the function's simplicity, the analytical computation
 907 of its derivatives, and the absence of a pole at the core location. Figure 2 provides a visualization
 908 of a recorded event, with the plot depicting the charge recorded by each PMT as a function of the
 909 distance to the reconstructed shower core. Through the application of the SFCF, core locations can
 910 be identified with a median error of approximately 2 meters for large events and about 4 meters for
 911 smaller ones, assuming the gamma-ray event core impacts directly upon the HAWC detector array
 912 [34]. It is noted that as the core's distance from the array increases, the precision in locating the
 913 core diminishes, highlighting the importance of proximity in the accuracy of core reconstruction.

914 **3.2.2 Angle Reconstruction**

915 After establishing the core position, the next step is angle reconstruction. This process deter-
916 mines the primary particle's trajectory. The angle of arrival is indicative of the originating gamma
917 ray's direction. It correlates to the cosmic source of the gamma-ray. We deduce this angle using
918 the timing of PMT hits [34].

919 The air shower's front is conically shaped, not flat. This shape arises from the travel patterns
920 of secondary particles. An event example is illustrated in Fig. 3.7. Far from the core, secondary
921 particles undergo multiple scattering. They also travel longer distances [36]. Particle sampling
922 decreases with distance from the core. This decrease results in measurable delays in arrival times
923 [36, 34]. Simulations provide a corrective measure for these effects. The correction is a function of
924 shower parameters [34]. It adjusts both curvature and sampling. The distance from the shower core
925 and the charge recorded by PMTs are crucial to this correction. A function based on simulation and
926 Crab Nebula observations is used for this purpose [34]. This correction is essential for accurate
927 reconstruction.

928 Corrections lead to the χ^2 minimization step. This technique fits a plane to the timing data of
929 the PMTs. It then calculates the shower's angle of arrival. The zenith and azimuth angles are the
930 result of this fitting [36]. The local angles are converted to celestial coordinates. These coordinates
931 allow correlation with gamma-ray sources. Right ascension (RA) and declination (Dec) are used
932 for this purpose. RA is akin to longitude, and Dec to latitude.

933 The reconstructed angle's resolution ranges from 0.1° to 1° . This range depends on the incoming
934 particle's energy and zenith angle [36]. The analysis uses a curvature/sampling correction. This
935 correction applies a quadratic function based on distance from the core [34]. The adjustment
936 improves angular resolution. However, discrepancies between simulation and observation persist.
937 These discrepancies introduce systematic errors into the analysis [34].

938 Angle reconstruction is vital for the HAWC Observatory. It accurately traces primary particles
939 back to their cosmic sources. This tracing allows for exact correlations with known gamma-ray
940 sources.

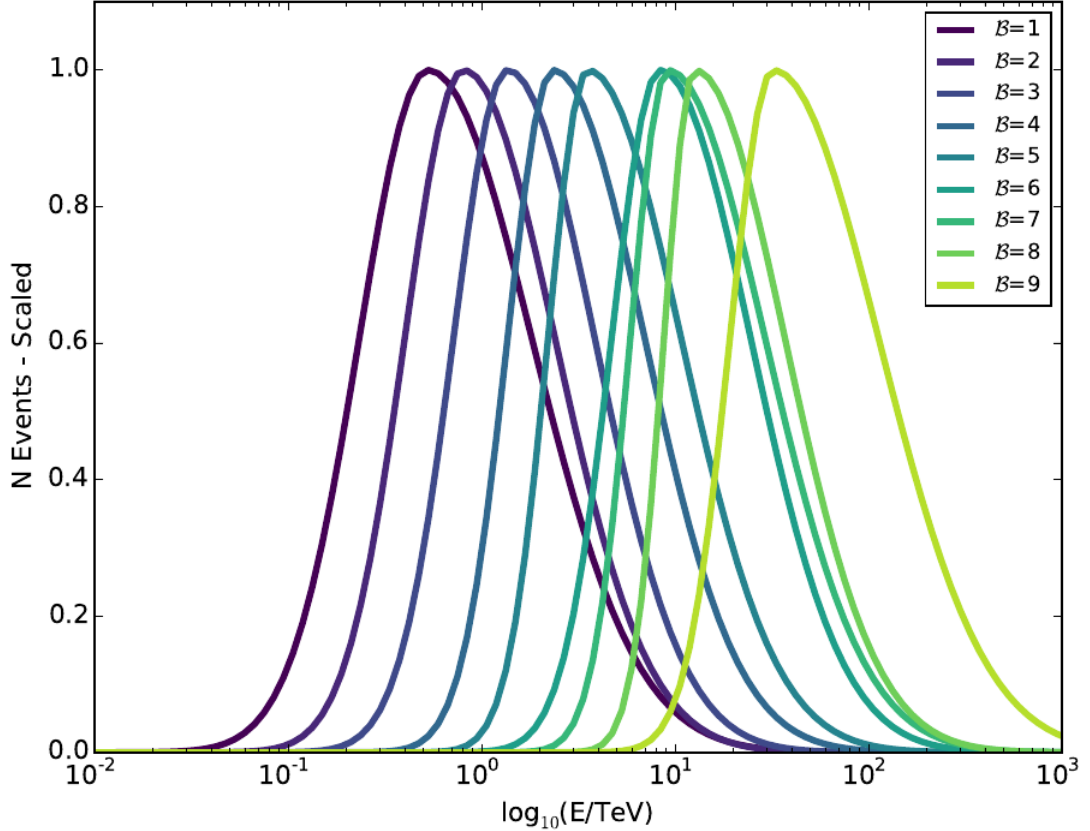


Figure 3.9 Simulated normalized energy distribution of each f_{hit} bin defined in Tab. 3.1. Monte Carlo simulation of gamma-rays with $E^{-2.63}$ spectral shape and simulated source at 20° declination. Figure from [34].

941 3.2.3 f_{hit} Energy Estimation

942 The HAWC Observatory quantifies the primary particle energy of air showers using a metric

943 known as f_{hit} . This ratio compares the count of PMTs involved in the event reconstruction to the

944 total number of functional PMTs at the time [34]. The main array consists of about 1200 PMTs,

945 but the count may vary due to maintenance or other operational factors.

946 Events are stratified into several f_{hit} bins. Each bin corresponds to a specific range of angular

947 resolutions, enabling a structured approach to event analysis based on the extent of the shower

948 footprint, Fig. 3.8. The f_{hit} metric, while effective, has several limitations. It is dependent on

949 the zenith angle and the spectral characteristics presumed for the observed source. The variable

950 also reaches a saturation point around 10 TeV, after which the detector's ability to discriminate

951 between higher energy levels diminishes [34]. Furthermore, the energy distribution for each f_{hit}

Bin	Lower Edge %	Upper Edge %	Θ_{68} ($^{\circ}$)
1	6.7	10.5	1.05
2	10.5	16.2	0.69
3	16.2	24.7	0.50
4	24.7	35.6	0.39
5	35.6	48.5	0.30
6	48.5	61.8	0.28
7	61.8	74.0	0.22
8	74.0	84.0	0.20
9	84.0	100	0.17

Table 3.1 Definitions of f_{hit} energy estimator bins. Bins are defined by the fraction of available PMTs that are triggered during an air shower event. The angular resolution, Θ_{68} , is the bin containing 68% of events [34].

952 bin is notably broad, see Fig. 3.9. In response to these limitations, HAWC has developed more
 953 intricate algorithms for energy estimation. These algorithms incorporate the zenith angle and
 954 the distribution of charge around the shower core for a more accurate assessment of the primary
 955 particle’s energy, particularly at energies surpassing 10 TeV [36].

956 The relationship between f_{hit} and primary energy is complex. Atmospheric attenuation can
 957 cause high-energy showers to present a smaller footprint, misrepresenting their energy in the f_{hit}
 958 metric. This effect is captured in simulations that chart the actual energy distribution across f_{hit}
 959 categories [36]. Such distributions vary with the declination of the source and the theoretical
 960 energy spectrum used in the model.

961 3.2.4 Neural Network Energy Estimation

962 The energy estimation for photon events at the HAWC Observatory is refined through an
 963 artificial neural network (NN) algorithm. This method, based on the Toolkit for Multivariate
 964 Analysis NN, adopts a multilayer-perceptron model with logistic activation functions across its
 965 layers. The structure includes two hidden layers, the first with 15 nodes and the second with 14,
 966 designed to process input variables through a framework optimized to closely estimate primary
 967 energies [38].

968 The NN is trained to minimize a specific error function that measures discrepancies between the
 969 NN’s energy predictions and the actual energies from Monte Carlo simulations. This minimization

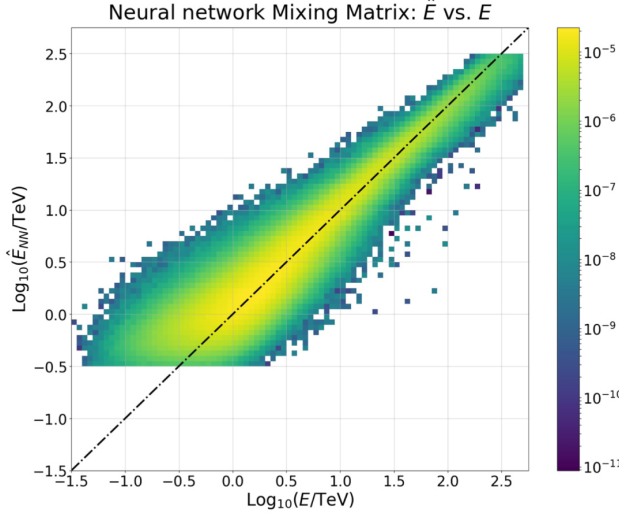


Figure 3.10 Neural Network energy estimator performance compared to true energy. The dotted line is the identity line where the estimator and injection agree. Gamma/hadron separation cuts were applied with the energy estimation. Figure pulled from [37]

970 targets an error function that incorporates the relative importance of each event, weighting the
 971 importance to mimic an E-2 power law spectrum. This approach helps achieve a uniform error
 972 rate across energies ranging from 1 to 100 TeV. The optimization process leverages the Broyden-
 973 Fletcher-Goldfarb-Shanno algorithm, ensuring a precise calibration of the NN's 479 weights [37].

974 The spectral analysis employs a binned likelihood method, using a forward-folding technique to
 975 accommodate the energy estimate's bias and resolution. This analysis benefits from a 2D binning
 976 scheme that categorizes events by both their f_{hit} value and estimated energy. The decision to use
 977 this scheme over a simple energy-based binning lies in the correlation between gamma/hadron
 978 separation parameters and the angular resolution with both the size and energy of the event. The
 979 spectrum of interest is dissected into nine f_{hit} bins, each further divided into 12 energy bins,
 980 spanning from 0.316 TeV to 316 TeV, encompassing a total of 108 bins [37]. However, not all
 981 bins contribute to the final analysis—those with low probability of event population or insufficient
 982 Monte Carlo simulation accuracy are excluded. This selective approach focuses on the central 99%
 983 of events by estimated energy within each f_{hit} category, effectively removing outliers and ensuring
 984 a robust fit [37].

985 Input variables for the NN are selected to capture key characteristics of the air shower: energy

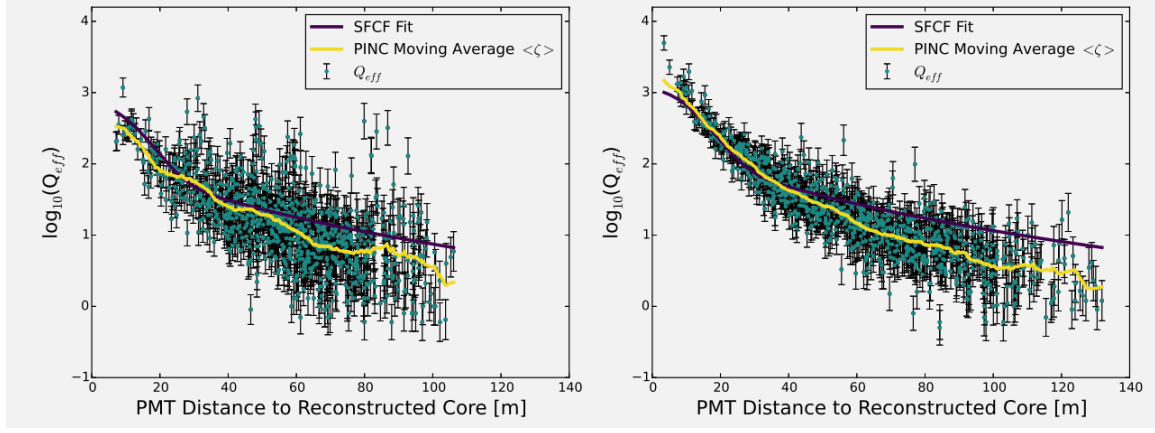


Figure 3.11 Lateral distribution functions (LDFs) for cosmic ray (left) and a photon candidate from the Crab Nebula (right). Cosmic ray LDF has clearly isolated hits far from the reconstructed shower core. Gamma-ray shower shows a more cuspy event [34].

986 deposition, containment, and atmospheric attenuation. The algorithm calculates energy deposition
 987 using the fraction of PMTs and tanks activated, alongside the logarithm of the normalization from
 988 the lateral distribution fit. Containment is inferred from the distance between the shower core and
 989 the array's center, while atmospheric attenuation is evaluated using the reconstructed zenith angle
 990 and a detailed analysis of the shower's lateral charge distribution [38, 37].

991 This refined NN energy estimation methodology is an integral component of HAWC's toolkit,
 992 enabling precise analysis of high-energy gamma-ray events. It represents a significant advancement
 993 in the field, offering deeper insights into cosmic phenomena by accurately mapping observed shower
 994 characteristics to primary particle energies.

995 3.2.5 G/H Discrimination

996 At the HAWC Observatory, distinguishing between air showers initiated by gamma rays and
 997 those by hadronic cosmic rays is fundamental for astrophysical data purity. The separation process
 998 leverages differences in shower characteristics: electromagnetic showers from gamma rays typically
 999 display fewer muons and a smoother distribution, whereas hadronic showers are more chaotic due
 1000 to the abundance of muons and hadronic sub-showers.

1001 Discrimination Parameters Two primary parameters facilitate the identification of cosmic-ray
 1002 events [34]:

1003 Compactness (C): This parameter evaluates the charge captured by PMTs, particularly focusing

1004 on the PMT with the highest effective charge beyond a 40-meter radius from the shower core.
1005 Compactness is inversely proportional to this effective charge, as higher charges at extended
1006 distances from the core are indicative of hadronic showers. It is mathematically expressed as:

$$C = \frac{N_{\text{hit}}}{CxPE_{40}} \quad (3.2)$$

1007 PINCness (P): PINCness quantifies the "clumpiness" of a shower using the charges recorded by
1008 PMTs. It is computed from the logarithm of the effective charge of each PMT hit, compared to an
1009 expected average for that annular region. A higher PINCness suggests a less smooth distribution,
1010 typical of hadronic showers. The formula is:

$$P = \frac{1}{N} \sum_{i=0}^N \frac{(\zeta_i - \langle \zeta_i \rangle)^2}{\sigma_{\zeta_i}^2} \quad (3.3)$$

1011 These parameters are accurately modeled in simulations, aligning well with observational data near
1012 gamma-ray sources like the Crab Nebula. Figures illustrating the lateral distributions for represen-
1013 tative cosmic-ray and photon candidate showers, as well as the distribution of these discrimination
1014 parameters, affirm their efficacy [34].

1015 Optimization and Application The discrimination technique has remained consistent, but cut
1016 values have been reoptimized in each 2D bin based on f_{hit} and estimated energy. This refinement
1017 enhances the selection of high-energy events. Each bin ensures at least 50% efficiency for gamma-
1018 ray detection, with efficiencies extending up to nearly 100% in certain bins [34, 37].

1019 3.3 Background Estimation: Direct Integration

1020 The ratio of cosmic rays to gamma rays can be as high as 10,000 to 1, depending on the energy.
1021 At HAWC, we confront a significant challenge even after gamma/hadron cuts: our gamma-ray data
1022 is still inundated with cosmic-ray events. To tackle this, we rely on the direct integration method
1023 developed by Milagro [39]. This method capitalizes on the cosmic rays' isotropic nature resulting
1024 from their deflection by interstellar magnetic fields.

1025 The direct integration method estimates background events by integrating over a stable two-
1026 hour period of detector operation. The expected number of background events at a particular sky

1027 location (ϕ, θ) is determined by integrating the normalized detector's efficiency with the all-sky
1028 event rate:

$$N_{\text{exp}}(\phi, \theta) = \int \int E(\text{ha}, \theta) \cdot R(t) dt dt \quad (3.4)$$

1029 Here, $E(\text{ha}, \theta)$, represents the detector's efficiency, which varies with local coordinates (hour angle
1030 and declination). $R(t)$ is the event rate as a function of time [39].

1031 Our background estimation is expected to falter in high-energy ranges where cosmic-ray events
1032 are less frequent due to enhanced gamma/hadron discrimination. Sparsity in our background and
1033 data also arise at the limits of HAWC's sensitivity and during short-term analyses of transient
1034 events. HAWC addresses these issues by using a pixel size of 0.5° in our background calculations
1035 to maintain robustness in our estimation [34, 36]. In constructing the background model, it's crucial
1036 to exclude areas of the sky with known gamma-ray sources. Regions containing the Crab Nebula,
1037 Mrk 421, Mrk 501, and the Galactic Plane are masked to prevent their significant gamma-ray
1038 signals from biasing our background estimate [34].

1039

CHAPTER 4

ICECUBE NEUTRINO OBSERVATORY

1040 **4.1 The Detector**

1041 **4.2 Events Reconstruction and Data Acquisition**

1042 **4.2.1 Angle**

1043 **4.2.2 Energy**

1044 **4.3 Northern Test Site**

1045 **4.3.1 PIgeon remote dark rate testing**

1046 **4.3.2 Bulkhead Construction**

CHAPTER 5

GLORY DUCK: MULTI-WAVELENGTH SEARCH FOR DARK MATTER ANNIHILATION TOWARDS DWARF SPHEROIDAL GALAXIES

5.1 Introduction

The field of astrophysics now has several instruments and observatories sensitive to high energy gamma-rays. The energy sensitivity for the modern gamma-ray program spans many orders of magnitude. Figure 5.1 demonstrates these comparable sensitivities across energies for the five experiments: Fermi-LAT, HAWC, HESS, MAGIC, and VERITAS.

Each of the five experiments featured in Figure 5.1 have independently searched for DM annihilation from dwarf spheroidal galaxies (dSph) and set limits on annihilation cross-section of WIMPs. Intriguingly, there are regions of substantial overlap in their energy sensitivities. This clearly motivates an analysis that combines data from these five. Each experiment has unique gamma-ray detection methods and their weaknesses and strengths can be leveraged with each other. The HAWC gamma-ray observatory is extensively introduced in chapter 3, so it is not introduced here. A brief description of the remaining experiments are in the following paragraphs.

The Large Area Telescope (LAT) is a pair conversion telescope mounted on the NASA Fermi satellite in orbit \sim 550 km above the Earth [41]. LAT's field of view covers about 20% of the whole sky, and it sweeps the whole sky approximately every 3 hours. LAT's gamma-ray energy sensitivity ranges from 20 MeV up to 1 TeV. Previous DM searches towards dSphs using Fermi-LAT are published in [42] and [43].

The High Energy Spectroscopic System (HESS), Major Atmospheric Gamma Imaging Cherenkov (MAGIC), and Very Energetic Radiation Imaging Telescope Array System (VERITAS) are arrays of Imaging Atmospheric Cherenkov Telescopes (IACT). These telescopes observe the Cherenkov light emitted from gamma-ray showers in the Earth's atmosphere. The field of view for these telescopes is no larger than 5° with energy sensitivities ranging from 30 GeV up to 100 TeV [44, 45, 46]. IACTs are able to make precise observations in selected regions of the sky, however can only be operated in ideal dark conditions. HESS's observations of the dwarves

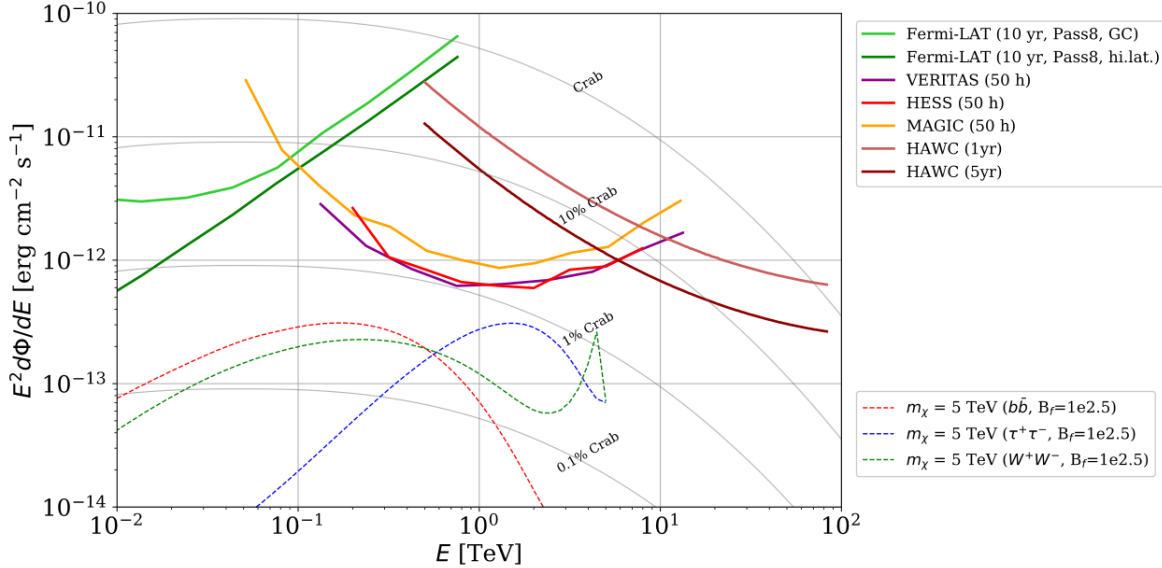


Figure 5.1 Sensitivities of five gamma-ray experiments compared to percentages of the Crab nebula’s emission and dark matter annihilation. Solid lines present estimated sensitivities to power law spectra [FACT CHECK THIS] for each experiment. Green lines are Fermi-LAT sensitivities where lighter green is the sensitivity to the galactic center and dark green is its sensitivity to higher declinations. Orange, red, and purple solid lines represent the MAGIC, HESS, and VERITAS 50 hour sensitivities respectively. The maroon and brown lines are the HAWC 1 year and 5 year sensitivities. Across four decades of gamma-ray energy, these experiments have similar sensitivities on the order 10^{-12} erg $\text{cm}^{-2}\text{s}^{-1}$. The dotted lines are estimated dark matter fluxes assuming $m_\chi = 5$ TeV DM annihilating to bottom quarks (red), tau leptons (blue), and W bosons (green). Faded gray lines outline percentage flux of the Crab nebula. Figure is an augmented version of [40]

1073 Sculptor and Carina were between January 2008 and December 2009. HESS’s observations of
 1074 Coma Berenices were taken from 2010 to 2013, and Fornax was observed in 2010 [47, 48, 49].
 1075 MAGIC provided deep observations of Segue1 between 2011 and 2013 [50]. MAGIC also provides
 1076 data for three additional dwarves: Coma Berenices, Draco, and Ursa Major II where observations
 1077 were made in: January - June 2019 [51], March - September 2018 [51], and 2014 - 2016 [52]
 1078 respectively. VERITAS provided data for Boötes I, Draco, Segue 1, and Ursa Minor from 2009 to
 1079 2016 [53].

1080 This chapter presents the Glory Duck analysis, the name given for the search for dark matter
 1081 annihilation from dSph by combining data from the five gamma-ray observatories: Fermi-LAT,
 1082 HAWC, HESS, MAGIC, and VERITAS. Specifically, the methods in analysis and modeling are
 1083 presented for the HAWC gamma-ray observatory. This work will be published in the Journal of

1084 Cosmology and Astroparticle Physics and presented at the International Cosmic Ray Conference
1085 in 2019, 2021, and 2023 [54, 55, 56] and others.

1086 **5.2 Dataset and Background**

1087 This section enumerates the data analysis and background estimation methods used for HAWC's
1088 study of dSphs. Section 5.2.1 and Section 5.2.2 are most useful for fellow HAWC collaborators
1089 looking to replicate the Glory Duck analysis.

1090 **5.2.1 Itemized HAWC files**

1091 These files are only available withing HAWC's internal documentation and collaborators. They
1092 are not meant for public access, and are presented here so that HAWC collaborators can reproduce
1093 results accurately.

- 1094 • Detector Response: `response_aerie_svn_27754_systematics_best_mc_test_noBr`
1095 `oadpulse\10pctlogchargesmearing_0.63qe_25kHzNoise_run5481_curvature`
1096 `0_index3.root`
- 1097 • Data Map: `maps-20180119/liff/maptree_1024.root`
- 1098 • Spectral Dictionary: `DM_CirrelliSpectrum_dict_gammas.npy`
- 1099 • Analysis wiki: https://private.hawc-observatory.org/wiki/index.php/Glory_Duck_Multi-Experiment_Dark_Matter_Search

1101 **5.2.2 Software Tools and Development**

1102 This analysis was performed using HAL and 3ML [34, 57] in Python version 2. I built software
1103 to implement the *A Poor Particle Physicist Cookbook for Dark Matter Indirect Detection* (PPPC)
1104 [58] DM spectral model and dSphs spatial model from [59] for HAWC analysis. A NumPy version
1105 of this dictionary was made for both Py2 and Py3. The code base for creating this dictionary is
1106 linked on my GitLab sandbox:

- 1107 • Py2: [Dictionary Generator \(Deprecated\)](#)

1108 • Py3: [PPPC2Dict](#)

1109 The analysis was performed using the f_{hit} framework as used and described in the HAWC Crab
1110 paper [34]. The Python2 NumPy dictionary file for gamma-ray final states is `dmCirSpecDict.npy`.
1111 The corresponding Python3 file is `DM_CirrelliSpectrum_dict_gammas.npy`. These files can
1112 also be used for decay channels and the PPPC describes how [58]. All other software used for data
1113 analysis, DM profile generation, and job submission to SLURM are also kept in my sandbox for
1114 [the Glory Duck](#) project.

1115 **5.2.3 Data Set and Background Description**

1116 The HAWC data maps used for this analysis contain 1017 days of data between runs 2104
1117 (2014-11-26) and 7476 (2017-12-20). They were generated from pass 4.0 reconstruction. The
1118 analysis is performed using the f_{hit} energy binning scheme with bins (1-9) similar to what was done
1119 for the Crab and previous HAWC dSph analysis [34, 60]. Bin 0 was excluded as it has substantial
1120 hadronic contamination and poor angular resolution.

1121 This analysis was done on dSphs because of their large DM mass content relative to baryonic
1122 mass. We consider the following to estimate the background to this study.

- 1123 • The dSphs' angular extent are small relative to HAWC's spatial resolution, so the analysis is
1124 not sensitive to large or small scale anisotropies.
- 1125 • The dSphs used in this analysis are off the galactic plane and therefore not contaminated by
1126 diffuse emission from the galaxy.
- 1127 • The dSphs are baryonically faint relative to their expected dark matter content and are not
1128 expected to contain high energy gamma-ray sources.

1129 Therefor we make no additional assumptions on the background from our sources and use
1130 HAWC's standard direct integration method for background estimation [34]. The largest background
1131 under this consideration is from an isotropic flux of cosmic rays. The contamination of this hadronic
1132 flux is worse at lower energies where HAWC's gamma/hadron discrimination worse. It is possible

1133 for gamma rays from DM annihilation to scatter in transit to HAWC via Inverse Compton Scattering
1134 (ICS). This was investigated and its impact on the flux is negligible. Supporting information on
1135 this is in Section 5.7.1

1136 **5.3 Analysis**

1137 The expected differential photon flux from DM-DM annihilation to standard model particles,
1138 $d\Phi_\gamma/dE_\gamma$, over solid angle, Ω , is described by the familiar equation.

$$\frac{d\Phi_\gamma}{dE_\gamma} = \frac{\langle\sigma v\rangle}{8\pi m_\chi^2} \frac{dN_\gamma}{dE_\gamma} \times \int_{\text{source}} d\Omega \int_{l.o.s} dl \rho_\chi^2 J(r, \theta') \quad (5.1)$$

1139 Where $\langle\sigma v\rangle$ is the velocity weighted annihilation cross-section. $\frac{dN}{dE}$ is the expected differential
1140 number of photons produced at each energy per annihilation. m_χ is the rest mass of the supposed
1141 DM particle. ρ_χ is the DM density. J is the astrophysical J-factor and is defined as

$$J = \int d\Omega \int_{l.o.s} dl \rho_\chi^2(r, \theta') \quad (5.2)$$

1142 l is the distance to the source from Earth. r is the radial distance from the center of the source. θ' is
1143 the half angle defining a cone containing the DM source. How each component is synthesized and
1144 considered for HAWC's analysis is presented in the following sections. Section 5.3.1 presents the
1145 particle physics model for DM annihilation. Section 5.3.2 presents the spatial distributions built
1146 for each dSph.

1147 **5.3.1 $\frac{dN_\gamma}{dE_\gamma}$ - Particle Physics Component**

1148 For these spectra, we import the PPPC with Electroweak (EW) corrections [58]. Public versions
1149 of the imported tables are provided by the [authors online](#). The spectrum is implemented as a model
1150 script in astromodels for 3ML. The EW corrections were previously not considered for HAWC and
1151 are significant for DM annihilating to EW coupled SM particles such as all leptons, and the γ ,
1152 Z , and W bosons [60]. Figure 5.2 demonstrates the significance of EW corrections for W boson
1153 annihilation. Across EW SM channels, the gamma-ray spectra become harder than spectra without
1154 EW corrections. Tables from the PPPC were reformatted into Python NumPy dictionaries for
1155 collaboration-wide use. A class in astromodels was developed to include the EW correction from
1156 the PPPC and is aptly named `PPPCSpectra` within `DM_models.py`.

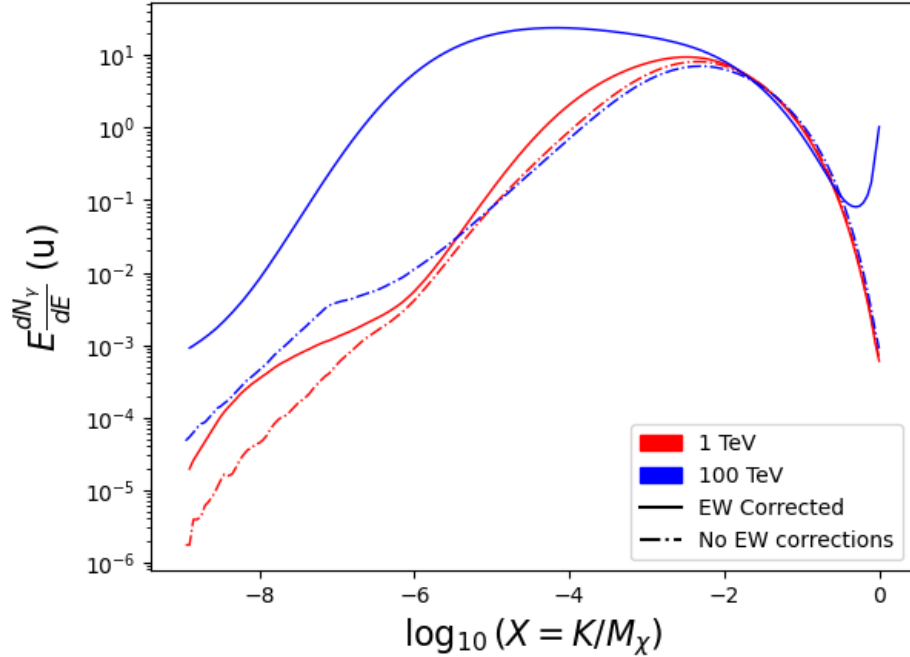


Figure 5.2 Effect of Electroweak (EW) corrections on expected DM annihilation spectrum for $\chi\chi \rightarrow W^-W^+$. Solid lines are spectral models that consider EW corrections. Dash-dot lines are spectral models without EW corrections. Red lines are models for $M_\chi = 1$ TeV. Blue lines represent models for $M_\chi = 100$ TeV. All models are sourced from the PPPC4DMID [58].

1157 5.3.2 J- Astrophysical Component

1158 The J-factor profiles for each source are imported from Geringer-Sameth (referred to with \mathcal{GS})
 1159 [59]. \mathcal{GS} fits the Zhao DM profile to the dSphs which has a DM density described as [61]

$$\rho(r) = \frac{\rho_0}{(r/R_s)^\gamma (1 + (r/R_s)^\alpha)^{(\beta-\gamma)}}. \quad (5.3)$$

1160 R_s is the scale radius and free parameter in the model. γ is the logarithmic slope in the region
 1161 $r \ll R_s$. β is the logarithmic slope in the region $r \gg R_s$. α is known as the sharpness of transition
 1162 where $r \approx R_s$. The classic Navarro-Frenk-White [62] (NFW) can be retrieved from Zhao by fixing
 1163 $(\alpha, \beta, \gamma) = (1, 3, 1)$.

1164 \mathcal{GS} best fits were pulled from the publication as $J(\theta)$, where θ is the angular separation from
 1165 the center of the source. HAWC requires maps in terms of $\frac{dJ}{d\Omega}$, so the conversion from the maps
 1166 was done in the following way...

1167 First, convert the angular distances to solid angles

$$\Omega = 2 \cdot \pi(1 - \cos(\theta)) \quad (5.4)$$

1168 which reduces with a small angle approximation to $\pi\theta^2$. Next, the central difference for both the
1169 ΔJ and $\Delta\Omega$ value were calculated from the discretized $J(\theta)$ with the central difference stencil:

$$\Delta\phi_i = \phi_{i+1} - \phi_{i-1} \quad (5.5)$$

1170 Where ϕ is either Ω or J . These were done separately in case the grid spacing in θ was not uniform.
1171 Finally, these lists are divided so that we are left with an approximation of the $dJ/d\Omega$ profile that
1172 is a function of θ . Admittedly, this is an approximation method for the map which introduces small
1173 errors compared to the true profile estimate. This was checked as a systematic against the author's
1174 profiling of the spatial distribution and is documented in Section 5.8.1.

1175 With $\frac{dJ}{d\Omega}(\theta)$, a map is generated, first by filling in the north-east quadrant of the map. This
1176 quadrant is then reflected twice, vertically then horizontally, to fill the full map. Maps are then
1177 normalized by dividing the discrete 2D integral of the map. The 2D integral was a simple height
1178 of bins, Newton's integral:

$$p^2 \cdot \sum_{i,j=0}^{N,M} \frac{dJ}{d\Omega}(\theta_{i,j}, \phi_{i,j}) \quad (5.6)$$

1179 These maps are HEALpix maps with NSIDE 16384 and saved in the .fits format. The hyper fine
1180 resolution was selected to better preserve the total expected counts after integrating Eq. (5.1) with
1181 the detector response.

1182 Another DM spatial distribution model from Bonnivard (\mathcal{B}) [63] was used for the Glory Duck
1183 study. However, to save computational time, limits from \mathcal{GS} were scaled to \mathcal{B} instead of each
1184 experiment performing a full study a second time. How these models compare is demonstrated
1185 for each dSph in Figure 5.16 and Figure 5.17 Plots of these maps are provided for each source
1186 in chapter A Examples of the two most impactful dSphs derived from \mathcal{GS} , Segue1 and Coma
1187 Berenices are featured in Figure 5.3

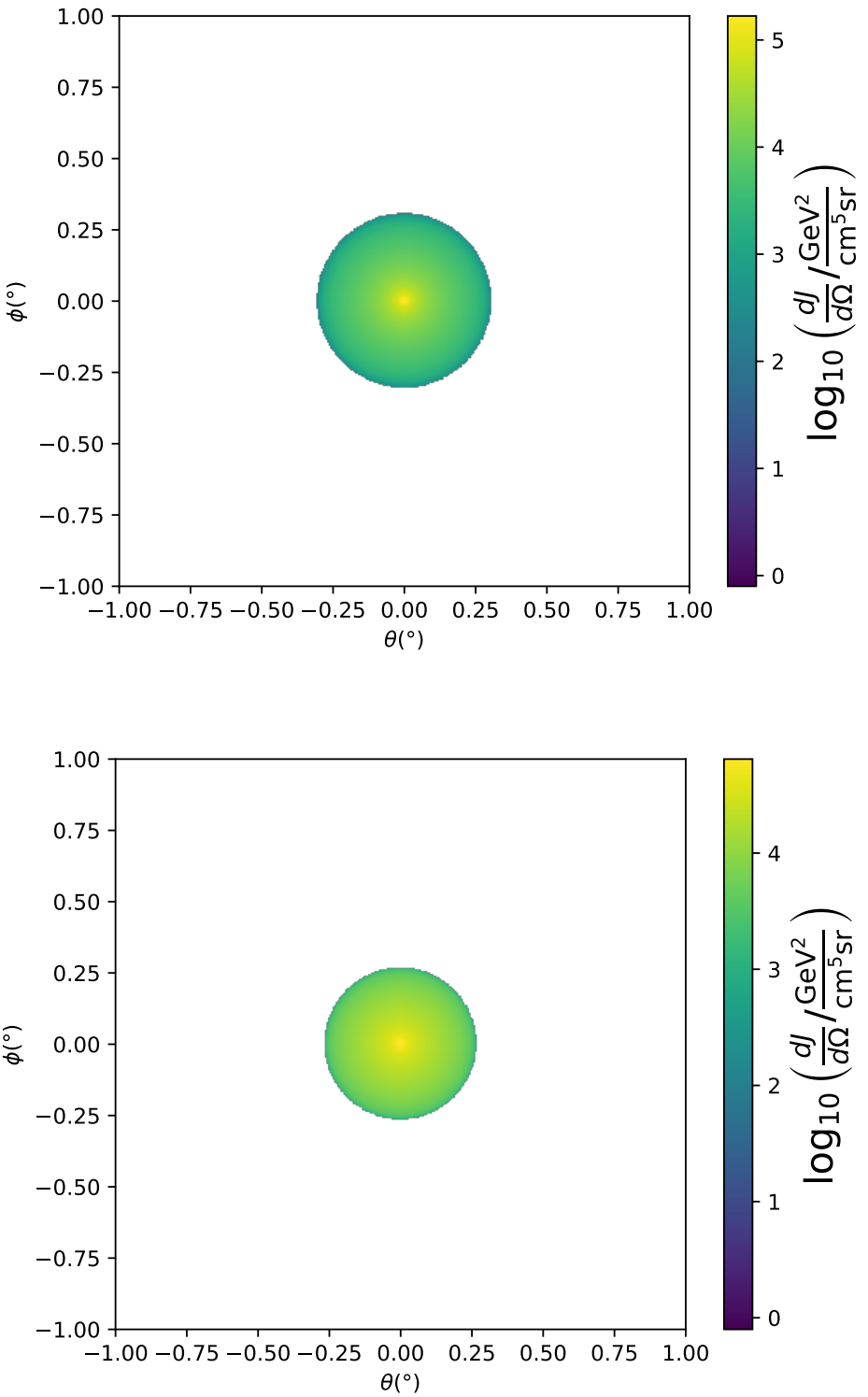


Figure 5.3 $\frac{dJ}{d\Omega}$ maps for Segue1 (top) and Coma Berenices (bottom). Origin is centered on the specific dwarf spheroidal galaxies (dSph). X and Y axes are the angular separation from the center of the dwarf. Profile is truncated at the scale radius. Plots of the remaining 11 dSph HAWC studied are linked in Fig. A.1.

1188 **5.3.3 Source Selection and Annihilation Channels**

1189 We use many of the dSphs presented in HAWC’s previous dSph DM search [60]. HAWC’s
1190 sources for Glory Duck include Boötes I, Coma Berenices, Canes Venatici I + II, Draco, Hercules,
1191 Leo I, II, + IV, Segue 1, Sextans, and Ursa Major I + II. A full description of all sources used
1192 in Glory Duck is found in Table 5.1. Triangulum II was excluded from the Glory Duck analysis
1193 because of large uncertainties in its J factor. Ursa Minor was excluded from HAWC’s contribution
1194 to the combination because the source extension model extended Ursa Minor beyond HAWC’s field
1195 of view. Ursa Minor was not expected to contribute significantly to the combined limit, so work
1196 was not invested in a solution to include Ursa Minor.

1197 This analysis improves on the previous HAWC dSph paper [60] in the following ways. Pre-
1198 viously, the dSphs were treated and implemented as point sources. For this analysis, dSphs are
1199 modeled and treated as extended source. The impact of this change with respect to the upper limit
1200 is source dependent and is explored in Section 5.7.2. Previously, the particle physics model used for
1201 gamma-ray spectra from DM annihilation did not have EW corrections where the PPPC includes
1202 them. Finally, the gamma-ray ray dataset is much larger. The study performed here analyzes over
1203 1000 days of data compared to 507.

1204 The SM annihilation channels probed for the Glory Duck combination include $b\bar{b}$, $e\bar{e}$, $\mu\bar{\mu}$, $\tau\bar{\tau}$,
1205 $t\bar{t}$, W^+W^- , and ZZ . A summary of all sources, with a description of each experiments’ sensitivity
1206 to the source, is provided in Table 5.2.

1207 **5.4 Likelihood Methods**

1208 **5.4.1 HAWC Likelihood**

1209 For every analysis bin in energy, f_{hit} bins (1-9), and location, we can expect N signal events and
1210 B background events. The expected number of excess signal events from dark matter annihilation,
1211 S , is estimated by convolving Equation (5.1) with HAWC’s energy response and pixel point spread
1212 functions. I then compute the test statistic (TS) with the log-likelihood ratio test,

$$TS_{\max} = -2 \ln \left(\frac{\mathcal{L}_0}{\mathcal{L}_{\max}} \right) \quad (5.7)$$

Table 5.1 Summary of the relevant properties of the dSphs used in the present work. Column 1 lists the dSphs. Columns 2 and 3 present their heliocentric distance and galactic coordinates, respectively. Columns 4 and 5 report the J -factors of each source given from the \mathcal{GS} and \mathcal{B} independent studies and their estimated $\pm 1\sigma$ uncertainties. The values $\log_{10} J$ (\mathcal{GS} set) [59] correspond to the mean J -factor values for a source extension truncated at the outermost observed star. The values $\log_{10} J$ (\mathcal{B} set) [63] are provided for a source extension at the tidal radius of each dSph. **Bolded sources are within HAWC’s field of view and provided to the Glory Duck analysis.**

Name	Distance (kpc)	l, b ($^{\circ}$)	$\log_{10} J$ (\mathcal{GS} set) $\log_{10}(\text{GeV}^2\text{cm}^{-5}\text{sr})$	$\log_{10} J$ (\mathcal{B} set) $\log_{10}(\text{GeV}^2\text{cm}^{-5}\text{sr})$
Boötes I	66	358.08, 69.62	$18.24^{+0.40}_{-0.37}$	$18.85^{+1.10}_{-0.61}$
Canes Venatici I	218	74.31, 79.82	$17.44^{+0.37}_{-0.28}$	$17.63^{+0.50}_{-0.20}$
Canes Venatici II	160	113.58, 82.70	$17.65^{+0.45}_{-0.43}$	$18.67^{+1.54}_{-0.97}$
Carina	105	260.11, -22.22	$17.92^{+0.19}_{-0.11}$	$18.02^{+0.36}_{-0.15}$
Coma Berenices	44	241.89, 83.61	$19.02^{+0.37}_{-0.41}$	$20.13^{+1.56}_{-1.08}$
Draco	76	86.37, 34.72	$19.05^{+0.22}_{-0.21}$	$19.42^{+0.92}_{-0.47}$
Fornax	147	237.10, -65.65	$17.84^{+0.11}_{-0.06}$	$17.85^{+0.11}_{-0.08}$
Hercules	132	28.73, 36.87	$16.86^{+0.74}_{-0.68}$	$17.70^{+1.08}_{-0.73}$
Leo I	254	225.99, 49.11	$17.84^{+0.20}_{-0.16}$	$17.93^{+0.65}_{-0.25}$
Leo II	233	220.17, 67.23	$17.97^{+0.20}_{-0.18}$	$18.11^{+0.71}_{-0.25}$
Leo IV	154	265.44, 56.51	$16.32^{+1.06}_{-1.70}$	$16.36^{+1.44}_{-1.65}$
Leo V	178	261.86, 58.54	$16.37^{+0.94}_{-0.87}$	$16.30^{+1.33}_{-1.16}$
Leo T	417	214.85, 43.66	$17.11^{+0.44}_{-0.39}$	$17.67^{+1.01}_{-0.56}$
Sculptor	86	287.53, -83.16	$18.57^{+0.07}_{-0.05}$	$18.63^{+0.14}_{-0.08}$
Segue I	23	220.48, 50.43	$19.36^{+0.32}_{-0.35}$	$17.52^{+2.54}_{-2.65}$
Segue II	35	149.43, -38.14	$16.21^{+1.06}_{-0.98}$	$19.50^{+1.82}_{-1.48}$
Sextans	86	243.50, 42.27	$17.92^{+0.35}_{-0.29}$	$18.04^{+0.50}_{-0.28}$
Ursa Major I	97	159.43, 54.41	$17.87^{+0.56}_{-0.33}$	$18.84^{+0.97}_{-0.43}$
Ursa Major II	32	152.46, 37.44	$19.42^{+0.44}_{-0.42}$	$20.60^{+1.46}_{-0.95}$
Ursa Minor	76	104.97, 44.80	$18.95^{+0.26}_{-0.18}$	$19.08^{+0.21}_{-0.13}$

Table 5.2 Summary of dSph observations by each experiment used in this work. A ‘-’ indicates the experiment did not observe the dSph for this study. For Fermi-LAT, the exposure at 1 GeV is given. For HAWC, $|\Delta\theta|$ is the absolute difference between the source declination and HAWC latitude. HAWC is more sensitive to sources with smaller $|\Delta\theta|$. For IACTs, we show the zenith angle range, the total exposure, the energy range, the angular radius θ of the signal or ON region, the ratio of exposures between the background-control (OFF) and signal (ON) regions (τ), and the significance of gamma-ray excess in standard deviations, σ .

Source name	Fermi-LAT	HAWC	H.E.S.S, MAGIC, VERITAS						
	Exposure (10^{11} s m 2)	$ \Delta\theta $ ($^\circ$)	IACT	Zenith ($^\circ$)	Exposure (h)	Energy range (GeV)	θ ($^\circ$)	τ	S (σ)
Boötes I	2.6	4.5	VERITAS	15 – 30	14.0	100–41000	0.10	8.6	-1.0
Canes Venatici I	2.9	14.6	–	–	–	–	–	–	–
Canes Venatici II	2.9	15.3	–	–	–	–	–	–	–
Carina	3.1	–	H.E.S.S.	27 – 46	23.7	310 – 70000	0.10	18.0	-0.3
Coma Berenices	2.7	4.9	H.E.S.S.	47 – 49	11.4	550 – 70000	0.10	14.4	-0.4
			MAGIC	5 – 37	49.5	60 – 10000	0.17	1.0	–
			MAGIC	29 – 45	52.1	70 – 10000	0.22	1.0	–
Draco	3.8	38.1	VERITAS	25 – 40	49.8	120 – 70000	0.10	9.0	-1.0
Fornax	2.7	–	H.E.S.S.	11 – 25	6.8	230 – 70000	0.10	45.5	-1.5
Hercules	2.8	6.3	–	–	–	–	–	–	–
Leo I	2.5	6.7	–	–	–	–	–	–	–
Leo II	2.6	3.1	–	–	–	–	–	–	–
Leo IV	2.4	19.5	–	–	–	–	–	–	–
Leo V	2.4	–	–	–	–	–	–	–	–
Leo T	2.6	–	–	–	–	–	–	–	–
Sculptor	2.7	–	H.E.S.S.	10 – 46	11.8	200 – 70000	0.10	19.8	-2.2
Segue I	2.5	2.9	MAGIC	13 – 37	158.0	60 – 10000	0.12	1.0	-0.5
			VERITAS	15 – 35	92.0	80 – 50000	0.10	7.6	0.7
Segue II	2.7	–	–	–	–	–	–	–	–
Sextans	2.4	20.6	–	–	–	–	–	–	–
Ursa Major I	3.4	32.9	–	–	–	–	–	–	–
Ursa Major II	4.0	44.1	MAGIC	35 – 45	94.8	120 – 10000	0.30	1.0	-2.1
Ursa Minor	4.1	–	VERITAS	35 – 45	60.4	160 – 93000	0.10	8.4	-0.1

1213 where \mathcal{L}_0 is the null hypothesis, or no DM emission, likelihood. \mathcal{L}^{\max} is the best fit signal
 1214 hypothesis where $\langle\sigma v\rangle$ maximizes the likelihood. We calculate the likelihood of each source and
 1216 model, assuming events are Poisson distributed, with

$$\mathcal{L} = \prod_i \frac{(B_i + S_i)^{N_i} e^{-(B_i + S_i)}}{N_i!} \quad (5.8)$$

1217 where S_i is the sum of expected number of signal counts. B_i is the number of background counts
 1218 observed. N_i is the total number of counts.

1219 I also calculate an upper limit on $\langle\sigma v\rangle$ by calculating the 95% confidence level (CL). For the
 1220 CL, we define a parameter, TS_{95} , as

$$TS_{95} \equiv \sum_{\text{bins}} \left[2N \ln \left(1 + \frac{\epsilon S_{\text{ref}}}{B} \right) - 2\epsilon S_{\text{ref}} \right] \quad (5.9)$$

1221 where the expected signal counts from a dSph is scaled by ϵ . S_{ref} is the expected number of excess
 1222 counts in a bin from DM emission from a dSph with a corresponding annihilation cross-section,
 1223 $\langle\sigma v\rangle$. We scan ϵ such that

$$2.71 = TS_{\max} - TS_{95} \quad (5.10)$$

1224 HAWC's exclusive results are provided in Section 5.5.

1225 5.4.2 Glory Duck Joint Likelihood

1226 The joint likelihood for the 5-experiment combination was done similarly as Section 5.4.1. We
 1227 calculate upper limits on $\langle\sigma v\rangle$ from the TS, Eq. (5.7), and define the likelihood ratio more generally

$$\lambda(\langle\sigma v\rangle | \mathcal{D}_{\text{dSphs}}) = \frac{\mathcal{L}(\langle\sigma v\rangle; \hat{\nu} | \mathcal{D}_{\text{dSphs}})}{\mathcal{L}(\widehat{\langle\sigma v\rangle}; \hat{\nu} | \mathcal{D}_{\text{dSphs}})} \quad (5.11)$$

1228 $\mathcal{D}_{\text{dSphs}}$ is the totality of observations across experiments and dSphs. ν are the nuisance parameters
 1229 which are the J factors in this study. $\widehat{\langle\sigma v\rangle}$ and $\hat{\nu}$ are the respective estimate that maximize \mathcal{L}
 1230 globally. Finally, $\hat{\nu}$ is the set of nuisance parameters that maximize \mathcal{L} for a fixed value of $\langle\sigma v\rangle$.

1231 The *complete* joint likelihood, \mathcal{L} that encompasses all observations from all instruments and
 1232 dSphs can be factorized into *partial* functions for each dSph l (with $\mathcal{L}_{\text{dSph},l}$) and its J factor (\mathcal{J}_l):

$$\mathcal{L}(\langle\sigma v\rangle; \nu | \mathcal{D}_{\text{dSphs}}) = \prod_{l=1}^{N_{\text{dSphs}}} \mathcal{L}_{\text{dSph},l}(\langle\sigma v\rangle; J_l, \nu_l | \mathcal{D}_l) \times \mathcal{J}_l(J_l | J_{l,\text{obs}}, \sigma_{\log J_l}). \quad (5.12)$$

1233 For this study, $N_{\text{dSphs}} = 20$ is the number of dSphs studied. \mathcal{D}_l are the gamma-ray observations
 1234 of dSph, l . ν_l are the nuisance parameters modifying the gamma-ray observations of dSph, l ,
 1235 but excludes \mathcal{J}_l . \mathcal{J}_l is the J factor for dSph, l , as defined in Equation (5.2), and it is a nuisance
 1236 parameter whose value is unknown. $\log_{10} J_{l,\text{obs}}$ and $\sigma_{\log J_l}$ are obtained by fitting a log-normal
 1237 function of $J_{l,\text{obs}}$ to the posterior distribution of J_l [64]. $\log_{10} J_{l,\text{obs}}$ and $\sigma_{\log J_l}$ values are provided
 1238 in Table 5.1. The term \mathcal{J}_l constraining J_l is written as:

$$\mathcal{J}_l (J_l | J_{l,\text{obs}}, \sigma_{\log J_l}) = \frac{1}{\ln(10) J_{l,\text{obs}} \sqrt{2\pi} \sigma_{\log J_l}} \exp\left(-\frac{(\log_{10} J_l - \log_{10} J_{l,\text{obs}})^2}{2\sigma_{\log J_l}^2}\right). \quad (5.13)$$

1239 Both the \mathcal{GS} and \mathcal{B} , displayed in Table 5.1, sets of J factors are used in this analysis. Equation (5.13)
 1240 is also normalized, so it can also be interpreted as a probability density function (PDF) for $J_{l,\text{obs}}$.
 1241 From Equation (5.1), we can also see that $\langle \sigma v \rangle$ and J_l are degenerate when computing $\mathcal{L}_{\text{dSph},l}$.
 1242 Therefore, as noted in [65], it is sufficient to compute $\mathcal{L}_{\text{dSph},l}$ versus $\langle \sigma v \rangle$ for a fixed value of J_l .
 1243 We used $J_{l,\text{obs}}(\mathcal{GS})$ reported in Tab. 5.1, in order to perform the profile of \mathcal{L} with respect to J_l .
 1244 The degeneracy implies that for any $J'_l \neq J_{l,\text{obs}}$ (in practice in our case we used $J'_l = J_{l,\text{obs}}(\mathcal{B})$ to
 1245 compute results from a different set of J factors):

$$\mathcal{L}_{\text{dSph},l} (\langle \sigma v \rangle; J'_l, \nu_l | \mathcal{D}_l) = \mathcal{L}_{\text{dSph},l} \left(\frac{J'_l}{J_{l,\text{obs}}} \langle \sigma v \rangle; J_{l,\text{obs}}, \nu_l | \mathcal{D}_l \right), \quad (5.14)$$

1246 which is a straightforward rescaling operation that reduces the computational needs of the profiling
 1247 operation since:

$$\mathcal{L} (\langle \sigma v \rangle; \hat{\nu} | \mathcal{D}_{\text{dSphs}}) = \prod_{l=1}^{N_{\text{dSphs}}} \max_{J_l} \left[\mathcal{L}_{\text{dSph},l} (\langle \sigma v \rangle; J_l, \hat{\nu}_l | \mathcal{D}_l) \times \mathcal{J}_l (J_l | J_{l,\text{obs}}, \sigma_{\log J_l}) \right]. \quad (5.15)$$

1248 In addition, Eq. (5.14) enables the combination of data from different gamma-ray instruments and
 1249 observed dSphs via tabulated values of $\mathcal{L}_{\text{dSph},l}$, or equivalently of λ from Eq. (5.11) as was done in
 1250 this work, versus $\langle \sigma v \rangle$. $\mathcal{L}_{\text{dSph},l}$ is computed for a fixed value of J_l and profiled with respect to all
 1251 instrumental nuisance parameters ν_l , these nuisance parameters are discussed in more detail below.
 1252 These values are produced by each detector independently and therefore there is no need to share
 1253 sensitive low-level information used to produce them, such as event lists. Figure 5.4 illustrates the
 1254 multi-instrument combination technique used in this study with a comparison of the upper limit

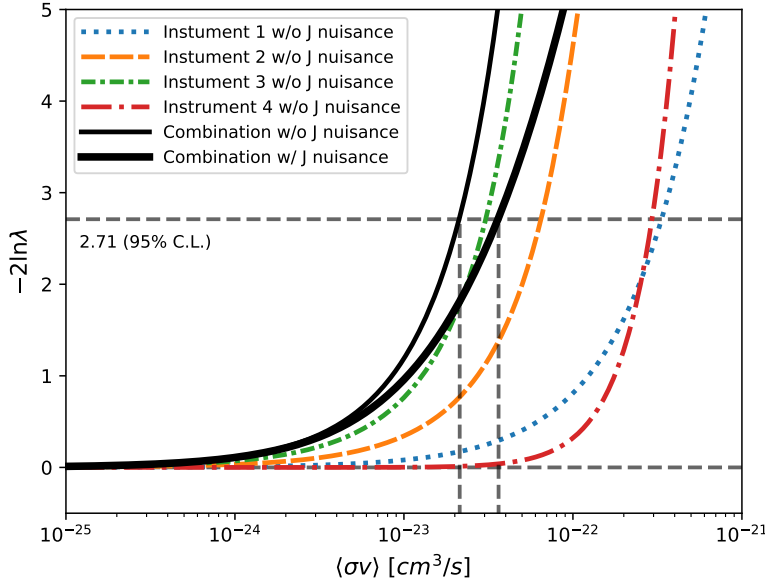


Figure 5.4 Illustration of the combination technique showing a comparison between $-2 \ln \lambda$ provided by four instruments (colored lines) from the observation of the same dSph without any J nuisance and their sum, *i.e.* the resulting combined likelihood (thin black line). According to the test statistics of Equation (5.7), the intersection of the likelihood profiles with the line $-2 \ln \lambda = 2.71$ indicates the 95% C.L. upper limit on $\langle\sigma v\rangle$. The combined likelihood (thin black line) shows a smaller value of upper limit on $\langle\sigma v\rangle$ than those derived by individual instruments. We also show how the uncertainties on the J factor effects the combined likelihood and degrade the upper limit on $\langle\sigma v\rangle$ (thick black line). All likelihood profiles are normalized so that the global minimum $\widehat{\langle\sigma v\rangle}$ is 0. We note that each profile depends on the observational conditions in which a target object was observed. The sensitivity of a given instrument can be degraded and the upper limits less constraining if the observations are performed in non-optimal conditions such as a high zenith angle or a short exposure time.

1255 on $\langle\sigma v\rangle$ obtained from the combination of the observations of four experiments towards one dSph
 1256 versus the upper limit from individual instruments. It also shows graphically the effect of the
 1257 J -factor uncertainty on the combined observations.

1258 The *partial* joint likelihood function for gamma-ray observations of each dSph ($\mathcal{L}_{\text{dSph},l}$) is
 1259 written as the product of the likelihood terms describing the $N_{\text{exp},l}$ observations performed with
 1260 any of our observatories:

$$\mathcal{L}_{\text{dSph},l} (\langle\sigma v\rangle; J_l, \nu_l | \mathcal{D}_l) = \prod_{k=1}^{N_{\text{exp},l}} \mathcal{L}_{lk} (\langle\sigma v\rangle; J_l, \nu_{lk} | \mathcal{D}_{lk}), \quad (5.16)$$

1261 where each \mathcal{L}_{lk} term refers to an observation of the l -th dSph with associated k -th instrument

1262 responses. $N_{\text{exp},l}$ varies from dSph to dSph and can be inferred from Table 5.2.

1263 Each collaboration separately analyzes their data for \mathcal{D}_{lk} corresponding to dSph l and gamma-
 1264 ray detector k , using as many common assumptions as possible in the analysis. HAWC's treatment
 1265 was described earlier in Section 5.4.1 whereas the specifics of the remaining experiments is left to
 1266 the publication. We compute the values for the likelihood functions \mathcal{L}_{lk} (see Eq. (5.16)) for a fixed
 1267 value of J_l and profile over the rest of the nuisance parameters ν_{lk} . Then, values of λ from Eq. (5.11)
 1268 are computed as a function of $\langle \sigma v \rangle$, and shared using a common format. Results are computed for
 1269 seven annihilation channels, W^+W^- , ZZ , $b\bar{b}$, $t\bar{t}$, e^+e^- , $\mu^+\mu^-$, and $\tau^+\tau^-$ over 62 m_χ values between
 1270 5 GeV and 100 TeV provided in [58]. The $\langle \sigma v \rangle$ range is defined between 10^{-28} and $10^{-18} \text{cm}^3 \cdot \text{s}^{-1}$,
 1271 with 1001 logarithmically spaced values. The likelihood combination, i.e. Equation (5.12), and
 1272 profile over the J -factor to compute the profile likelihood ratio λ , Equation (5.11), are carried out
 1273 with two different public analysis software packages, namely `gLike` [66] and `LklCom` [67], that
 1274 provide the same results [68].

1275 As mentioned previously, each experiment computes the \mathcal{L}_{lk} from Equation (5.11) differently.
 1276 The remainder of this section highlights the differences in this calculation across the experiments.
 1277 Four experiments, namely *Fermi*-LAT, H.E.S.S., HAWC and MAGIC, use a binned likelihood to
 1278 compute the \mathcal{L}_{lk} . For these experiments, for each observation \mathcal{D}_{lk} of a given dSph l carried out
 1279 using a given gamma-ray detector k , the binned likelihood function is:

$$\mathcal{L}_{lk} (\langle \sigma v \rangle; J_l, \nu_{lk} | \mathcal{D}_{lk}) = \prod_{i=1}^{N_E} \prod_{j=1}^{N_P} \left[\mathcal{P}(s_{lk,ij}(\langle \sigma v \rangle, J_l, \nu_{lk}) + b_{lk,ij}(\nu_{lk}) | N_{lk,ij}) \right] \times \mathcal{L}_{lk,\nu} (\nu_{lk} | \mathcal{D}_{\nu_{lk}}) \quad (5.17)$$

1280 where N_E and N_P are the number of considered bins in reconstructed energy and arrival direction,
 1281 respectively; \mathcal{P} represents a Poisson PDF for the number of gamma-ray candidate events $N_{lk,ij}$
 1282 observed in the i -th bin in energy and j -th bin in arrival direction, when the expected number is
 1283 the sum of the expected mean number of signal events s_{ij} (produced by DM annihilation) and of
 1284 background events b_{ij} ; $\mathcal{L}_{lk,\nu}$ is the likelihood term for the extra ν_{lk} nuisance parameters that vary
 1285 from one instrument k to another. The expected counts for signal events s_{ij} for a given dSph l and

1286 detector k is given by:

$$s_{ij}(\langle\sigma\nu\rangle, J) = \int_{E'_{\min,i}}^{E'_{\max,i}} dE' \int_{P'_{\min,j}}^{P'_{\max,j}} d\Omega' \int_0^\infty dE \int_{\Delta\Omega_{tot}} d\Omega \int_0^{T_{\text{obs}}} dt \frac{d^2\Phi(\langle\sigma\nu\rangle, J)}{dEd\Omega} \text{IRF}(E', P' | E, P, t) \quad (5.18)$$

1287 where E' and E are the reconstructed and true energies, P' and P the reconstructed and true
1288 arrival directions; $E'_{\min,i}$, $P'_{\min,j}$, $E'_{\max,i}$, and $P'_{\max,j}$ are their lower and upper limits of the i -th
1289 energy bin and the j -th arrival direction bin; T_{obs} is the (dead-time corrected) total observation
1290 time; t is the time along the observations; $d^2\Phi/dEd\Omega$ is the DM flux in the source region (see
1291 Equation (5.1)); and $\text{IRF}(E', P' | E, P, t)$ is the IRF, which can be factorized as the product of the
1292 effective collection area of the detector $A_{\text{eff}}(E, P, t)$, the PDFs for the energy estimator $f_E(E' | E, t)$,
1293 and arrival direction $f_P(P' | E, P, t)$ estimators. Note that for Fermi-LAT, HAWC, MAGIC, and
1294 VERITAS the effect of the finite angular resolution is taken into account through the convolution
1295 of $d\Phi/dEd\Omega$ with f_P in Equation (5.18), whereas in the cases of H.E.S.S. f_P is approximated by a
1296 delta function. This approximation has been made in order to maintain compatibility of the result
1297 with what has been previously published. The difference introduced by this approximation is $< 5\%$
1298 for all considered dSphs. A more comprehensive review of the differences between the analyses of
1299 different instruments can be found in [40].

1300 5.5 HAWC Results

1301 13 of the 20 dSphs considered for the Glory Duck analysis are within HAWC's field of view.
1302 These dSph are analyzed for emission from DM annihilation according to the likelihood method
1303 described in Section 5.4. The 13 likelihood profiles are then stacked to synthesize a combined
1304 limit on the dark matter cross-section, $\langle\sigma\nu\rangle$. This combination is done for the 7 SM annihilation
1305 channels used in the Glory Duck analysis. Figure 5.5 shows the combined limit for all annihilation
1306 channels with HAWC only observations. We also perform 300 studies of Poisson trials on the
1307 background. These trials are used to produce HAWC sensitivities with $\pm 1\sigma$ and $\pm 2\sigma$ uncertainty
1308 bands which were shared with the other collaborators for combination. The results on fitting to
1309 HAWC's Poisson trials of the DM hypothesis is shown in Figure 5.7 for all the DM annihilation
1310 channels studied for Glory Duck.

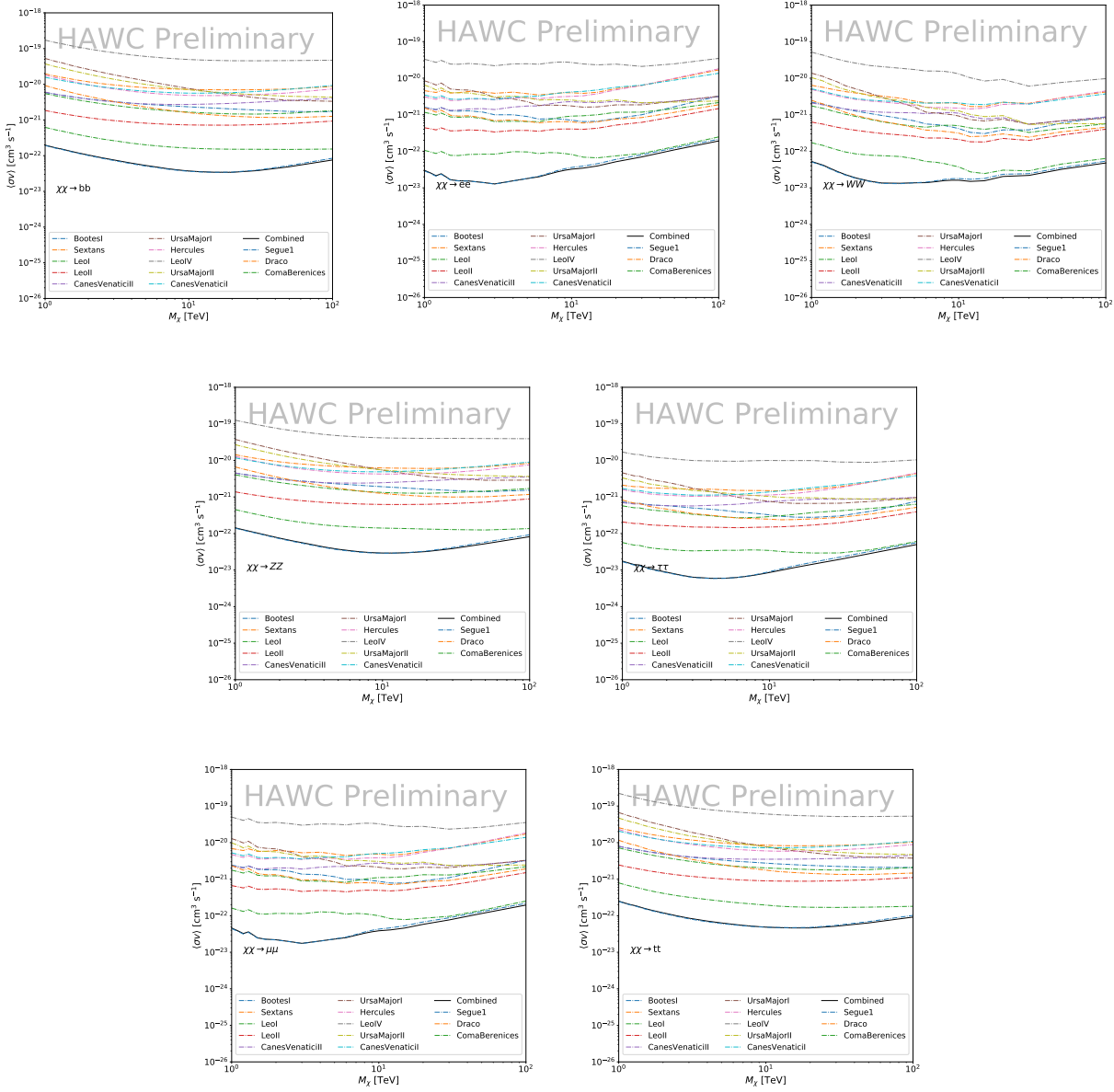


Figure 5.5

1311 No DM was found in HAWC observations. HAWC's limits are dominated by the dSphs Segue1
1312 and Coma Berenices. The remaining 11 dSphs do not contribute significantly to the limit because
1313 they are at high zenith and/or have much smaller J factors. Even though some remaining dSphs
1314 have large J factors, they are towards the edge of HAWC's field of view where HAWC analysis is
1315 less sensitive.

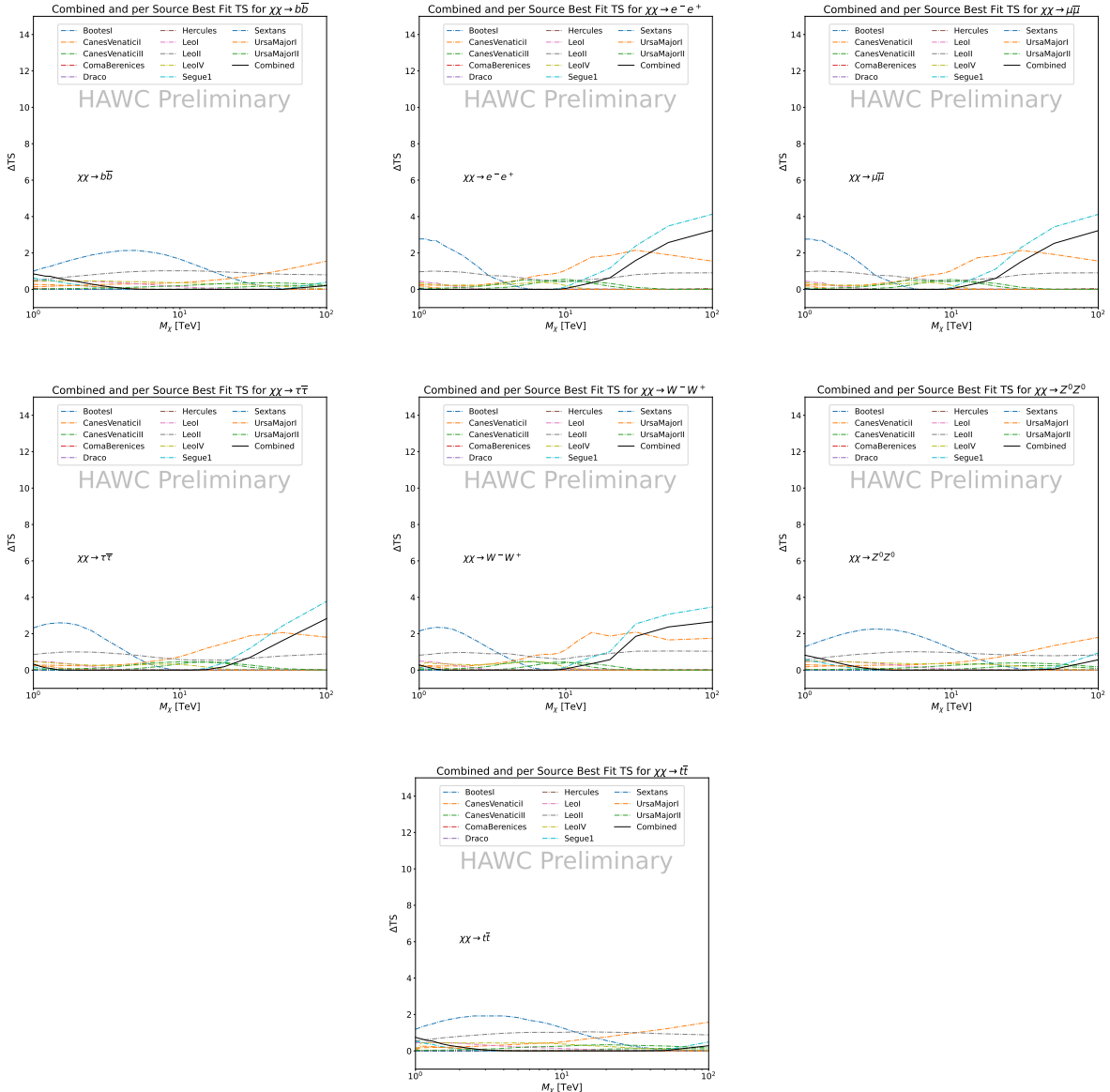


Figure 5.6 HAWC TS values for best fit $\langle\sigma v\rangle$ versus m_χ for seven SM annihilation channels with J factors from \mathcal{GS} . The solid black line shows the combined best fit TS values. The colored, dashed lines are the TS values for each of the 13 sources HAWC studied.

1316 5.6 Glory Duck Combined Results

1317 The crux of this analysis is that HAWC's results are combined with 4 other gamma-ray observa-
 1318 tories: Fermi-LAT, H.E.S.S., MAGIC, and VERITAS. No significant DM emission was observed
 1319 by any of the five instruments. We present the upper limits on $\langle\sigma v\rangle$ assuming seven independent
 1320 DM self annihilation channels, namely W^+W^- , Z^+Z^- , $b\bar{b}$, $t\bar{t}$, e^+e^- , $\mu^+\mu^-$, and $\tau^+\tau^-$. The 68%

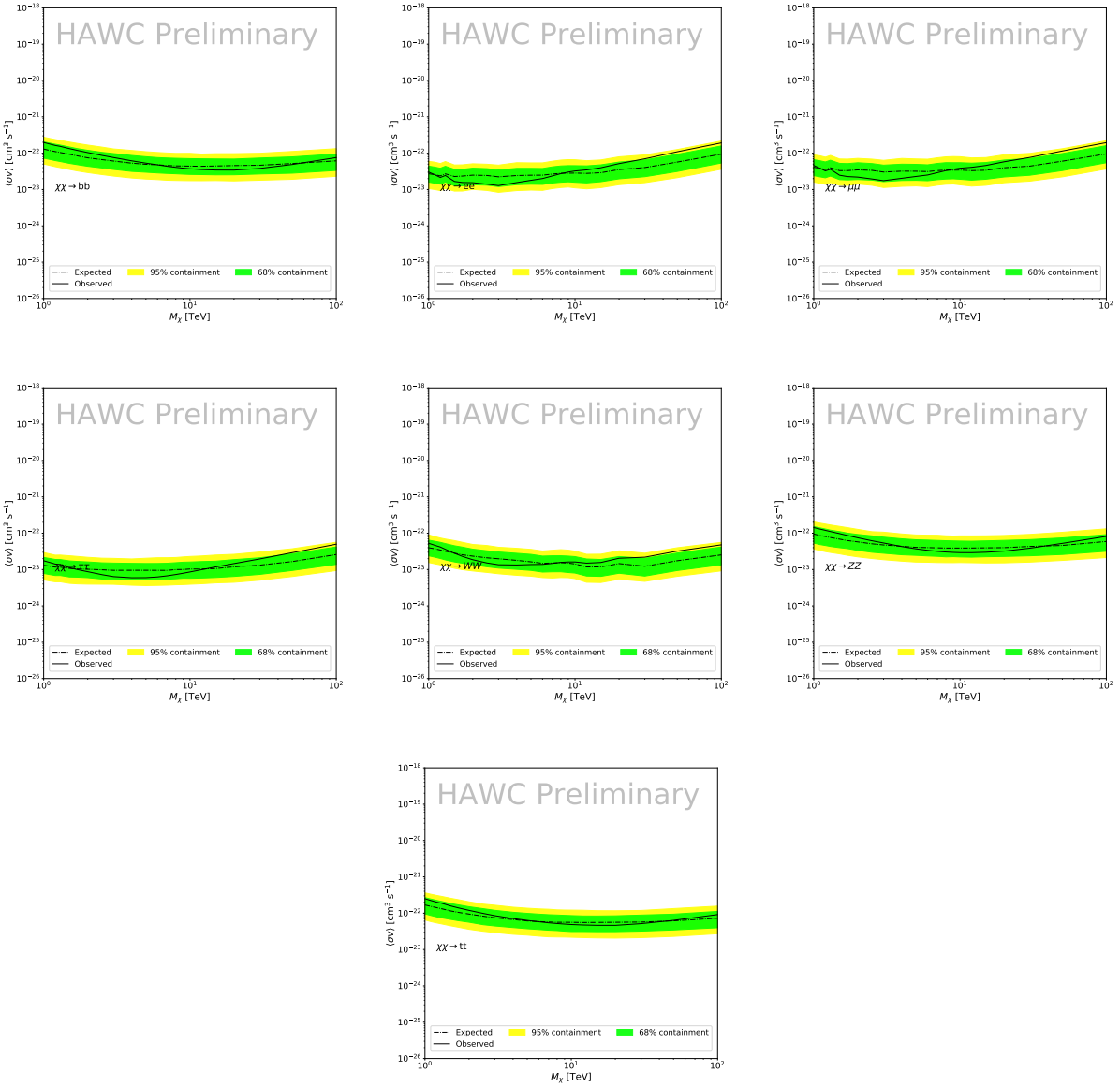


Figure 5.7 HAWC Brazil bands at 95% confidence level on $\langle\sigma v\rangle$ versus DM mass for seven annihilation channels with J -factors from GS [69]. The solid line represents the combined limit from 13 dSphs. The dashed line is the expected limit. The green band is the 68% containment. The yellow band is the 95% containment.

1321 and 95% containment bands are produced from 300 Poisson realizations of the null hypothesis
 1322 corresponding to each of the combined datasets. These 300 realizations are combined identically
 1323 to dSph observations. The containment bands and the median are extracted from the distribution
 1324 of resulting limits on the null hypothesis. These 300 realizations are obtained either by fast simu-
 1325 lations of the OFF observations, for H.E.S.S., MAGIC, VERITAS, and HAWC, or taken from real

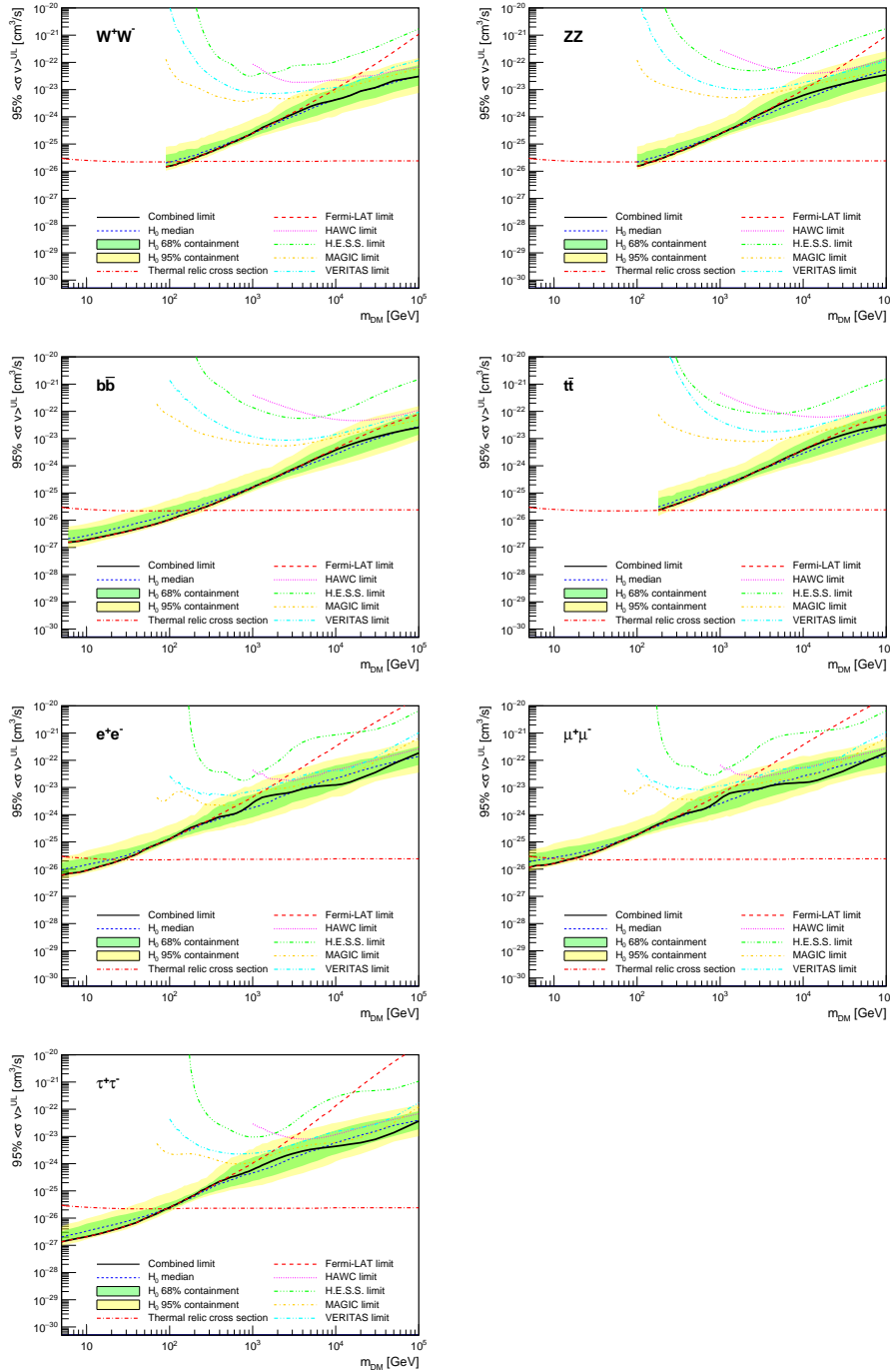


Figure 5.8 Upper limits at 95% confidence level on $\langle\sigma v\rangle$ in function of the DM mass for eight annihilation channels, using the set of J factors from Ref. [69] (\mathcal{GS} set in Table 5.1). The black solid line represents the observed combined limit, the black dashed line is the median of the null hypothesis corresponding to the expected limit, while the green and yellow bands show the 68% and 95% containment bands. Combined upper limits for each individual detector are also indicated as solid, colored lines. The value of the thermal relic cross-section in function of the DM mass is given as the red dotted-dashed line [70].

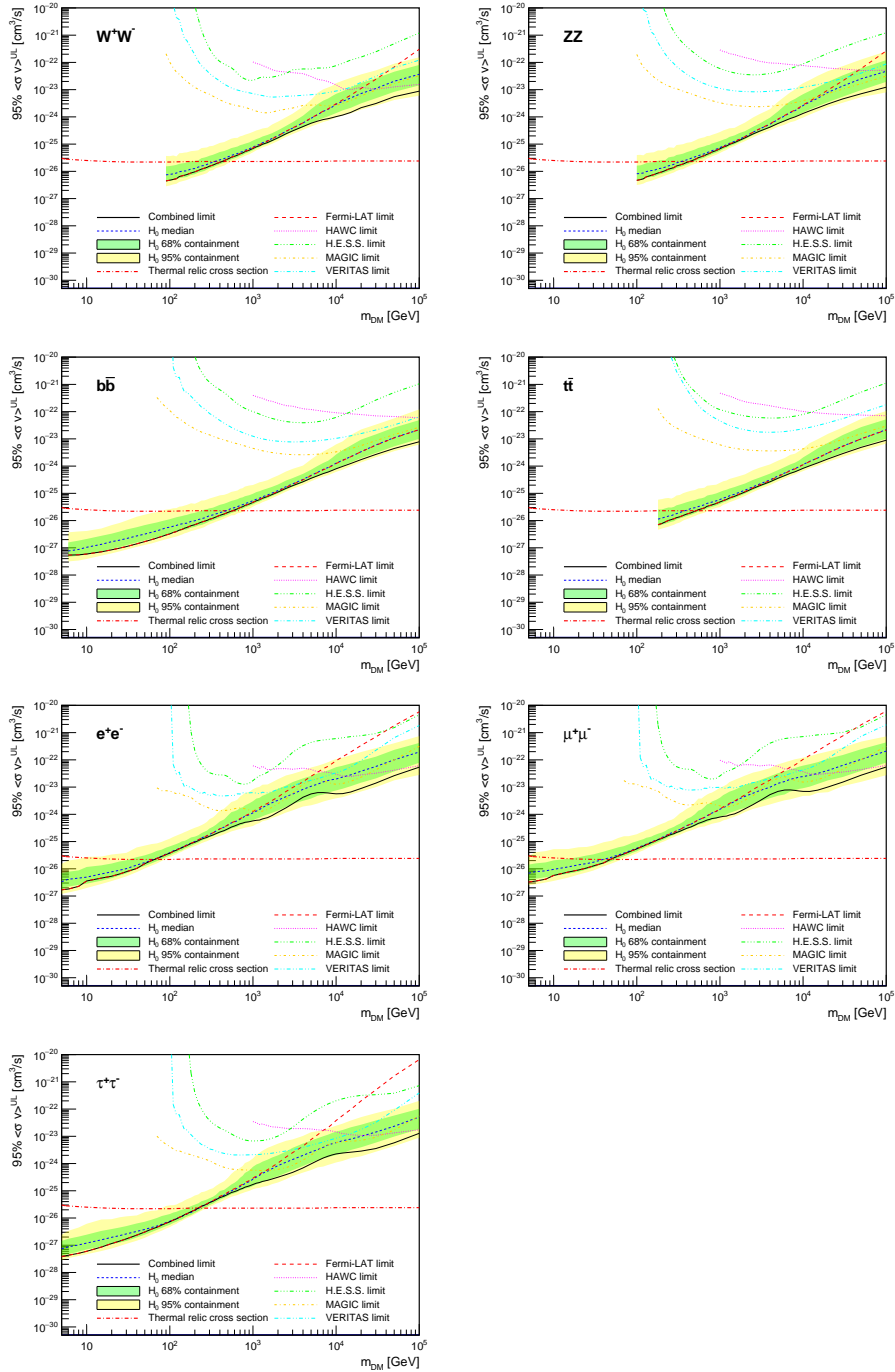


Figure 5.9 Same as Fig. 5.8, using the set of J factors from Ref. [63, 71] (\mathcal{B} set in Table 5.1).

1326 observations of empty fields of view in the case of Fermi-LAT [64, 72, 73].

1327 The obtained limits are shown in Figure 5.8 for the $\mathcal{G}\mathcal{S}$ set of J -factors [69] and in Figure 5.9
 1328 for the \mathcal{B} set of J -factors [63, 71]. The combined limits are presented with their 68% and 95%
 1329 containment bands, and are expected to be close to the median limit when no signal is present.

1330 We observe agreement with the null hypothesis for all channels, within 2σ standard deviations,
1331 between the observed limits and the expectations given by the median limits. Limits obtained from
1332 each detector are also indicated in the figures, where limits for all dSphs observed by the specific
1333 instrument have been combined.

1334 Below ~ 300 GeV, the *Fermi*-LAT dominates the DM limits for all annihilation channels. From
1335 ~ 300 GeV to ~ 2 TeV, *Fermi*-LAT continues to dominate for the hadronic and bosonic DM channels,
1336 yet the IACTs (H.E.S.S., MAGIC, and VERITAS) and *Fermi*-LAT all contribute to the limit for
1337 leptonic DM channels. For DM masses between ~ 2 TeV to ~ 10 TeV, the IACTs dominate leptonic
1338 DM annihilation channels, whereas both the *Fermi*-LAT and the IACTs dominate bosonic and
1339 hadronic DM annihilation channels. From ~ 10 TeV to ~ 100 TeV, both the IACTs and HAWC
1340 contribute significantly to the leptonic DM limit. For hadronic and bosonic DM, the IACTs and
1341 *Fermi*-LAT both contribute strongly.

1342 We notice that the limits computed using the \mathcal{B} set of J -factor are always better compared to the
1343 ones calculated with the \mathcal{GS} set. For the W^+W^- , Z^+Z^- , $b\bar{b}$, and $t\bar{t}$ channels, the ratio between the
1344 limits computed with the two sets of J -factor is varying between a factor of ~ 3 and ~ 5 depending
1345 on the energy, with the largest ratio around 10 TeV. For the channels e^+e^- , $\mu^+\mu^-$, and $\tau^+\tau^-$, the
1346 ratio lies between ~ 2 to ~ 6 , being maximum around 1 TeV. Examining Figure 5.16 and Figure 5.17
1347 in Section 5.8, these differences are explained by the fact that the \mathcal{B} set provides higher J -factors
1348 for the majority of the studied dSphs, with the notable exception of Segue I. The variation on the
1349 ratio of the limits for the two sets is due to different dSph dominating the limits depending on the
1350 energy. One set, \mathcal{B} , pushes the range of which thermal cross-section which can be excluded to
1351 higher mass. This comparison demonstrates the magnitude of systematic uncertainties associated
1352 with the choice of the J -factor calculation. The \mathcal{GS} and \mathcal{B} sets present a difference in the limits for
1353 all channels of about This difference is explained, see Figure 5.16 and Figure 5.17, by the fact that
1354 the \mathcal{B} set provides higher J -factors for all dSph except for Segue I.

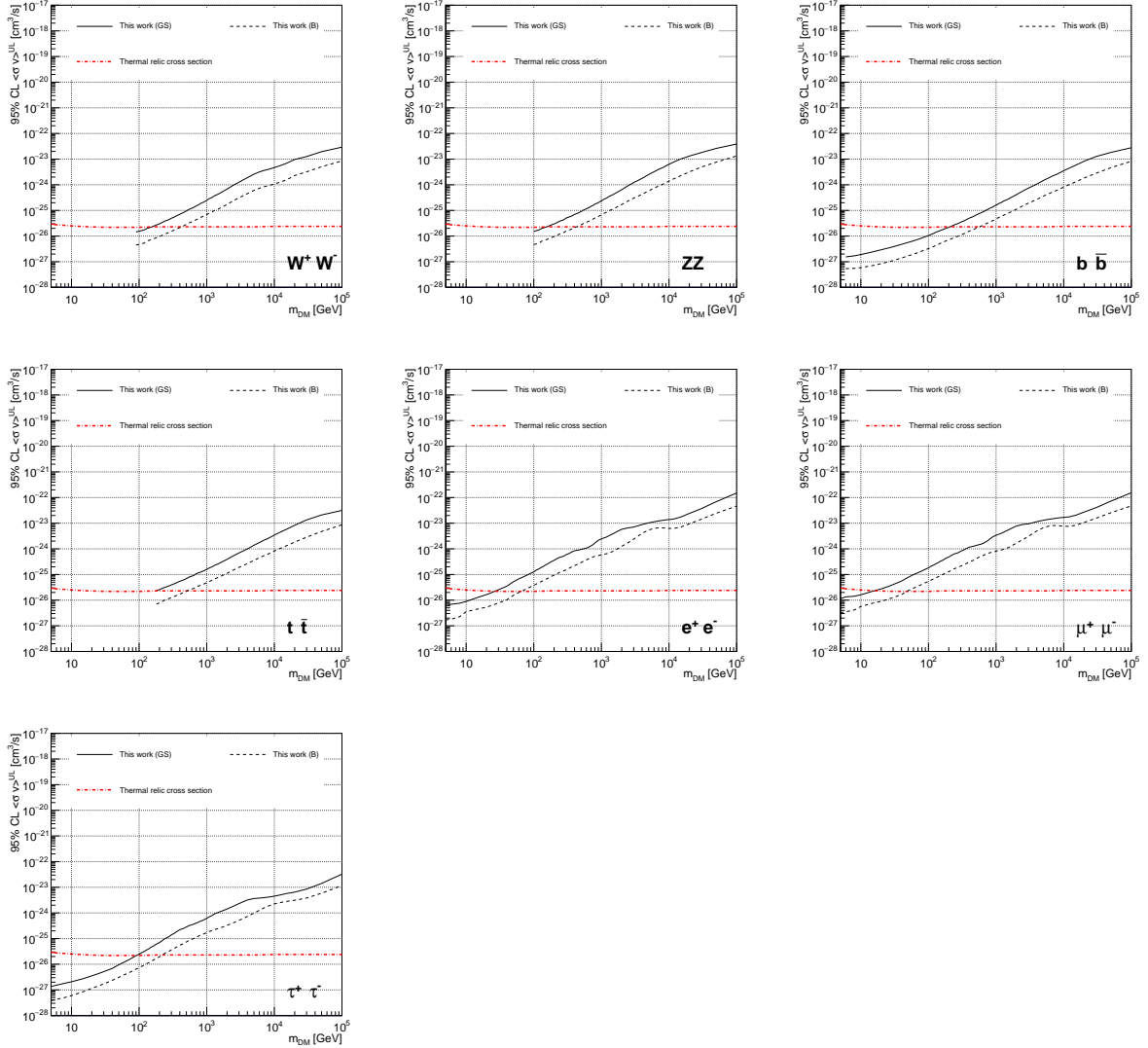


Figure 5.10 Comparisons of the combined limits at 95% confidence level for each of the eight annihilation channels when using the J factors from Ref. [69] (\mathcal{GS} set in Table 5.1), plain lines, and the J factor from Ref. [63, 71] (\mathcal{B} set in Table 5.1), dashed lines. The cross-section given by the thermal relic is also indicated [70].

1355 5.7 HAWC Systematics

1356 5.7.1 Inverse Compton Scattering

1357 The DM-DM annihilation channels produce many high energy electrons regardless of the
 1358 primary annihilation channel. These high energy electrons can produce high energy gamma-rays
 1359 through Inverse Compton Scattering (ICS). If this effect is strong, it would change the morphology
 1360 of the source and increase the total expected gamma-ray counts from any source. The PPPC [58]

1361 provides tools in Mathematica for calculating the impact of ICS for an arbitrary location in the
1362 sky for a specified annihilation channel. We calculated the change in gamma-ray counts for DM
1363 annihilation to primary $e\bar{e}$ for RA and Dec corresponding to Segue1 and Coma Berenices. These
1364 dSphs were chosen because they are the strongest contributors to the limit. $e\bar{e}$ was selected because
1365 it would have the largest number of high energy electrons. The effect was found to be on the order
1366 of 10^{-7} on the gamma-ray spectrum. As a result, this systematic is not considered in our analysis.

1367 **5.7.2 Point Source Versus Extended Source Limits**

1368 The previous DM search toward dSph approximated the dSphs as point sources [60]. In
1369 this analysis, the dSphs are implemented as extended with J-factor distributions following those
1370 produced by [69]. The resolution of the cited map is much finer than HAWC's angular resolution.
1371 The vast majority of the J-factor distribution is represented on the central HAWC pixel of the dSph
1372 spatial map. However, the neighboring 8 pixels are not negligible and contribute to our limit.

1373 Figure 5.11 shows a substantial improvement to the limit for Segue1. Fig. 5.12 however showed
1374 identical limits. These disparities are best explained by the relative difference in their J-Factors.
1375 Both dSphs pass almost overhead the HAWC detector, however Segue1 has the larger J-Factor
1376 between the two. Adjacent pixels to the central pixel will therefore contribute to the limits. This is
1377 the case for other dSph that are closer to the zenith of the HAWC detector.

1378 Comparison plots for all sources and the combined limit can be found in the sandbox for the
1379 Glory Duck project.

1380 **5.7.3 Impact of Pointing Systematic**

1381 During the analysis it was discovered that directional reconstruction of gamma-rays had a
1382 systematic bias at large zenith angles. Slides describing this systematic can be found [here](#). Shown
1383 on the presentation is dependence on the pointing systematic on declination. New spatial profiles
1384 were generated for every dSph and limits were computed for the adjusted declination.

1385 Section 5.7.3 demonstrates the impact of this systematic for all DM annihilation channels
1386 studied by HAWC. The impact is a tiny improvement, yet mostly identical, to the combined limits.

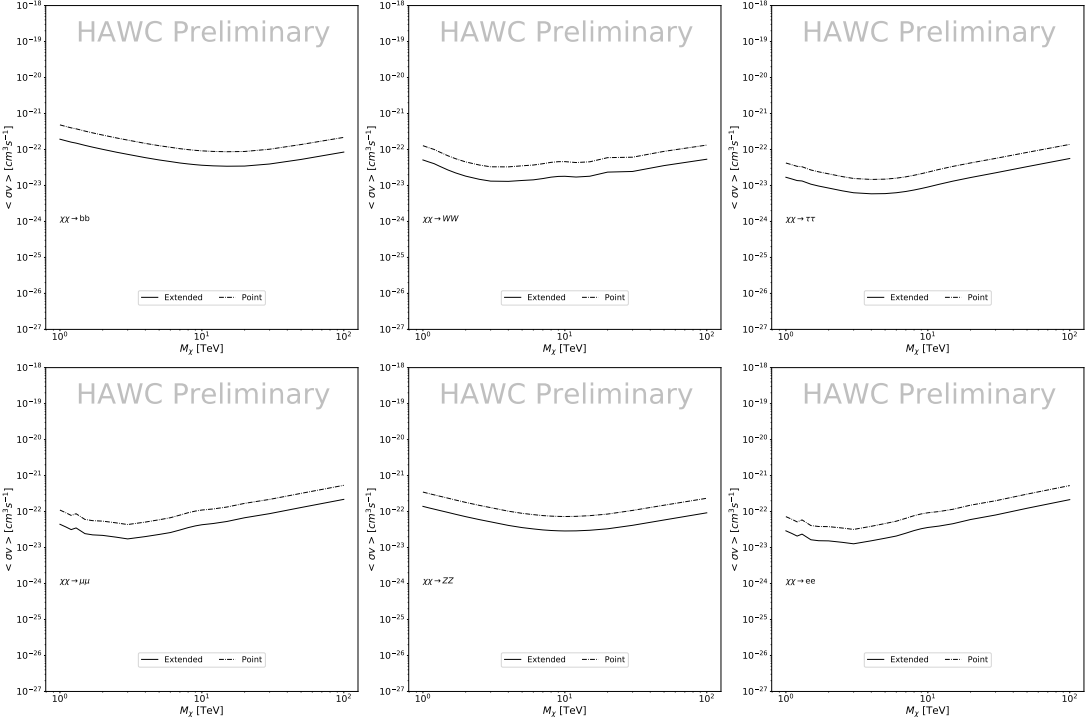


Figure 5.11 Comparisons of the combined limits at 95% confidence level for a point source analysis and extended source using [69] \mathcal{GS} J-factor distributions and PPPC [58] annihilation spectra. Shown are the limits for Segue1 which will have the most significant impact on the combined limit. 6 of the 7 DM annihilation channels are shown. Solid lines are extended source studies. Dashed lines are point source studies. Overall, the extended source analysis improves the limit by a factor of 2.

1387 5.8 J-factor distributions

1388 5.8.1 Numerical integration of \mathcal{GS} maps

1389 It was discovered well after the HAWC analysis was completed that the published tables from
 1390 \mathcal{GS} [59] quoted median J -factors were computed in a non-trivial manner. The assumption myself
 1391 and collaborators had been that the published tables represented the J -factor as a function of θ for
 1392 the best global fit model on a per-source basis. However, this is not the case. Instead, what is
 1393 published are the best fit model for each dwarf that only considers stars up to the angular separation
 1394 θ . Therefore, the model is changing for each value of θ for each dwarf. Yet, the introduced features
 1395 from unique models at each θ are much smaller than the angular resolution of HAWC. It is not
 1396 expected for these effects to impact the limits and TS greatly as a result.

1397 Median J -factor model profiles were provided by the authors. New maps were generated

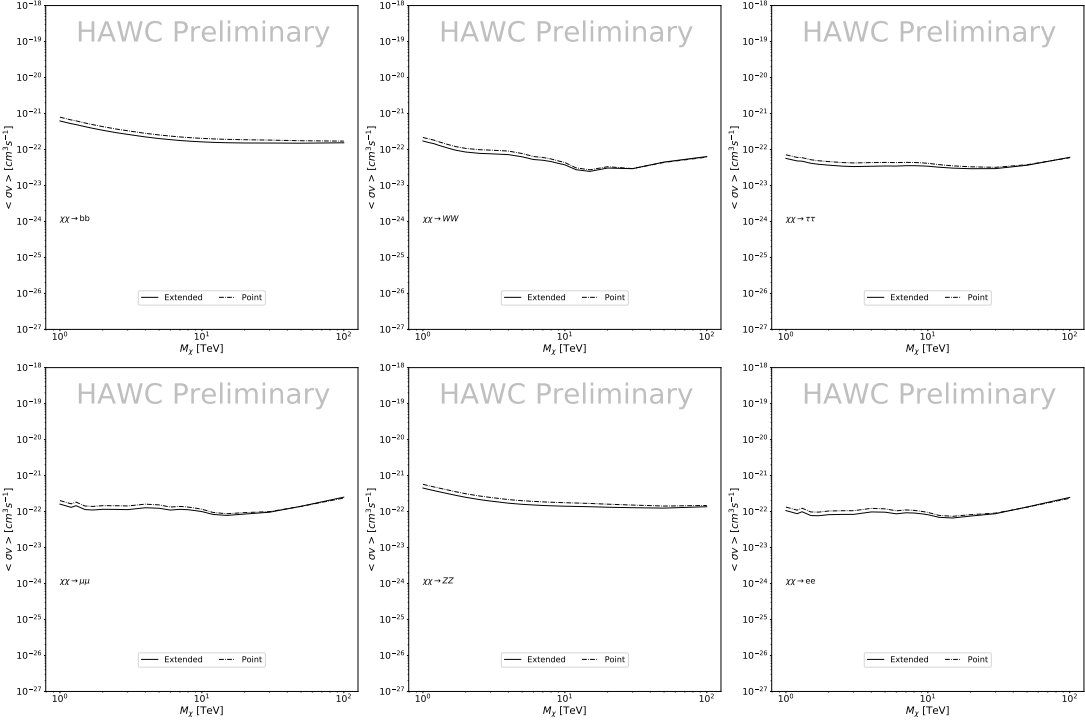


Figure 5.12 Same as Fig. 5.11 on Coma Berenices. This dSph also contributes significantly to the limit. The limits are identical in this case.

1398 and analyzed for Segue1 and Coma Berenices. Figure 5.14 shows the differential between maps
 1399 generated with the method from Section 5.8.1 and from the authors of [59]. These maps were
 1400 reanalyzed for all SM DM annihilation channels. Upper limits for these channels are shown in
 1401 Figure 5.15

1402 From Figure 5.15, we can see that the impact of these model difference was no substantial.
 1403 The observed impact was a fractional effect which is much smaller than the impact from selecting
 1404 another DM spatial distribution model as was shown in Figure 5.10.

1405 **5.8.2 \mathcal{GS} Versus \mathcal{B} spatial models**

1406 We show in this appendix a comparison between the J -factors computed by Geringer-Sameth
 1407 *et al.* [69] (the \mathcal{GS} set) and the ones computed by Bonnivard *et al.* [63, 71] (the \mathcal{B} set). The
 1408 \mathcal{GS} J -factors are computed through a Jeans analysis of the kinematic stellar data of the selected
 1409 dSphs, assuming a dynamic equilibrium and a spherical symmetry for the dSphs. They adopted
 1410 the generalized DM density distribution, known as Zhao-Hernquist, introduced by [61], carrying

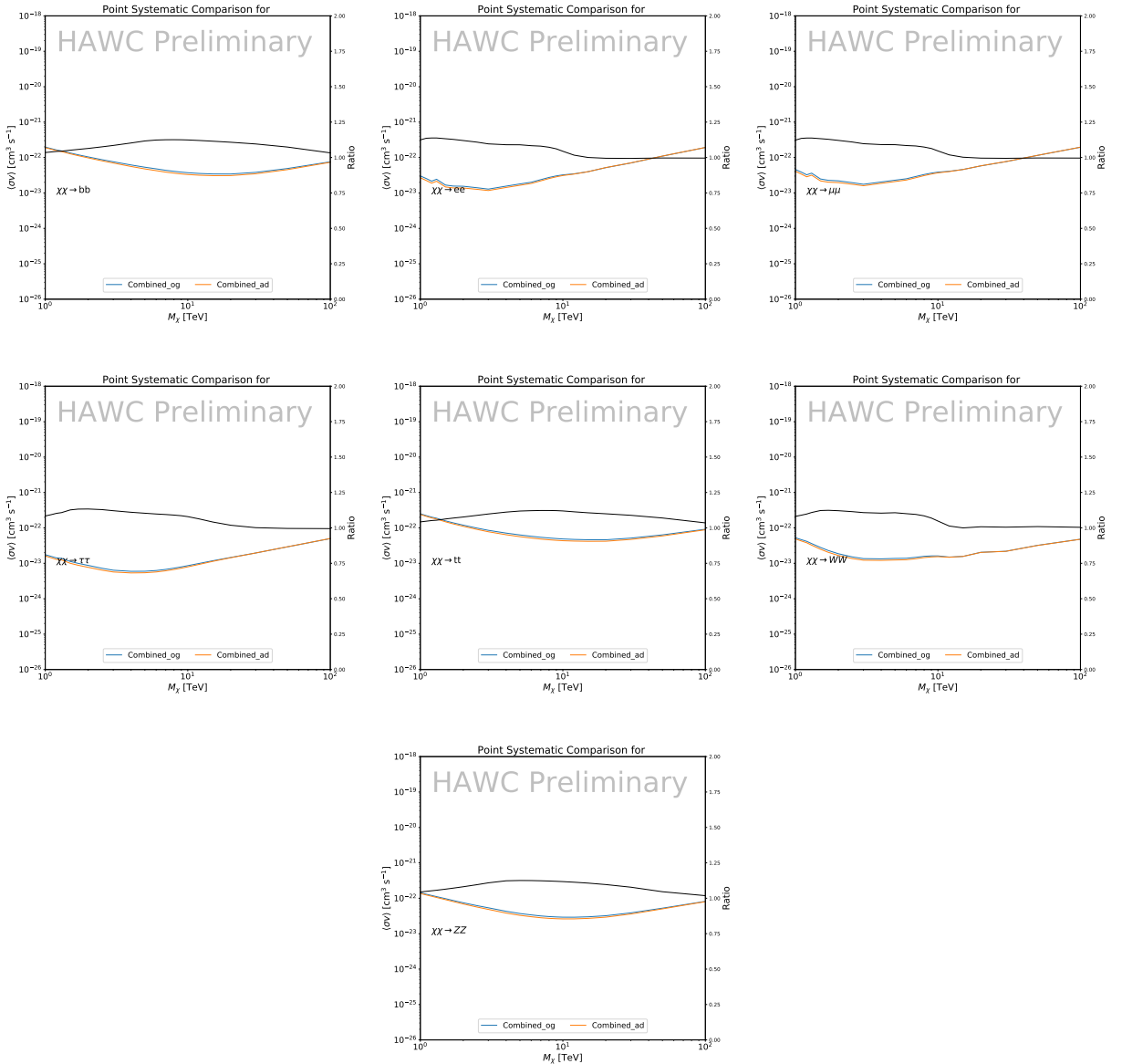


Figure 5.13 Comparison of combined limits when correcting for HAWC's pointing systematic. All DM annihilation channels are shown. The solid black line is the ratio between published limit to the declination corrected limit. The blue solid line or "Combined_og" represented the limits computed for Glory Duck. The solid orange line or "Combined_ad" represented the limits computed after correcting for the pointing systematic.

1411 three additional index parameters to describe the inner and outer slopes, and the break of the
 1412 density profile. Such a profile parametrization allows the reduction of the theoretical bias from
 1413 the choice of a specific radial dependency on the kinematic data. In other words, the increase of
 1414 free parameters with the use of the Zhao-Hernquist profile allows a better description of the mass

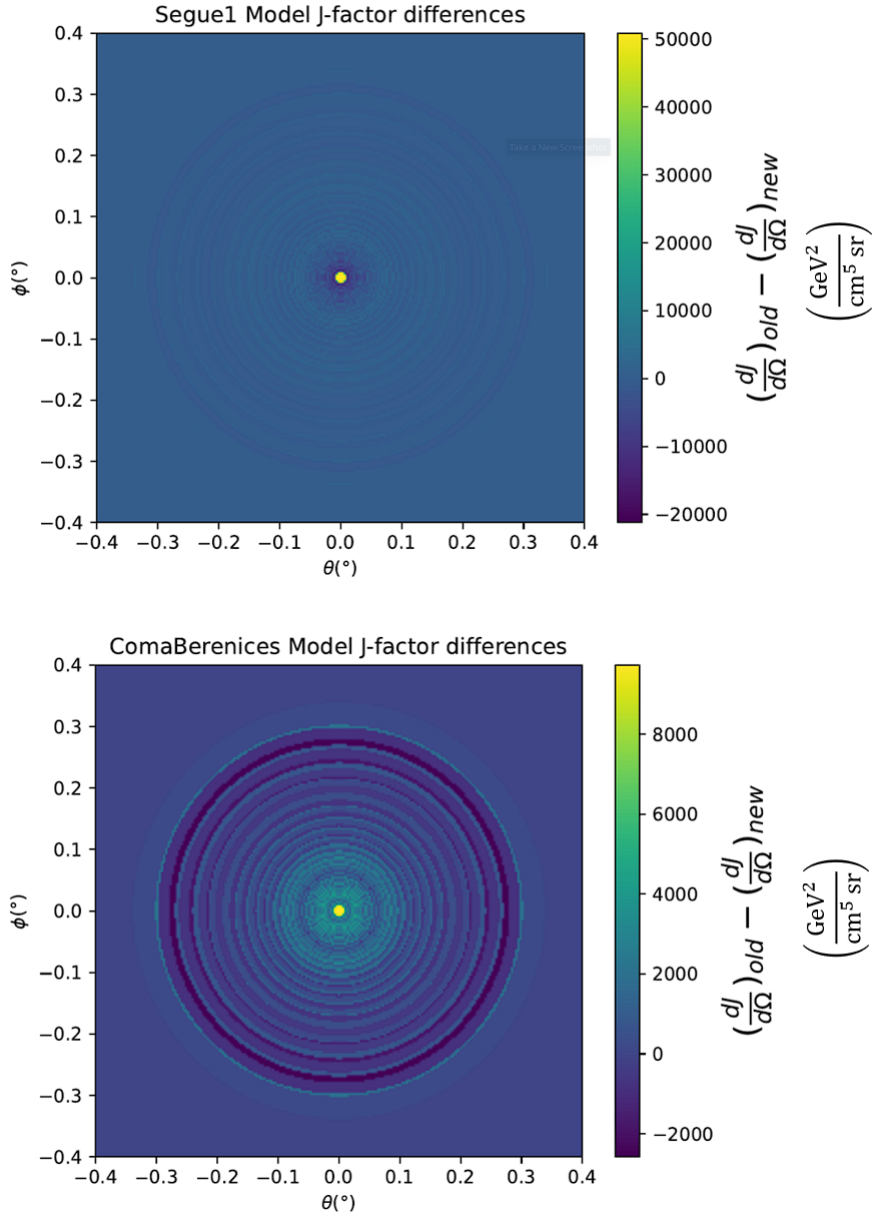


Figure 5.14 Differential map of dJ/Ω from model built in Section 5.8.1 and profiles provided directly from authors. (Top) Differential from Segue1. (bottom) Differential from Coma Berenices. Note that their scales are not the same. Segue1 shows the deepest discrepancies which is congruent with its large uncertainties. Both models show anuli where unique models become apparent.

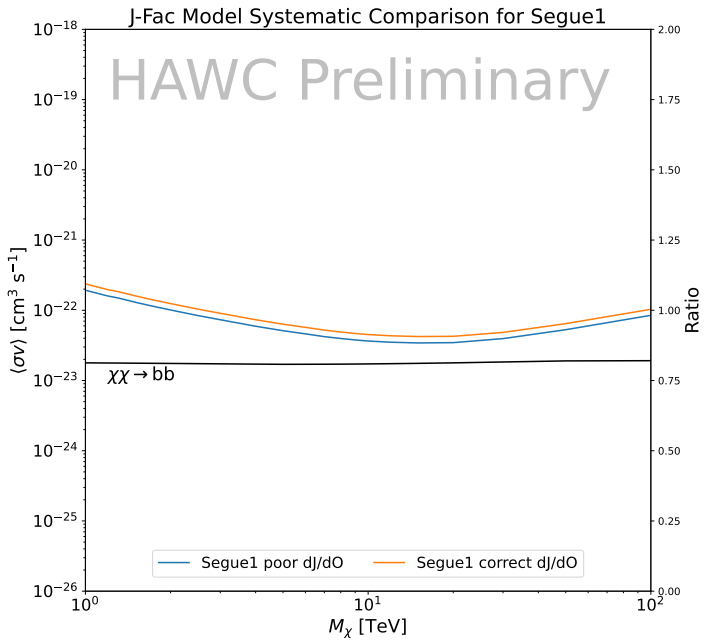
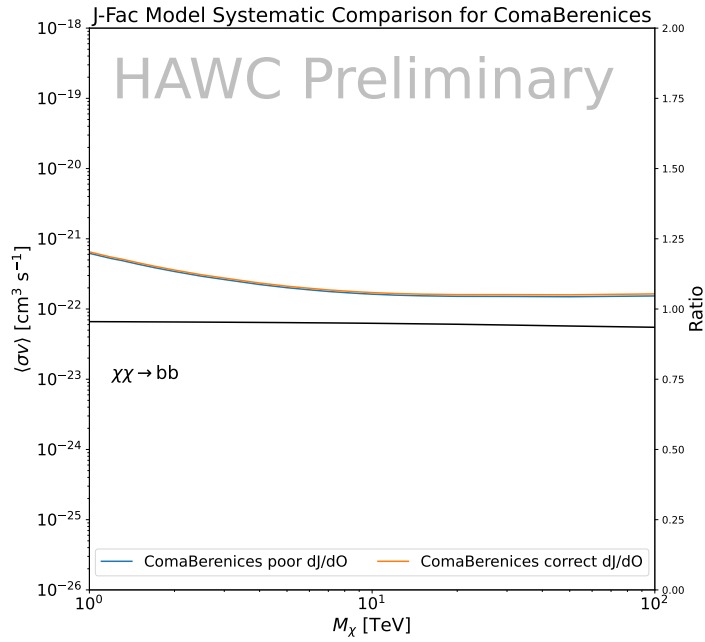


Figure 5.15 HAWC limits for Coma Berenices (top) and Segue1 (bottom) for two different map sets. Blue lines are limits calculated on maps with poor model representation. Orange lines are limits calculated on spatial profiles provided by the authors of [59]. Black line is the ratio of the poor spatial model limits to the corrected spatial models. The left y-axis measures $\langle \sigma v \rangle$ for the blue and orange lines. The right y-axis measures the ratio and is unitless.

1415 density distribution of dark matter.

1416 In addition, a constant velocity anisotropy profile and a Plummer light profile [74] for the stellar
1417 distribution were assumed. The velocity anisotropy profile depends on the radial and tangential
1418 velocity dispersion. However, its determination remains challenging since only the line-of-sight
1419 velocity dispersion can be derived from velocity measurements. Therefore, the parametrization of
1420 the anisotropy profile is obtained from simulated halos (see [75] for more details). They provide the
1421 values of the J -factors of regions extending to various angular radius up to the outermost member
1422 star.

1423 The \mathcal{B} J -factors were computed through a Jeans analysis taking into account the systematic
1424 uncertainties induced by the DM profile parametrization, the radial velocity anisotropy profile, and
1425 the triaxiality of the halo of the dwarf galaxies. They performed a more complete study of the dSph
1426 kinematics and dynamics than \mathcal{GS} for the determination of the J -factor. Conservative values of the
1427 J -factors where obtained using an Einasto DM density profile [76], a realistic anisotropy profile
1428 known as the Baes & Van Hese profile [77] which takes into account that the inner regions can be
1429 significantly non-isotropic, and a Zhao-Hernquist light profile [61].

1430 For both sets, J -factor values are provided for all dSphs as a function of the radius of the
1431 integration region [69, 63, 71]. Table 5.1 shows the heliocentric distance and Galactic coordinates
1432 of the twenty dSphs, together with the two sets of J -factor values integrated up to the outermost
1433 observed star for \mathcal{GS} and the tidal radius for \mathcal{B} . Both J -factor sets were derived through a Jeans
1434 analysis based on the same kinematic data, except for Draco where the measurements of [78] have
1435 been adopted in the computation of the \mathcal{B} value. The computations for producing the \mathcal{GS} and \mathcal{B}
1436 samples differ in the choice of the DM density, velocity anisotropy, and light profiles, for which the
1437 set \mathcal{B} takes into account some sources of systematic uncertainties.

1438 Figure 5.16 and Figure 5.17 show the comparisons for the J -factor versus the angular radius
1439 for each of the 20 dSphs used in this study. The uncertainties provided by the authors are also
1440 indicated in the figures. For the \mathcal{GS} set, the computation stops at the angular radius corresponding
1441 to the outermost observed star, while for the \mathcal{B} set, the computation stops at the angular radius

1442 corresponding to the tidal radius.

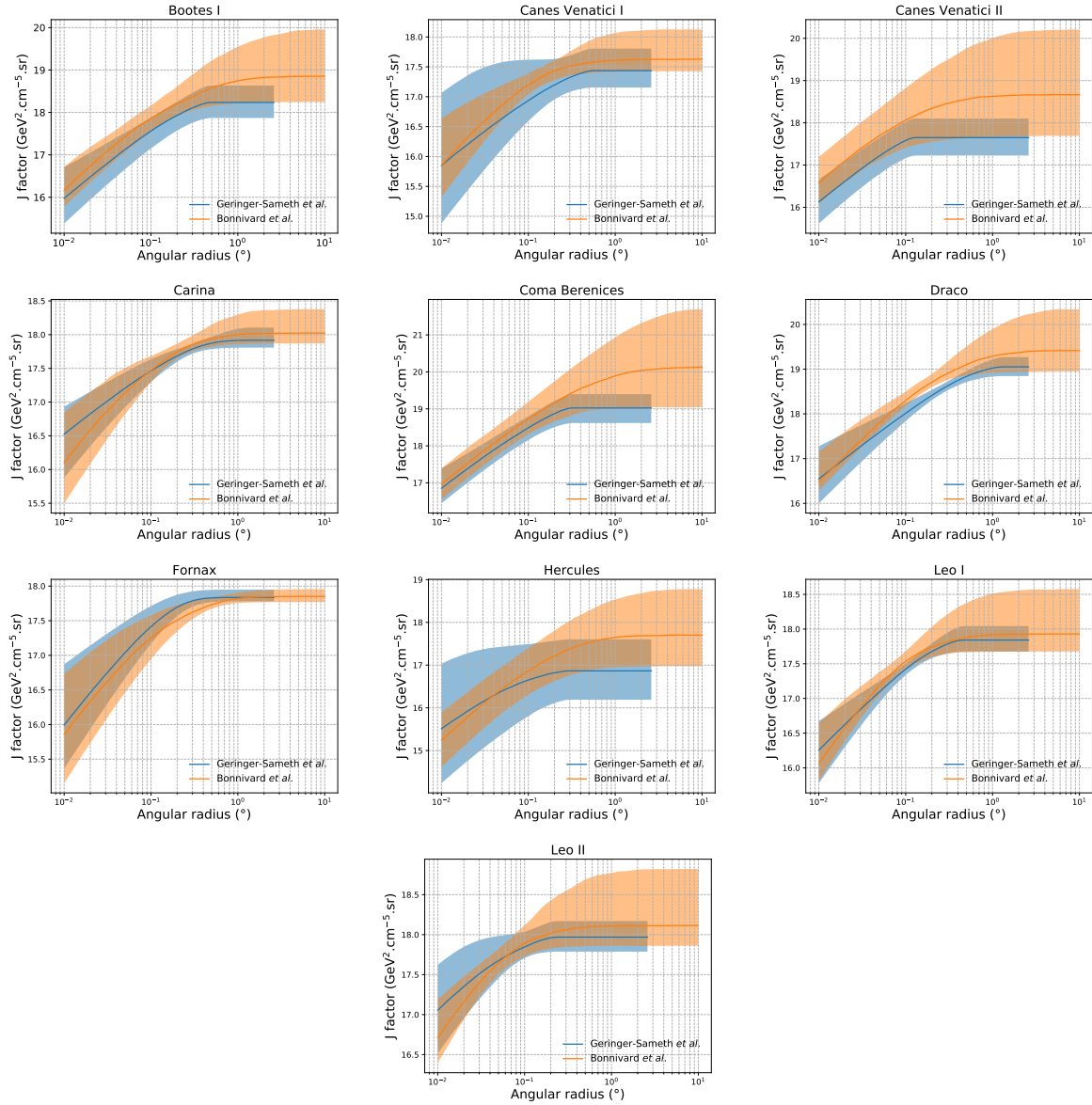


Figure 5.16 Comparisons between the J -factors versus the angular radius for the computation of J factors from Ref. [69] (\mathcal{GS} set in Table 5.1) in blue and for the computation from Ref. [63, 71] (\mathcal{B} set in Tab. 5.1) in orange. The solid lines represent the central value of the J -factors while the shaded regions correspond to the 1σ standard deviation.

1443 5.9 Discussion and Conclusions

1444 In this multi-instrument analysis, we have used observations of 20 dSphs from the gamma-ray
 1445 telescopes Fermi-LAT, H.E.S.S., MAGIC, VERITAS, and HAWC to perform a collective DM
 1446 search annihilation signals. The data were combined across sources and detectors to significantly

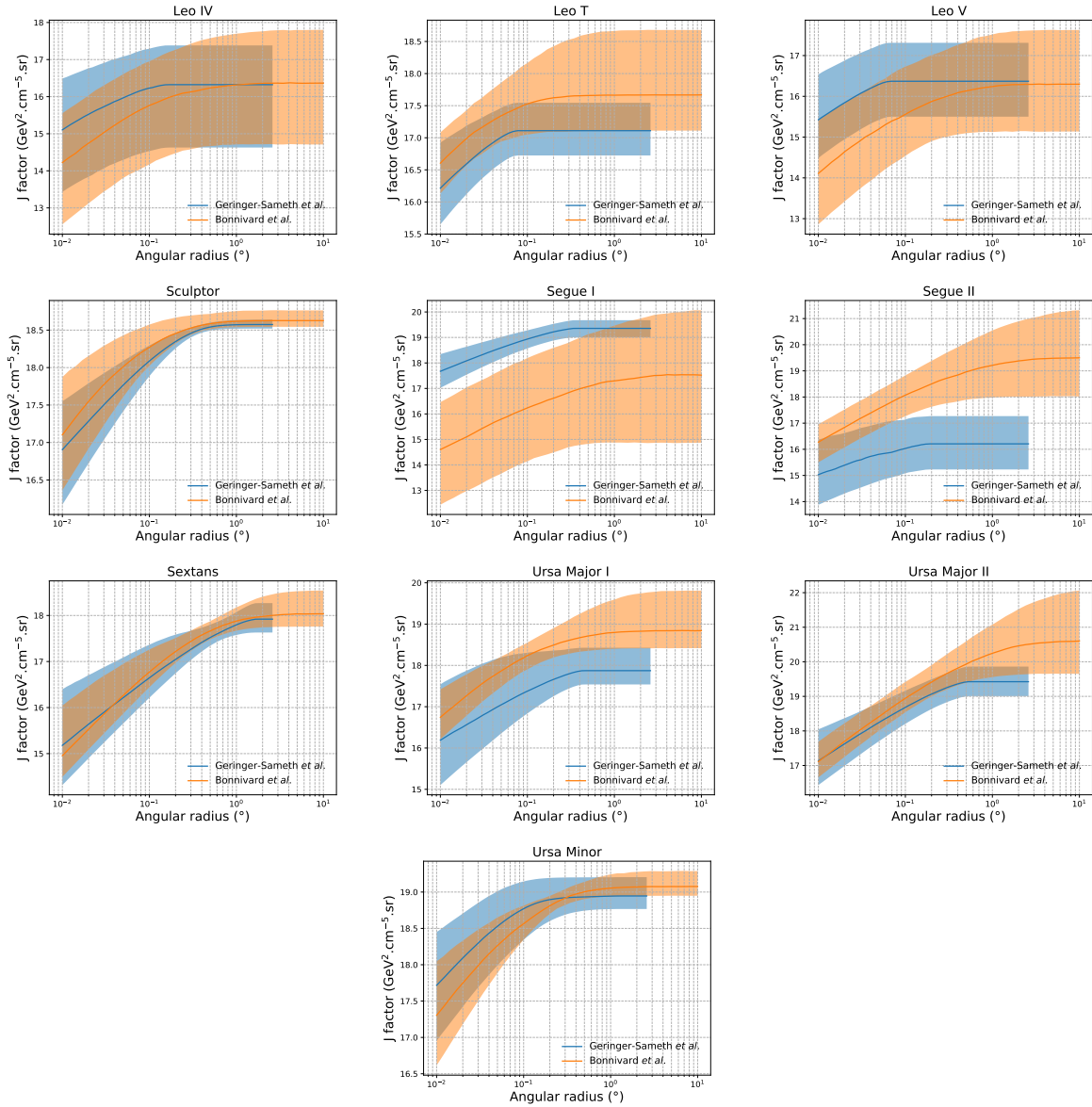


Figure 5.17 Comparisons between the J -factors versus the angular radius for the computation of J factors from Ref. [69] (\mathcal{GS} set in Tab. 5.1) in blue and for the computation from Ref. [63, 71] (\mathcal{B} set in Tab. 5.1) in orange. The solid lines represent the central value of the J -factors while the shaded regions correspond to the 1σ standard deviation.

increase the sensitivity of the search. We have observed no significant deviation from the null, no DM hypothesis, and so present our results in terms of upper limits on the annihilation cross-section for seven potential DM annihilation channels.

Fermi-LAT brings the most stringent constraints for continuum channels below approximately 1 TeV. The remaining detectors dominate at higher energies. Overall, for multi-TeV DM mass,

1452 the combined DM constraints from all five telescopes are 2-3 times stronger than any individual
1453 telescope for multi-TeV DM.

1454 Derived from observations of many dSphs, our results produce robust limits given the DM
1455 content of the dSphs is relatively well constrained. The obtained limits span the largest mass
1456 range of any WIMP DM search. Our combined analysis improves the sensitivity over previously
1457 published results from each detector which produces the most stringent limits on DM annihilation
1458 from dSphs. These results are based on deep exposures of the most promising known dSphs with
1459 the currently most sensitive gamma-ray instruments. Therefore, our results constitute a legacy of
1460 a generation of gamma-ray instruments on WIMP DM searches towards dSphs. Our results will
1461 remain the reference in the field until a new generation of more sensitive gamma-ray instruments
1462 begin operations, or until new dSphs with higher J -factors are discovered.

1463 This analysis serves as a proof of concept for future multi-instrument and multi-messenger
1464 combination analyses. With this collaborative effort, we have managed to sample over four orders
1465 in magnitude in gamma-ray energies with distinct observational techniques. Determining the nature
1466 of DM continues to be an elusive and difficult problem. Larger datasets with diverse measurement
1467 techniques could be essential to tackling the DM problem. A future collaboration using similar
1468 techniques as the ones described in this paper could grow even beyond gamma rays. The models we
1469 used for this study include annihilation channels with neutrinos in the final state. Advanced studies
1470 could aim to merge our results with those from neutrino observatories with large data sets. Efforts
1471 are already underway to add data from the IceCube, ANTARES, and KM3NeT observatories to
1472 these gamma-ray results.

1473 From this work, a selection of the best candidates for observations, according to the latest
1474 knowledge on stellar dynamics and modelling techniques for the derivation of the J -factors on
1475 the potential dSphs targets, is highly desirable at the time that new experiments are starting their
1476 dark matter programs using dSphs. Given the systematic uncertainty inherent to the derivation of
1477 the J -factors, an informed observational strategy would be to select both objects with the highest
1478 J -factors that could lead to DM signal detection, and objects with robust J -factor predictions, i.e.

1479 with kinematic measurements on many bright stars, which would strengthen the DM interpretation
1480 reliability of the observation outcome.

1481 This analysis combines data from multiple telescopes to produce strong constraints on astro-
1482 physical objects. From this perspective, these methods can be applied beyond just DM searches.
1483 Almost every astrophysical study can benefit from multi-telescope, multi-wavelength gamma-ray
1484 studies. We have enabled these telescopes to study the cosmos with greater precision and detail.
1485 Many astrophysical searches can benefit from multi-instrument gamma-ray studies, for which our
1486 analysis lays the foundation.

CHAPTER 6

MULTITHREADING HAWC ANALYSES FOR DARK MATTER SEARCHES

6.1 Introduction

HAWC's current software suite, plugins to 3ML and HAL [68, 34], do not fully utilize computational advancements of recent decades. Said advancements include the proliferation of Graphical Processing Units (GPUs), and multithreading on multicore processors. The analysis described in chapter 5 took up to 3 months of wall time waiting for the full gambit of data analysis and simulation of background to compute. Additionally, with the updated 2D energy binning scheme, f_{hit} and Neural Network (NN), the time needed to compute expected to grow. Although excessive computing time was, in part, from an intense use of a shared computing cluster, it was evident that there was room for improvement. In HAWC's next generation dSph DM search, I decided to develop codes that would utilize the multicore processors on modern high performance computing clusters. The results of this work are featured in this chapter and brought a human timing improvement to computation that scales approximately as $1/N$ where N is the number of threads.

6.2 Dataset and Background

This section enumerates the data and background methods used for HAWC's multithreaded study of dSphs. Section 6.2.1 and Section 6.2.2 are most useful for fellow HAWC collaborators looking to replicate a multithreaded dSph DM search.

6.2.1 Itemized HAWC files

These files are only available within HAWC's internal documentation and collaborators. They are not meant for public access, and are presented here so that HAWC collaborators can reproduce results accurately.

- Detector Resolution: `refit-Pass5-Final-NN-detRes-zenith-dependent.root`
- Data Map: `Pass5-Final-NN-maptree-ch103-ch1349-zenith-dependent.root`
- Spectral Dictionary: `HDMspectra_dict_gamma.npy`

1511 **6.2.2 Software Tools and Development**

1512 This analysis was performed using HAL and 3ML [34, 57] in Python3. I built software
1513 in collaboration with Michael Martin and Letrell Harris to implement the *Dark Matter Spectra*
1514 *from the Electroweak to the Planck Scale* (HDM) [79] and dSphs spatial model from [80] for
1515 HAWC analysis. A NumPy dictionary of HDM, `HDMspectra_dict_gamma.npy`, was made for
1516 portability within the collaboration. These dictionaries were generated from the [git repository](#) [79].
1517 The analysis was performed using the Neural Network energy estimator for Pass 5.F. A description
1518 of this estimator was provided in chapter 3. [TODO: Define a subsection when it's written](#), and its
1519 key, relevant improvements are an improved energy estimation and improved sensitivities at higher
1520 zenith angles. All other software used for data analysis, DM profile generation, and job submission
1521 to SLURM are also kept in my sandbox in the [Dark Matter HAWC](#) project. The above repository
1522 also incorporates the model inputs used previously in Glory Duck, described in chapter 5, so Glory
1523 Duck remains compatible with modern software.

1524 **6.2.3 Data Set and Background Description**

1525 The HAWC data maps used for this analysis contain 2565 days of data between runs 2104 and
1526 7476. They were generated from pass 5.f reconstruction. The analysis is performed using the NN
1527 energy estimator with bin list:

1528 B1C0Ea, B1C0Eb, B1C0Ec, B1C0Ed, B1C0Ee, B2C0Ea, B2C0Eb, B2C0Ec, B2C0Ed, B2C0Ee,
1529 B3C0Ea, B3C0Eb, B3C0Ec, B3C0Ed, B3C0Ee, B3C0Ef, B4C0Eb, B4C0Ec, B4C0Ed, B4C0Ee,
1530 B4C0Ef, B5C0Ec, B5C0Ed, B5C0Ee, B5C0Ef, B5C0Eg, B6C0Ed, B6C0Ee, B6C0Ef, B6C0Eg,
1531 B6C0Eh, B7C0Ee, B7C0Ef, B7C0Eg, B7C0Eh, B7C0Ei, B8C0Ee, B8C0Ef, B8C0Eg, B8C0Eh,
1532 B8C0Ei, B8C0Ej, B9C0Ef, B9C0Eg, B9C0Eh, B9C0Ei, B9C0Ej, B10C0Eg, B10C0Eh,
1533 B10C0Ei, B10C0Ej, B10C0Ek, B10C0El

1534 Bin 0 was excluded as it has substantial hadronic contamination and poor angular resolution.

1535 Background considerations and source selection was identical to Section 5.2.3, and no additional
1536 arguments are provided here. Many of the HAWC systematics explored in Section 5.7 also apply

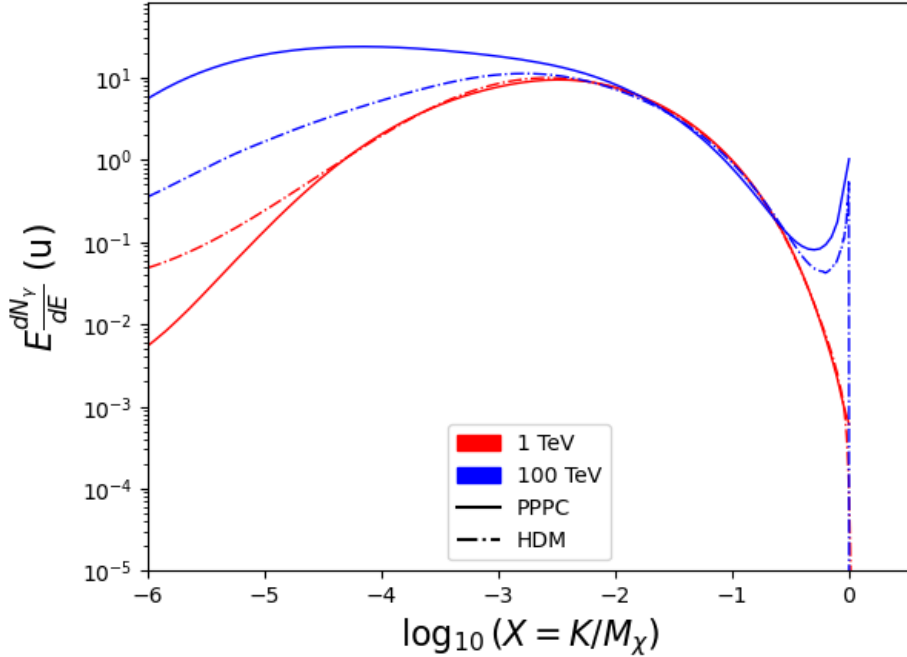


Figure 6.1 Spectral hypotheses from PPPC [58] and HDM [79] for DM annihilation: $\chi\chi \rightarrow W^-W^+$. Solid lines are spectral models with EW corrections from the PPPC. Dash-dot lines are spectral models from HDM. Red lines are models for $M_\chi = 1$ TeV. Blue lines represent models for $M_\chi = 100$ TeV.

1537 for this DM search and are not added upon here.

1538 **6.3 Analysis**

1539 The analysis and its systematics are almost identical to Section 5.3. Importantly, we use the
 1540 same **TODO: fix this ref** Equation (5.1) and Equation (5.2) for estimating the gamma-ray flux at
 1541 HAWC from our sources.

1542 **6.3.1 $\frac{dN_\gamma}{dE_\gamma}$ - Particle Physics Component**

1543 For these spectra, we import HDM with Electroweak (EW) corrections and additional correc-
 1544 tions for neutrinos above the EW scale [79]. The spectra are implemented as a model script in
 1545 astromodels for 3ML. A comprehensive description of EW corrections and neutrino considerations
 1546 are provided later in Sec. 8.

1547 Figure 6.1 demonstrates the impact of changes implemented in HDM on DM annihilation to W
 1548 bosons. A class in astromodels was developed to include HDM and is aptly named **HDMspectra**
 1549 within `DM_models.py`. The SM DM annihilation channels studied here are $\chi\chi \rightarrow$:

1550 e^+e^- , $\mu^+\mu^-$, $\tau^+\tau^-$, $b\bar{b}$, $t\bar{t}$, gg , W^+W^- , ZZ , $c\bar{c}$, $u\bar{u}$, $d\bar{d}$, $s\bar{s}$, $\nu_e\bar{\nu}_e$, $\nu_\mu\bar{\nu}_\mu$, $\nu_\tau\bar{\nu}_\tau$, $\gamma\gamma$, hh .

1551 For $\gamma\gamma$ and ZZ , a substantial fraction of the signal photons are expected to have $E_\gamma = m_\chi$ [79].
 1552 This introduces δ -function that is much narrower than the energy resolution of the HAWC detector.
 1553 To ensure that this feature is not lost in the likelihood fits, the 'line' feature is convolved with a
 1554 Gaussian kernel with a 1σ width of $0.05 \cdot m_\chi$ and total kernel window of $\pm 4\sigma$. This differs from
 1555 HAWC's previous line study where 30% of HAWC's energy resolution was used for the kernel [81].
 1556 The NN energy estimator's strength compared to f_{hit} at low gamma-ray energy enables narrower
 1557 kernels [79]. $\chi\chi \rightarrow \gamma\gamma$ and ZZ spectral hypotheses are shown in Figure 6.2. We did not explore
 1558 how well we reconstruct injected signal events for various kernels widths. This is a systematic
 1559 that should be tested before publication to journal. Spectral models for the remaining annihilation
 1560 channels are plotted for each m_χ in Figure B.1.

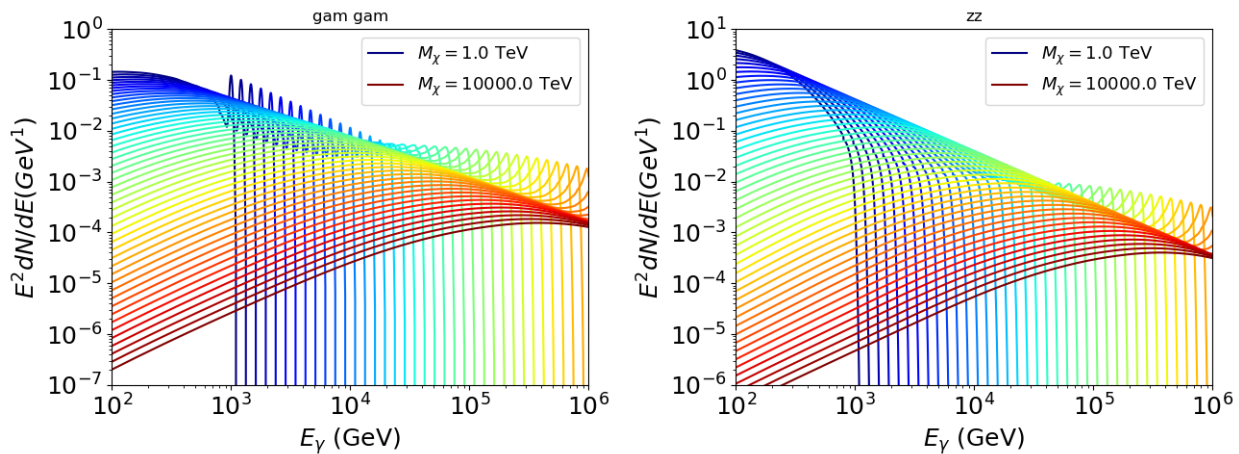


Figure 6.2 Photon spectra for $\chi\chi \rightarrow \gamma\gamma$ (left) and $\chi\chi \rightarrow ZZ$ (right) after Gaussian convolution of line features. Both spectra have δ -features at photon energies equal to the DM mass. Bluer lines are annihilation spectra with lower DM mass. Redder lines are spectra from larger DM mass. All spectral models are sourced from the Heavy Dark Matter models [79]. Axes are drawn roughly according to the energy sensitivity of HAWC.

1561 **6.3.2 J Astrophysical Components**

1562 The J-factor profiles for each source are imported from Louis Strigari et al. (referred to with
 1563 \mathcal{LS}) [80]. The \mathcal{LS} catalog fits a Navarro–Frenk–White (NFW) [62] spatial DM distributions to

1564 the dSphs which has a DM density of

$$\rho(r) = \frac{\rho_0}{\frac{r}{R_s} \left(1 + \frac{r}{R_s}\right)^2}. \quad (6.1)$$

1565 ρ_0 and the scale radius, R_s are free parameters fit for each dSph. r is the distance from the center
1566 of the dSph.

1567 Profiles in $\frac{dJ}{d\Omega}(\theta)$ up to an angular separation $\theta = 0.5^\circ$ were provided directly from the authors.

1568 Map generation from these profiles were almost identical to Section 5.3.2 except that a higher order
1569 trapezoidal integral was used for the normalization of the square, uniformly-spaced map:

$$p^2 \cdot \sum_{i=0}^N \sum_{j=0}^M w_{i,j} \frac{dJ}{d\Omega}(\theta_{i,j}, \phi_{i,j}) \quad (6.2)$$

1570 p is the angular side of one pixel in the map. $w_{i,j}$ is a weight assigned the following ways:

1571 $w_{i,j} = 1$ if $(\theta_{i,j}, \phi_{i,j})$ is fully within the region of integration

1572 $w_{i,j} = 1/2$ if $(\theta_{i,j}, \phi_{i,j})$ is on an edge of the region of integration

1573 $w_{i,j} = 1/4$ if $(\theta_{i,j}, \phi_{i,j})$ is on a corner of the region of integration

1574 Figure 6.3 shows the median and $\pm 1\sigma$ maps used as input for this DM annihilation study.

1575 6.3.3 Source Selection and Annihilation Channels

1576 HAWC's sources for this multithreaded analysis include Coma Berenices, Draco, Segue 1, and
1577 Sextans. \mathcal{LS} observed up to 43 sources in its publication, however only 4 of the best fit profiles
1578 were provided at the time this thesis was written. A full description of each source used in this
1579 analysis is found in Table 6.1.

1580 This analysis improves on chapter 5 in the following ways. Previously, the particle physics
1581 model used for gamma-ray spectra from DM annihilation was from the PPPC [58] which missed
1582 important considerations relevant for the neutrino sector. HDM is used to account for this shortfall
1583 [79]. HDM also models DM to the Planck scale which permits HAWC to probe PeV scale DM. For
1584 this study, we sample DM masses: 1 TeV - 10 PeV with 6 mass bins per decade in DM mass. In

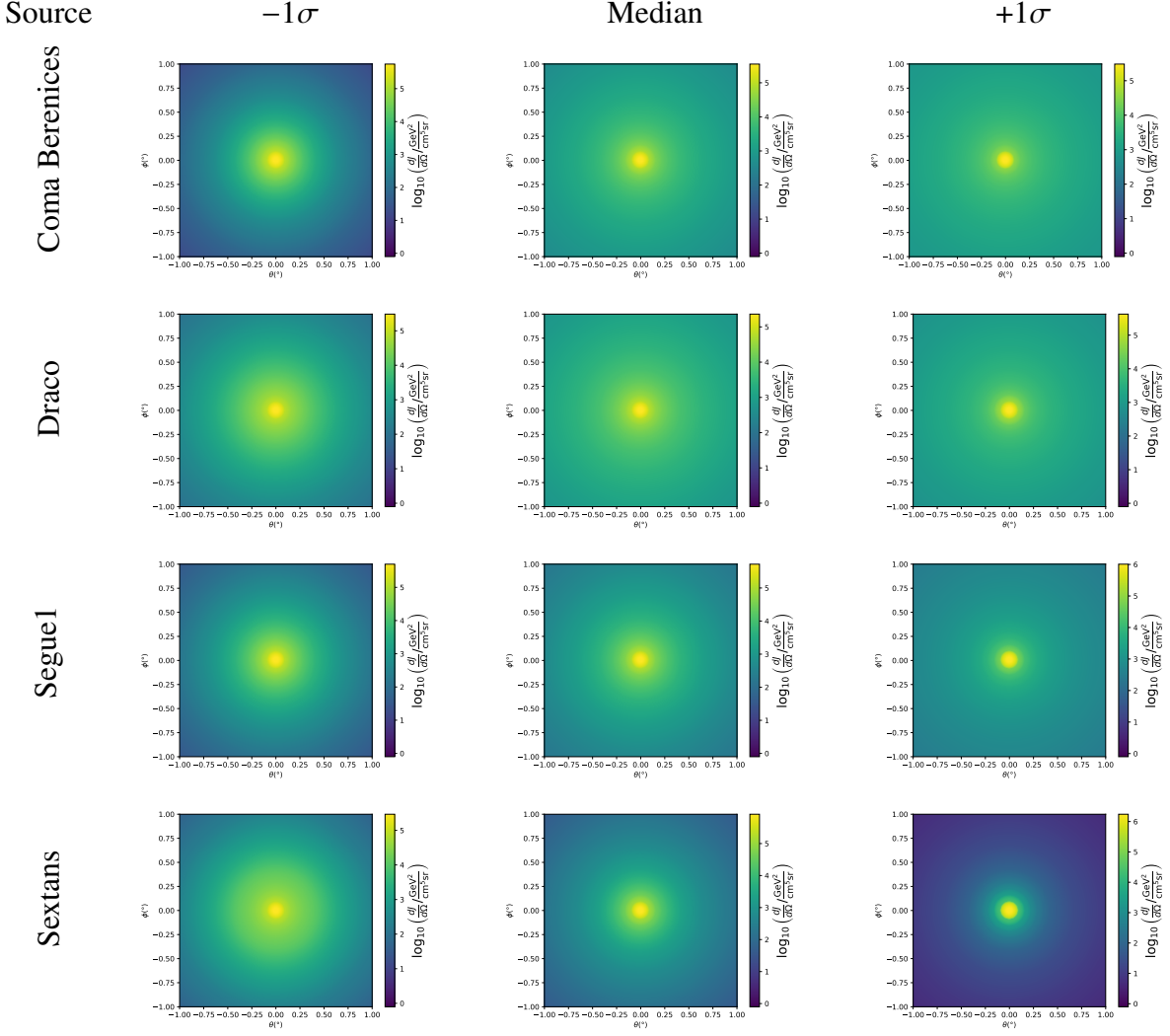


Figure 6.3 $\frac{dJ}{d\Omega}$ maps for Coma Berenices, Draco, Segue1, and Sextans. Columns are divided for the $\pm 1\sigma$ uncertainties in $dJ/d\Omega$ around the mean value from \mathcal{LS} [80]. Origin is centered on the specific dwarf spheroidal galaxies (dSph). θ and ϕ axes are the angular separation from the center of the dwarf. Profiles are truncated at 1° and flattened beyond.

1585 the case of line spectra ($\chi\chi \rightarrow \gamma\gamma$, or ZZ), we double the mass binning to 12 DM mass bins per
 1586 decade in DM mass.

1587 \mathcal{LS} provides 25 sources within HAWC's field of view. Additionally, NFW [62] DM distributions
 1588 have fewer parameters than Zhao [61], so \mathcal{LS} fits ultra-faint dwarves which expands the number of
 1589 sources. However, all sources were not provided by the authors in time for the completion of this
 1590 dissertation. Finally, the gamma-ray ray dataset is much larger. The study performed here analyzes
 1591 2565 days of data compared to 1017 days analyzed in chapter 5.

1592 **6.4 Likelihood Methods**

1593 These are identical to Section 5.4.1 and no additional changes are made to the likelihood. Bins
1594 in this analysis are expanded to include HAWC’s NN energy estimator.

1595 **6.5 Computational Methods: Multithreading**

1596 Previously, as in Section 5.3, the likelihood was minimized for one model at a time. One model
1597 in this case representing a DM annihilation channel (CHAN), DM mass (m_χ), and dSph ((SOURCE)).
1598 In an effort to conserve human and CPU time, jobs submitted for high performance computing
1599 contained a list of m_χ to iterate over for likelihood fitting. Jobs were then trivially parallelized
1600 for each permutation of the two lists: CHANS and SOURCES. The lists for CHANS and SOURCES are
1601 found in Section 6.3.1 and Table 6.1, respectively. Initially, 11 m_χ were serially sampled for one
1602 job defined by a [CHAN, SOURCE] tuple. Computing the likelihoods would take between 1.5 to 2 hrs,
1603 stochastically, for a job. We expect to compute likelihoods for data and 300 Poisson background
1604 trials. The estimated CPU time based on the above for all CHAN (N = 17) and SOURCE (M = 25)
1605 was estimated to 127,925 jobs. In total, 1,407,175 likelihood fits and profiles would be computed
1606 for the 11 mass bins we wished to study. The estimated CPU time ranged between 8k CPU days
1607 to 10k CPU days. Human time is more challenging to estimate as job allocation is stochastic and
1608 highly dependent on what other users are submitting. Yet, it is unlikely that all jobs would run
1609 simultaneously. Therefore, we can expect human time to be about as long as was seen in chapter 5

Name	Distance (kpc)	l, b ($^\circ$)	$\log_{10} J$ (\mathcal{LS} set) $\log_{10}(\text{GeV}^2 \text{cm}^{-5} \text{sr})$
Coma Berenices	44	241.89, 83.61	$19.00^{+0.36}_{-0.35}$
Draco	76	86.37, 34.72	$18.83^{+0.12}_{-0.12}$
Segue I	23	220.48, 50.43	$19.12^{+0.49}_{-0.58}$
Sextans	86	243.50, 42.27	$17.73^{+0.13}_{-0.12}$

Table 6.1 Summary of the relevant properties of the dSphs used in the present work. Column 1 lists the dSphs. Columns 2 and 3 present their heliocentric distance and galactic coordinates, respectively. Column 4 reports the J -factors of each source given from the \mathcal{LS} studies and estimated $\pm 1\sigma$ uncertainties. The values $\log_{10} J$ (\mathcal{LS} set) [80] correspond to the mean J -factor values for a source extension truncated at 0.5° .

1610 which was on the order of months to fully compute on a smaller analysis. A visual aid to describe
1611 how jobs were organized is provided in Figure 6.4.

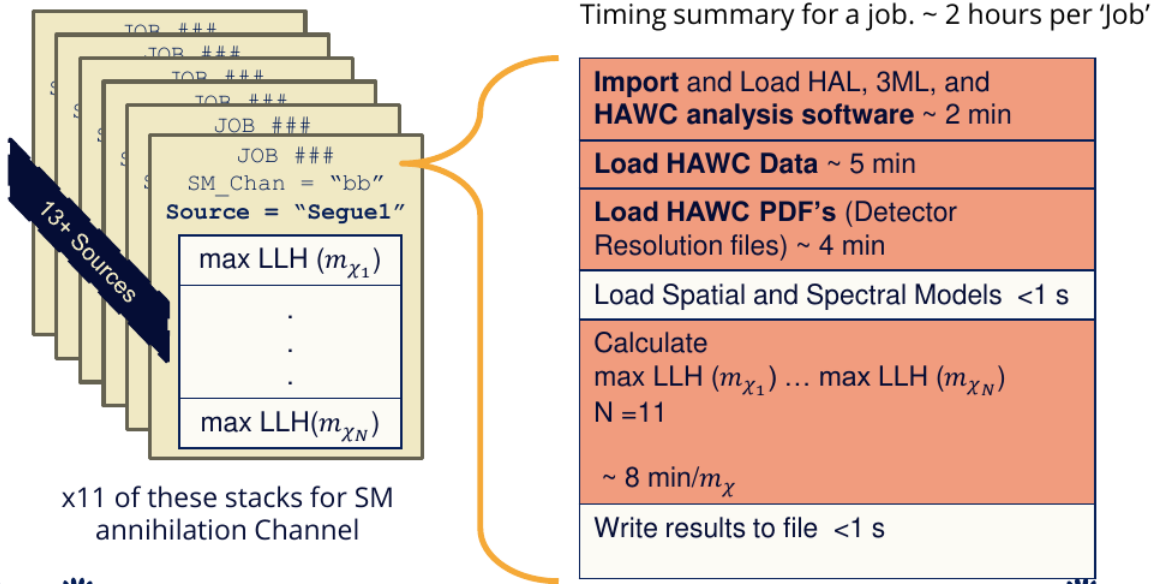


Figure 6.4 Infographic on how jobs and DM computation was organized in Section 5.3. Jobs were built for each permutation of CHANS and SOURCES shown by the left block in the figure. Each job, which took on the order 2 hrs to compute, had the following work flow: 1. Import HAWC analysis software, 2 min to run. 2. Load HAWC count maps, 5 min to run. 3. Load HAWC energy and spatial resolutions, 4 min. 5. Load DM spatial source templates and spectral models, less than 1 s. 6. Perform likelihood fit on data and model, about 8 min per DM mass. 7. Write results to file, less than 1s.

1612 The computational needs for this next generation DM analysis are extreme and is unlike other
1613 analyses performed on HAWC. It became clear that there was a lot to gain from optimizing how
1614 the likelihoods are computed. This section discusses how multi-threading was applied to solve and
1615 reduce HAWC's computing of likelihoods for large parameter spaces like in DM searches.

1616 6.5.1 Relevant Foundational Information

1617 The profiling of the likelihood for HAWC is done via gradient descent where the normalization
1618 of Equation (5.1) (linearly correlated with $\langle \sigma v \rangle$) is rescaled in the descent. Additionally, we sample
1619 the likelihood space for a defined list of $\langle \sigma v \rangle$'s described in Section 5.4.2. The time to compute
1620 these values is not predictable or consistent because many variables can change across the full
1621 model-space. Comprehensively, these variables are:

1622 • m_χ : DM rest mass
 1623 • CHAN : DM annihilation channel in SM.
 1624 • SOURCE : dSph. Involves a spatial template AND coordinate in HAWC data.
 1625 • $\langle\sigma v\rangle$: Effectively the flux normalization and free parameter in the likelihood fit.
 1626 Therefore, we develop an asynchronous, functional-parallel coding pattern. Asynchronous meaning
 1627 the instructions within a function are independent and permitted to be out of sync with sibling
 1628 computations. Functional-parallel meaning that instructions are the subject of parallelization
 1629 rather than threading the likelihood computation. This is close to trivial parallelization seen in
 1630 Figure 6.4 except that we seek to consolidate the loading stages (software, data, and detector
 1631 resolution loading). Multiple asynchronous threads are expected to reduce total serial processing
 1632 time and total overhead across the entire project in addition to saving human time.

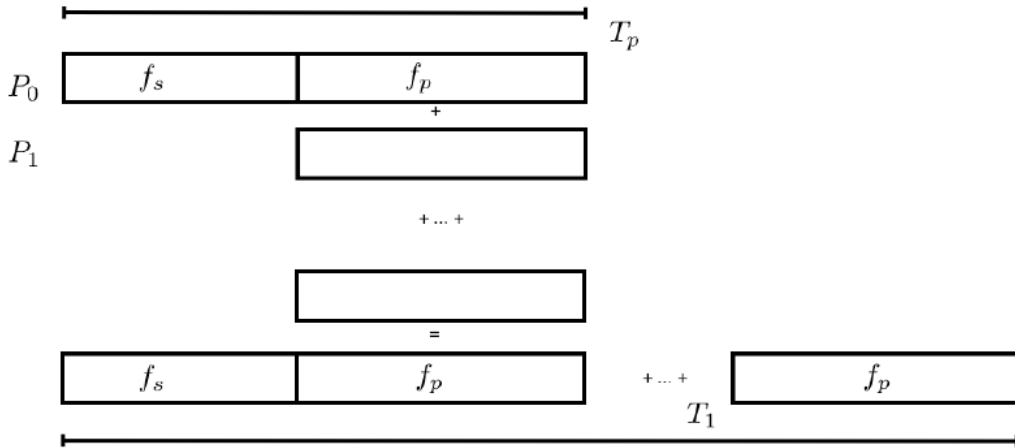


Figure 6.5 Graphic of Gustafson parallel coding pattern. f_s is the fraction of a program, in time, spent on serial computation. f_p is the fraction of computing time that is parallelizable. T_p is the total time for a parallel program to run. T_1 is the total time for a parallel program to run if only 1 processor is allocated. P_N is the N -th processor where it's row is the computation the processor performs. The Gustafson pattern is most similar to what is implemented for this analysis. Figure is pulled from [82].

1633 We need a way to measure and compare the expected speedup and efficiency gain for this
 1634 asynchronous coding pattern. I pull inspiration for timing measurement from [82] and use *Amdahl's*

1635 law with hybrid programming. Hybrid programming meaning that the computation is a mix of
 1636 distributed and shared memory programming. If we assume the code is fully parallelizable over p
 1637 processors and c threads, the ideal speedup is simply pc , and ideal run-time is $T_1/(pc)$. T_1 is the
 1638 total time for a parallel program to run if only 1 processor is allocated. However, the coding pattern
 1639 contains some amount of unavoidable serial computation, as shown in Figure 6.5. In our case, the
 1640 run time, $T_{p,c}$, is estimated to be

$$T_{p,c} = \frac{T_1}{pc} (1 + F_s(c - 1)). \quad (6.3)$$

1641 F_s is the fraction of CPU time dedicated to serial computation. The expected speedup, $S_{p,c}$, is

$$S_{p,c} \equiv \frac{T_1}{T_{p,c}} = \frac{pc}{1 + F_s(c - 1)}. \quad (6.4)$$

1642 From Equation (6.4), we can see that the speed-up scales with p/F_s . We are free to minimize F_s
 1643 asymptotically by enlarging the total models that are submitted to the thread pool, thereby shrinking
 1644 the CPU fraction dedicated to serial operation. We are also free to define exactly how many threads
 1645 and processors we utilize, yet eventually hit a hard cap at the hardware available on our computing
 1646 cluster. HAWC uses Intel Xeon™processors with 48 cores and 96 threads. We see that a successful
 1647 code will scale well as the expected speedup is inversely correlated with F_s . As the total number
 1648 of models sampled grows, the speedup will also.

1649 6.5.2 Implementation

1650 The multithreaded code was written in Python3 and is documented in the `dark_matter_hawc`
 1651 [repository](#) within the script named `mpu_analysis.py`. A version of the script as of April 25
 1652 **TODO: make sure to update on this date** is also provided in Section B.2. It has many dependencies
 1653 including the HAWC analysis software. Figure 6.6 displays the workflow of a job with 3 threads.
 1654 Within a job, SOURCE is kept fixed and CHANS remains 17 elements long. More m_χ are sampled
 1655 from 11 bins up to 49 (for $\gamma\gamma$ and ZZ) and 25 (for remaining CHANS) which amounts to 12 or 6
 1656 mass bins per decade. m_χ and CHANS are permuted into a 473 element list which is split evenly
 1657 across N threads where N is [2, 8, 16]. For each m_χ -CHAN tuple, 1001 $\langle\sigma v\rangle$ values are sampled in

Timing summary for a multi-threaded job.

Import and Load HAL, 3ML, and HAWC analysis software ~ 2 min		
Load HAWC Data ~ 5 min		
Load HAWC PDF's (Detector Resolution files) ~ 4 min		
Load Spatial Model < 1s		
Load Spectra Models <1 s	Load Spectra Models <1 s	Load Spectra Models <1 s
Calculate max LLH (Chan_0, m_{χ_1}) ... max LLH (Chan_?, m_{χ_N}) N = TOTAL/N_THREADS ~ 8 min/Spec_model	Calculate max LLH (Chan_?, m_{χ_1}) ... max LLH (Chan_?, m_{χ_N}) N = TOTAL/N_THREADS ~ 8 min/Spec_model	Calculate max LLH (Chan_?, m_{χ_1}) ... max LLH (Chan_?, m_{χ_N}) N = TOTAL/N_THREADS ~ 8 min/Spec_model
Write results to file <1 s	Write results to file <1 s	Write results to file <1 s
Join Threads and terminate < 1s		

Figure 6.6 Task chart for one multithreaded job developed for this project. Green blocks indicate a shared resource across the threads AND computation performed serially. Red blocks indicate functional parallel processing within each thread. 3 threads are represented here, yet many more can be employed during the full analysis. Jobs are defined by the SOURCE as these require unique maps to be loaded into the likelihood estimator. The m_{χ} , CHAN, and $\langle \sigma v \rangle$ variables are entered into the thread pool and allocated as evenly as possible across the threads.

1658 the likelihood, and the value of $\langle \sigma v \rangle$ that maximizes the likelihood is found. Although rare, fits
1659 that failed are handled on a case by case basis.

1660 6.5.3 Performance

M Tasks	$T_{p,c}$ (hr:min:s)			
	$T_{1,1}$	$T_{1,2}$	$T_{1,8}$	$T_{1,16}$
50	1:40:37.5	0:52:43.7	0:19:13.8	0:13:44.0
74	2:22:30.0	1:15:00.6	0:25:21.3	0:15:49.8
100	(3:07:51.9)	1:40:10.5	0:30:44.4	0:20:01.4
200	(6:02:20.6)	-	1:00:32.0	0:30:35.0
473	(13:58:40.3)	-	2:01:41.4	1:07:53.2

Table 6.2 Timing summaries for analyses for serial and multithreaded processes. M tasks is the number of functional-parallel tasks ran for the computation. $T_{p,c}$ is a single run time in hours:minutes:seconds for runs utilizing p nodes and c threads. Runs are run interactively on the same computer to maximize consistency. Empty entries are indicated with '-'. (·) entries are estimated entries extrapolated from data earlier in the column.

1661 We see a significant reduction to wall time needed for our dSph analyses to run. Table 6.2

1662 shows the timing summaries for analyses of different sizes and thread counts. Additionally, the
 1663 efficiency gained when consolidating the serial loading of data is also apparent in our ability to
 1664 study many more tasks in about the same amount of wall time as a smaller serial computation. Trials
 1665 represented in the table were run on an AMD Opteron® processor 6344 with 48 cores, 2 threads per
 1666 core; 2.6 GHz clock. This is not the same architecture used for analysis on the HAWC computing
 1667 cluster however they are similar enough that results shown here are reasonably representative of
 1668 computing on the HAWC computing cluster. I use Tab. 6.2 for the inferences and conclusions in
 1669 the following paragraphs.

1670 First, we want to find T_s , the time of serial computation. From Fig. 6.5, the timing for our
 1671 coding pattern can be written as

$$T_s + Mt_p = T_{1,1}^M. \quad (6.5)$$

1672 M is the number of functional-parallel tasks (represented as column 1 of Tab. 6.2), and t_p is the
 1673 average time to complete a single parallel task. $T_{1,1}^M$ is the total time for a parallel program to run if
 1674 only 1 processor is allocated for M parallel task. With two runs of different M (M_1 and M_2), we
 1675 can use a system of equations to compute

$$T_s = 803.1\text{s} \text{ and } t_p = 104.6\text{s} \quad (6.6)$$

1676 Now, we have specific estimation for the fraction of serial computing time, F_s :

$$F_s = \frac{803.1}{803.1 + 104.6 \cdot M}. \quad (6.7)$$

1677 The maximum M for this study is 473 which evaluates to: $F_s = 0.016$ or 1.6% of computing time.
 1678 Table 6.3 shows the resulting speedups.

1679 We see a speedup that generally exceeds expectations from Eq. (6.4) for real trail runs. We also
 1680 see that there are diminishing returns as the number of threads increases. For small jobs with large c ,
 1681 both the expected and observed speedup are significantly smaller than c . One thing not considered
 1682 in Eq. (6.4) is the time incurred via communication latency. Communication latency increases
 1683 with the number of threads and contributes to diminishing returns. Additionally, these values are

M Tasks	F_s	$S_{1,2}$	$S_{1,8}$	$S_{1,16}$
50	1.33 E-1	1.90 [1.76]	5.23 [4.14]	6.35 [5.34]
74	9.40 E-2	1.90 [1.83]	5.62 [4.82]	9.00 [6.64]
100	7.13 E-2	1.88 [1.87]	6.11 [5.34]	9.38 [7.73]
200	3.70 E-2	- [1.93]	5.98 [6.36]	11.85 [10.29]
473	1.60 E-2	- [1.97]	6.89 [7.20]	12.35 [12.91]

Table 6.3 Speed up summaries for analyses for serial and multithreaded processes. M tasks is the number of functional-parallel tasks ran for the computation. $S_{p,c}$ is a single speedup comparison for runs utilizing p nodes and c threads. [·] are the estimated speedups calculated from Tab. 6.2, Eq. (6.7), and Eq. (6.4). Empty entries are indicated with '-'.

for single runs and do not consider the stochastic variation expected in a shared high performance computing resource. Therefor, these results are not strictly conclusive, yet demonstrate the merits of multi-threading. We see very clearly that there is a lot to gain, and this new coding pattern will expand HAWC's analysis capabilities.

6.6 Analysis Results

3 of the 43 $\mathcal{L}\mathcal{S}$ dSphs considered for the multithreaded analysis. These dSph are analyzed for emission from DM annihilation according to the likelihood method described in Section 5.4. The three likelihood profiles are then stacked to synthesize a combined limit on the dark matter annihilation cross-section, $\langle\sigma v\rangle$. This combination is done each of the 17 SM annihilation channels. Figure 6.7 and Fig. 6.8 show the combined limits for all annihilation channels with HAWC's observations. Test statistics of the best fit $\langle\sigma v\rangle$ values for each m_χ and CHAN are shown in Fig. 6.9 and Fig. 6.10. We also compare these limits to HAWC's Glory Duck limits shown in Section 5.5. The comparison to Glory Duck are featured in Fig. 6.11 for all the DM annihilation channels studied for Glory Duck. A full comparison is provided in the appendix in Fig. B.2, Fig. B.3, and Fig. B.4. Here, we show updated limits for $\chi\chi \rightarrow b\bar{b}, e\bar{e}, \mu\bar{\mu}, \tau\bar{\tau}, t\bar{t}, W^+W^-$, $\gamma\gamma$ and ZZ . For the first time ever, we show limits for $\chi\chi \rightarrow c\bar{c}, s\bar{s}, u\bar{u}, d\bar{d}, \nu_e\bar{\nu}_e, \nu_\mu\bar{\nu}_\mu, \nu_\tau\bar{\nu}_\tau, gg$, and hh .

No DM was found in HAWC observations. The largest excess found in HAWC data was for DM annihilating to W -bosons or $\nu_e\bar{\nu}_e$ for $m_\chi = 10$ TeV at significance 2.11σ and 2.14σ respectively. HAWC's limits and excesses are dominated by Segue1. Coma Berenices shows excesses at higher DM mass, yet no similar excesses were observed in Segue1 or Sextans. Sextans did not contribute

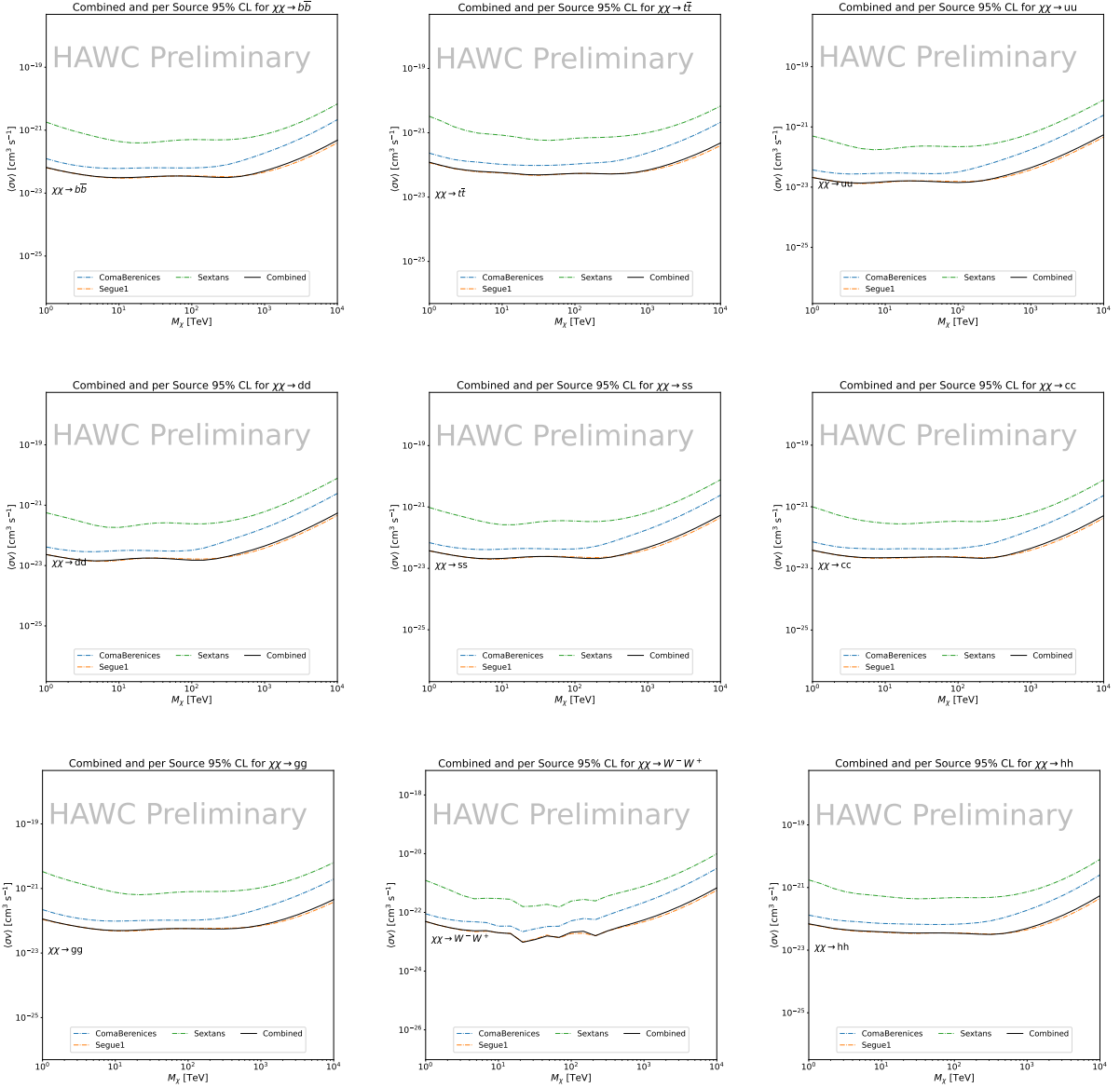


Figure 6.7 HAWC upper limits at 95% confidence level on $\langle\sigma v\rangle$ versus m_χ for $\chi\chi \rightarrow b\bar{b}$, $t\bar{t}$, $u\bar{u}$, $d\bar{d}$, $s\bar{s}$, $c\bar{c}$, gg , W^+W^- , and hh . Limits are with $\mathcal{L}\mathcal{S}$ J -factors [80]. The solid line represents the observed combined limit. Dashed lines represent limits from individual dSphs.

1704 significantly to signal excesses or the combined limit as it is at high zenith. Draco was not included
 1705 as the PDF of some of our analysis bins were wider than what is reasonable for a point source
 1706 analysis. Draco is at a high zenith for HAWC, so the effort required to include it was not justified
 1707 by the benefits.

1708 We did not generate background trials in time of writing this thesis. These are not shown and

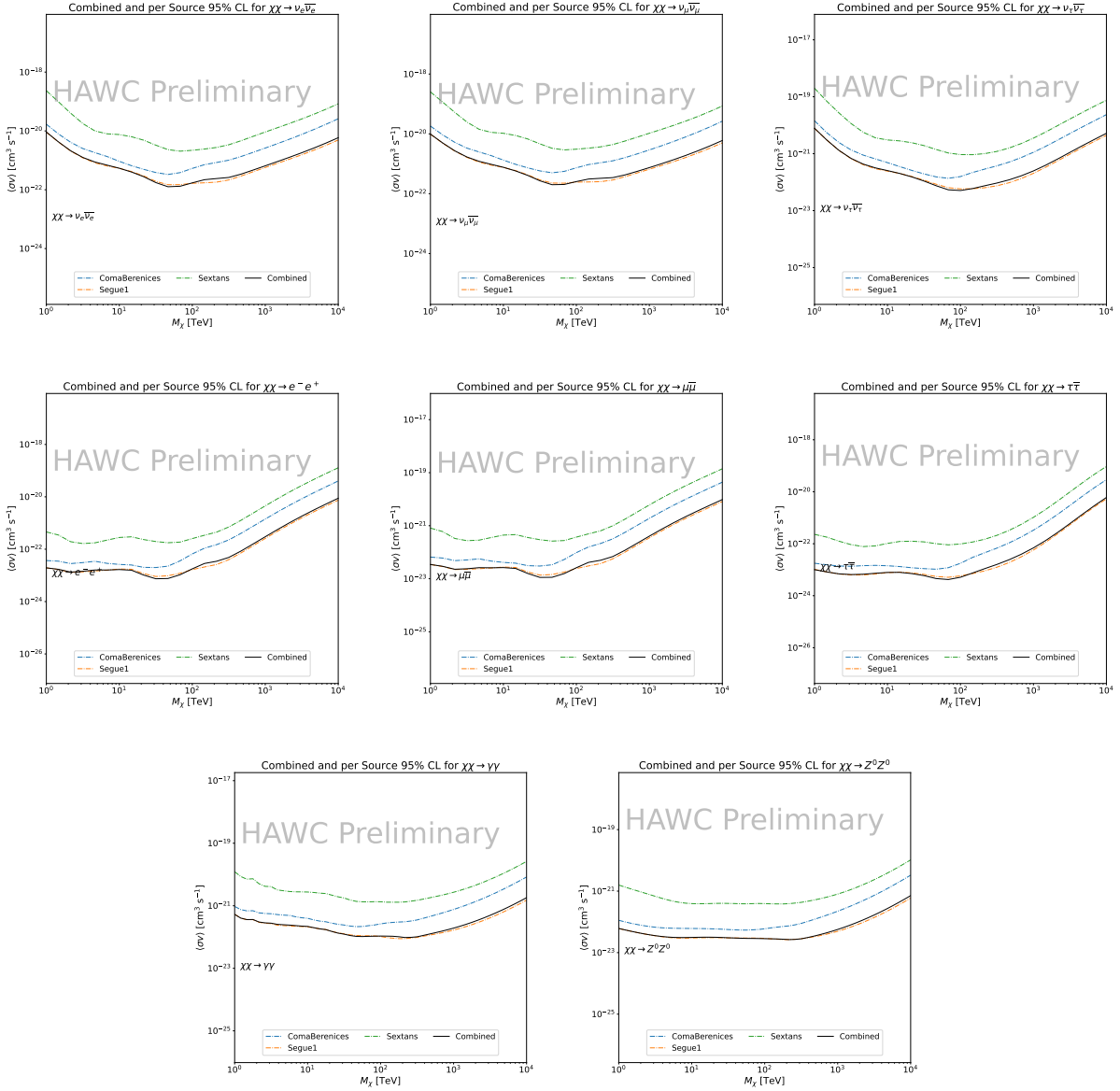


Figure 6.8 HAWC upper limits at 95% confidence level on $\langle\sigma v\rangle$ versus m_χ for $\chi\chi \rightarrow \nu_e \bar{\nu}_e$, $\nu_\mu \bar{\nu}_\mu$, $\nu_\tau \bar{\nu}_\tau$, $e \bar{e}$, $\mu \bar{\mu}$, $\tau \bar{\tau}$, $\gamma\gamma$ and ZZ . Limits use $\mathcal{L}S$ J -factors [80]. The solid line represents the observed combined limit. Dashed lines represent limits from individual dSphs.

1709 are an immediate next step for this analysis before publication.

1710 When comparing these results to Section 5.5, we see an overall decrease to the confidence limit
 1711 therefore improvement to HAWC's expected sensitivity. This improvement is generally stronger
 1712 than a doubling of data, or a factor $\sqrt{2}$ decrease. The comparison is somewhat complex and
 1713 dependent on the dSph and SM annihilation channel. Figure 6.11 shows the comparisons of limits

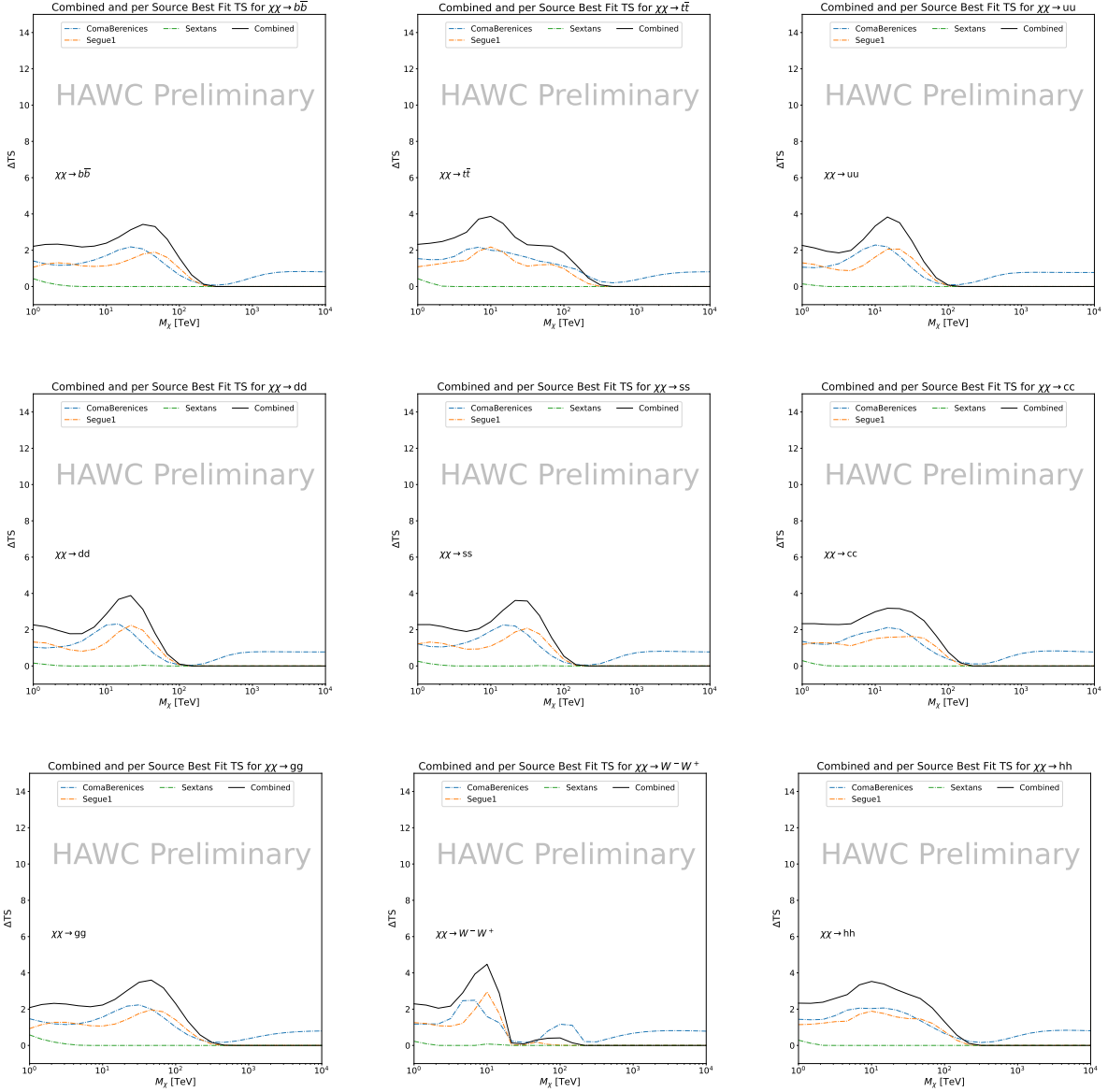


Figure 6.9 HAWC TS values for best fit $\langle\sigma v\rangle$ versus m_χ for SM annihilation channels: $\chi\chi \rightarrow b\bar{b}$, $t\bar{t}$, $u\bar{u}$, $d\bar{d}$, $s\bar{s}$, $c\bar{c}$, gg , W^-W^+ , and hh . Limits use \mathcal{LS} J -factors. The solid black line shows the combined best fit TS values. The colored, dashed lines are the TS values from each dSph.

1714 calculated for this analysis and Glory Duck (Section 5.5). Segue 1 and Coma Berenices are low
 1715 zenith where improvements to HAWC's analysis come only from energy estimation. Differences
 1716 between these two are dominantly from their differences in J -factor, half-light radii of the dSphs,
 1717 and the particle physics inputs. Substantial gains in HAWC's analysis methods (pass 5.F) were
 1718 made at high zenith which is important for sources like Sextans. The HDM particle physics model

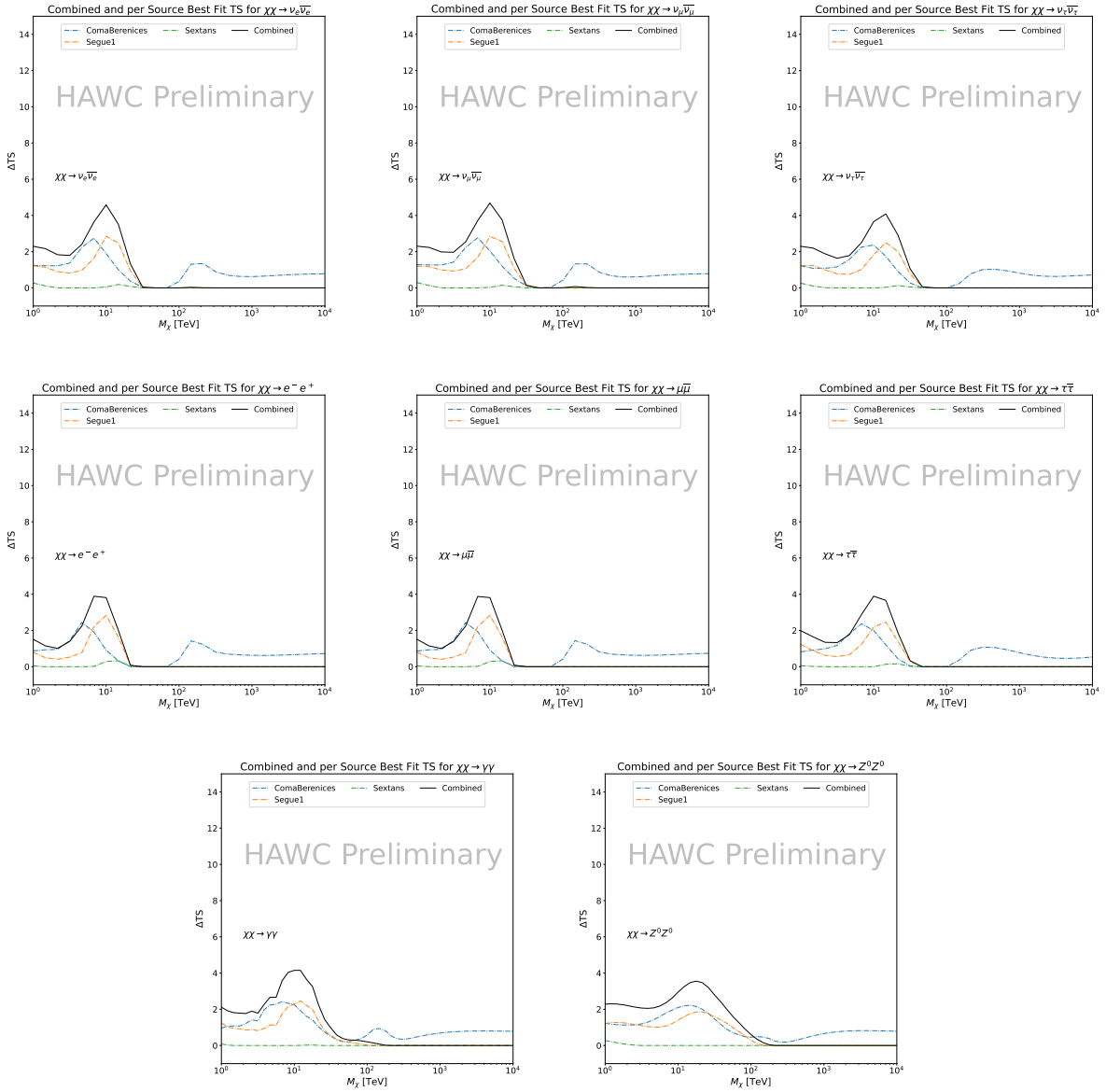


Figure 6.10 HAWC TS values for best fit $\langle\sigma v\rangle$ versus m_χ for SM annihilation channels: $\chi\chi \rightarrow \nu_e \bar{\nu}_e$, $\nu_\mu \bar{\nu}_\mu$, $\nu_\tau \bar{\nu}_\tau$, $e^- e^+$, $\mu \bar{\mu}$, $\tau \bar{\tau}$, $\gamma\gamma$ and ZZ . Limits use \mathcal{LS} J -factors. The solid black line shows the combined best fit TS values. The colored, dashed lines are the TS values from each dSph.

1719 produces almost identical spectra to the PPPC for $\chi\chi \rightarrow e^- e^+$. This channel can be used to
 1720 compare limits between dSph spatial models. Overhead sources see minimal improvement to the
 1721 limits, while high zenith sources see an order of magnitude improvement for all DM masses. Softer
 1722 SM annihilation channels see broad improvements to the limit compared to harder channels.

1723 **6.7 Systematics**

1724 Systematics to this analysis are identical to what was performed earlier in Glory Duck, Sec-
1725 tion 5.7. We are also sensitive to the choice in spatial template, and this was explored in Section 5.7.2
1726 and Section 5.8.2.

1727 **6.8 Conclusion and Discussion**

1728 In this multithreaded analysis, we have used observations of 3 dSphs from HAWC to perform
1729 a collective DM annihilation search towards dSphs. The data were combined across sources
1730 to significantly increase the sensitivity of the search. Advanced computational techniques were
1731 deployed to accelerate wall-time spent analyzing by an order of magnitude. We have observed
1732 no significant deviation from the null, no DM hypothesis, and so present our results in terms of
1733 upper limits on the velocity-weighted cross-section, $\langle\sigma v\rangle$, for seventeen potential DM annihilation
1734 channels across four decades of DM mass.

1735 This analysis serves as a proof of concept for multithreaded HAWC analyses with large parameter
1736 spaces. Larger datasets with fast techniques will be essential to tackling the DM problem. The
1737 models we used for this study include annihilation channels with neutrinos in the final state.
1738 Advanced studies could aim to merge our results with those from neutrino observatories with large
1739 data sets.

1740 A full HAWC analysis will include systematic studies of the J -factor distributions. Additionally,
1741 because of the timing reduction, the study can be doubled in size to include DM decay. We have not
1742 yet received the remaining spatial profiles to the \mathcal{LS} catalog, and limits can be quickly computed
1743 once these are received. Finally, statistical studies with Poisson variation of HAWC's background
1744 are essential to a comprehensive understanding of our observed excesses.

Segue1

Coma Berenices

Sextans

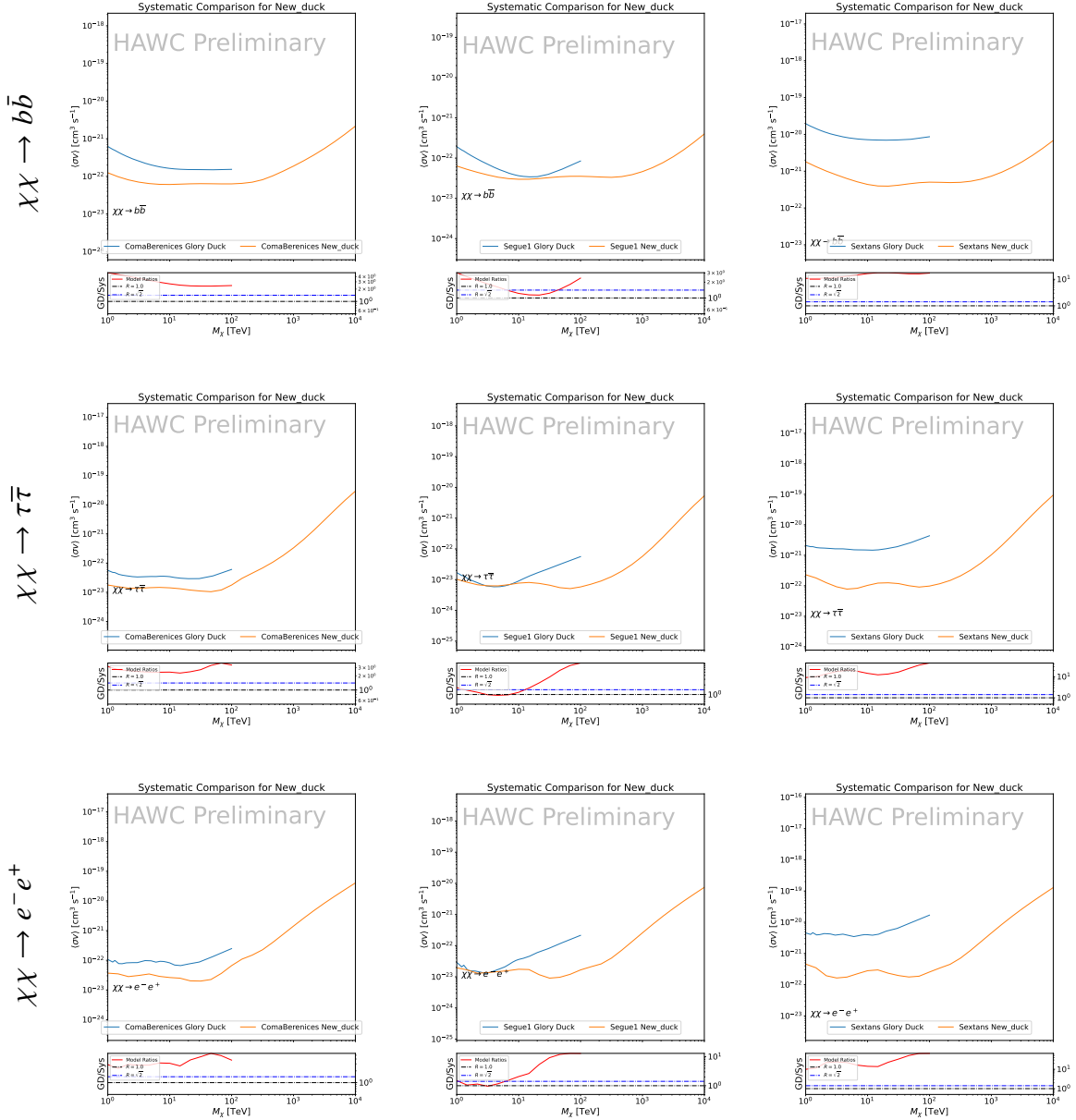


Figure 6.11 Comparison of HAWC limits from this analysis to Glory Duck (Fig. 5.5) for 3 dSphs and 3 DM annihilation channels: $b\bar{b}$, $\tau\bar{\tau}$, and $e\bar{e}$. Each sector shows the 95% confidence limit from Glory Duck (blue line) and this analysis (orange line) in the top plot. The lower plot features the ratio in log scale of Glory Duck to this analysis in a red solid line. Horizontal dashed lines are for ratios of 1.0 (black) and $\sqrt{2}$ (blue). Ratios larger than 1.0 are for limits smaller, or stricter, than Glory Duck. Ratios larger than $\sqrt{2}$ indicates limits are stricter than a simple doubling of the Glory Duck data.

CHAPTER 7

HEAVY DARK MATTER ANNIHILATION SEARCH WITH ICECUBE'S NORTH SKY TRACK DATA

7.1 Introduction

Neutrinos are another astrophysical messenger than can travel long distances without significant attenuation or deflection. Additionally, Neutrinos come in three flavors which triples the multiplicity of the particles we are searching for. Uniquely, they interact less readily than photons especially above PeV energies. Neutrinos therefore provide another window through which we can perform dark matter searches.

The previous IceCube DM annihilation analysis towards dwarf galaxies was performed in 2013 [83] which, in technical terms, is more than a minute ago. This is in spite of IceCube's crucial sensitivity afforded from neutrino spectral lines [84]. A lot has changed in IceCube since its previous DM annihilation search such as, additional strings, more sophisticated analysis methods, and more accurate theory modeling. It has come time for IceCube to make a DM dSph contribution.

IceCube is sensitive to annihilating DM for DM masses above 1 TeV. Additionally, IceCube's sensitivity is comparable gamma-ray observatories in spectral models that produce hard neutrino features. The goal of this analysis is to perform a DM annihilation search using the Northern Sky Tracks datasets. The search will only be towards dwarf spheroidal galaxies (dSph) for the strengths mentioned in Section 5.3.3. These sources are treated as point sources for IceCube with little loss to sensitivity or model dependence on how the DM is distributed. DM masses from 500 GeV to 100 PeV are considered for this analysis. Several DM annihilation channels available from the HDMspectra [79] are studied in this analysis. This chapter presents the analysis work for IceCube to update our DM searches toward dSphs.

7.2 Dataset and Background

This section enumerates the data and background methods used for IceCube's study of dSphs. Section 7.2.1 and Section 7.2.2 are most useful for fellow IceCube collaborators looking to replicate this analysis.

1771 **7.2.1 Itemized IceCube files**

1772 These files are only available within IceCube’s internal documentation and wikis. They are not
1773 meant for public access, and are presented here so that IceCube collaborators can reproduce results
1774 accurately.

1775 • Software Environment: CVMFS Py3-v4.1.1

1776 • Data Sample: Northern Tracks NY86v5p1

1777 • Analysis Software: csky ([nu_dark_matter](#))

1778 • Analysis wiki: https://wiki.icecube.wisc.edu/index.php/Dark_Matter_Annihilation_Search_towards_dwarf_spheroidals_with_NST_and_DNN_Cascades

1780 • Project repository

1781 **7.2.2 Software Tools and Development**

1782 This analysis was performed inside IceCube’s CVMFS (3.4.1.1) software environment using
1783 csky for likelihood calculations. Csky at first did not come with dark matter spectral models nor
1784 could accommodate custom flux models. We developed these capacities for single source and
1785 stacked source studies for this analysis. The analysis code is held in a separate repository from
1786 csky. The [nu_dark_matter branch of csky](#) manages the input of custom dark matter spectra and
1787 accompanied DM astrophysical source. Csky also enables the use of multithreading which was
1788 shown to be crucial for DM searches (see Sec. 6). Csky then calculates likelihoods with a selected
1789 data sample. The [IceCube Dark Matter dSph repository](#) manages the generation of spectral models
1790 for neutrinos, physics parameter extraction from n_{sig} , J -factor per source inputs, and bookkeeping
1791 for the large parameter space. The project repository required a secondary software environment
1792 for neutrino oscillations. How to launch and run those calculations are documented in the project
1793 repository and the Docker image is additionally saved in Section C.1.

1794 **7.2.3 Data Set and Background Description**

1795 For this analysis, I use the Northern Sky Tracks (NST) Sample (Version V005-P01). The sample
1796 contains up-going track-like events, usually from ν_μ and ν_τ , with a superior angular resolution
1797 compared to the cascade dataset. This sample covers 10.4 years of data (IC86_2011-2021). The
1798 accepted neutrino energy range used for the analysis is unique from most other IceCube searches
1799 because DM spectra are hard with large contributions close to $E_\nu = m_\chi$. Therefore, the sampled
1800 energy range is $1 < \log(E_\nu/\text{GeV}) < 9.51$ with step size 0.125.

1801 The strengths of a dwarf analysis is that there are no additional background considerations
1802 beyond nominal, baseline background estimations (see Section 5.2.3). For NST, the nominal
1803 contributions come from atmospheric neutrinos and isotropic astrophysical neutrinos. We estimate
1804 the background by scrambling NST data along Right Ascension.

1805 **7.3 Analysis**

1806 The expected differential neutrino flux from DM-DM annihilation to standard model particles,
1807 $d\Phi_\nu/dE_\nu$, over solid angle, Ω is described by the familiar equation.

$$\frac{d\Phi_\nu}{dE_\nu} = \frac{\langle\sigma\nu\rangle}{8\pi m_\chi^2} \frac{dN_\nu}{dE_\nu} \times \int_{\text{source}} d\Omega \int_{l.o.s} \rho_\chi^2 dl(r, \theta') \quad (7.1)$$

1808 This is identical to Eq. (5.1) except that there are 3 neutrino flavors, so there are a corresponding
1809 3 flux equations. Section 5.3 has a complete description of each term in Eq. (7.1). Additionally,
1810 neutrinos oscillate between flavors which needs to be considered for the expected neutrino flux
1811 at Earth. Section 7.3.1 presents the particle physics model and processing for DM annihilation.
1812 Section 7.3.2 presents the spatial distributions built for each dSph.

1813 **7.3.1 $\frac{dN_\nu}{dE_\nu}$ - Particle Physics Component**

1814 Neutrino spectra from heavy DM annihilation were generated using HDMspectra [79] and
1815 χ arov [85]. HDMspectra has tables for the decay and annihilation of heavy DM for different
1816 dark DM and SM primary annihilation channels. The simulation includes electroweak or gluon
1817 radiative corrections and higher order loop corrections from the W and Z bosons (WWZ and $WW\gamma$).
1818 These corrections are especially important for accurately estimating the prompt neutrino flux. This

1819 publication also pushes the simulated DM mass to the Plank scale (1 EeV), however this study will
1820 not explore that high.

1821 An important feature in the spectra is that neutrino line channels will be accompanied by a low
1822 energy tail [79], see Fig. 7.1. Thus, the Earth will not fully attenuate a heavy neutrino line-like
1823 signal from high declination sources where the neutrino flux must first traverse through the Earth.
1824 The DM annihilation channels that feature lines include all leptonic channels: $\nu_{e,\mu,\tau}$, e , μ , and τ . We
1825 use the `xarov` software to propagate and oscillate the neutrinos from the source to Earth. Because
1826 these sources are quite large in absolute terms, and also far (order 10 kpc or more), the resulting
1827 flavor spectra are the averages of the transition probabilities [85]:

$$P(\nu_\alpha \rightarrow \nu_\beta) \approx \begin{bmatrix} 0.55 & 0.18 & 0.27 \\ 0.18 & 0.44 & 0.38 \\ 0.27 & 0.38 & 0.35 \end{bmatrix} \quad (7.2)$$

1828 Examples of the spectra before and after propagation are shown in Fig. 7.1.

1829 When calculating the expected contribution to n_s , only ν_μ and ν_τ are considered as NST's
1830 effective area to ν_e is negligible [86]. Therefore, the expected composite neutrino spectrum is the
1831 sum of the two flavors: $\frac{dN\nu_\mu}{dE\nu_\mu} + \frac{dN\nu_\tau}{dE\nu_\tau}$. The spectral tables are then converted to splines to condense
1832 information, enable random sampling of the spectra, and reduce computing times. The spectral
1833 splines are finally implemented as a DM class in csky.

1834 7.3.1.1 Treatment of Neutrino Line Features

1835 All DM annihilation channels into leptons $\chi\chi \rightarrow [\nu_{e,\mu,\tau}, e, \mu, \tau]$ develop a prominent and
1836 narrow spectral line feature. For all neutrino flavors, this line is visible and prominent in all m_χ
1837 studied in this analysis. For charged leptons, the feature typically manifests at $m_{ch} > 10$ TeV, yet
1838 its prominence varies slightly between the flavors. Examples for lines in the annihilation spectra
1839 with neutrinos or charged leptons are provided in Fig. 7.1.

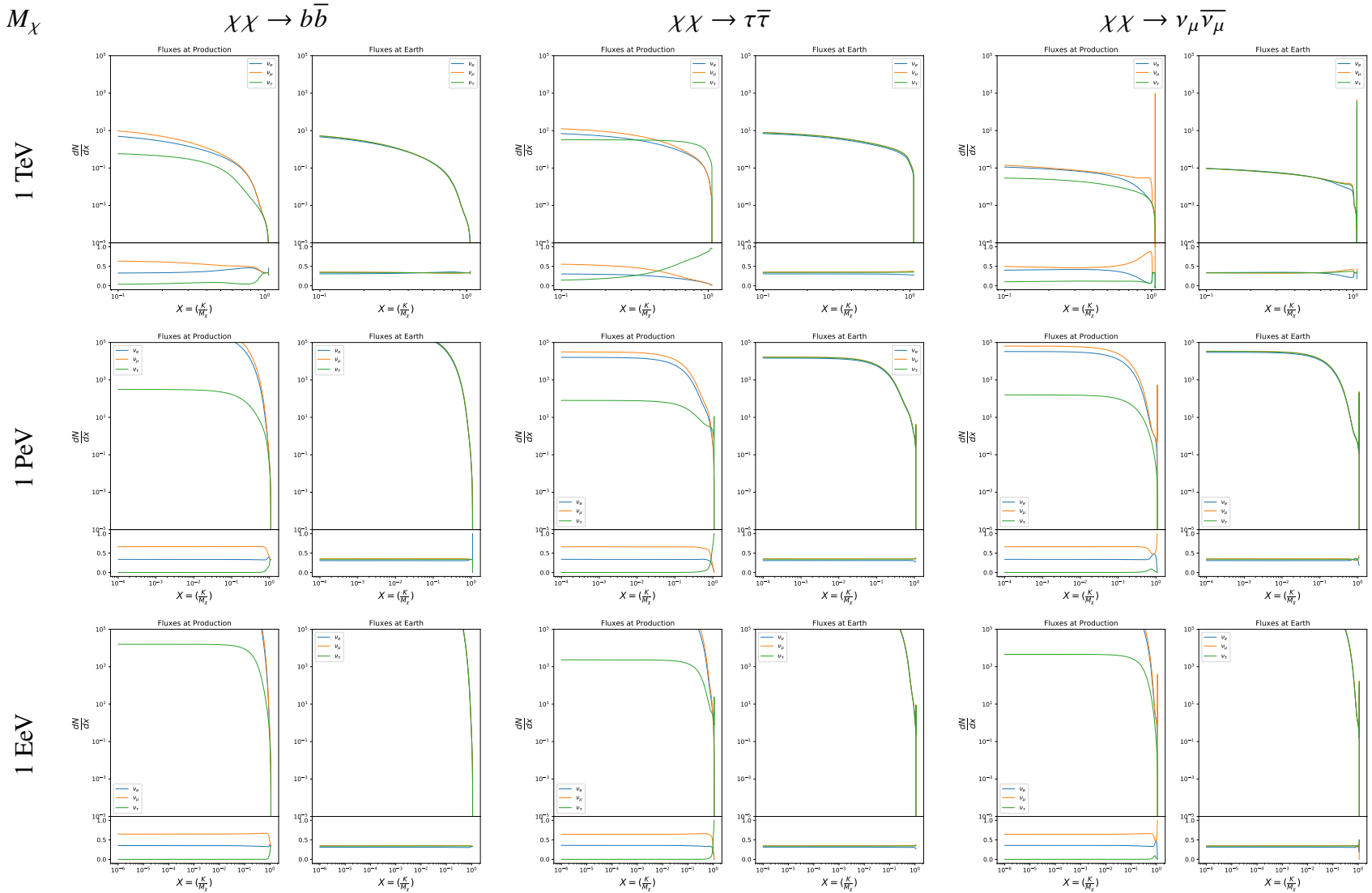


Figure 7.1 Neutrino spectra at production (left panels) and after oscillation at Earth (right panels). Blue, orange, and green lines are the ν_e , ν_μ , and ν_τ spectra respectively. Top panels show the spectra in $\frac{dN}{dE}$. Lower panels plot the flavor ratio to $\nu_e + \nu_\mu + \nu_\tau$. SM annihilation channels $b\bar{b}$, $\tau\bar{\tau}$, and $\nu_\mu \bar{\nu}_\mu$ are shown for $M_\chi = 1$ Pev, TeV, and EeV.

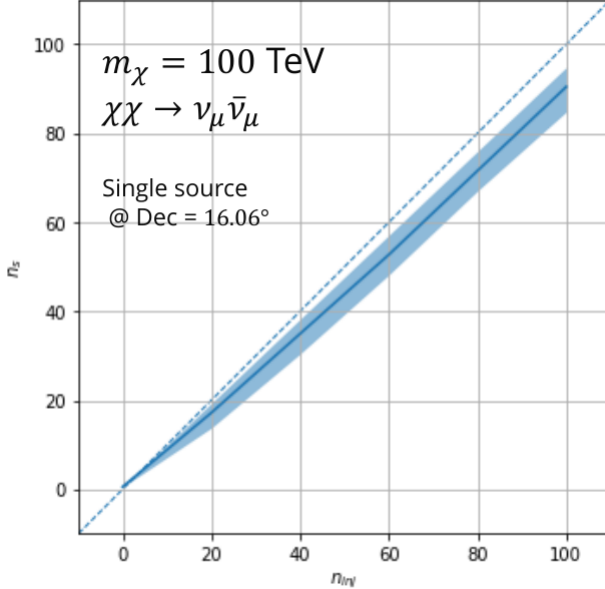


Figure 7.2 Signal recovery for 100 TeV DM annihilation into $\nu_\mu \bar{\nu}_\mu$ for a source at Dec = 16.06°. n_{inj} is the number of injected signal events in simulation. n_s is the number of reconstructed signal events from the simulation data. Although the uncertainties are small and tight, the reconstructed n_s are systematically underestimated.

1840 The neutrino line feature is so narrow relative the sampled energy range that the random
 1841 sampling of the spectra and likelihood fitting rarely capture the line in computation. As a result,
 1842 often the best fit to simulation of background will always floor to TS = 0 and the signal recovery
 1843 systematically underestimates the signal (see Fig. 7.2).

1844 To remedy this, we take a similar approach to the IceCube’s decay analysis [87] and the previous
 1845 gamma-ray study in Section 6.3.1. Two smoothing kernels were tested (Gaussian and uniform)
 1846 to widen the line feature. The widths were tuned such that the signal recovery approached unity
 1847 for DM mass 100 TeV to 1 PeV for a source at Segue 1’s declination, 16.06°. Near horizon
 1848 was chosen in order to isolate loss in signal recovery away from Earth’s attenuation of very high
 1849 energy neutrinos and atmospheric backgrounds. The kernel convolution needed closely preserve
 1850 the integrated counts of neutrinos. The optimized kernel parameters for all lines are summarized
 1851 as:

- 1852 • Gaussian kernel with 1σ width = $1.75\text{E-}3 \cdot m_\chi$
- 1853 • Minimum energy included in convolution = $\text{MIN}[0.995 \cdot m_\chi, E(\nu_{\text{line}}) - 4\sigma]$

- 1854 • Maximum energy included in convolution = $\text{MAX}[1.005 \cdot m_\chi, E(\nu_{\text{line}}) + 4\sigma]$

1855 where $E(\nu_{\text{line}})$ is the neutrino energy where the neutrino line is at the maximum.

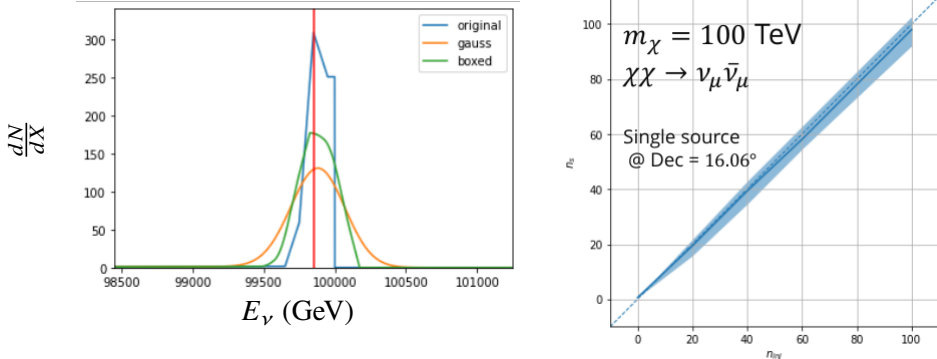


Figure 7.3 Left panel shows the two kernels overlaying the original spectrum from $\chi\text{aron}\nu$ after propagation to Earth [85]. The vertical red line indicates where the original neutrino line is maximized. Blue line is the output from $\chi\text{aron}\nu$. Green line is the spectrum after convolution with a flat kernel. Orange line is the spectrum after Gaussian convolution. Right panel shows the signal recovery of the spectral model using the Gaussian kernel with parameters enumerated above.

1856 These parameters broadly improved the signal recovery of the line spectra. An example is in
1857 Fig. 7.3. Analysis level signal recovery studies are expanded upon in Section 7.6.

1858 7.3.1.2 Spline Fitting

1859 In an effort to reduce computational work, memory burden, and align with point source methods
1860 used for NGC1068 [88], spectral splines were created and adopted for estimating the neutrino flux
1861 for the different spectral models. Software was written to generate, book keep, and calculate values
1862 on the splines.

1863 When using splines, one has to be careful of the goodness to fit. The spline software used
1864 here, Photospline [89], uses the penalized spline technique [90]. Through the penalized technique,
1865 poor fits are penalized according to the accuracy of the nominal value, and the smoothness of the
1866 first and second derivatives. However, this construction does not penalize on the integral of the
1867 fit distribution which is critical in low signal studies, such as DM searches. There are additional
1868 caveats when testing the goodness to fit to the MC generated above for all DM annihilation channels.

- 1869 • The splines must be Log10(*) in Energy and dN/dX to account for the exponential nature of
 1870 the flux.
- 1871 • The fidelity of the fit matters more at $E_\nu \approx m_\chi$ where the model uncertainties are minimal
 1872 and physical considerations (like the cut-off) are most important.
- 1873 • The fidelity of the fit matters less at low E_ν as the model uncertainties are large AND
 1874 IceCube's sensitivity diminishes significantly below 500 GeV.
- 1875 • Total integrated counts should be well-preserved.

1876 The resulting cost function was built to evaluate the goodness of spline fits to account for the above
 1877 considerations.

$$e_i = x_i \cdot \left(\frac{dN_i}{dX_i} - 10^{\hat{e}_i} \right) \quad (7.3)$$

1878 Where \hat{e}_i is the spline estimator's value for x_i . $x_i = E_{\nu_i}/m_\chi$. $\frac{dN_i}{dX_i}$ is the flux value from MC. I then
 1879 take the RMS of the error distribution and the resulting value, err, is used to evaluate the fidelity of
 1880 the spectral spline.

$$\text{err} = \sqrt{\frac{1}{x_{\max} - x_{\min}} \int_{x_{\min}}^{x_{\max}} e^2 dx} \quad (7.4)$$

1881 x_{\min} and x_{\max} are the scope of the error evaluation and are provided in Tab. 7.1.

1882 Each SM channel had unique tolerances for 'err'. Channels with very hard cut-offs had looser
 1883 tolerance for err because a significant error would be generated from single counts over/underes-
 1884 timated at the cut-off. Soft channels do not share this issue, so the tolerance is much stricter. All
 1885 annihilation channels from HDM are modeled well below IceCube's NST sensitivity which falls
 1886 off substantially below 100 GeV [86]. We do not think it is necessary to evaluate the spline fits
 1887 below 100 GeV and use this value as the default lower cut-off. Yet, HDM's model uncertainties
 1888 at $E_\nu < 10^{-6} \cdot m_\chi$ span an order of magnitude [79]. We also choose not to evaluate the splines
 1889 below this critical value if it is within IceCube's sensitivity. Finally, the smoothing of the spectral
 1890 lines in leptonic annihilation channels are ignored for evaluating the fit. We used the lower limit of

$\chi\chi \rightarrow$	GOOD	OK	FAIL	Limits of err calc [X_{min}, X_{max}]
$Z^0 Z^0, W^+ W^-$	1.0E-3	1.0E-3, 1.0E-2	1.0E-2	MAX[100GeV/ m_χ , 10^{-6}], 1.0
$t\bar{t}, hh$	1.0E-5	1.0E-5, 1.0E-4	1.0E-4	MAX[100GeV/ m_χ , 10^{-6}], 1.0
$b\bar{b}, d\bar{d}, u\bar{u}$	9.0E-7	9.0E-7, 9.0E-6	9.0E-6	MAX[100GeV/ m_χ , 10^{-6}], 1.0
$\nu\bar{\nu}_{e,\mu,\tau}$	1.0E-3	1.0E-3, 1.0E-2	1.0E-2	MAX[100GeV/ m_χ , 10^{-6}], MIN[0.995, ($E_n(\nu_{line}) - 4\sigma$)/ M_χ]
$e\bar{e}, \mu\bar{\mu}, \tau\bar{\tau}$	1.0E-3	1.0E-3, 1.0E-2	1.0E-2	MAX[100GeV/ m_χ , 10^{-6}], MIN[0.995, ($E_n(\nu_{line}) - 4\sigma$)/ M_χ]

Table 7.1 Spline err tolerances used for input in particle physics component to Eq. (5.1). Column 1 is the DM annihilation channel being fit. Columns 2, 3, and 4 are the tolerances for "GOOD" (pass), "OK" requires inspection, and "FAIL" (tune and refit) respectively. Column 5 has the X ranges over which the error is evaluated. MAX/MIN [\cdot, \cdot] takes the maximum or minimum of the two enclosed values.

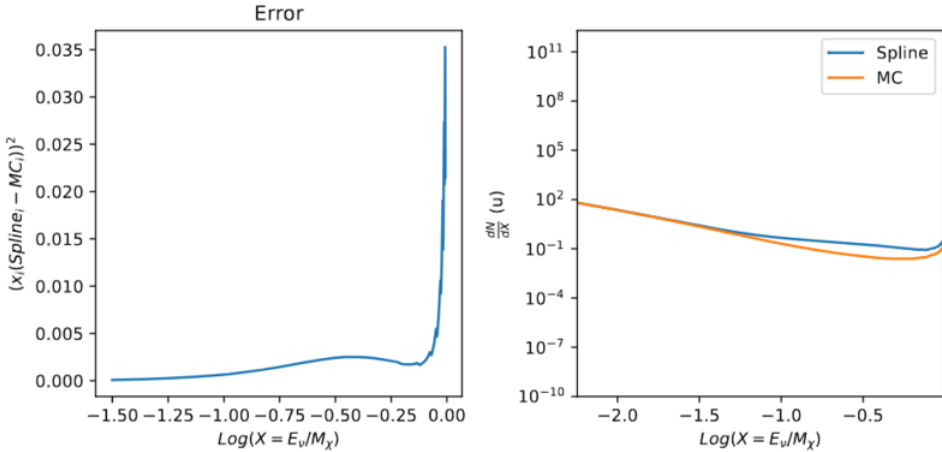


Figure 7.4 Example spline that failed the fit. Failed splines are corrected on a case by case basis unless the SM channel has a systematic problem fitting the splines. In this case, I made a bookkeeping error and loaded the incorrect spectral model

1891 the kernel mask as the upper limit of evaluation. Table 7.1 summarizes the tolerances for the DM
 1892 annihilation channels used for this analysis.

1893 The errors are then assesed in two ways. First, FAIL and OK are directly plotted with e_i as a
 1894 function of x with the full spline and MC. An example of a single failure is provided in Fig. 7.4.
 1895 Second, a summary plot of all the splines is plotted and colors coded. Figure C.1 are the spline
 1896 summaries as of writing this thesis. The goal broadly is to eliminate all red and inspect yellow
 1897 statuses.

1898 The ν_e spectra at Earth are not considered in this analysis, so no work was done to refine the

1899 spline fits for this flavor. Finally, I perform a visual inspection of the splines to verify that the spline
1900 fitting did not introduce spurious features that would corrupt the likelihood fitting.

1901 7.3.1.3 Composite Neutrino Spectra

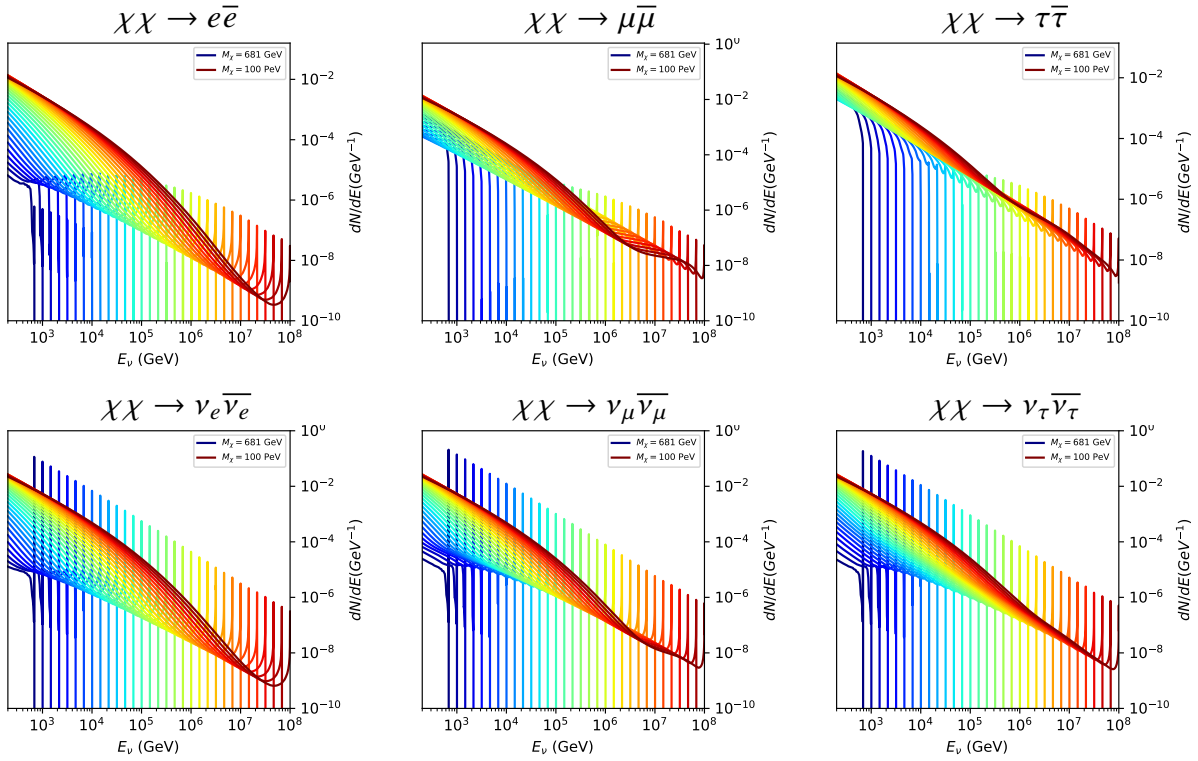


Figure 7.5 Summary of input spectral models that were smoothed with Gaussian kernels. Spectral models are for $\chi\chi \rightarrow e\bar{e}$, $\mu\bar{\mu}$, $\tau\bar{\tau}$, $\nu_e\bar{\nu}_e$, $\nu_\mu\bar{\nu}_\mu$, and $\nu_\tau\bar{\nu}_\tau$. These spectra are the composite ($\nu_\mu + \nu_\tau$) of neutrino flavors. Every spectral model used for this analysis is featured as a colored solid line. Bluer lines are for low m_χ models. m_χ ranges from 681 GeV to 100 PeV. HDM [79], χ arov [85], and Photospline [89] are used to generate these spectra. Energy (x-axis) was chosen to roughly represent the energy sensitivity of NST.

1902 With all the previously mentioned pieces, we are ready to fully assemble a comprehensive
1903 description of the particle physics term dN/dE in Eq. (7.1).

$$\frac{dN_\nu}{dE_\nu \oplus} = \left(\frac{dN_{\nu_e}}{dE_{\nu_e}} + \frac{dN_{\nu_\mu}}{dE_{\nu_\mu}} + \frac{dN_{\nu_\tau}}{dE_{\nu_\tau}} \right)_{\text{src}} \cdot \mathbf{P}(\nu_\alpha \rightarrow \nu_\beta) \quad (7.5)$$

1904 Figure 7.5 shows the spectral models that required Gaussian smoothing, the leptonic annihilation
1905 channels. The remaining models where the only processing were spline fitting and neutrino
1906 oscillation are documented in Section C.3. Notice that the different neutrino flavors are unique,

1907 especially in their low energy tails. Therefore, this analysis will be sensitive to DM annihilating to
1908 the distinct neutrino flavors.

1909 **7.3.2 *J*- Astrophysical Component**

1910 For this analysis, we re-adopt the \mathcal{GS} model [59] used in Sec. 5 for dSphs. These models
1911 are based on a modified Navarro-Frenk-White (NFW) profile where the indices of the NFW
1912 (traditionally 1,3,1) are allowed to float. The angular width of these sources is much smaller than
1913 the angular resolution of IceCube NST [88]. We therefore treat these sources as point sources
1914 in this analysis, and forgo generating maps. These sources and the \mathcal{GS} model have already been
1915 discussed at length in Section 5.3.2 and is not repeated here. IceCube uses identical sources to
1916 Tab. 5.1 except we analyze source with declinations above 0.0° .

1917 **7.3.3 Source Selection and Annihilation Channels**

1918 We use all the dSphs presented in IceCube’s previous dSph DM search [83] and expand beyond
1919 it. IceCube’s sources for this analysis studies include Boötes I, Canes Venatici I, Canes Venatici II,
1920 Coma Berenices, Draco, Hercules, Leo I, Leo II, Leo V, Leo T, Segue 1, Segue 2, Ursa Major I,
1921 Ursa Major II, and Ursa Minor. A full description of all sources used is in Table 5.1. Sources with
1922 declinations less than 0.0 are excluded from this analysis.

1923 This analysis improves on the previous IceCube dSph paper [83] in the following ways. Previ-
1924 ously, the IceCube detector was not yet completed to the 86 string configuration. Many more dSphs
1925 will be observed, from 4 to 15. Previously, the particle physics model used for neutrino spectra
1926 from DM annihilation did not have EW corrections where they are now included [79]. The spectral
1927 models also predict substantial differences between the neutrino flavors, so this analysis will be the
1928 first DM dwarf analysis to discriminate between primary neutrino flavors. The study performed
1929 here studies 10.4 years of data.

1930 The SM annihilation channels probed for this study include $\chi\chi \rightarrow$

1931 $b\bar{b}, t\bar{t}, u\bar{u}, d\bar{d}, e\bar{e}, \mu\bar{\mu}, \tau\bar{\tau}, ZZ, W^+W^-, \nu_e\bar{\nu}_e, \nu_\mu\bar{\nu}_\mu$, and $\nu_\tau\bar{\nu}_\tau$

1932 **7.4 Likelihood Methods**

1933 I use the Point-Source search likelihood which is widely used in IceCube analyses. The
1934 likelihood function is defined as the following:

$$L(n_s) = \prod_{i=1}^N \left[\frac{n_s}{N} S_i + \left(1 - \frac{n_s}{N}\right) B_i \right] \quad (7.6)$$

1935 where i is an event index, S and B are the signal PDF and background PDF respectively. For a joint
1936 analysis where the sources are stacked the likelihood is expanded in the simplified way:

$$L(n_s) = \prod_{i=1}^{N_{\text{sources}}} L_i(n_s) \quad (7.7)$$

1937 Where L_i is the likelihood from the i -th source in the stacked analysis. The Test Statistic (TS)
1938 definition remains the same as Eq. (5.7)

1939 **7.5 Background Simulation**

1940 Before we look at data, we must first analyze background and signal injection to validate our
1941 analysis. We set out to characterize the TS distributions for each source, annihilation channel, and
1942 m_χ . Previous IceCube DM searches [87, 91] showed TS distributions that did not behave according
1943 to a χ^2 distribution with 1 degree of freedom. TS distributions can also vary significantly between
1944 DM mass and annihilation models. Therefore, Wilk's theorem may not be applicable to the analysis.
1945 Instead, a critical value is defined from many background trials. We study the TS distributions
1946 first for each source, then for the stacked analysis. The following sections show the results of the
1947 likelihood fitting for a suite of background trials.

1948 I assume that TS values are physical: $TS \geq 0$. $\epsilon[x]$ indicate the fraction of events where $TS < x$.
1949 For TS plots shown here, the decimal values of x are 1.0e-2 and 1.0e-3. Each subplot represents
1950 a simulation of 100,000 data-scrambled background trials. Section 7.5.1 show the background TS
1951 distributions obtained from Segue 1, a source with little Earth attenuation and large J -factor, and
1952 Ursa Major II, which has similarly large J -factor but significantly more Earth attenuation, assuming
1953 DM annihilation into $b\bar{b}$, $\tau\bar{\tau}$, and $\nu_\mu\bar{\nu}_\mu$. I show the TS distributions of a stacked study of 15 sources
1954 for all DM annihilation channels.

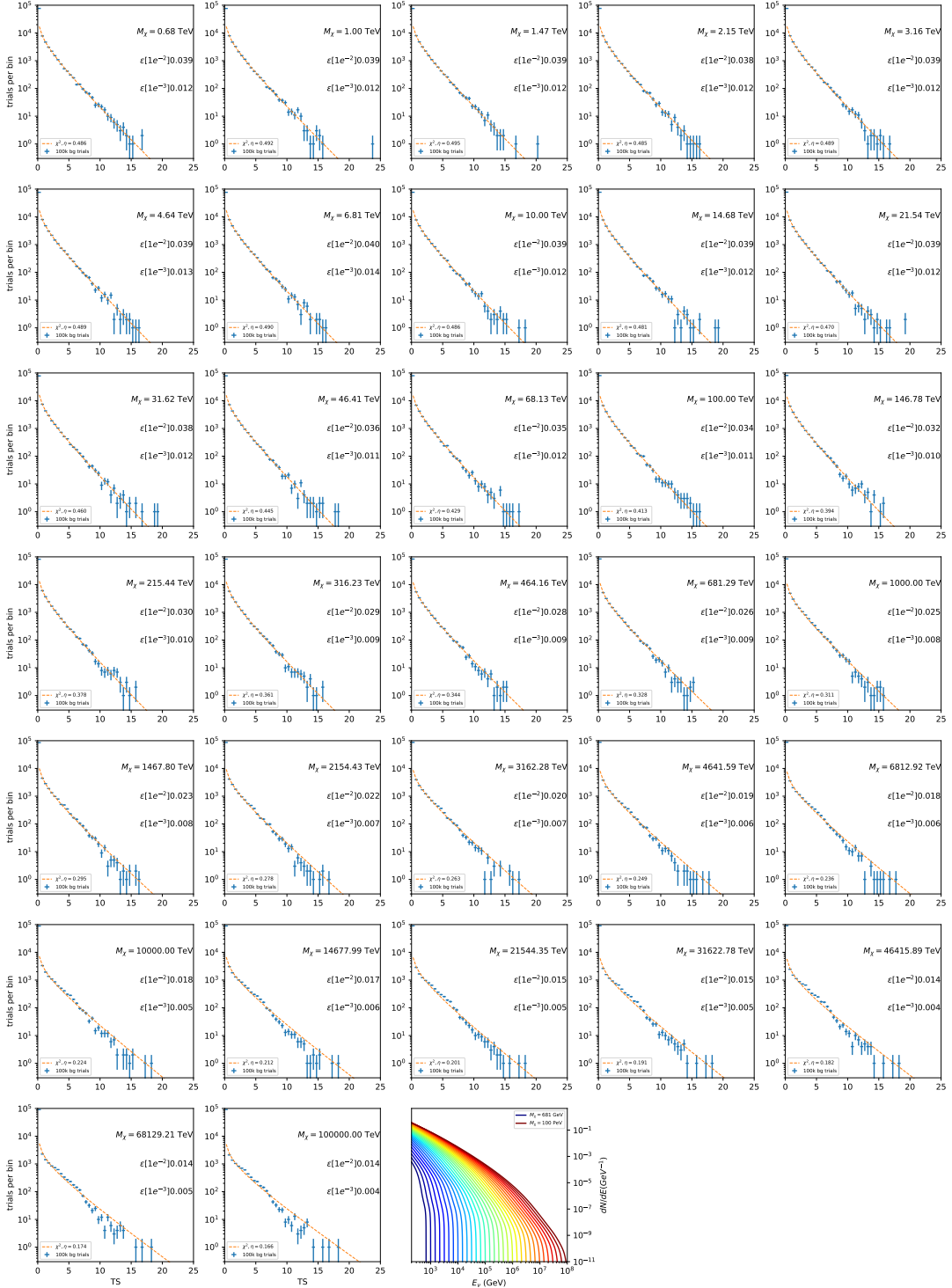


Figure 7.6 Test statistic (TS) distributions for Segue 1 and $\chi\chi \rightarrow b\bar{b}$. Each subplot, except the final, is the TS distribution for a specific DM mass listed in the subplot. Orange dashed lines are the traces for a χ^2 distribution with 1 degree of freedom. $\epsilon[\cdot]$ is the fraction of trials smaller than the bracketed value. The final subplot features the all DM spectral models, similar to Fig. 7.5, used as input for the TS distributions.

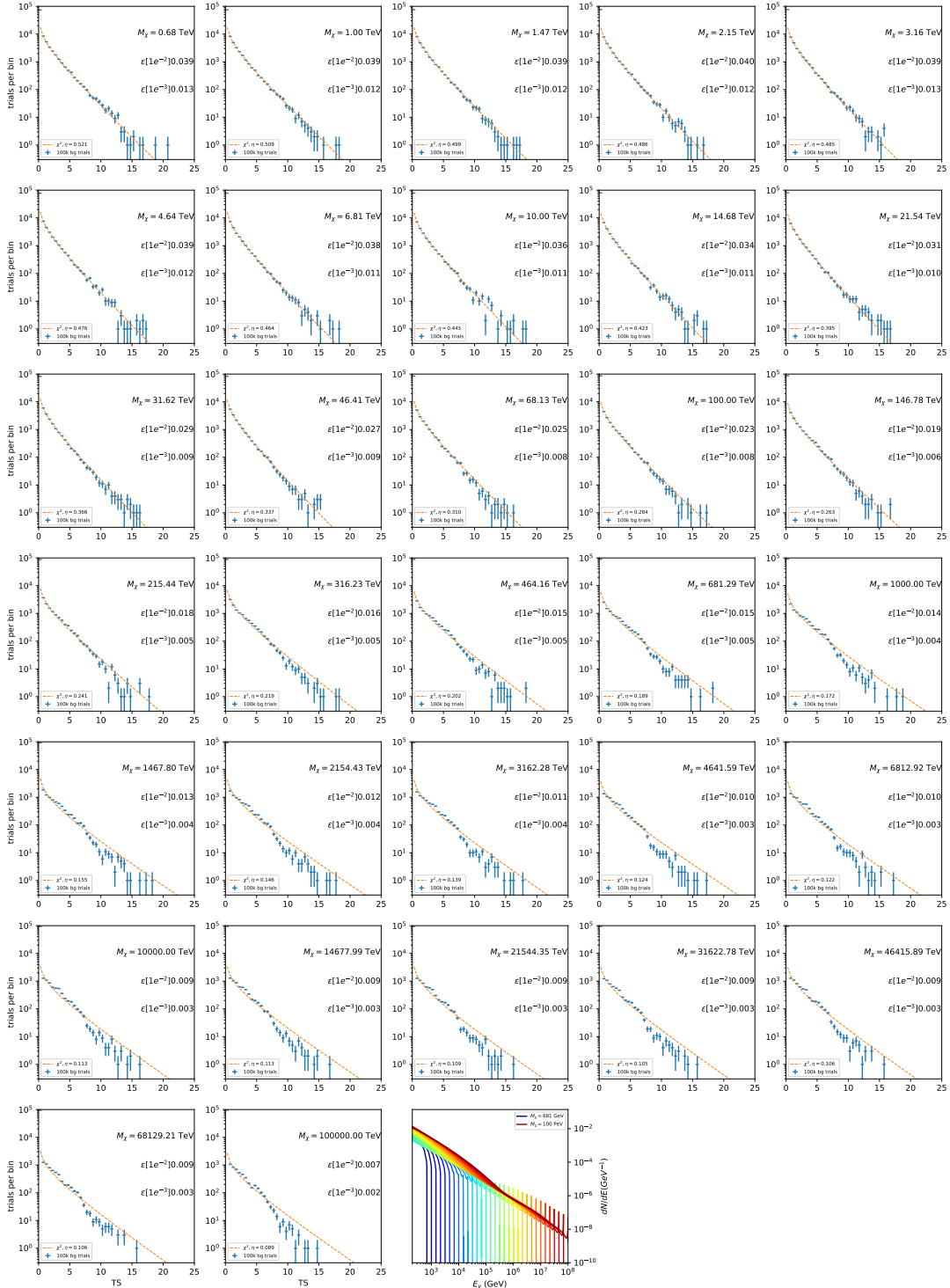


Figure 7.7 Same as Fig. 7.6 for Segue 1 $\chi\chi \rightarrow \tau\bar{\tau}$.

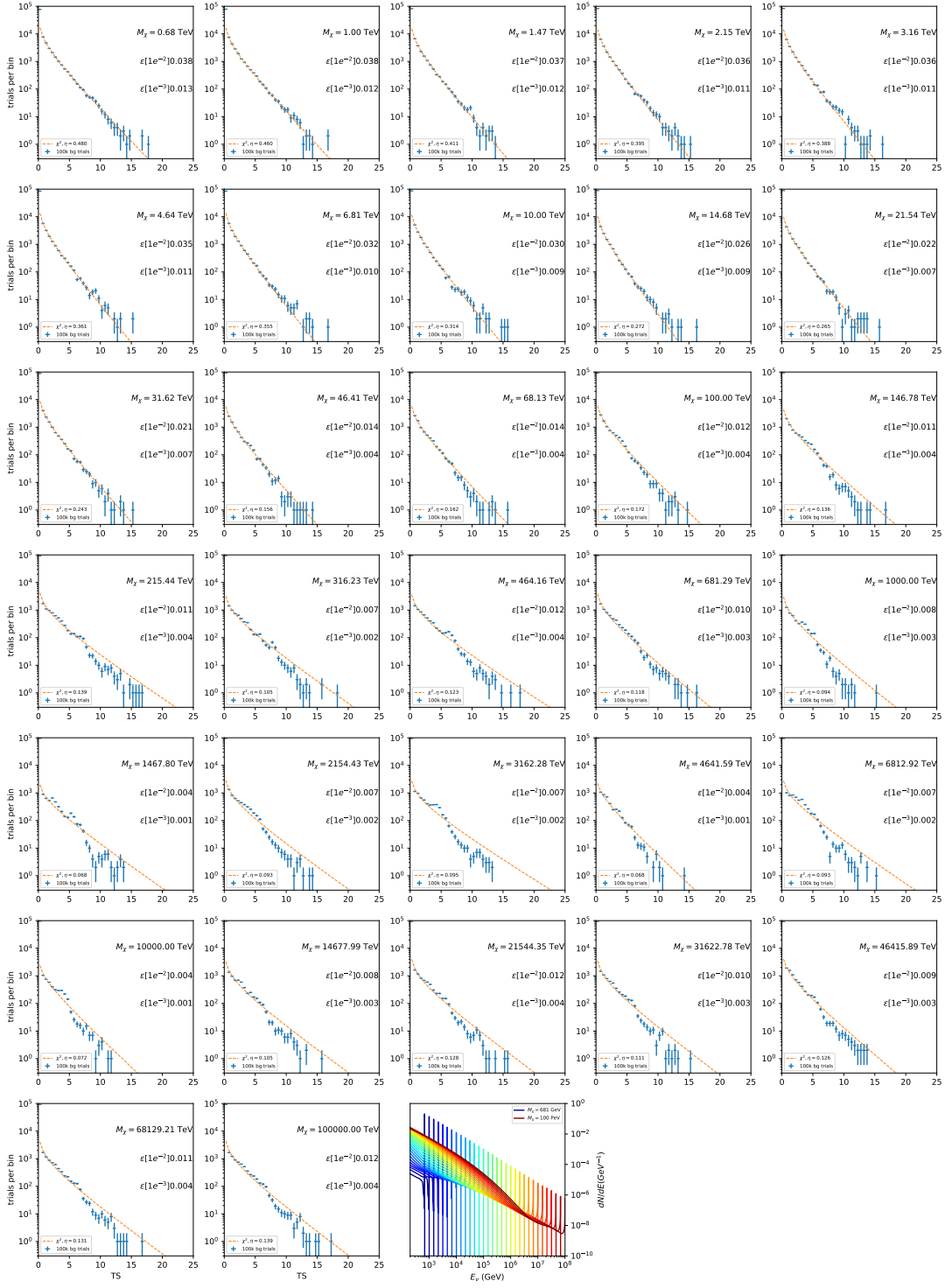


Figure 7.8 Same as Fig. 7.6 for Segue 1 $\chi\chi \rightarrow \nu_\mu\bar{\nu}_\mu$.

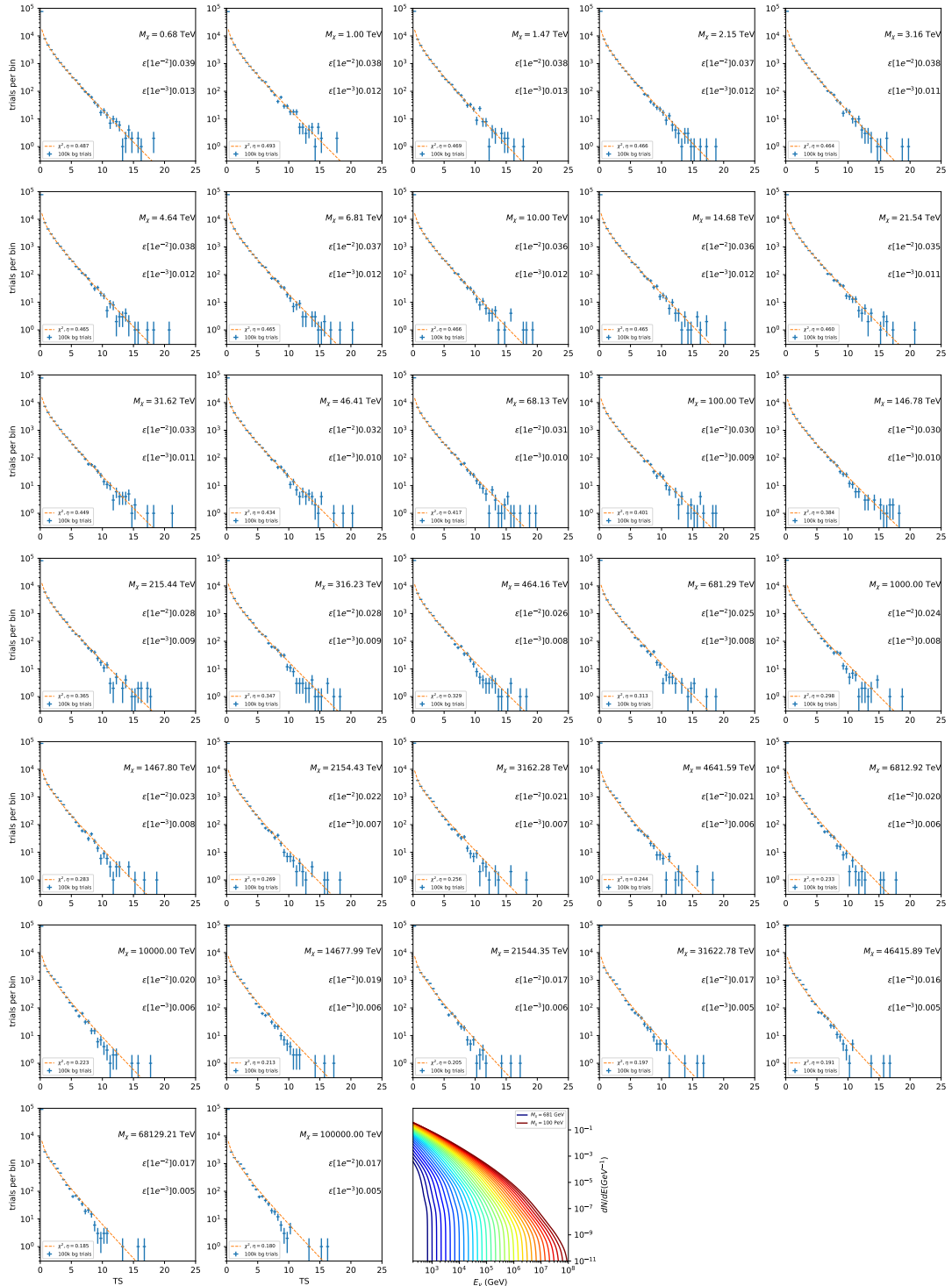


Figure 7.9 Same as Fig. 7.6 for Ursa Major II 1 $\chi\chi \rightarrow b\bar{b}$.

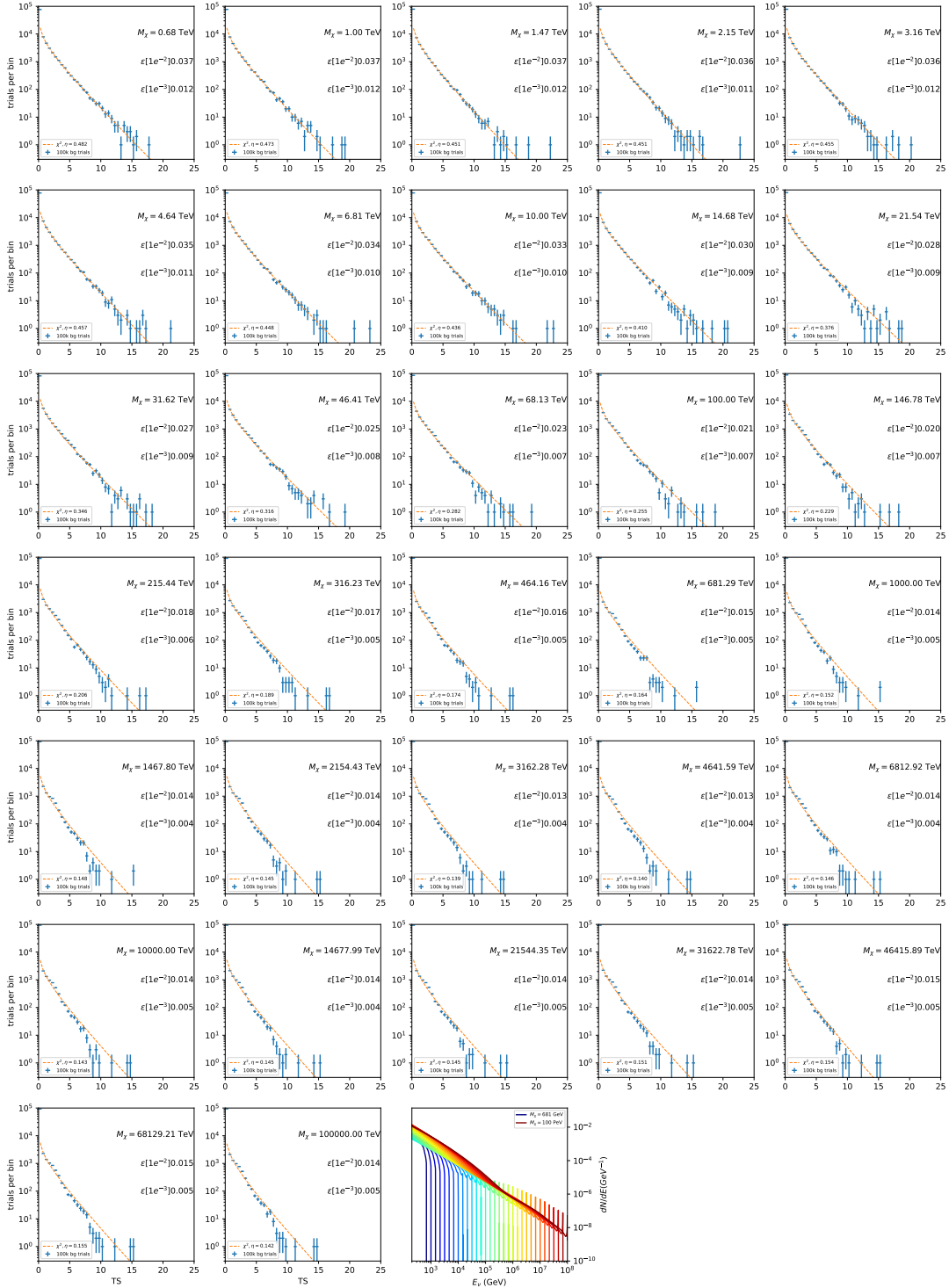


Figure 7.10 Same as Fig. 7.6 for Ursa Major II 1 $\chi\chi \rightarrow \tau\bar{\tau}$.

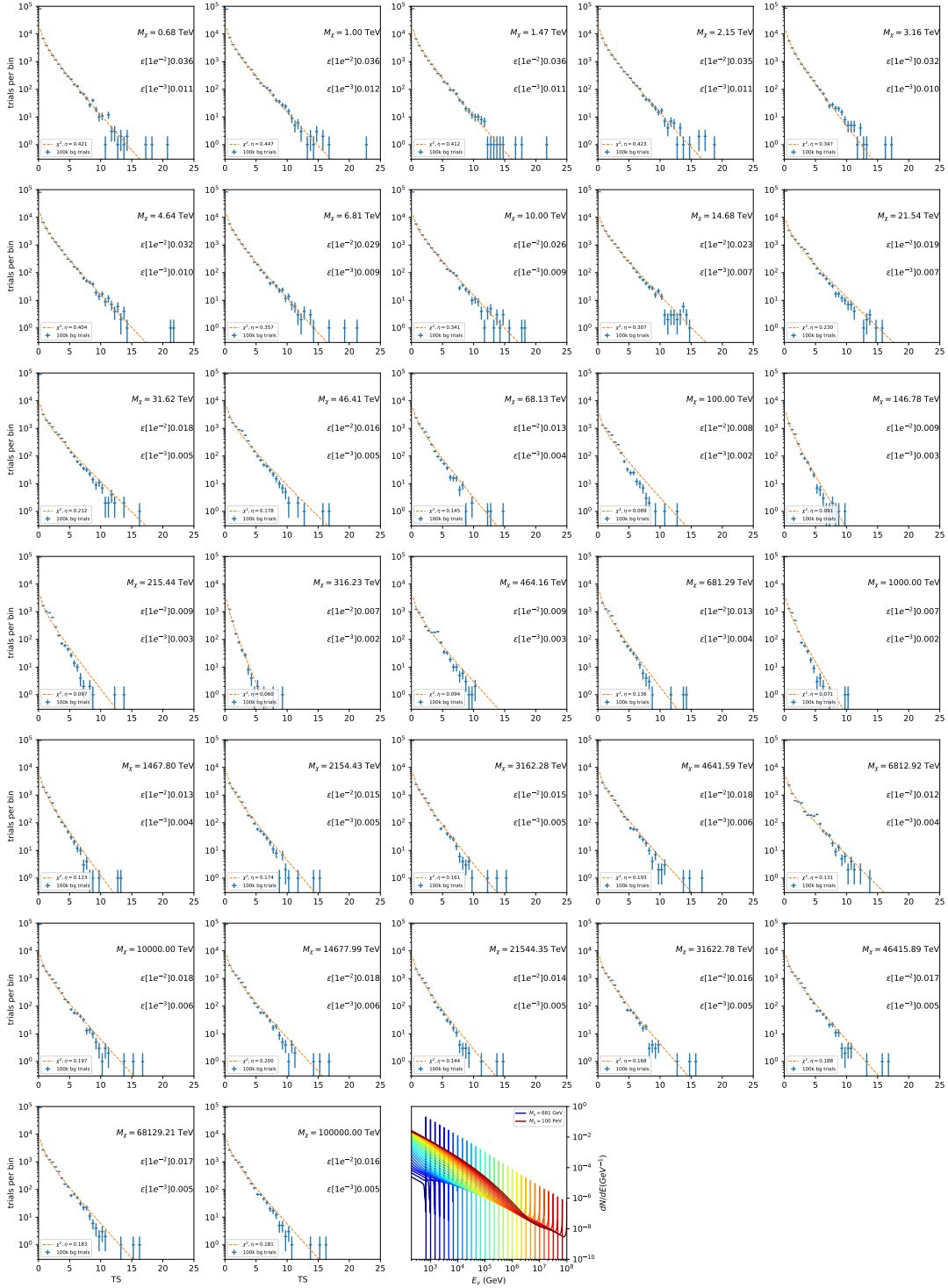


Figure 7.11 Same as Fig. 7.6 for Ursa Major II 1 $\chi\chi \rightarrow \nu_\mu\bar{\nu}_\mu$.

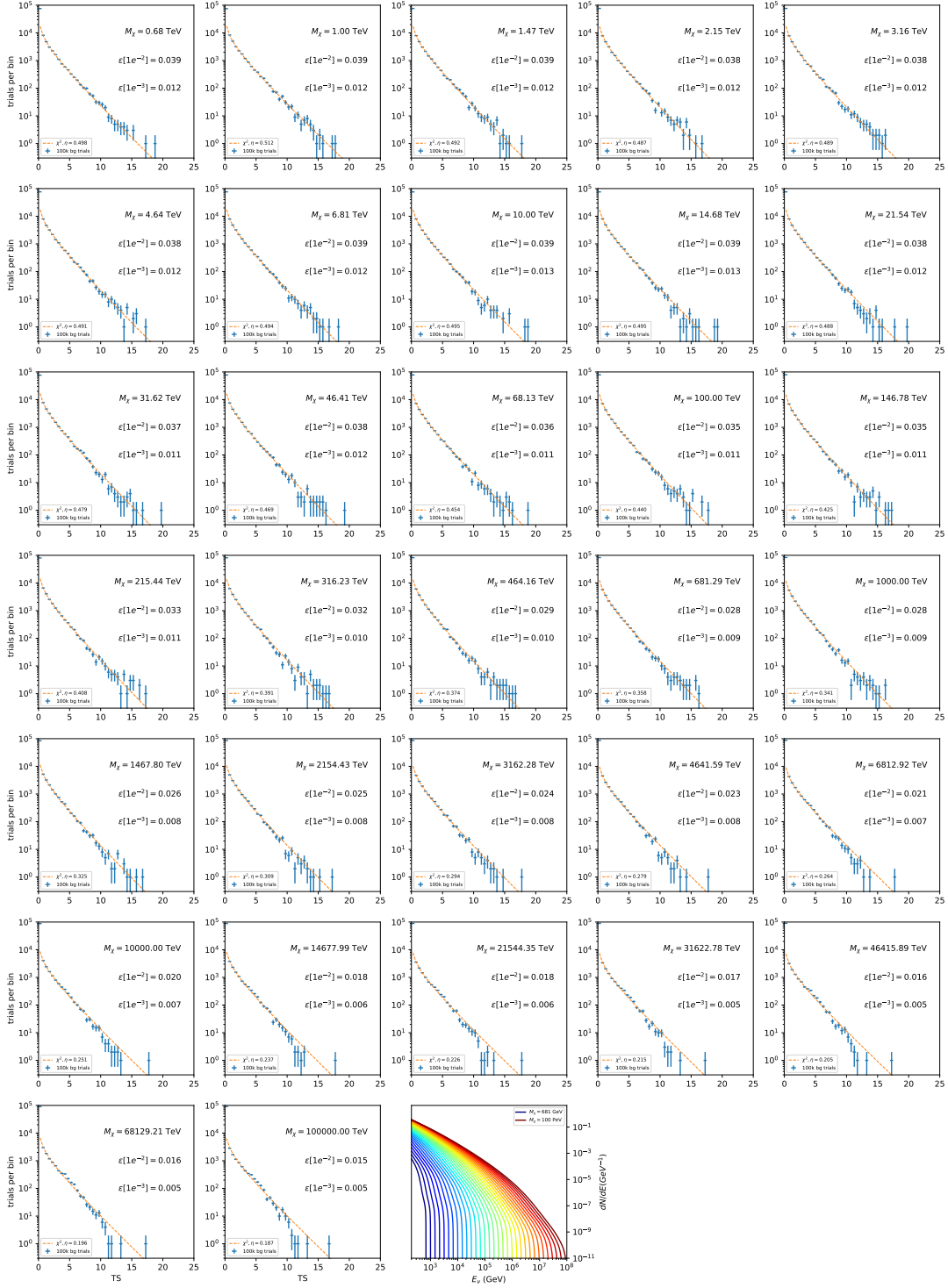


Figure 7.12 Same as Fig. 7.6 for 15, \mathcal{GS} J -factor, stacked sources and $\chi\chi \rightarrow b\bar{b}$.

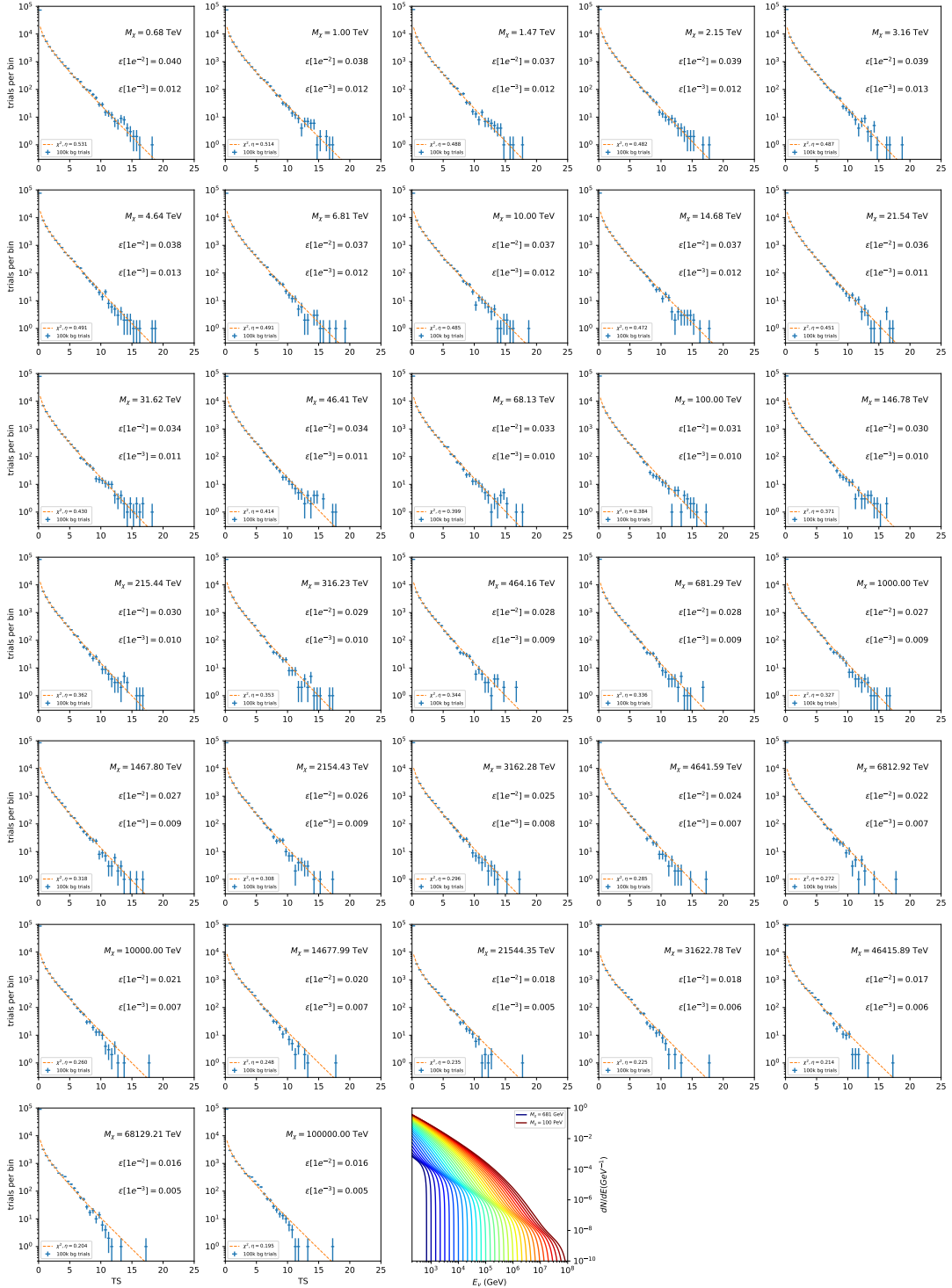


Figure 7.13 Same as Fig. 7.6 for 15, \mathcal{GS} J -factor, stacked sources and $\chi\chi \rightarrow t\bar{t}$.

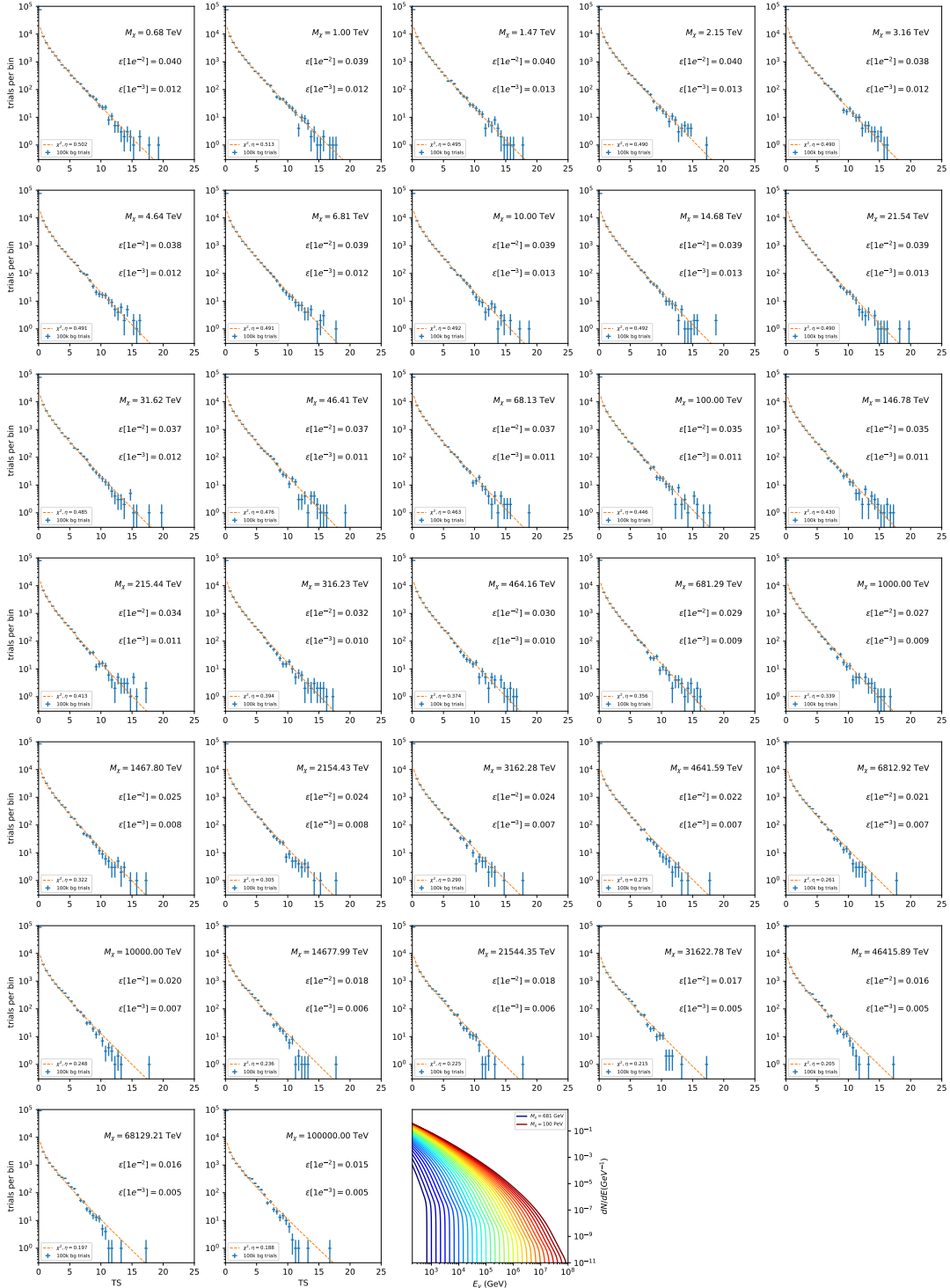


Figure 7.14 Same as Fig. 7.6 for 15, \mathcal{GS} J -factor, stacked sources and $\chi\chi \rightarrow u\bar{u}$.

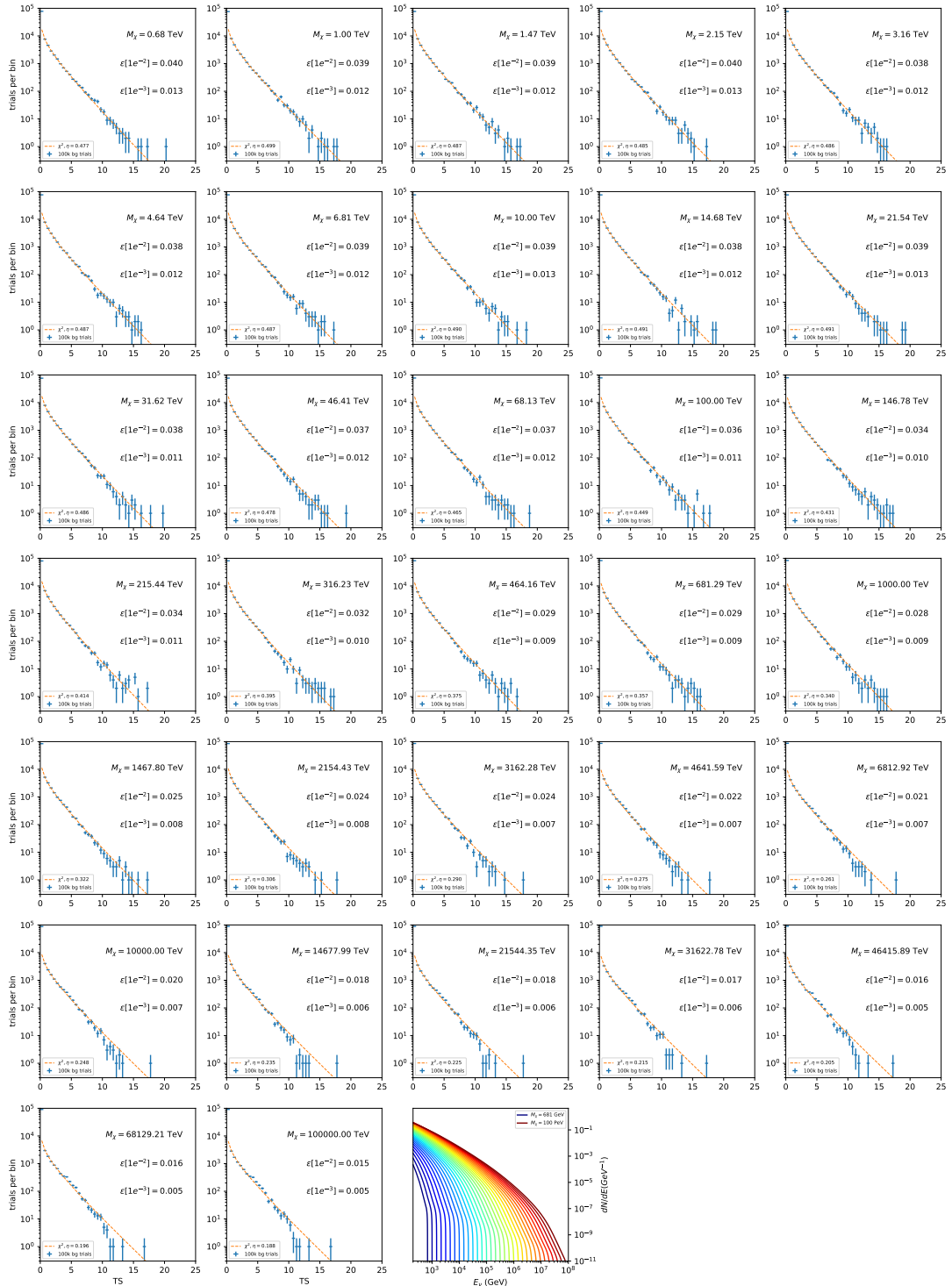


Figure 7.15 Same as Fig. 7.6 for 15, $\mathcal{G}\mathcal{S}$ J-factor, stacked sources and $\chi\chi \rightarrow d\bar{d}$.

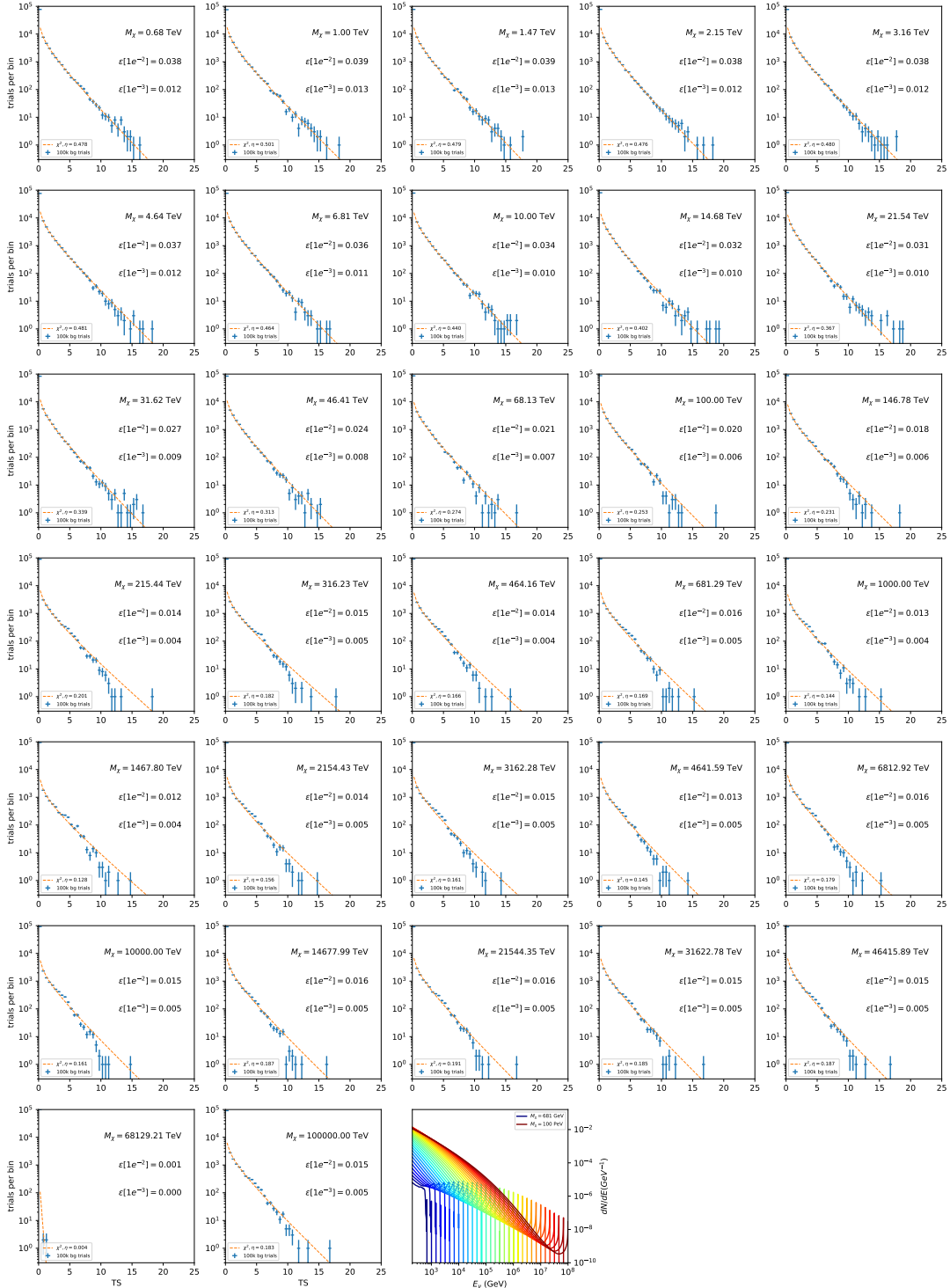


Figure 7.16 Same as Fig. 7.6 for 15, $\mathcal{G}\mathcal{S}$ J-factor, stacked sources and $\chi\chi \rightarrow e\bar{e}$.

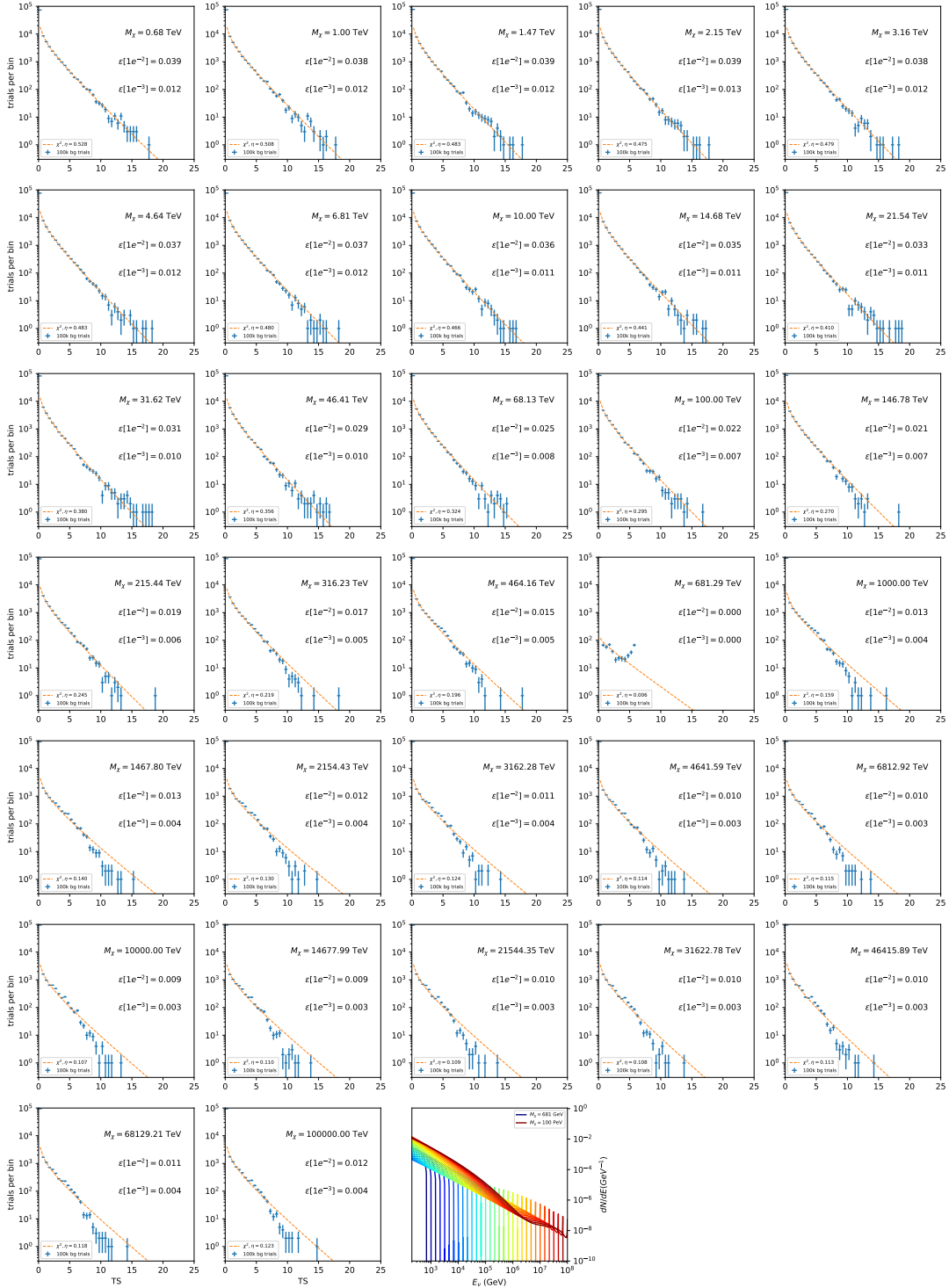


Figure 7.17 Same as Fig. 7.6 for 15, \mathcal{GS} J-factor, stacked sources and $\chi\chi \rightarrow \mu\bar{\mu}$.

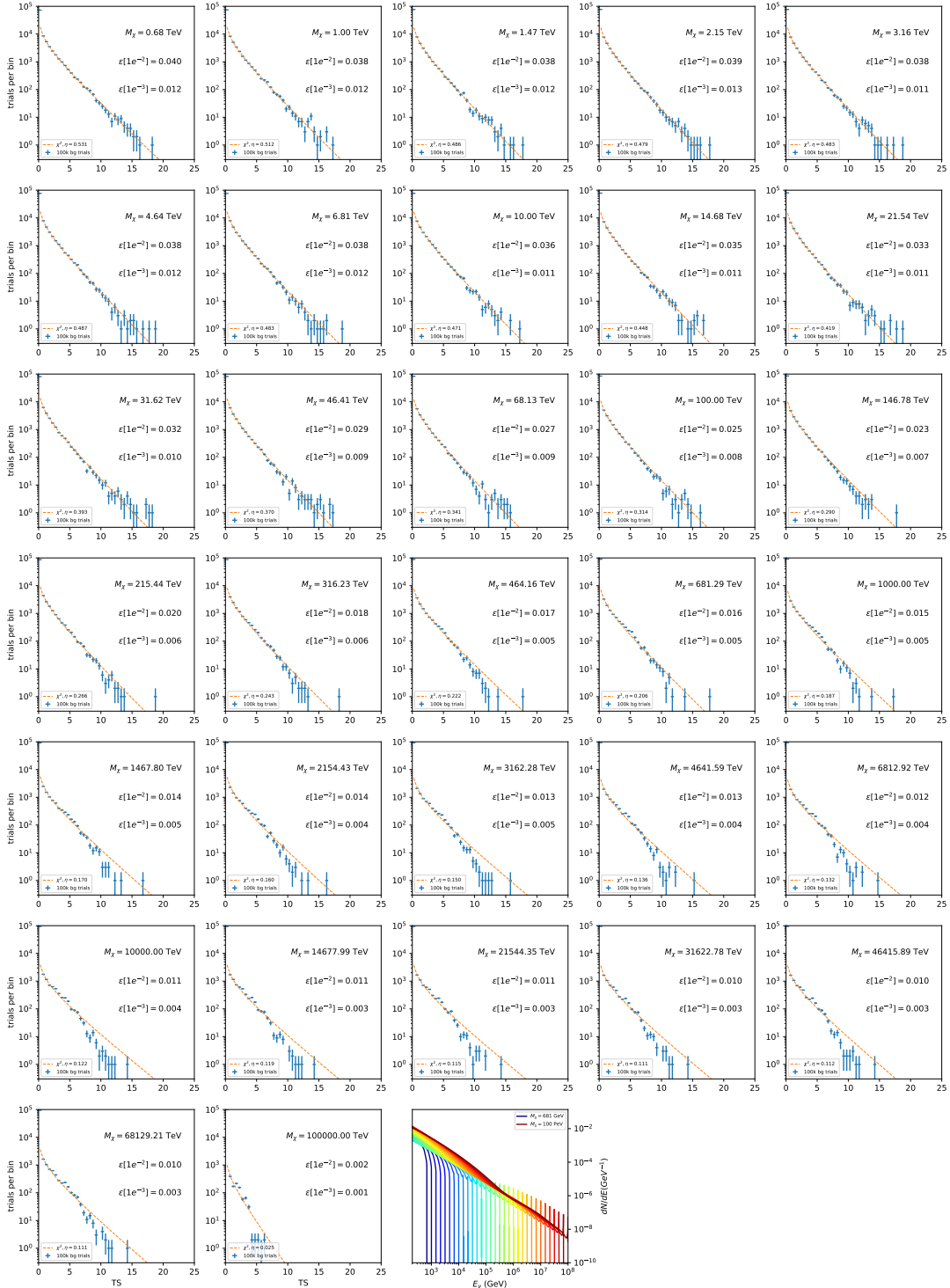


Figure 7.18 Same as Fig. 7.6 for 15, \mathcal{GS} J -factor, stacked sources and $\chi\chi \rightarrow \tau\bar{\tau}$.

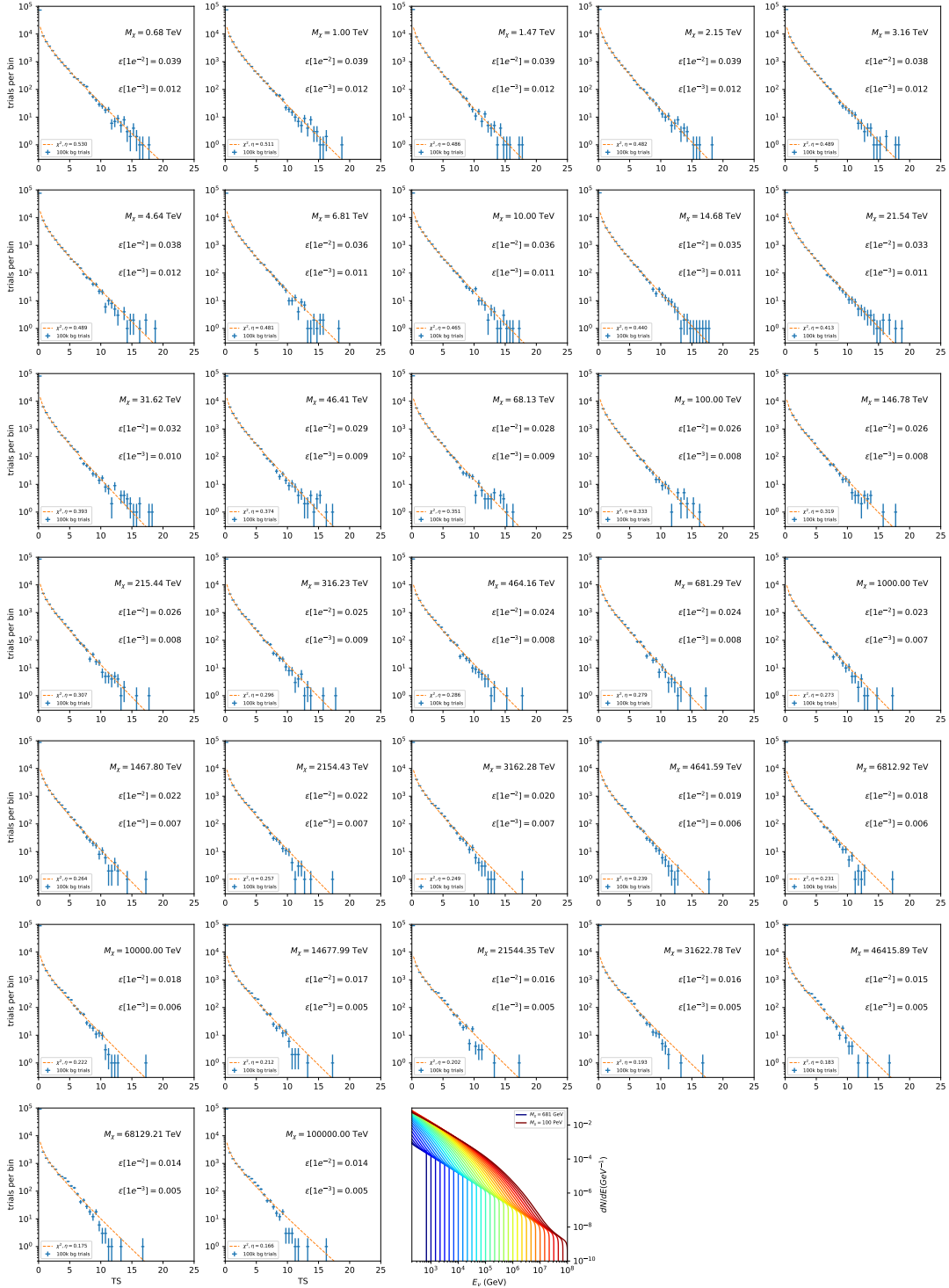


Figure 7.19 Same as Fig. 7.6 for 15, \mathcal{GS} J-factor, stacked sources and $\chi\chi \rightarrow W^+W^-$.

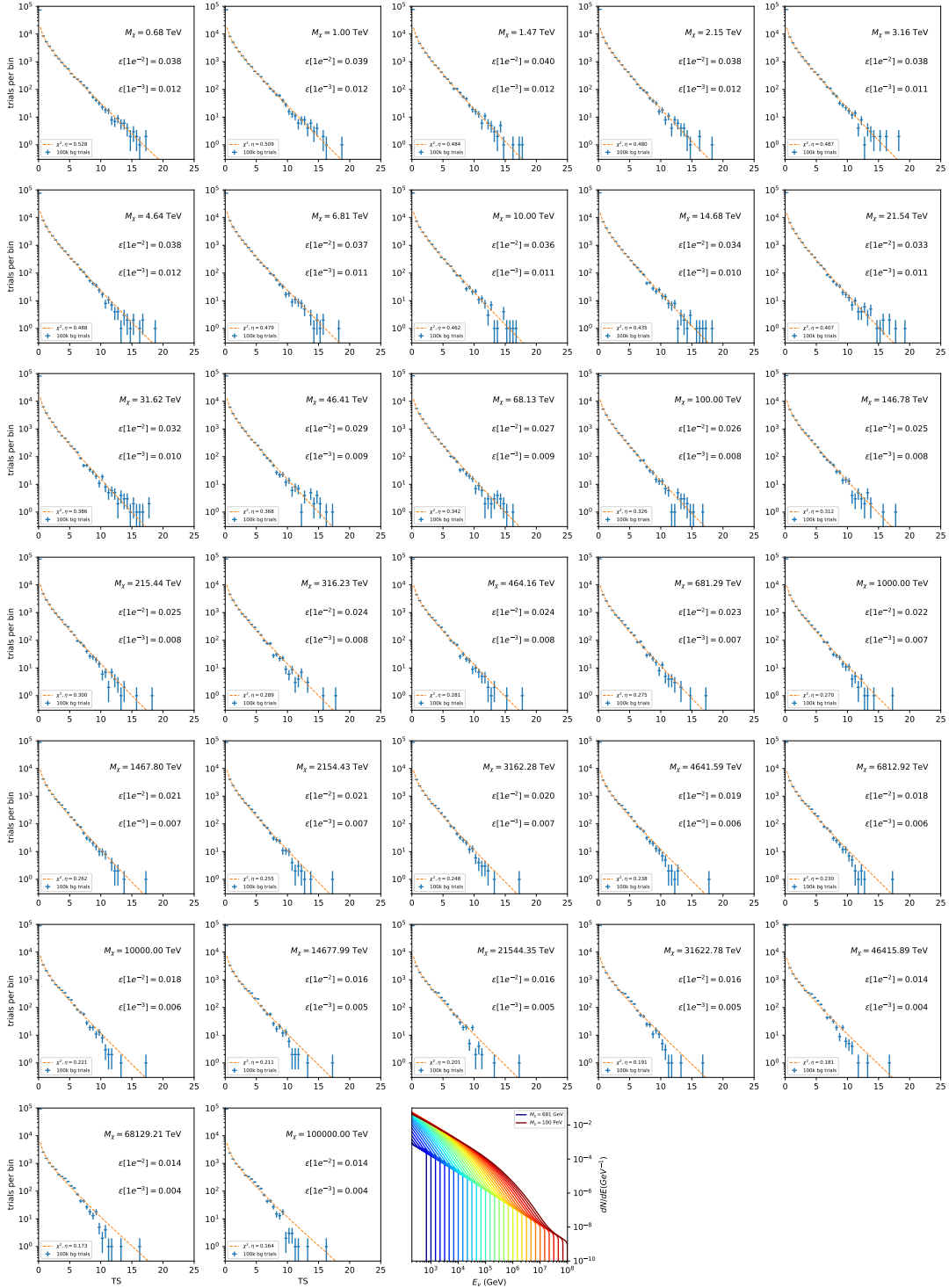


Figure 7.20 Same as Fig. 7.6 for 15, \mathcal{GS} J-factor, stacked sources and $\chi\chi \rightarrow ZZ$.

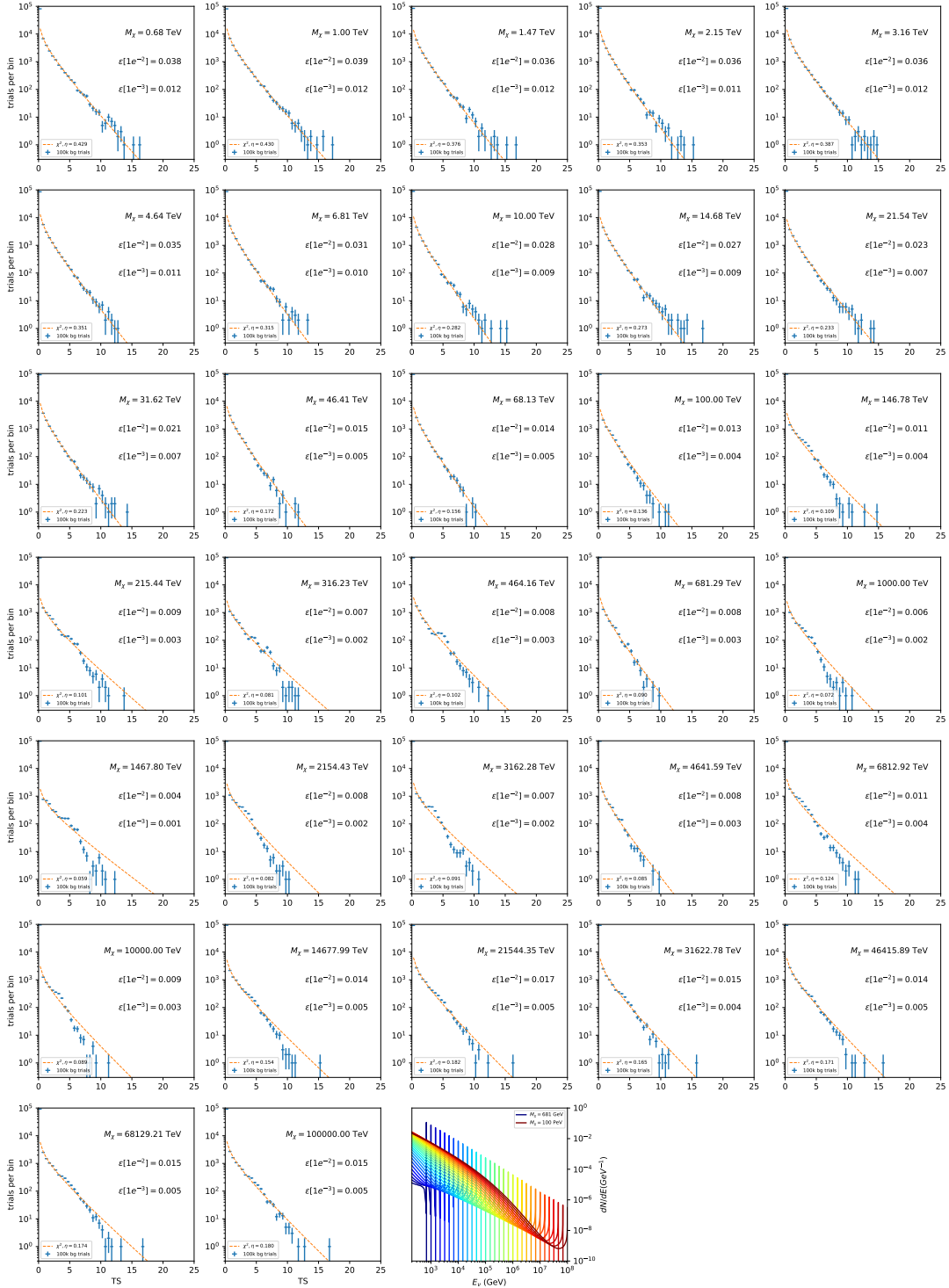


Figure 7.21 Same as Fig. 7.6 for 15, \mathcal{GS} J -factor, stacked sources and $\chi\chi \rightarrow \nu_e \bar{\nu}_e$.

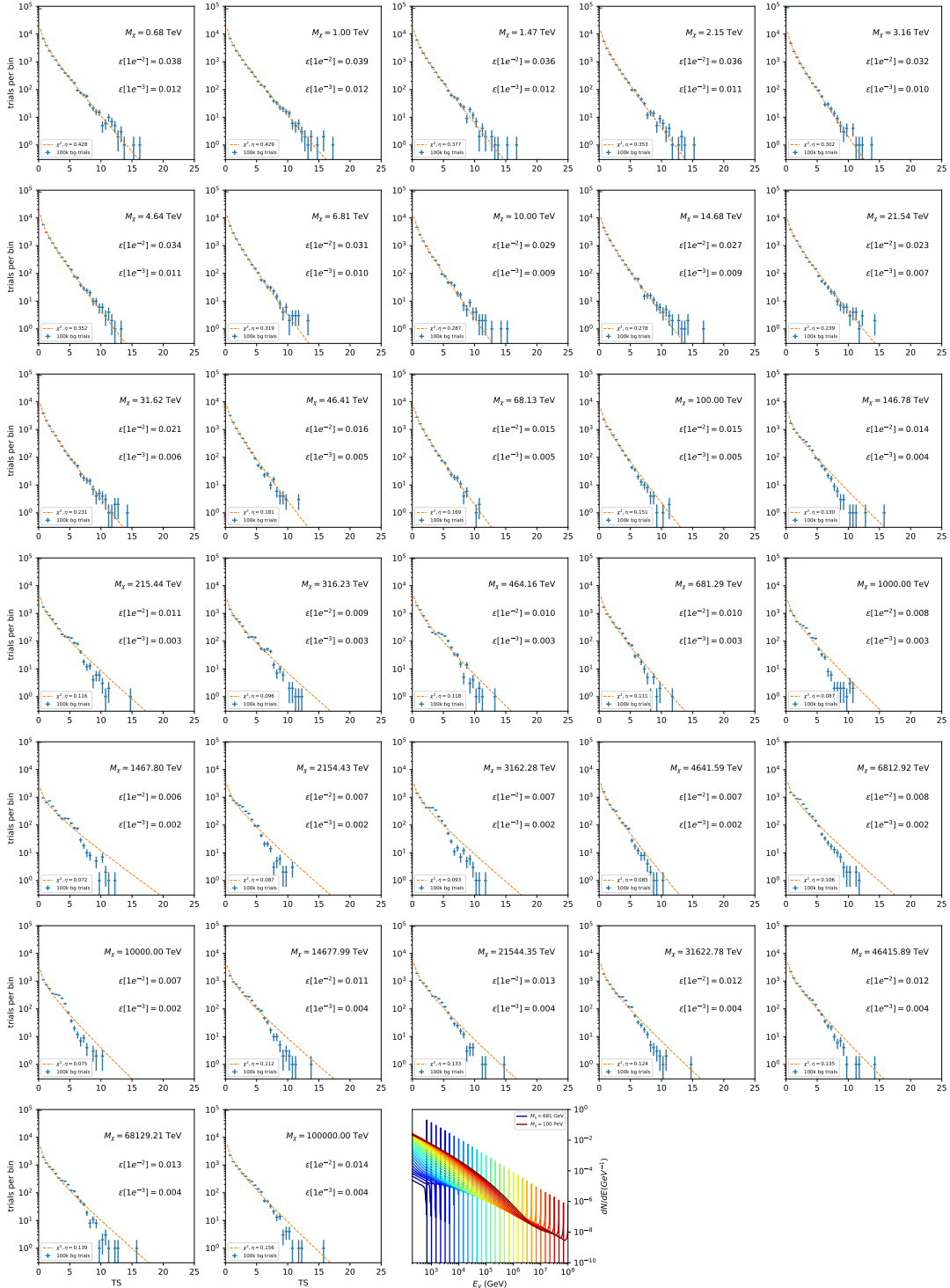


Figure 7.22 Same as Fig. 7.6 for 15, GS J-factor, stacked sources and $\chi\chi \rightarrow \nu_\mu \bar{\nu}_\mu$.

1955 **7.5.1 TS per Source**

1956 Figure 7.6 to Figure 7.11 present the TS distributions for Segue 1 and Ursa Major II for 100,000
1957 trials. More studies for all annihilation channels and remaining 13 sources were also performed
1958 and are documented in IceCube’s internal wiki.

1959 Almost every distribution produced follows a χ^2 distribution with 1 degree of freedom. This is
1960 more true for low m_χ than high m_χ models. These observations are important for future assumptions
1961 made in Sec. 8 and may justify statistical calculations assuming our test statistics follow a χ^2 with
1962 1 degree of freedom.

1963 **7.5.2 Stacked TS**

1964 Figure 7.12 to Figure 7.22 present the TS distributions for a stacked study of 15 sources with
1965 \mathcal{GS} J -factors on 100,000 trials. The presentation of these plots are identical to the single source
1966 distributions in Section 7.5.1. We see similar behaviour in the stacked TS distributions compared
1967 to the single source studies.

1968 **7.6 Signal Recovery**

1969 We also wish to understand how well the analysis is able to reconstruct signal neutrinos. In
1970 order to test this, we inject neutrinos from our spectral models randomly then attempt to discern
1971 the number of signal neutrinos in the simulated data. Figure 7.23 and Figure 7.24 show this study
1972 for $\chi\chi \rightarrow b\bar{b}$, $t\bar{t}$, and $\nu_\mu\bar{\nu}_\mu$ for a stacked analysis of 15 sources. Figure C.3 to Figure C.8 show
1973 identical studies for Segue 1 and Ursa Major II. We see that the analysis is conservative at smaller
1974 m_χ , yet improves at larger m_χ . We also see that the uncertainty is small for the neutrino annihilation
1975 spectra, and the uncertainty is larger for softer channels like $b\bar{b}$.

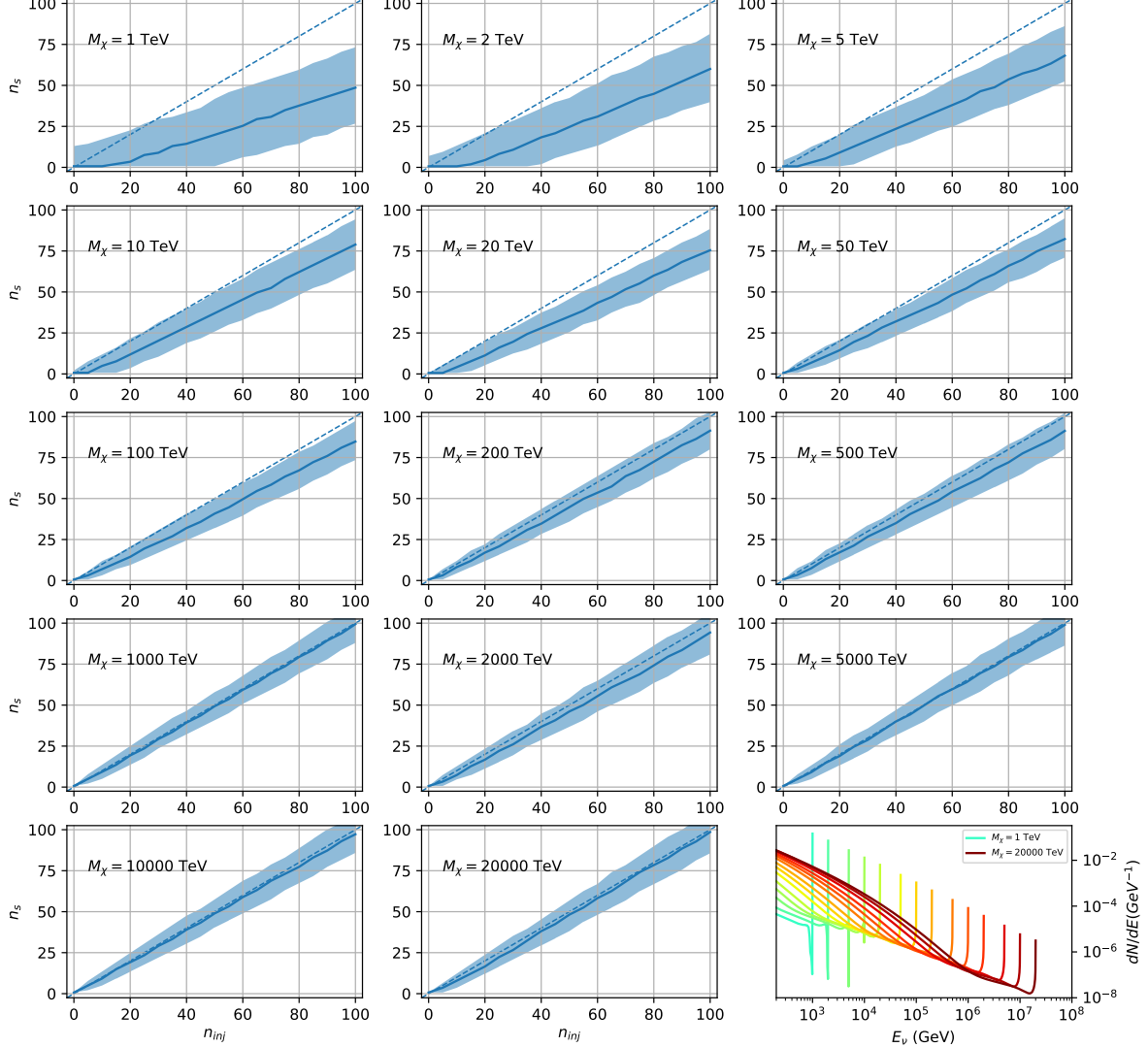


Figure 7.23 Signal Recovery study for an analysis with 15 stacked sources using the \mathcal{GS} J -factors [59]. Above shows 14 studies for DM mass ranging between 1 TeV and 20 PeV for $\chi\chi \rightarrow \mu_\mu\bar{\mu}_\mu$. The bottom right subplot features every spectral model used as input for the remaining subplots. The remaining subplots show n_{inj} as the number of signal events injected into background simulation. Whereas, n_s is the number of signal events recovered from analyzing the injected simulation. Blue line represents the median values of 100 simulations. Light blue bands show the 1σ statistical uncertainty around the median.

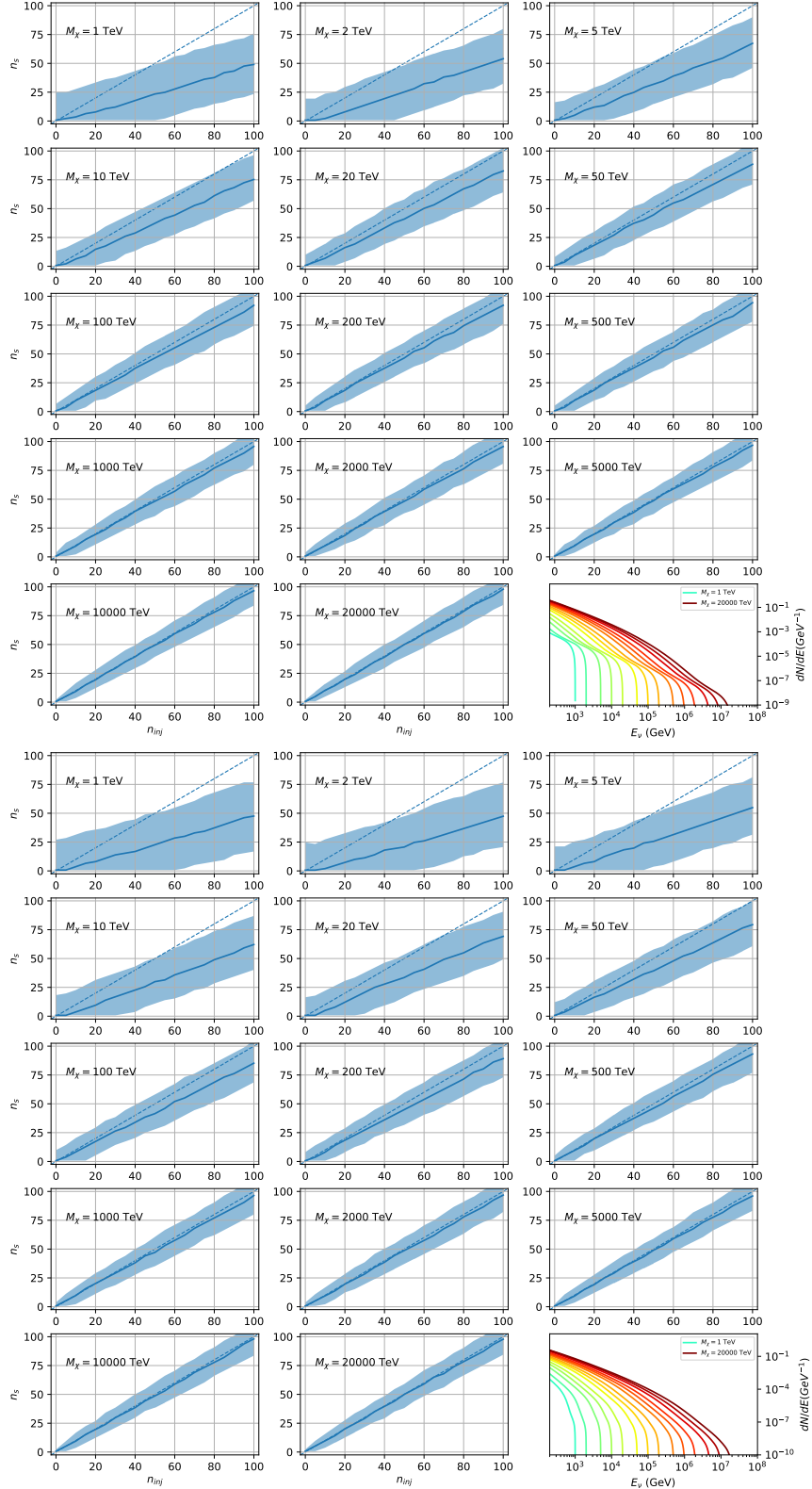


Figure 7.24 Same as Fig. 7.23 but for $\chi\chi \rightarrow t\bar{t}$ (top) and $b\bar{b}$ (bottom).

1976 **7.6.1 Sensitivities**

1977 In IceCube, we usually define the 90% confidence level (CL), as the minimum number of signal
1978 events (n_s) required to have a Type I error rate smaller than 0.5 and Type II error rate of 0.1. We
1979 compute n_s from the following equation

$$n_s = T_{\text{live}} \int_0^{\Delta\Omega} d\Omega \int_{E_{\min}}^{E_{\max}} dE_\nu A_{\text{eff}}(\hat{n}, E_\nu) \frac{d\Phi_\nu}{d\Omega dE_\nu}(\hat{n}, E_\nu), \quad (7.8)$$

1980 to extract the sensitivity on the dark matter velocity-weighted annihilation cross-section, $\langle\sigma v\rangle$. T_{live}
1981 is the detector live time, A_{eff} is the effective area of the detector, and E_{\min} , E_{\max} are the minimum,
1982 maximum energies of the expected neutrinos, respectively.

1983 Sensitivities are calculated for each source individually as if they were the only source and as a
1984 stack over 1000 trials. From Eq. (7.8) and Eq. (7.1) we can compute the $\langle\sigma v\rangle$ at a 90% confidence
1985 level. Figure 7.26 and Fig. 7.25 show the sensitivities for some DM annihilation channels. Not
1986 all channels computed successfully in time for the writing of this dissertation. Among channels
1987 missing include the charged leptons: e and τ .

1988 **7.7 Systematics**

1989 The current analysis plan is to compare these sensitivities to another J -factor catalog such as
1990 \mathcal{LS} [80] although this was not completed in time for this dissertation. Additionally, we set out to
1991 perform a standard suite of IceCube systematic studies which include: DOM efficiency, Hole ice,
1992 ice absorption, and photon scattering. We do study Earth attenuation, and Section 7.7.1 enumerates
1993 the impact of the Earth on our hardest neutrino spectra.

1994 **7.7.1 Earth Effects**

1995 We look to quantify the impact of the Earth on our sensitivity to $\chi\chi \rightarrow \nu_\mu \bar{\nu}_\mu$. This channel is
1996 expected to be among the significantly impacted annihilation channels because it has a significant
1997 contribution at PeV energies for $m_\chi \geq 1\text{PeV}$. The Earth is expected to attenuate these higher energy
1998 neutrinos. However, these neutrino spectra have significant low energy contributions, so we do not
1999 expect to entirely lose our sensitivity. This motivated a study examining our $\langle\sigma v\rangle$ sensitivity over
2000 all DM masses sampled for a selection of declinations.

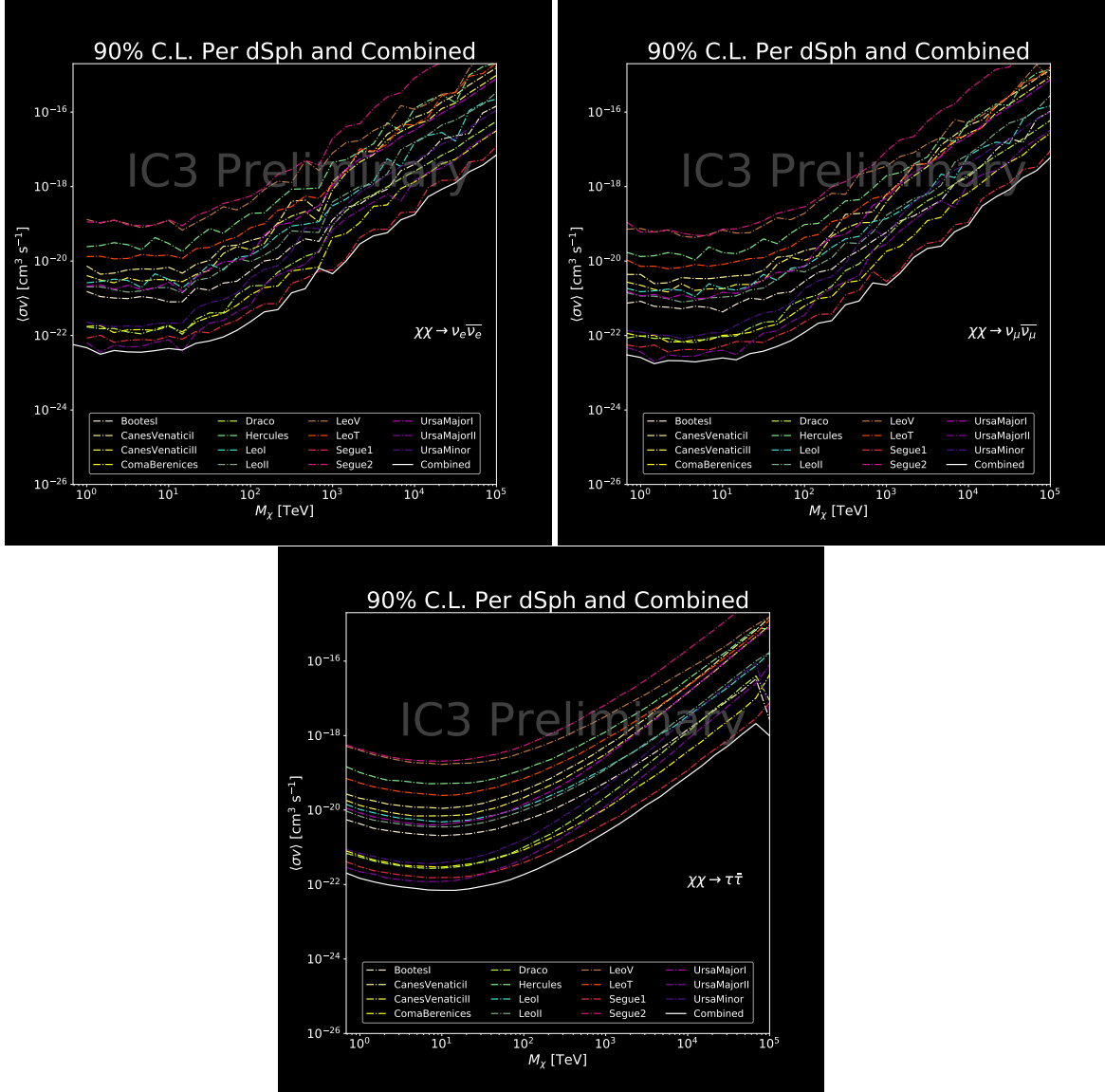


Figure 7.25 IceCube North Sky Track Sensitivities. Each panel shows sensitivity curves for various DM annihilation channels. Sensitivities are for the velocity-weighted cross-section $\langle\sigma v\rangle$ versus m_χ . Dotted, colored lines are sensitivities for individual sources. Solid white lines are for the combined sensitivity of all 15 \mathcal{GS} sources used in this study.

For this systematic study, I sample 6 DM masses per decade from 681 GeV to 100 PeV. I select declinations that are shared with sources in the \mathcal{GS} catalog: Boötes I, Canes Venatici II, Leo V, Ursa Major I, and Ursa Minor. I study a fake source who's J -factor is shared with Ursa Major II, but who's coordinates belong to the aforementioned list. The sensitivity studies performed for each source (Fig. 7.25 and Section C.5) provided n_s for 1000 trials which we extracted from Eq. (7.8). We derive $\langle\sigma v\rangle$ using $\log_{10} J = 19.42 \log_{10}(\text{GeV}^2 \text{cm}^{-5})$. Figure 7.28 shows the results.

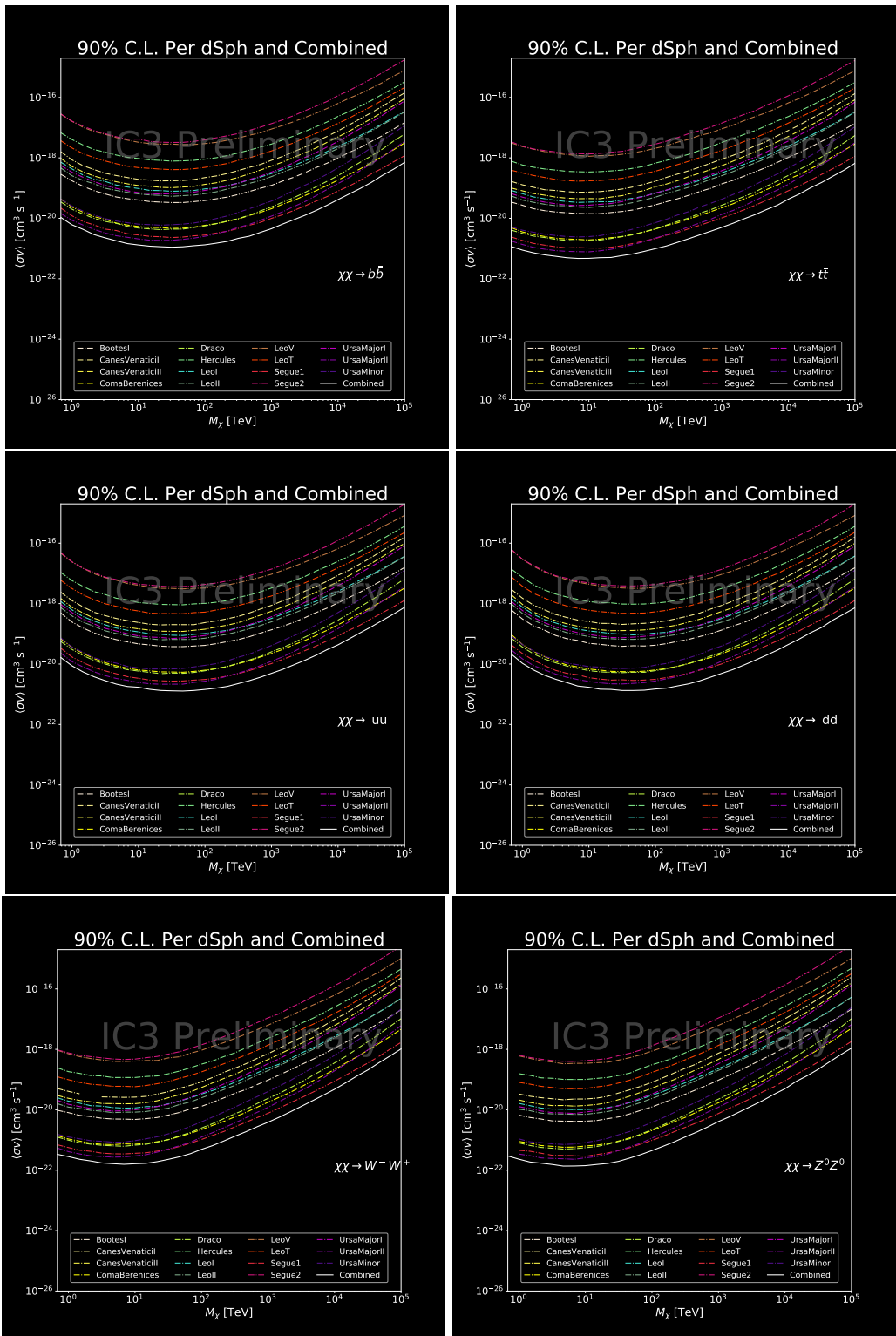


Figure 7.26 Same as Fig. 7.25 for three additional DM annihilation channels.

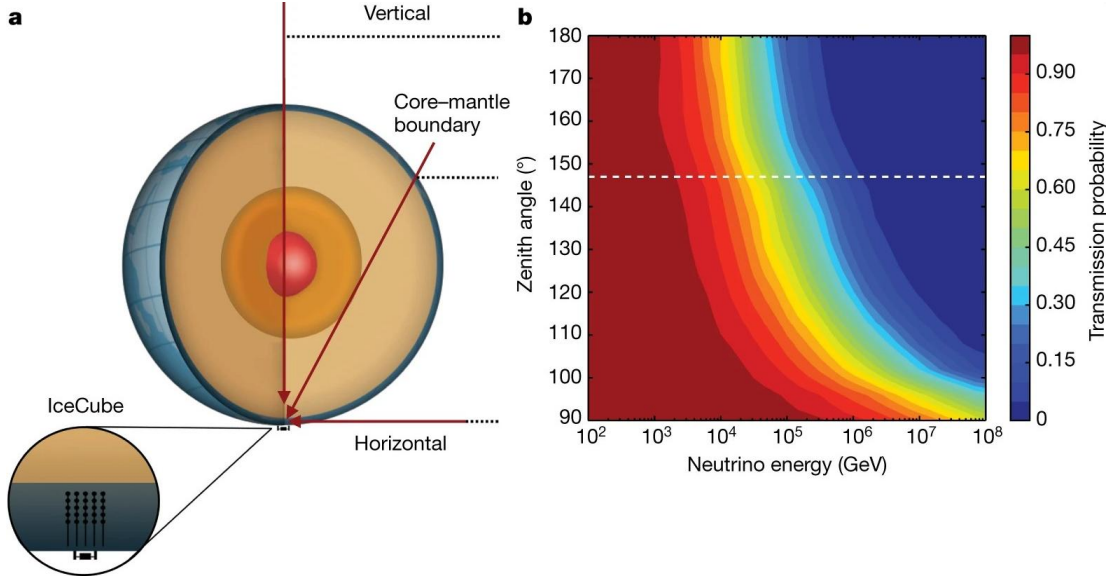


Figure 7.27 Panel A: Neutrino's from the Northern sky and incident on the IceCube detector will travel through the Earth. How much of the Earth these neutrinos travels is a function of zenith from the vertical axis. Panel B: SM prediction of neutrino transmission probabilities for neutrinos arriving at $90^\circ - 180^\circ$ zenith and with 100 GeV to 100 PeV energies. High-energy neutrinos traversing the whole Earth are completely absorbed, whereas low-energy neutrinos pass through unimpeded. Neutrinos coming from above the horizon will arrive unimpeded for all neutrino energies. Figure pulled from [92].

2007 Figure 7.28 shows that we have significant but diminishing sensitivity to sources at high
 2008 declination. We see in the worse case, the sensitivity at high declination is up to an order of
 2009 magnitude worse than at low declination. However, for $m_\chi < 1$ PeV, the sensitivities are very
 2010 similar. The comparable sensitivities imply that a stacking analysis with IceCube is most powerful
 2011 in the 500 GeV to 1 PeV region. Above 1 PeV, our limits and sensitivities are dominated by sources
 2012 near the horizon. When we additionally consider the J -factors, we expect Segue 1 to dominate
 2013 contributions to sensitivity and limits where $m_\chi > 1$ PeV.

2014 7.8 Conclusions

2015 We utilized advanced computing techniques like parallel programming and spline fitting of
 2016 particle physics Monte Carlo to greatly expand and refine IceCube's sensitivity to DM annihilation
 2017 from dSphs. Furthermore, we imported updated astrophysical and particle physics models that
 2018 better represent what we believe neutrino signals from DM annihilation should look like. We, for
 2019 the first time, build an analysis that is sensitive to PeV DM annihilation.

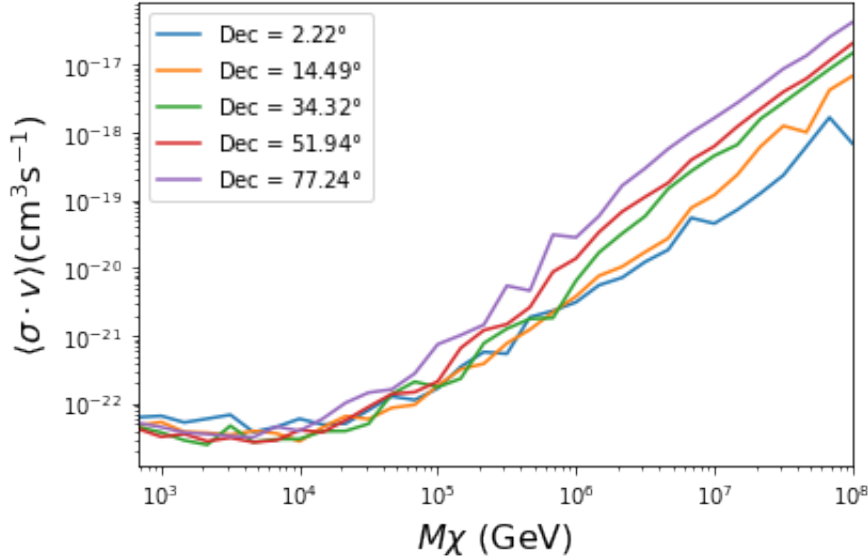


Figure 7.28 $\langle \sigma v \rangle$ sensitivities for 5 imaginary sources with $\log_{10} J = 19.42$ $\log_{10}(\text{GeV}^2 \text{cm}^{-5})$. Each imaginary source shares a declination with a source in Tab. 5.1

2020 When we compare to previous IceCube publications of dSphs [83], we see an order of magnitude
 2021 improvement to our sensitivity. This analysis has been working group approved within IceCube
 2022 and is currently under collaboration review before unblinding. These processes did not complete
 2023 in time for this dissertation. Therefore we do not show data for this thesis and is the clear next step.

2024 The test statistic distributions in this analysis also demonstrate more characteristic behavior
 2025 compared to previous DM analyses [87, 91]. With a 10-year dataset, we finally have enough
 2026 statistics to almost trivially combine with other photon observatories, such as HAWC. The first
 2027 groundwork for a multi-messenger DM search is provided with concluding remarks in chapter 8.

CHAPTER 8

2028

NU DUCK: CONCLUSIONS AND FUTURE DIRECTIONS

2029 **8.1 Conclusions**

2030 **TODo: Chat GPT the shit of everything below** In this work, three analyses were performed
2031 with data from the HAWC and IceCube observatories in order to explore some of the fundamental
2032 questions in particle astrophysics. The goal was to contribute to the understanding of the sources of
2033 cosmic rays, their acceleration mechanisms, and the nature of dark matter. The detection techniques
2034 and reconstruction methods for both observatories were described, along with the properties that
2035 make them ideal instruments to perform such searches.

2036 This dissertation used data from the HAWC detector to probe cutting-edge physics beyond
2037 the Standard Model. The techniques by which HAWC is able to detect cosmic gamma rays were
2038 demonstrated and the many advantages of HAWC in probing ultra-high energy gamma-ray physics
2039 were detailed. It was shown how HAWC data can be used to explore unanswered questions such as
2040 the nature of dark matter and the limits of Lorentz invariance. In particular, a search for evidence of
2041 WIMP dark matter in the Milky Way Galactic Halo was performed. To accomplish this, simulations
2042 of the dark matter density profile were combined with estimates of the HAWC sensitivity to dark
2043 matter-like energy spectra. This allowed strong constraints on dark matter annihilation and decay
2044 from the Galactic Halo to be derived that are insensitive to the large uncertainties arising from
2045 systematics in the dark matter spatial distribution. Multi-hundred TeV photon spectra were also
2046 significantly detected from HAWC sources within the Galactic Plane. These results lead to the
2047 strongest constraints on Lorentz invariance violation to be published at the time of writing.

2048 The work of this dissertation was made possible by the ongoing development of new algorithms
2049 and reconstruction techniques within the HAWC collaboration. Probing the Galactic Halo required
2050 the creation of a novel background estimation technique that relied on HAWC's wide field of view
2051 and strong ability to discriminate between gamma rays and cosmic rays. Meanwhile, the constraints
2052 on Lorentz invariance violation were enabled by the improved energy resolution from a machine
2053 learning technique. HAWC has recently completed a reprocessing of all archival data using an

2054 updated set of algorithms that can lead to compelling follow-up work on these results. Combining
 2055 the new background technique with the re-optimized energy estimators will allow for Galactic
 2056 dark matter to be probed at even higher masses, as well as for analyses that require precise energy
 2057 resolution such as gamma-ray line searches.

2058 **8.2 Future Directions: Multi-Messenger Dark Matter Search**

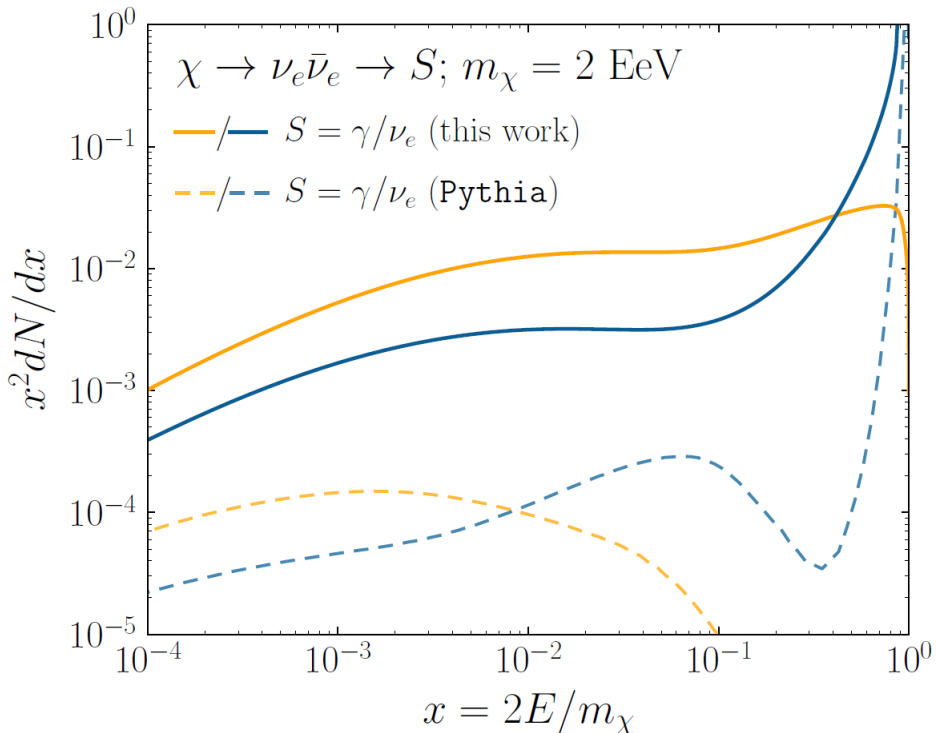


Figure 8.1 The prompt electron neutrino and photon spectrum resulting from the decay of a 2EeV DM particle to $\nu_e \bar{\nu}_e$, as currently being searched for at IceCube [5]. Solid curves represent the results of this work, and predict orders of magnitude more flux at certain energies than the dashed results of Pythia 8.2, one of the only existing methods to generate spectra at these masses. In both cases energy conservation is satisfied: there is a considerable contribution to a δ -function at $x = 1$, associated with events where an initial W or Z was never emitted and thus no subsequent shower developed. Large disagreements are generically observed at these masses for electroweak dominated channels, while the agreement is better for colored initial SM states.

2059 As I have shown previously in Sec. 5 and Sec. 6, we can build a fast and robust analysis
 2060 that shares tools with the field. The hope being that IceCube can eventually combine data with
 2061 gamma-ray observatories.



Figure 8.2 TODO: neutrino and bb plot with nu Sensitivities[NEEDS A SOURCE][FACT CHECK THIS]

MULTI-EXPERIMENT SUPPLEMENTARY FIGURES

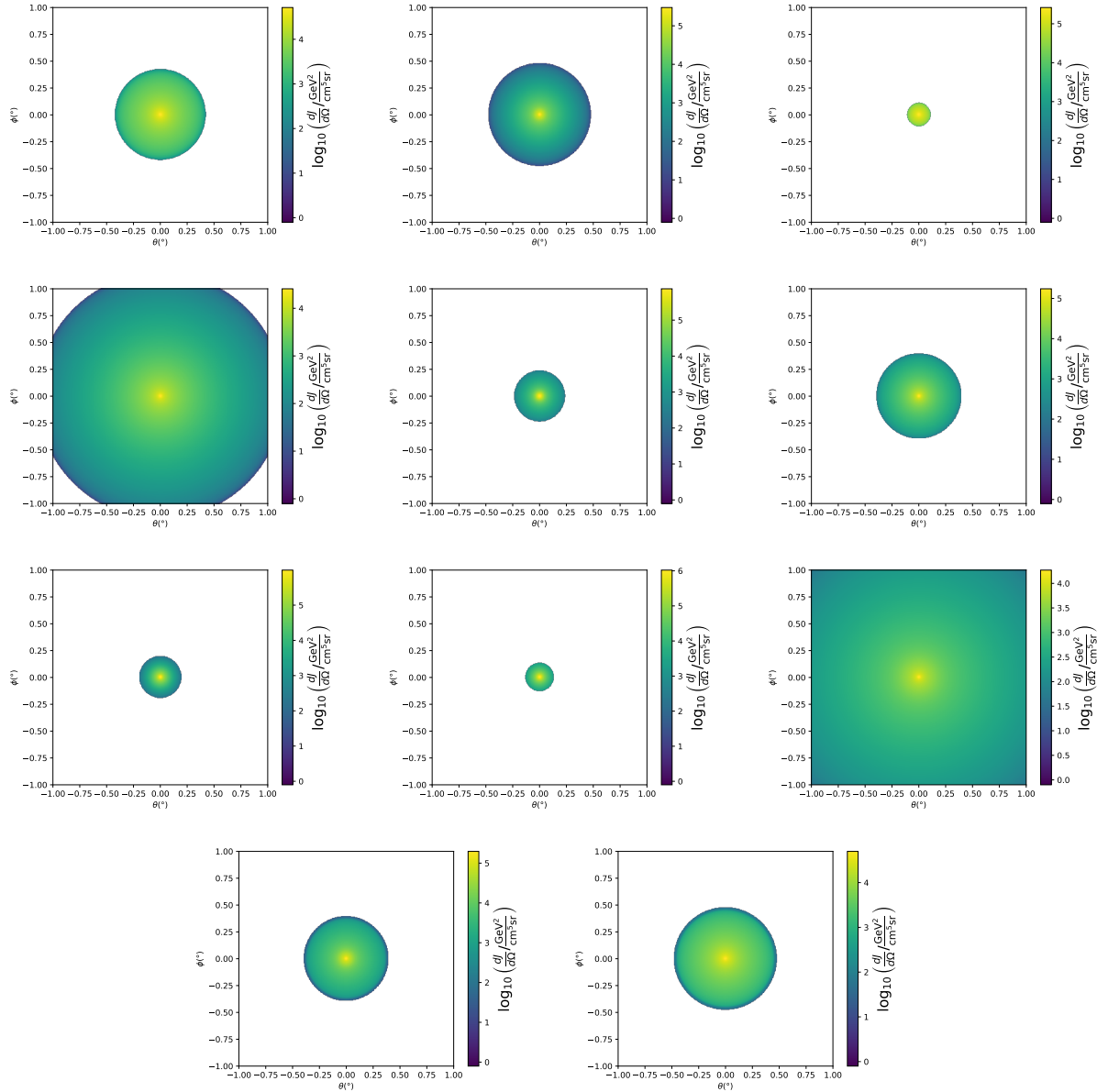


Figure A.1 Sister figure to Figure 5.3. Sources in the first row from left to right: Bootes I, Canes Venatici I, II. In second row: Draco, Hercules, Leo I. In the first row: Leo II, Leo IV, Sextans. In the final row: Ursa Major I, Ursa Major II.

APPENDIX B

2063 MULTITHREADING DARK MATTER ANALYSES SUPPLEMENTARY MATERIAL

2064 B.1 Remaining Spectral Models

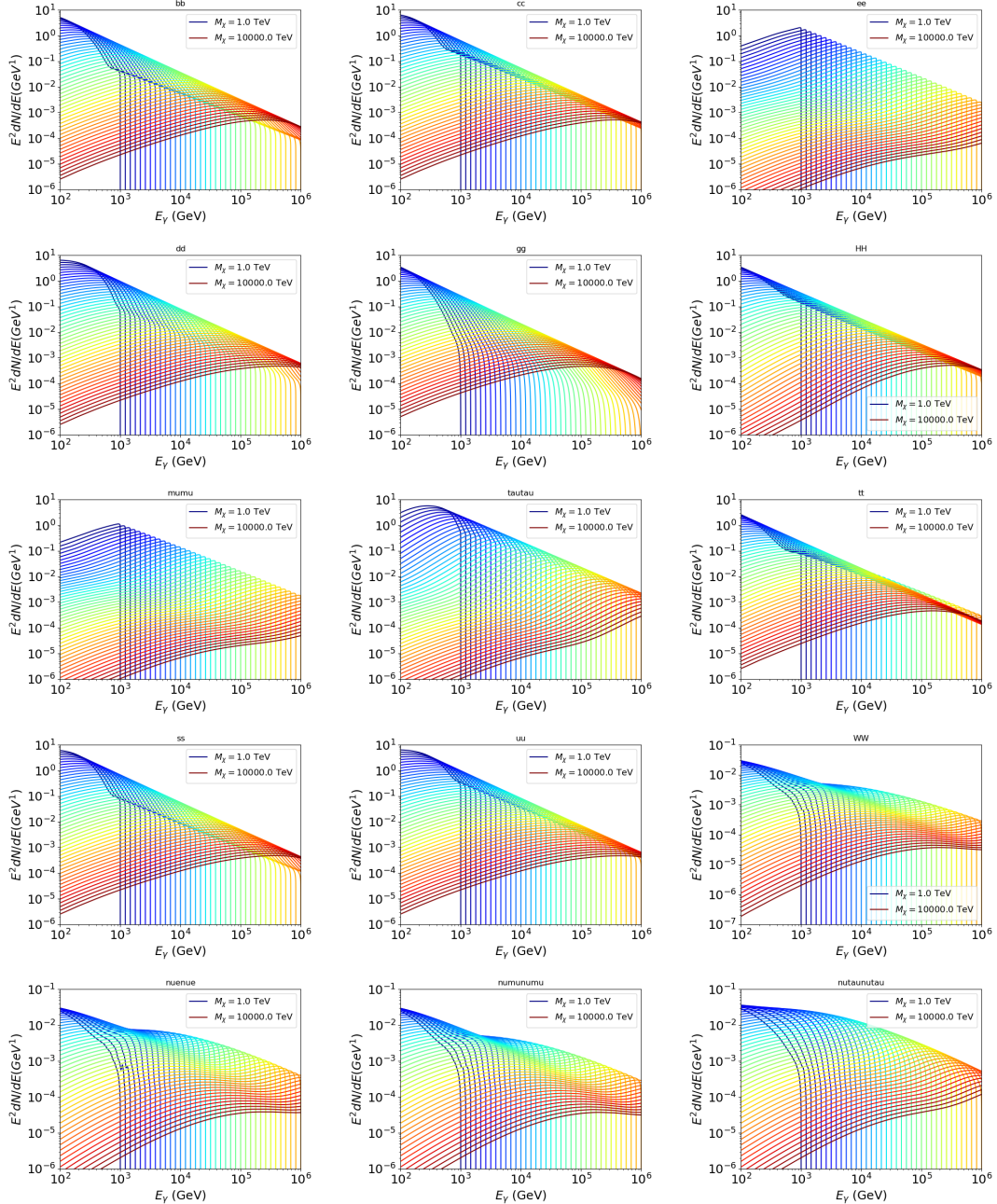


Figure B.1 Sister figure to Figure 6.2 for remaining SM primary annihilation channels studied for this thesis. These did not require any post generation smoothing and so are directly pulled from [79] with a binning scheme most helpful for a HAWC analysis.

2065 **B.2 mpu_analysis.py**

```
20661 import warnings
20672 with warnings.catch_warnings():
20683     warnings.simplefilter("ignore")
20694 # Python base libraries
20705 import os
20716 import sys
20727 import time
20738 # Import general libraries with namespace
20749 import matplotlib
20750 # Necessary for computing on cluster
20761 matplotlib.use("agg")
20772 import numpy as np
20783 import multiprocessing as mp
20794 # Import HAWC software
20805 sys.path.insert(1, os.path.join(os.environ['HOME'], 'hawc_software', 'threeML-
2081     analysis-scripts', 'fitModel'))
20826 from analysis_modules import *
20837 from threeML import *
20848 from hawc_hal import HAL, HealpixConeROI
20859 from threeML.minimizer.minimization import FitFailed
20860 # Import Dark Matter HAWC Libraries
20871 import analysis_utils as au
20882 import spectra as spec
20893 import sources as srcs
20904
20915 #* READ ONLY PATHS This block will change eventually
20926 MASS_LIST = './plotting/studies/nd/masses.txt'
20937 CHAN_LIST = './plotting/studies/nd/chans.txt'
20948
20959 #* WRITE PATHS, default location is to scratch
20960 OUT_PATH = os.path.join(os.environ["SCRATCH"], os.environ["USER"], 'New_duck')
```

```

20971 print('Our out path is going to be {}'.format(OUT_PATH))
20982
20993 # Define parallel Function. Can also be run serially
21004 def some_mass_fit(sigVs, datalist, shape, dSph, jfactor, mass_chan,
21015                 progress=None, log_file='', queue=None, i_job=0):
21026
21037     if progress is None:
21048         progress = [0]
21059     else: # Create log files for each thread
21060         log_file = log_file.replace('.log', '_ThreadNo_')
21071         log_file = log_file + str(i_job) + ".log"
21082         sys.stdout = open(log_file, "w")
21093
21104     fits = []
21115
21126     try:
21137         for m_c in mass_chan:
21148             print(f'Mass chan tuple: {m_c}')
21159             mass = int(m_c[0])
21160             ch = m_c[1]
21171             # Build path to output files
21182             outPath = os.path.join(OUT_PATH, ch, dSph)
21193             au.ut.ensure_dir(outPath)
21204
21215             if progress[i_job] < 0:
21226                 # If the master gets a Keyboard interrupt, commit suicide.
21237                 break
21248
21259                 ### Start Model Building for DM mass and SM channel #####
21260                 spectrum = spec.DM_models.HDMSpectra()
21271                 spectrum.set_channel(ch)
21282
21293                 myDwarf = ExtendedSource(dSph, spatial_shape=shape,

```

```

21304                     spectral_shape=spectrum)
21315
21326             spectrum.J = jfactor * u.GeV**2 / u.cm**5
21337             spectrum.sigmav = 1e-24 * u.cm**3 / u.s
21348             spectrum.set_dm_mass(mass * u.GeV)
21359
21360             spectrum.sigmav.bounds = (1e-30, 1e-12)
21371             model = Model(myDwarf)
21382             ##### End model Building #####
21393
21404             jl = JointLikelihood(model, datalist, verbose=False)
21415
21426             try:
21437                 result, lhdf = jl.fit(compute_covariance=False)
21448                 ts = -2.* (jl.minus_log_like_profile(1e-30) - jl.
2145 _current_minimum)
21469                 # Also profile the LLH vs sv
21470                 ll = jl.get_contours(spectrum.sigmav, sigVs[0],
21481                               sigVs[-1], len(sigVs),
21492                               progress=False, log=['False'])
21503
21514                 sigv_ll = au.ut.calc_95_from_profile(ll[0], ll[2])
21525                 # Write results to file
21536                 outFileLL = outPath+f"/LL_{dSph}_{ch}_mass{int(mass)}_GD.txt"
21547                 np.savetxt(outFileLL, (sigVs, ll[2]),
21558                               delimiter='\t', header='sigV\tLL\n')
21569
21570                 with open(outPath+f"/results_{dSph}_{ch}_mass{int(mass)}_GD.
2158 txt", "w") as results_file:
21591                     results_file.write("mDM [GeV]\tsigV_95\tsigV_B.F.\n")
21602
21613                     results_file.write("%i\t%.5E\t%.5E\t%.5E"%(mass, sigv_ll,
21624                                         ts, result.value[0]))

```

```

21635         # End write to file
21646     except FitFailed: # Don't kill all threads if a fit fails
21657         print("Fit failed. Go back and calculate this spectral model
2166     later")
21678             fits.append((ch, mass, -1, -1))
21689             with open(log_file+'.fail', 'w') as f_file:
21690                 f_file.write(f'{ch}, {mass}\n')
21701
21712             progress[i_job] += 1
21723             matplotlib.pyplot.close() # Prevent leaky memory
21734
21745             fits.append((ch, mass, result.value[0], ts))
21756             progress[i_job] += 1
21767             matplotlib.pyplot.close()
21778     except KeyboardInterrupt:
21789         progress[i_job] = -1
21790
21801     fits = np.array(fits)
21812     if queue is None:
21823         return fits
21834     else:
21845         queue.put((i_job, fits))
21856
21867 def main(args):
21878     masses = np.loadtxt(MASS_LIST, dtype=int)
21889     chans = np.loadtxt(CHAN_LIST, delimiter=',', dtype=str)
21890     mass_chan = au.ut.permute_lists(chans, masses)
21901
21912     print(f"DM masses for this study are: {masses}")
21923     print(f"SM Channels for this study are XX -> {chans}")
21934     print(mass_chan)
21945
21956     # extract information from input argument

```

```

2196    dSph = args.dSph
2197    data_mngr = au.ut.Data_Selector('P5_NN_2D')
2198    dm_profile = srcts.Spatial_DM(args.catalog, dSph, args.sigma, args.decay)
2199
2200    ### Extract Source Information ####
2201    if dm_profile.get_dec() < -22.0 or dm_profile.get_dec() > 62.0:
2202        raise ValueError("HAWC can't see this source D: Exitting now...")
2203
2204    print(f'{dSph} information')
2205    print(f'jfac: {dm_profile.get_factor()}\tRA: {dm_profile.get_ra()}\tDec: {dm_profile.get_dec()}\n')
2206
2207
2208    shape = SpatialTemplate_2D(fits_file=dm_profile.get_src_fits())
2209    ### Finish Extract Source Information ####
2210
2211    ### LOAD HAWC DATA ####
2212    roi = HealpixConeROI(data_radius=2.0, model_radius=8.0,
2213                           ra=dm_profile.get_ra(), dec=dm_profile.get_dec())
2214    bins = choose_bins.analysis_bins(args, dec=dm_profile.get_dec())
2215
2216    hawc = HAL(dSph, data_mngr.get_datmap(), data_mngr.get_detres(), roi)
2217    hawc.set_active_measurements(bin_list=bins)
2218    datalist = DataList(hawc)
2219    ### FINISH LOAD HAWC DATA ####
2220
2221    # set up SigV sampling. This sample is somewhat standardized
2222    sigVs = np.logspace(-28,-18, 1001, endpoint=True) # NOTE This will change
2223    whith HDM
2224
2225    if args.n_threads == 1:
2226        # No need to start || programming just iterate over the masses
2227        kw_arg = dict(sigVs=sigVs, datalist=datalist, shape=shape, dSph=dSph,
2228                      jfactor=dm_profile.get_factor(), mass_chan=mass_chan,

```

```

22298                 log_file=args.log)
22309             some_mass_fit(**kw_arg)
22310         else:
22311             # I Really want to suppress TQMD output
22312             from tqdm import tqdm
22313             from functools import partialmethod
22314             tqdm.__init__ = partialmethod(tqdm.__init__, disable=True)
22315
22316             x = np.array_split(mass_chan, args.n_threads)
22317             n_jobs = len(x)
22318
22319             print("Thread jobs summary by mass and SM channel")
22320             for xi in x:
22321                 print(f'{xi}')
22322
22323             queue = mp.Queue()
22324             progress = mp.Array('i', np.zeros(n_jobs, dtype=int))
22325
22326             # Define task pool that will be split amongsts threads
22327             kw_args = [dict(sigVs=sigVs, datalist=datalist, shape=shape,
22328                             dSph=dSph, jfactor=dm_profile.get_factor(),
22329                             mass_chan=mass_chan, progress=progress,
22330                             queue=queue, i_job=i, log_file=args.log)
22331                     for i, mass_chan in enumerate(x)]
22332
22333             # Define each process
22334             procs = [mp.Process(target=some_mass_fit, kwargs=kw_args[i]) \
22335                     for i in range(n_jobs)]
22336
22337             ### Start MASTER Thread only code block ###
22338             # Begin running all child threads
22339             for proc in procs: proc.start()
22340

```

```

22621     try:
22622
22623         # In this case, the master does nothing except monitor progress of
22624         the threads
22625
22626         # In an ideal world, the master thread also does some computation.
22627         n_complete = np.sum(progress)
22628
22629         while_count = 0
22630
22631
22632         while n_complete < len(mass_chan):
22633
22634
22635             if np.any(np.asarray(progress) < 0):
22636
22637                 # This was no threads are stranded when killing the script
22638
22639                 raise KeyboardInterrupt()
22640
22641             if while_count%1000 == 0:
22642
22643                 print(f'{np.sum(progress)} of {len(mass_chan)} finished')
22644
22645
22646             n_complete = np.sum(progress)
22647
22648             time.sleep(.25)
22649
22650             while_count += 1
22651
22652
22653
22654             except KeyboardInterrupt:
22655
22656                 # signal to jobs that it's time to stop
22657
22658                 for i in range(n_jobs):
22659
22660                     progress[i] = -2
22661
22662                     print('\nKeyboardInterrupt: terminating early.')
22663
22664             ### End MASTER Thread only code block ###
22665
22666
22667             fitss = [queue.get() for proc in procs]
22668
22669             print(fitss)
22670
22671             print(f'Thread statuses: {progress[:]}')
22672
22673
22674             # putting results in a file
22675
22676
22677             print("QUACK! All Done!")

```

```

22953
22964
22975 if __name__ == '__main__':
22986     import argparse
22997
23008     p = argparse.ArgumentParser(description="Run a DM annihilation analysis on
2301         a dwarf spheroidal for a specific SM channel for DM masses [1 TeV to 10
2302         PeV]")
23039
23040     # Dwarf spatial modeling arguements
23051     p.add_argument("-ds", "--dSph", type=str,
23062                     help="dwarf spheroidal galaxy to be studied", required=
2307     True)
23083     p.add_argument("-cat", "--catalog", type=str, choices=['GS15', 'LS20'],
23094                     default='LS20', help="source catalog used")
23105     p.add_argument("-sig", "--sigma", type=int, choices=[-1, 0, 1], default=0,
23116                     help="Spatial model uncertainty. 0 corresponds to the
2312 median. +/-1 correspond to the +/-1sigma uncertainty respectively.")
23137
23148     # Arguements for the energy estimators
23159     p.add_argument("-e", "--estimator", type=str,
23160                     choices=['P5_NHIT', 'P5_NN_2D'],
23171                     default="P5_NN_2D", required=False,
23182                     help="The energy estimator choice. Options are: P5_NHIT,
2319 P5_NN_2D. GP not supported (yet).")
23203     p.add_argument("--use-bins", default=None, nargs="*",
23214                     help="Bins to use for the analysis", dest="use_bins")
23225     p.add_argument('--select_bins_by_energy', default=None, nargs="*",
23236                     help="Does nothing. May fill in later once better
2324 understood")
23257     p.add_argument('--select_bins_by_fhit', default=None, nargs="*",
23268                     help="Also does nothing see above")
23279     p.add_argument( '-ex', '--exclude', default=None, nargs="*",

```

```

23280         help="Exclude Bins", dest="exclude")

23291

23302 # Computing and logging arguements.

23313 p.add_argument('-nt', '--n_threads', type=int, default=1,
23324                         help='Maximum number of threads spawned by script. Default
23335 is 4')

23345 p.add_argument('-log', '--log', type=str, required=True,
23356                         help='Name for log files. Especially needed for threads')

23367

23378 p.add_argument('--decay', action="store_true",
23389                         help='Set spectral DM hypothesis to decay')

23390

23401 args = p.parse_args()

23412 print(args.decay)

23423 if args.exclude is None: # default exclude bins 0 and 1
23434     args.exclude = ['B0C0Ea', 'B0C0Eb', 'B0C0Ec', 'B0C0Ed', 'B0C0Ee']

23445

23456 if args.decay: OUT_PATH += '_dec'
23467 else: OUT_PATH += '_ann'

23478

23489 OUT_PATH = OUT_PATH + '_' + args.catalog
23490 if args.sigma != 0: OUT_PATH += f'_{args.sigma}sig'

23501

23512 main(args)

```

2352 B.3 Comparison with Glory Duck

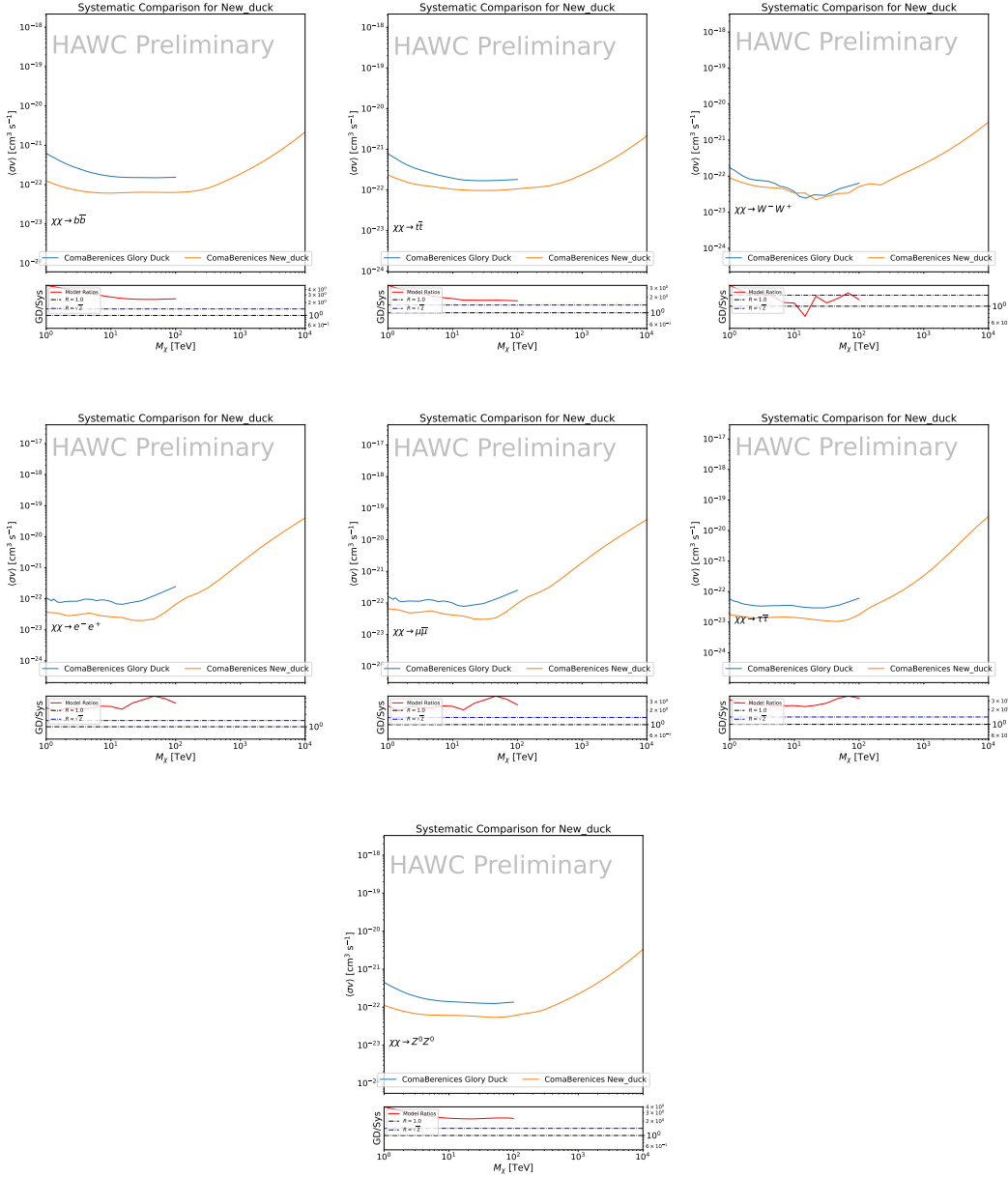


Figure B.2 Comparison of HAWC limits from this analysis to Glory Duck (Fig. 5.5) for Coma Berenices and 7 DM annihilation channels.

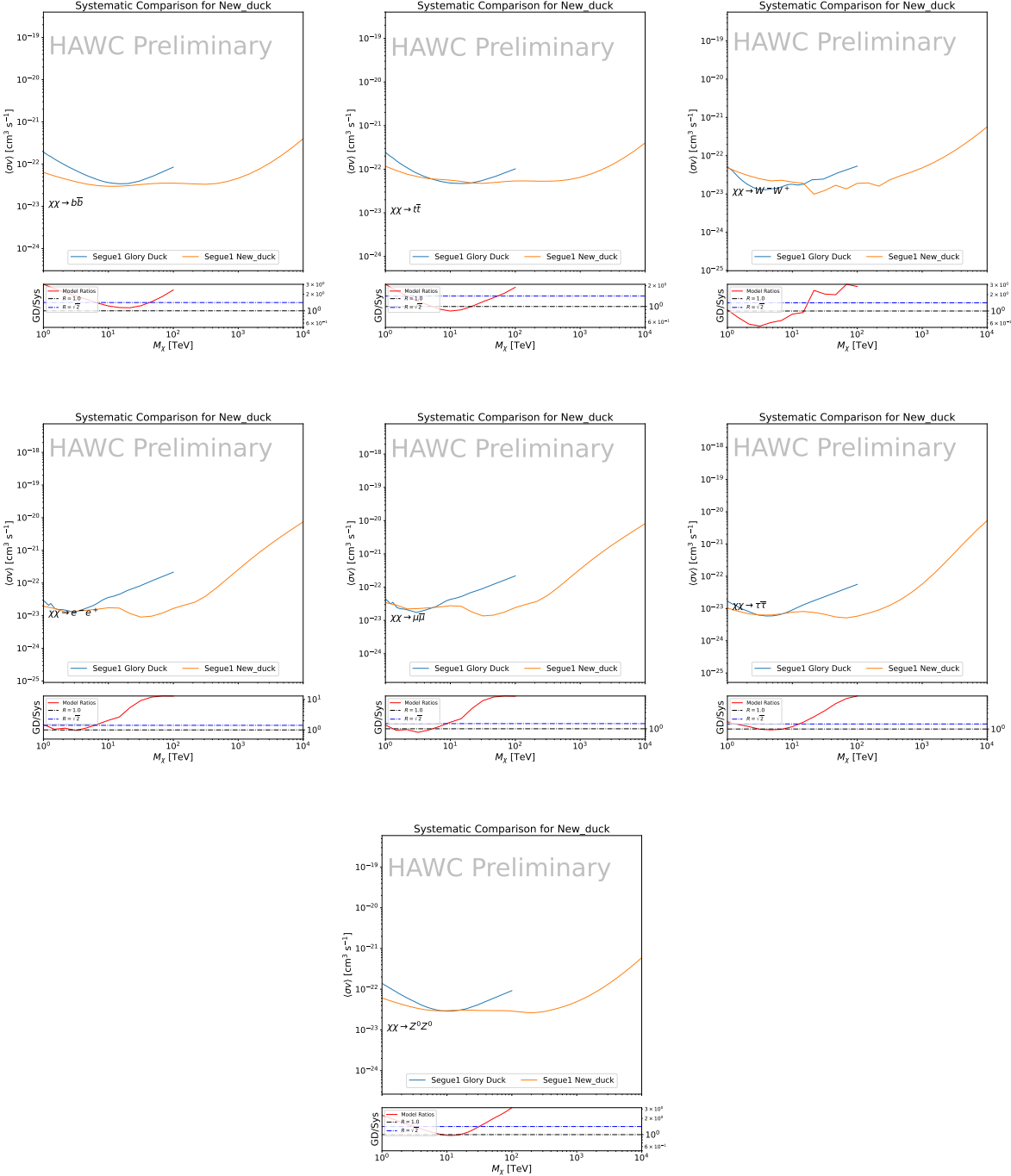


Figure B.3 Same as Fig. B.2 but for Segue 1.

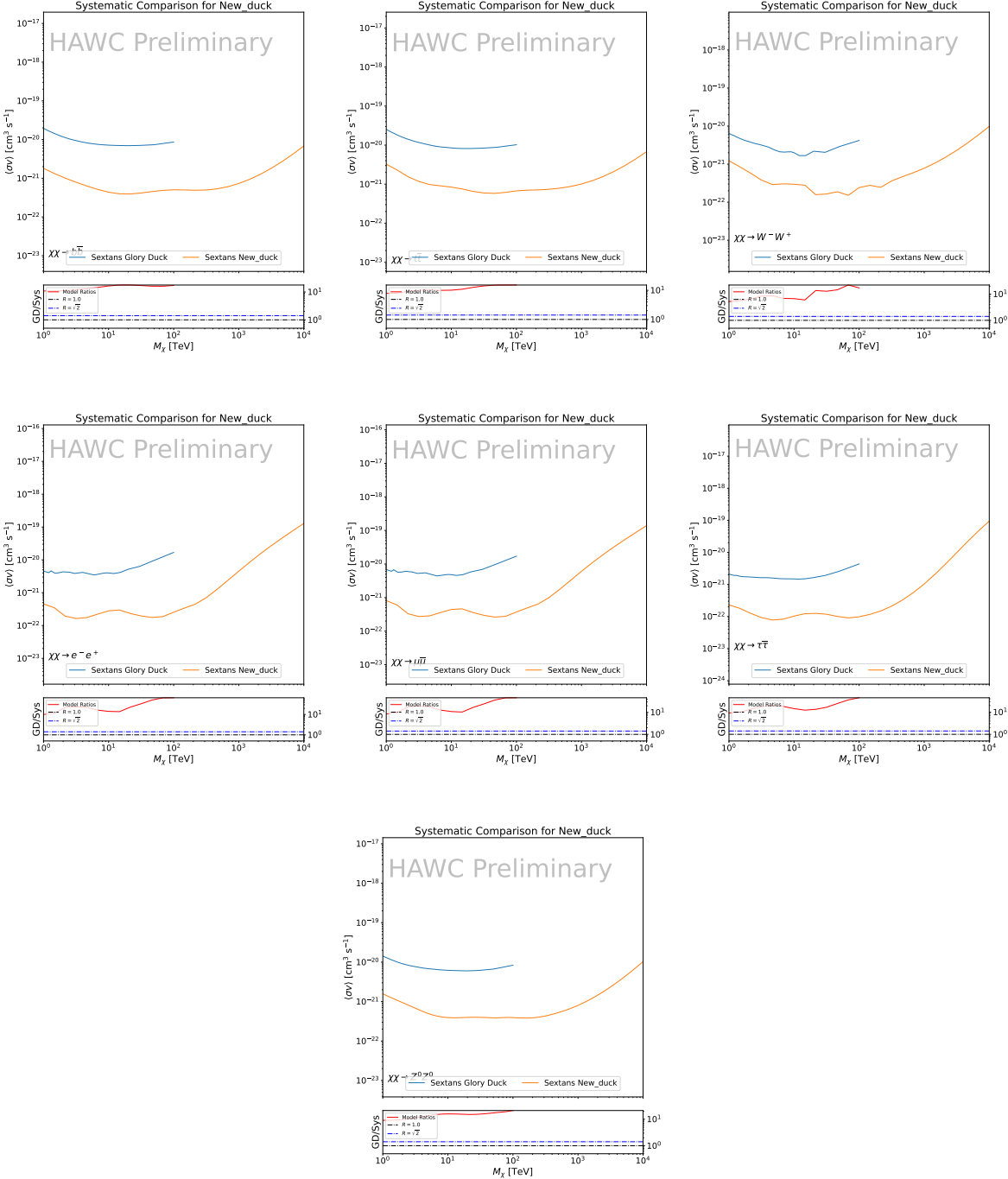


Figure B.4 Same as Fig. B.2 but for Sextans.

APPENDIX C

2353 ICECUBE HEAVY DARK MATTER ANALYSIS SUPPLEMENTARY MATERIAL

2354 C.1 Docker Image for Oscillating Neutrino Spectra

```
2355 1 FROM ubuntu:18.04
2356 2
2357 3 # Execute commands to install software packages
2358 4 RUN apt -y update
2359 5
2360 6     # Install utility programs
2361 7 RUN apt -y install vim wget git cmake
2362 8
2363 9 ARG DEBIAN_FRONTEND=noninteractive
2364 0
2365 1     # Install python
2366 2 RUN apt -y install python python-dev python-pip libjpeg-dev zlib1g-dev
2367 3
2368 4     # We need Python2 for installing Charon.
2369 5 RUN apt -y install python-numpy python-sympy python-matplotlib \
2370 6             python-sympy python-h5py python-astropy python-ipython
2371 7
2372 8     # Install dependencies of Charon : SQuIDS, NuSQuIDS
2373 9 RUN apt -y install libgsl-dev libgslcblas0 libgsl23 gsl-bin pkg-config
2374 0     # Install SQuIDS
2375 1 RUN mkdir /home/SQuIDS /home/SQuIDS_install
2376 2 WORKDIR /home/SQuIDS
2377 3 RUN git clone https://github.com/jsalvado/SQuIDS.git
2378 4 WORKDIR /home/SQuIDS/SQuIDS
2379 5 RUN git checkout 7ad9ba7c6ad06d1f0fa8418f937ebf1a403fef90
2380 6     # Before executing "make install" an environmental variable has to be set.
2381 7 ENV PKG_CONFIG_PATH=/home/SQuIDS/SQuIDS/lib
2382 8 RUN ./configure --prefix=../SQuIDS_install \
```

```

23839     && make
23840 RUN make install
23851
23862 # Set up an environmental variable that is required to install nuSQuIDS..
23873 ENV SQuIDS=/home/SQuIDS/SQuIDS
23884 ENV LD_LIBRARY_PATH=$SQuIDS/lib:$LD_LIBRARY_PATH
23895
23906 # Install NuSQuIDS
23917 RUN mkdir /home/nuSQuIDS
23928 WORKDIR /home/nuSQuIDS
23939 RUN git clone https://github.com/qrliu/nuSQuIDS.git
23940 WORKDIR /home/nuSQuIDS/nuSQuIDS
23951 RUN git checkout 072d8ef740e2fc7330f1fabaea94f0f4540c46f9
23962 RUN apt -y install libhdf5-dev hdf5-tools
23973 RUN apt -y install libboost1.65-all-dev
23984 RUN ./configure --with-squids=$SQuIDS --with-python-bindings --prefix=../
2399     nuSQuIDS_install \
24005     && make \
24016     && make install
24027
24038 # Set up an environmental variable for nuSQuIDS.
24049 ENV nuSQuIDS=/home/nuSQuIDS/nuSQuIDS
24050 ENV LD_LIBRARY_PATH=$nuSQuIDS/lib:$LD_LIBRARY_PATH
24061
24072 # Build the python bindings
24083 WORKDIR /home/nuSQuIDS/nuSQuIDS/resources/python/src
24094 RUN make
24105
24116 # Set up an environmental variable for the python bindings.
24127 ENV PYTHONPATH=$nuSQuIDS/resources/python/bindings/:$PYTHONPATH
24138
24149 # Install Charon in the /home/Charon/charon directory.
24150 RUN mkdir /home/Charon

```

```
24161 WORKDIR /home/Charon
24162 RUN git clone https://github.com/icecube/charon.git \
24163     && apt -y install unzip python-scipy
24164 WORKDIR charon
24165 RUN git checkout c531efe4e01dc364a60d1c83f950f04526ccd771
24166 RUN unzip ./charon/xsec/xsec.zip -d charon/xsec/ \
24167
24168 # Download neutrino spectra tables in the /home/Charon/charon/data directory
24169 .
24170     && mkdir ./charon/data
24171 WORKDIR ./charon/data
24172 RUN wget --no-check-certificate https://icecube.wisc.edu/~qliu/charon/
24173     SpectraEW.hdf5 \
24174     && wget --no-check-certificate https://icecube.wisc.edu/~qliu/charon/
24175     Spectra_PYTHIA.hdf5 \
24176     && wget --no-check-certificate https://icecube.wisc.edu/~qliu/charon/
24177     Spectra_noEW.hdf5
24178
24179 WORKDIR ../..
24180 RUN python setup.py install
24181 WORKDIR /home
```

2437 C.2 Spline Fitting Statuses

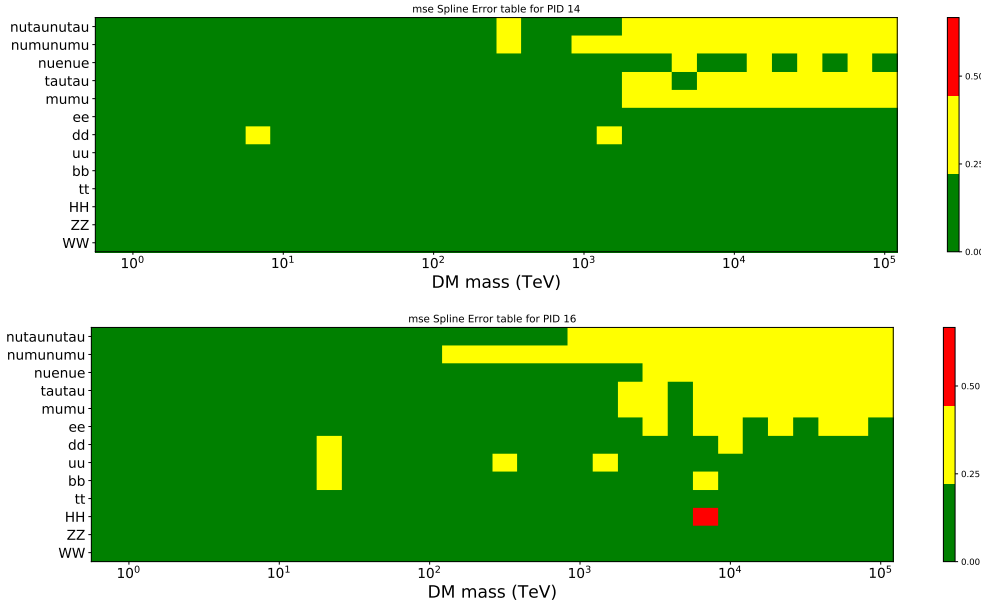


Figure C.1 Current status of spline tables according to constraints defined by Tab. 7.1. Green splines are splines that passed under the GOOD tolerance. Yellow are splines that are OK. Red are splines that FAIL. All yellow splines were inspected individually before running the analysis. Splines were made for the μ (PID 14; top panel) flavor and τ (PID 16; bottom panel) neutrino flavors.

2438 C.3 Neutrino Composite Spectra

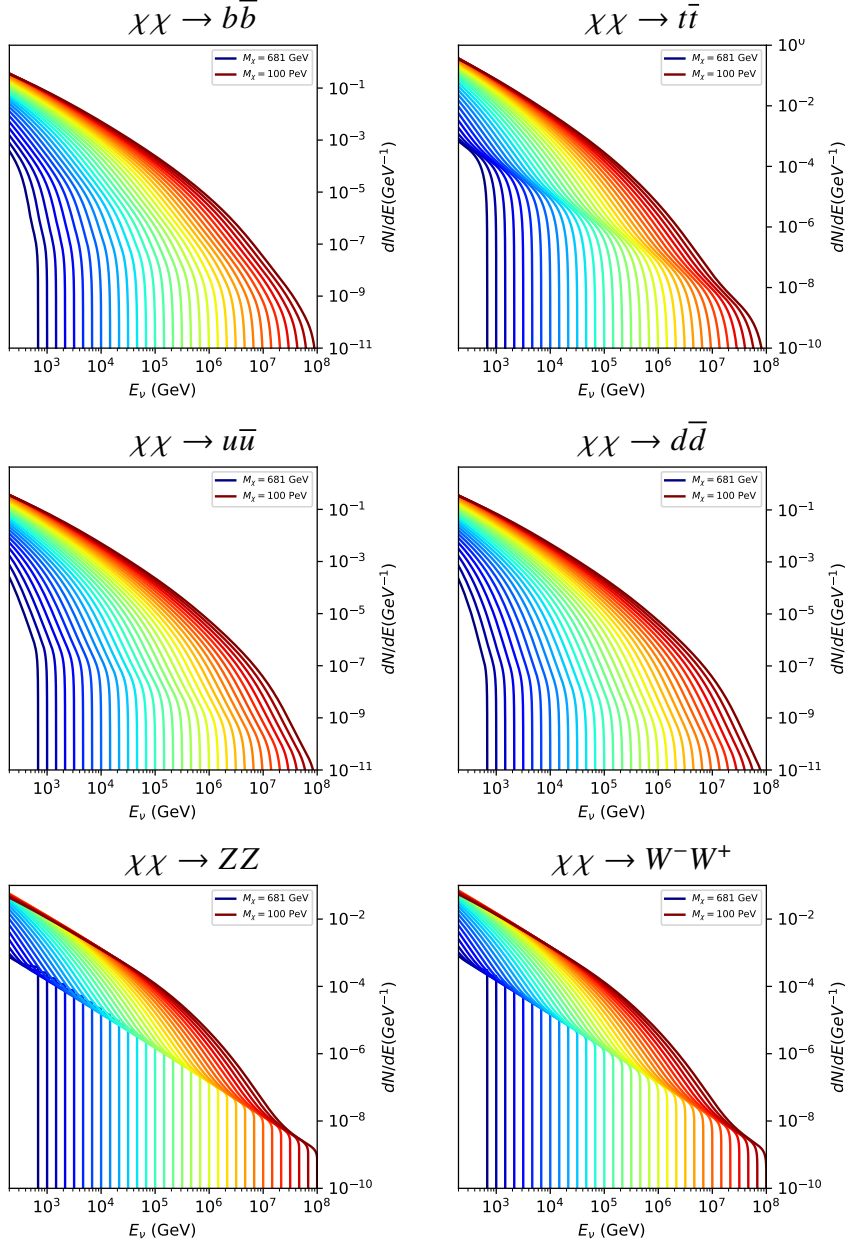


Figure C.2 Sister figure to Fig. 7.5 for annihilation channels that did not require kernel smoothing. These spectra are the composite ($\nu_\mu + \nu_\tau$) of neutrino flavors. Every spectral model used for this analysis is featured as a colored solid line. Bluer lines are for lower DM mass spectral models. DM masses range from 681 GeV to 100 PeV.

2439 C.4 Segue 1 And Ursa Major II Signal Recovery

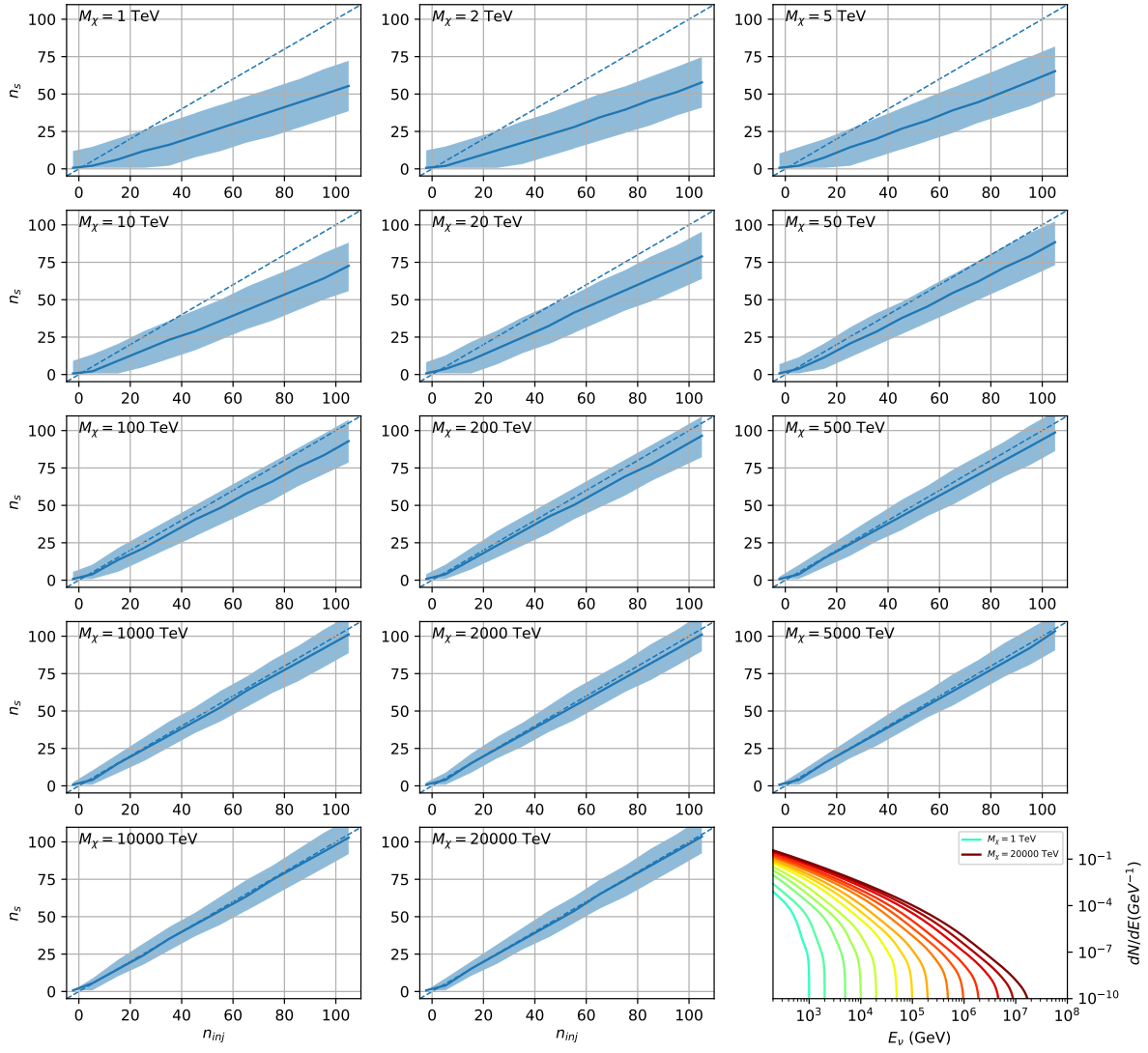


Figure C.3 Same as Fig. 7.23 but for Segue 1 and $\chi\chi \rightarrow b\bar{b}$.

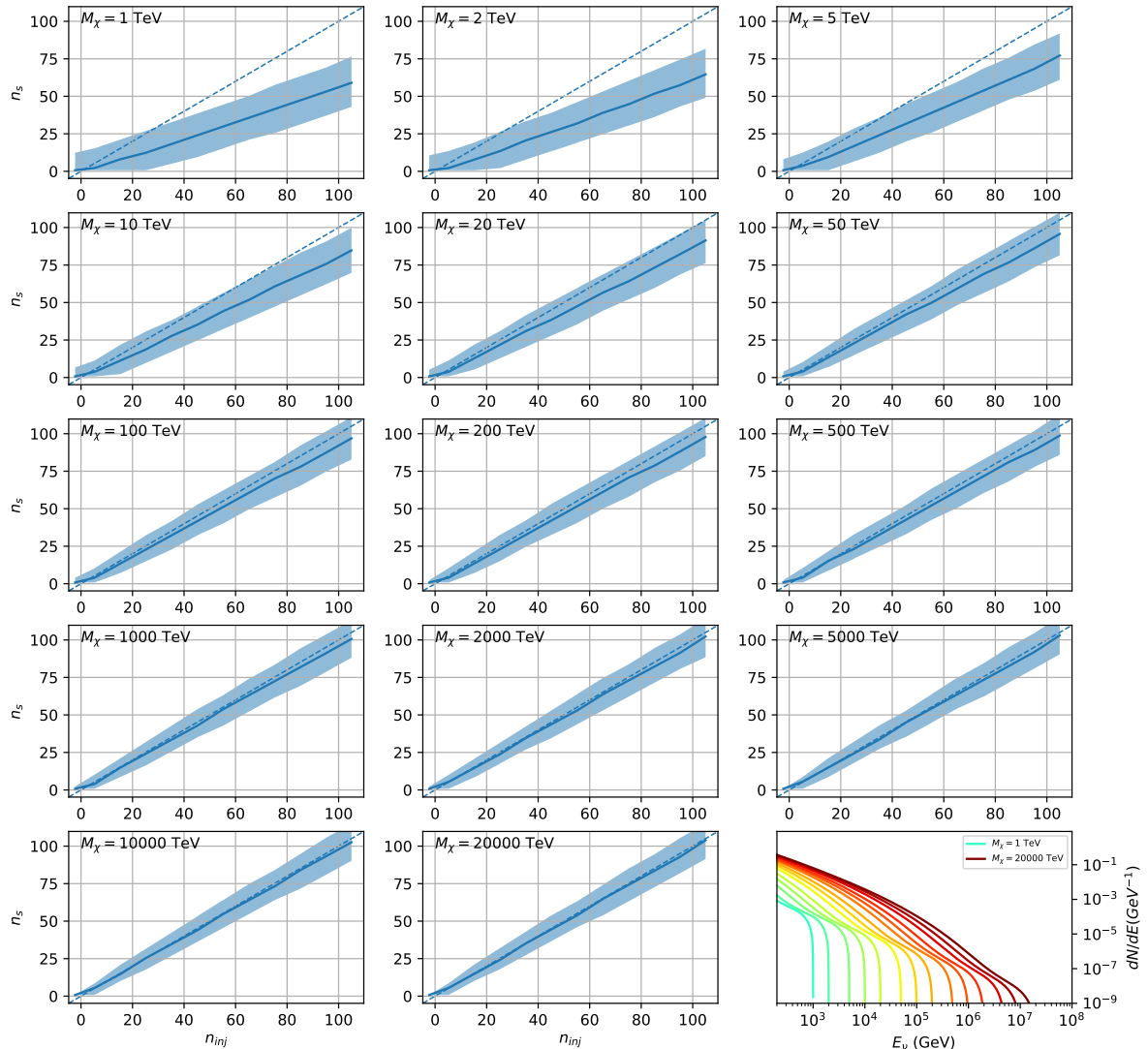


Figure C.4 Same as Fig. 7.23 but for Segue 1 and $\chi\chi \rightarrow t\bar{t}$.

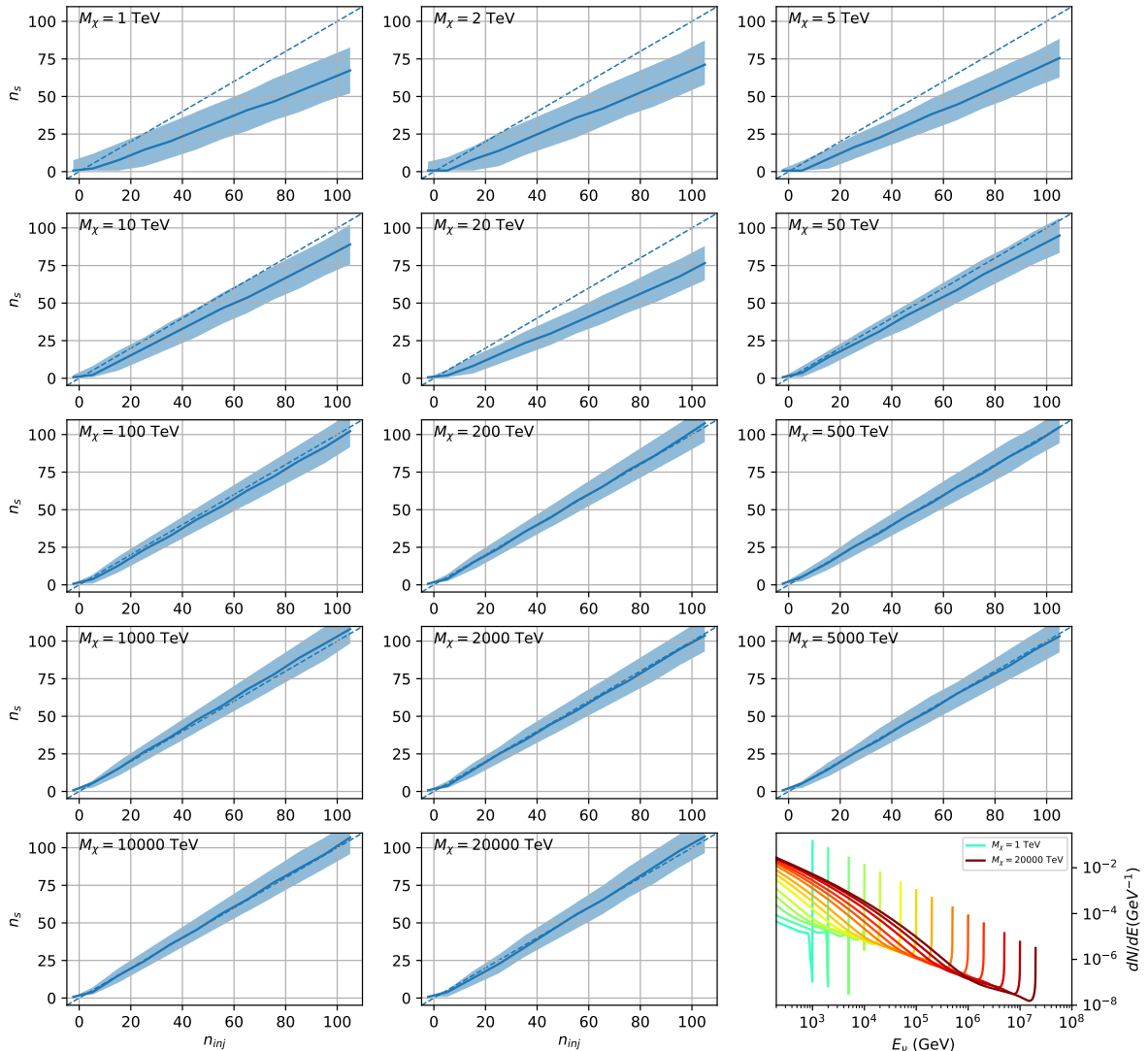


Figure C.5 Same as Fig. 7.23 but for Segue 1 and $\chi\chi \rightarrow \nu_\mu \bar{\nu}_\mu$.

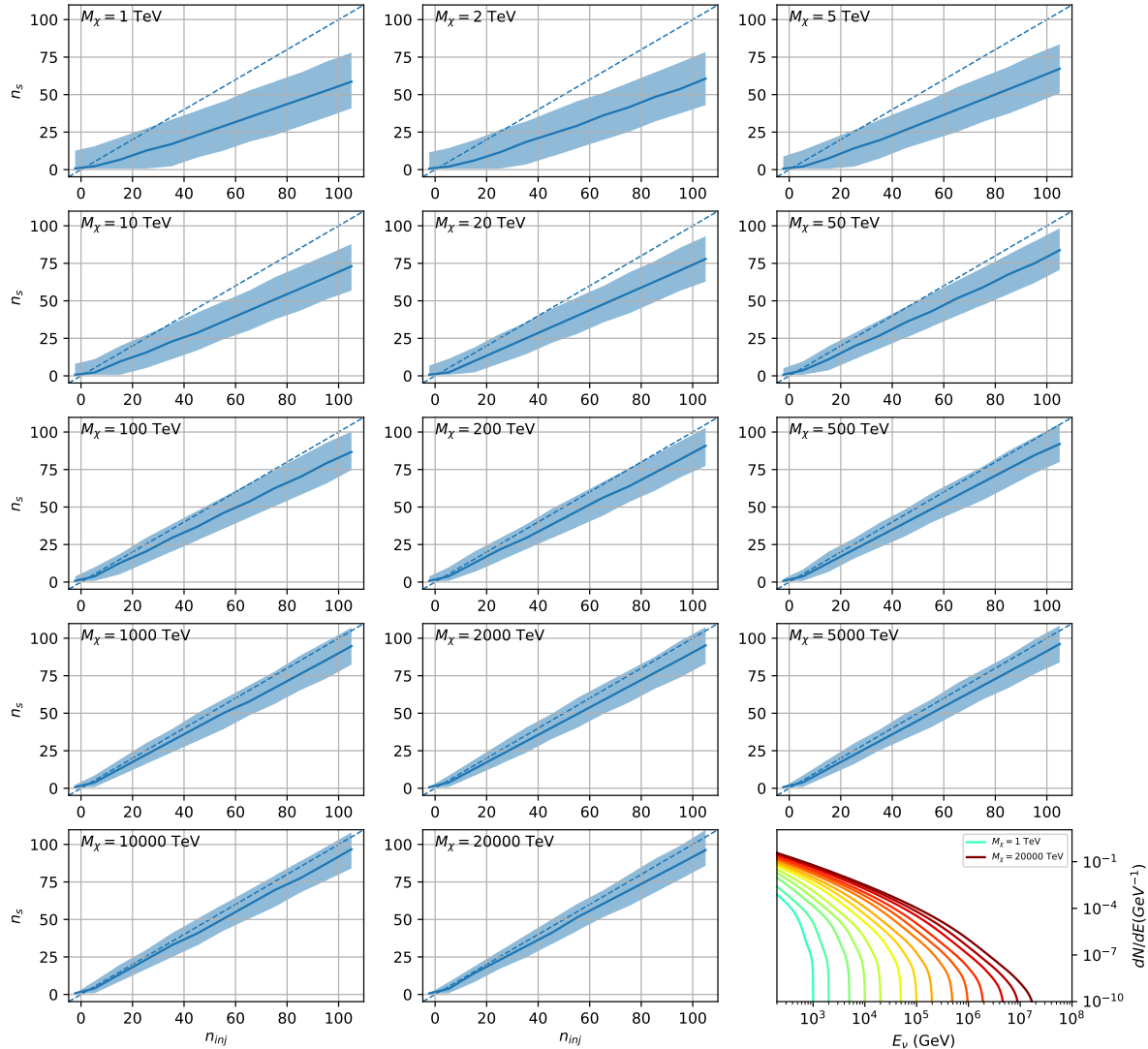


Figure C.6 Same as Fig. 7.23 but for Ursa Major II and $\chi\chi \rightarrow b\bar{b}$.

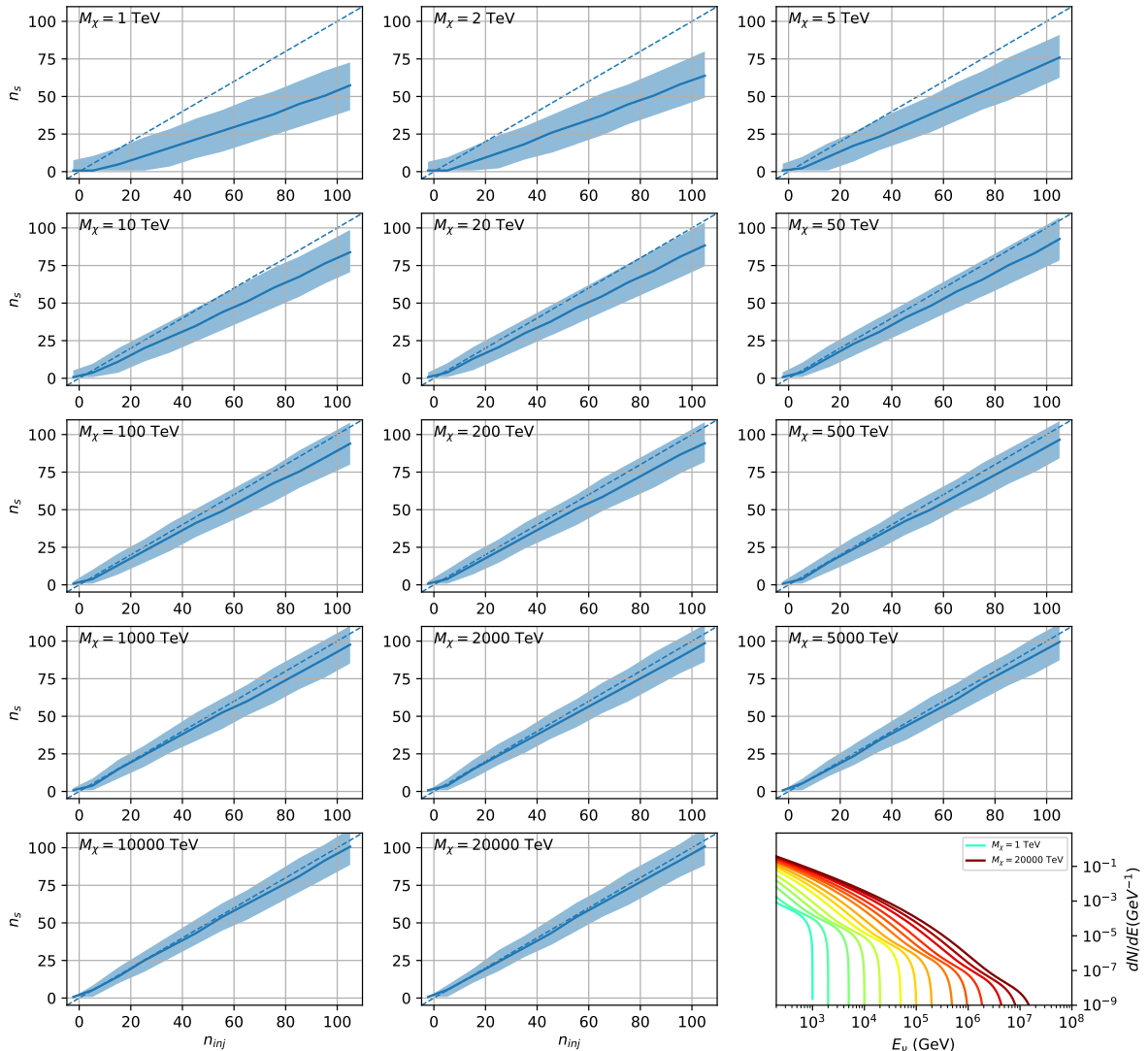


Figure C.7 Same as Fig. 7.23 but for Ursa Major II and $\chi\chi \rightarrow t\bar{t}$.

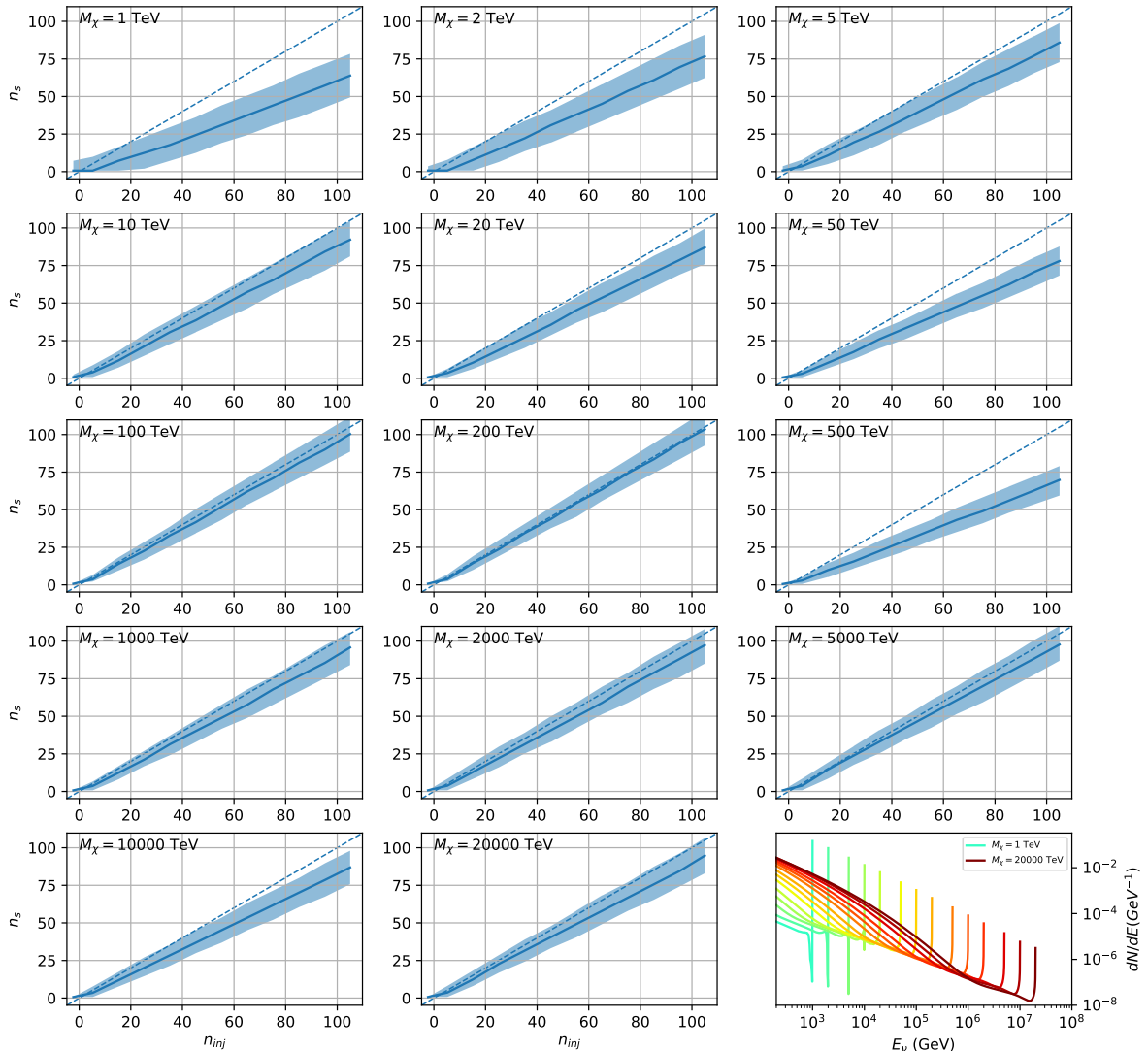


Figure C.8 Same as Fig. 7.23 but for Ursa Major II and $\chi\chi \rightarrow \nu_\mu \bar{\nu}_\mu$.

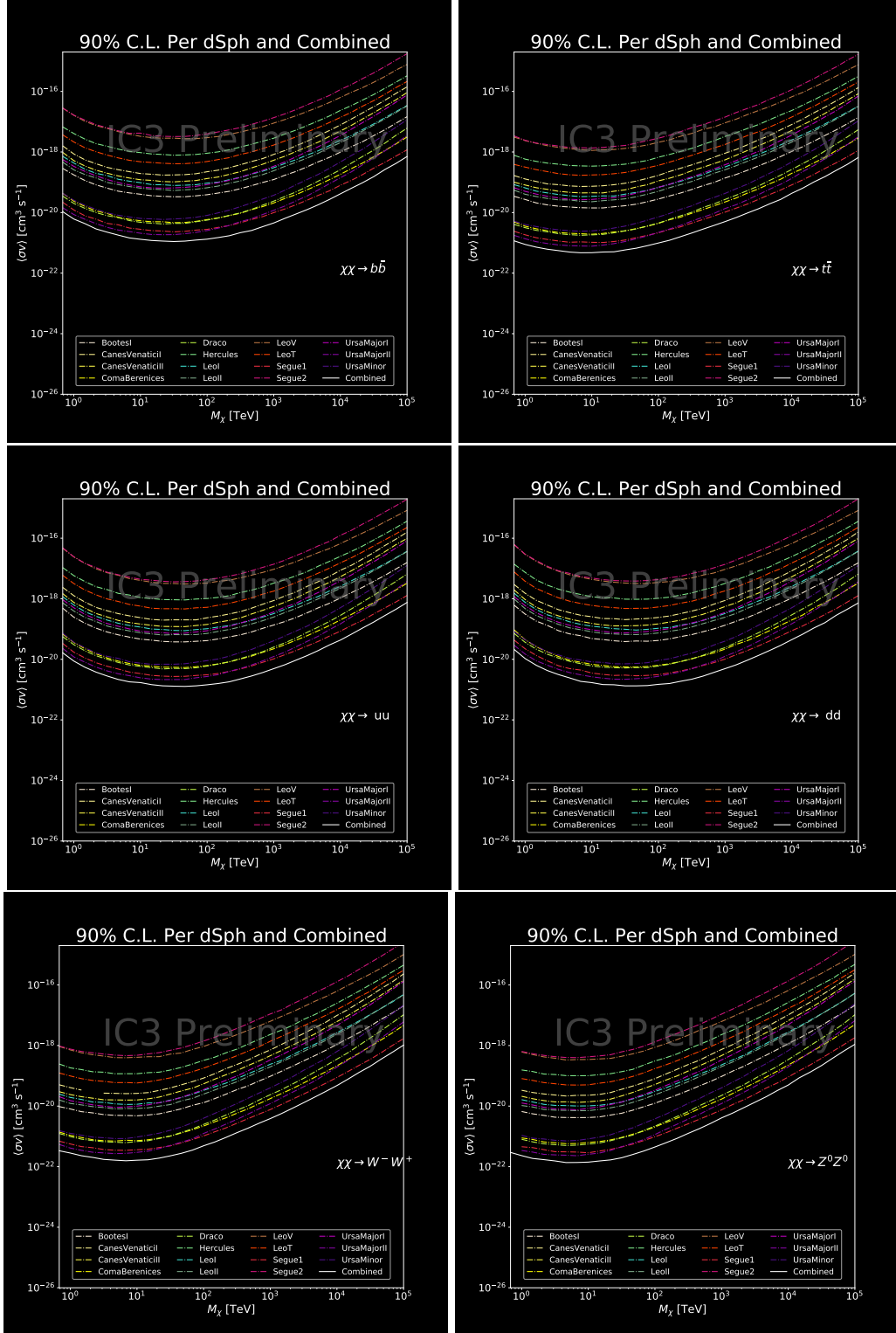


Figure C.9 IceCube North Sky Track Sensitivities for $n_s/\langle N \rangle$. n_s values are the counts fed into Eq. (7.8) to produce Fig. 7.26 and Fig. 7.25.

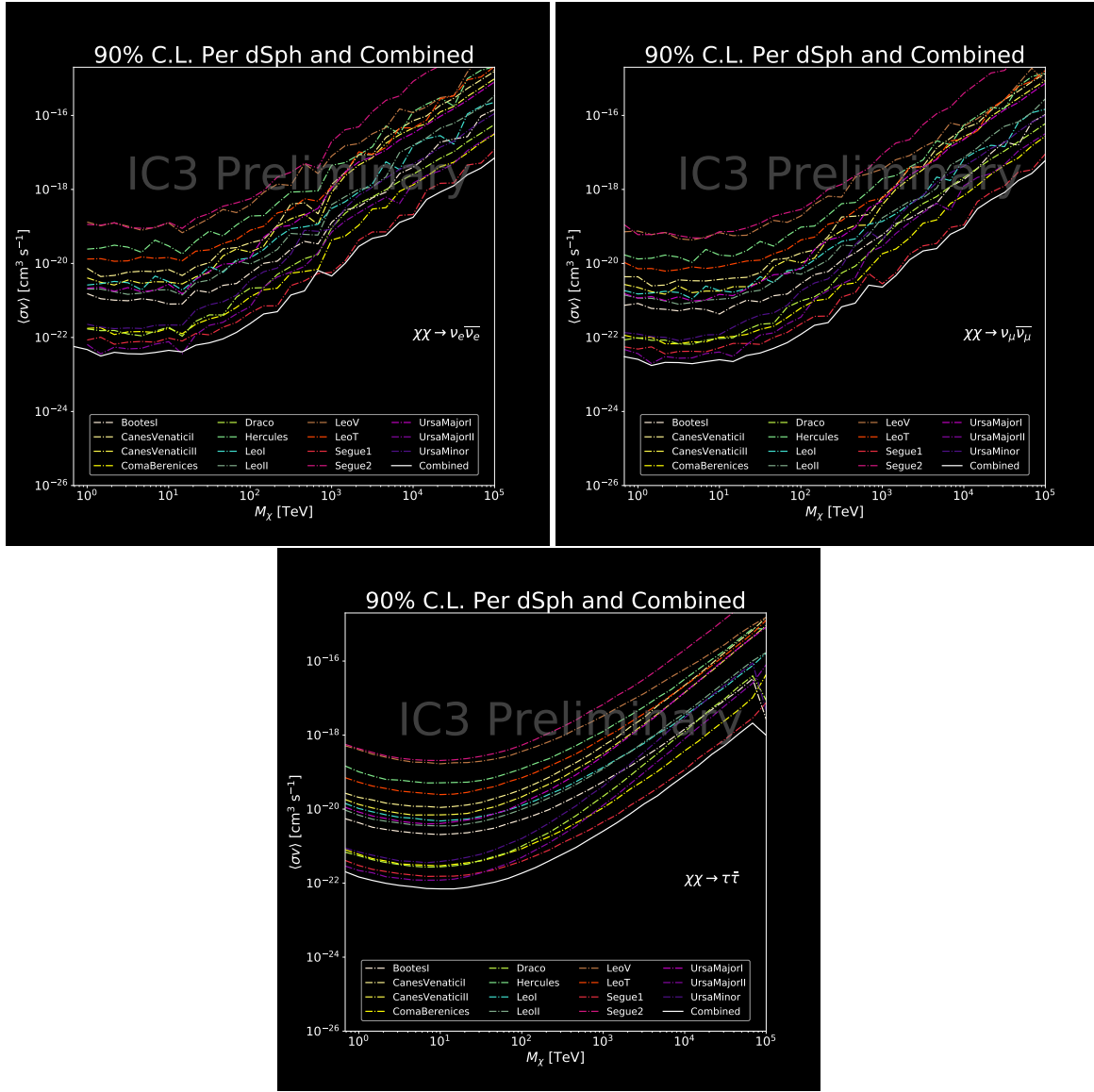


Figure C.10 Same as Fig. C.9 for three additional DM annihilation channels.

BIBLIOGRAPHY

- 2442 [1] Anne M. Green. “Dark matter in astrophysics/cosmology”. In: *SciPost Phys. Lect.*
 2443 *Notes* (2022), p. 37. doi: [10.21468/SciPostPhysLectNotes.37](https://doi.org/10.21468/SciPostPhysLectNotes.37). URL: <https://scipost.org/10.21468/SciPostPhysLectNotes.37>.
- 2445 [2] Bing-Lin Young. “A survey of dark matter and related topics in cosmology”. In: *Frontiers*
 2446 *of Physics* 12 (Oct. 2016). doi: <https://doi.org/10.1007/s11467-016-0583-4>.
 2447 URL: <https://doi.org/10.1007/s11467-016-0583-4>.
- 2448 [3] Gianfranco Bertone, Dan Hooper, and Joseph Silk. “Particle dark matter: evidence,
 2449 candidates and constraints”. In: *Physics Reports* 405.5 (2005), pp. 279–390. ISSN:
 2450 0370-1573. doi: <https://doi.org/10.1016/j.physrep.2004.08.031>. URL:
 2451 <https://www.sciencedirect.com/science/article/pii/S0370157304003515>.
- 2452 [4] Gianfranco Bertone and Dan Hooper. “History of dark matter”. In: *Rev. Mod. Phys.*
 2453 90 (4 Aug. 2018), p. 045002. doi: [10.1103/RevModPhys.90.045002](https://doi.org/10.1103/RevModPhys.90.045002). URL: <https://link.aps.org/doi/10.1103/RevModPhys.90.045002>.
- 2455 [5] Fritz Zwicky. “The Redshift of Extragalactic Nebulae”. In: *Helvetica Physica Acta* 6.
 2456 (1933), pp. 110–127. doi: [10.5169/seals-110267](https://doi.org/10.5169/seals-110267).
- 2457 [6] Vera C. Rubin and Jr. Ford W. Kent. “Rotation of the Andromeda Nebula from a
 2458 Spectroscopic Survey of Emission Regions”. In: *ApJ* 159 (Feb. 1970), p. 379. doi:
 2459 [10.1086/150317](https://doi.org/10.1086/150317).
- 2460 [7] K. G. Begeman, A. H. Broeils, and R. H. Sanders. “Extended rotation curves of spiral galax-
 2461 ies: dark haloes and modified dynamics”. In: *Monthly Notices of the Royal Astronomical So-*
 2462 *ciety* 249.3 (Apr. 1991), pp. 523–537. ISSN: 0035-8711. doi: [10.1093/mnras/249.3.523](https://doi.org/10.1093/mnras/249.3.523).
 2463 eprint: <https://academic.oup.com/mnras/article-pdf/249/3/523/18160929/mnras249-0523.pdf>. URL: <https://doi.org/10.1093/mnras/249.3.523>.
- 2465 [8] *Different types of gravitational lenses*. website. Feb. 2004. URL: <https://esahubble.org/images/heic0404b/>.
- 2467 [9] Douglas Clowe et al. “A Direct Empirical Proof of the Existence of Dark Matter”. In: *apjl*
 2468 648.2 (Sept. 2006), pp. L109–L113. doi: [10.1086/508162](https://doi.org/10.1086/508162). arXiv: [astro-ph/0608407](https://arxiv.org/abs/astro-ph/0608407)
 2469 [*astro-ph*].
- 2470 [10] Planck Collaboration and N. et. al. Aghanim. “Planck 2018 results I. Overview and the
 2471 cosmological legacy of Planck”. In: *A&A* 641 (2020). doi: [10.1051/0004-6361/201833880](https://doi.org/10.1051/0004-6361/201833880). URL: <https://doi.org/10.1051/0004-6361/201833880>.
- 2473 [11] Wayne Hu. *Matter Density Animation*. web. 2024. URL: <http://background.uchicago.edu/~whu/animbut/anim2.html>.

- 2475 [12] Wenlong Yuan et al. “A First Look at Cepheids in a Type Ia Supernova Host with JWST”. in:
2476 *The Astrophysical Journal Letters* 940.1 (Nov. 2022). doi: [10.3847/2041-8213/ac9b27](https://doi.org/10.3847/2041-8213/ac9b27).
2477 URL: <https://dx.doi.org/10.3847/2041-8213/ac9b27>.
- 2478 [13] Wendy L. Freedman. “Measurements of the Hubble Constant: Tensions in Perspective”. In:
2479 *The Astrophysical Journal* 919.1 (Sept. 2021), p. 16. doi: [10.3847/1538-4357/ac0e95](https://doi.org/10.3847/1538-4357/ac0e95).
2480 URL: <https://dx.doi.org/10.3847/1538-4357/ac0e95>.
- 2481 [14] Jodi Cooley. “Dark Matter direct detection of classical WIMPs”. In: *SciPost Phys. Lect.
2482 Notes* (2022), p. 55. doi: [10.21468/SciPostPhysLectNotes.55](https://doi.org/10.21468/SciPostPhysLectNotes.55). URL: <https://scipost.org/10.21468/SciPostPhysLectNotes.55>.
- 2484 [15] “Search for new phenomena in events with an energetic jet and missing transverse momentum
2485 in pp collisions at $\sqrt{s} = 13$ TeV with the ATLAS detector”. In: *Phys. Rev. D* 103
2486 (11 July 2021), p. 112006. doi: [10.1103/PhysRevD.103.112006](https://doi.org/10.1103/PhysRevD.103.112006). URL: <https://link.aps.org/doi/10.1103/PhysRevD.103.112006>.
- 2488 [16] *Jetting into the dark side: a precision search for dark matter*. website. July 2020. URL:
2489 <https://atlas.cern/updates/briefing/precision-search-dark-matter>.
- 2490 [17] Celine Armand et. al. “Combined dark matter searches towards dwarf spheroidal galaxies
2491 with Fermi-LAT, HAWC, H.E.S.S., MAGIC, and VERITAS”. in: *Proceedings of Science*.
2492 Vol. 395. Mar. 2022. doi: <https://doi.org/10.22323/1.395.0528>.
- 2493 [18] Tracy R. Slatyer. “Les Houches Lectures on Indirect Detection of Dark Matter”. In: *SciPost
2494 Phys. Lect. Notes* (2022), p. 53. doi: [10.21468/SciPostPhysLectNotes.53](https://doi.org/10.21468/SciPostPhysLectNotes.53). URL:
2495 <https://scipost.org/10.21468/SciPostPhysLectNotes.53>.
- 2496 [19] Christian W Bauer, Nicholas L. Rodd, and Bryan R. Webber. “Dark matter spectra from
2497 the electroweak to the Planck scale”. In: *Journal of High Energy Physics* 2021.1029-8479
2498 (June 2021). doi: [https://doi.org/10.1007/JHEP06\(2021\)121](https://doi.org/10.1007/JHEP06(2021)121).
- 2499 [20] Riccardo Catena and Piero Ullio. “A novel determination of the local dark matter density”.
2500 In: *Journal of Cosmology and Astroparticle Physics* 2010.08 (Aug. 2010), p. 004. doi:
2501 [10.1088/1475-7516/2010/08/004](https://doi.org/10.1088/1475-7516/2010/08/004). URL: <https://dx.doi.org/10.1088/1475-7516/2010/08/004>.
- 2503 [21] B. P. Abbott et al. “Observation of Gravitational Waves from a Binary Black Hole Merger”.
2504 In: *Phys. Rev. Lett.* 116 (6 Feb. 2016), p. 061102. doi: [10.1103/PhysRevLett.116.061102](https://doi.org/10.1103/PhysRevLett.116.061102). URL: <https://link.aps.org/doi/10.1103/PhysRevLett.116.061102>.
- 2506 [22] R. Abbasi et. al. “Observation of high-energy neutrinos from the Galactic plane”. In: *Science*
2507 380.6652 (June 2023), pp. 1338–1343.
- 2508 [23] NASA Goddard Space Flight Center. *Fermi’s 12-year view of the gamma-ray sky*. website.

- 2509 2022. URL: <https://svs.gsfc.nasa.gov/14090>.
- 2510 [24] Marco Cirelli et al. “PPPC 4 DM ID: a poor particle physicist cookbook for dark matter
2511 indirect detection”. In: *Journal of Cosmology and Astroparticle Physics* 2011.03 (Mar.
2512 2011), p. 051. doi: [10.1088/1475-7516/2011/03/051](https://doi.org/10.1088/1475-7516/2011/03/051). URL: <https://dx.doi.org/10.1088/1475-7516/2011/03/051>.
- 2514 [25] The HAWC Collaboration. “The High-Altitude Water Cherenkov (HAWC) observatory in
2515 México: The primary detector”. In: *Nuclear Instruments and Methods in Physics Research*
2516 *Section A: Accelerators, Spectrometers, Detectors and Associated Equipment* 1052 (2023),
2517 p. 168253. ISSN: 0168-9002. doi: <https://doi.org/10.1016/j.nima.2023.168253>.
2518 URL: <https://www.sciencedirect.com/science/article/pii/S0168900223002437>.
- 2520 [26] Alicia Lopez Oramas. “Multi-year Campaign of the Gamma-Ray Binary LS I +61° 303
2521 and Search for VHE Emission from Gamma-Ray Binary Candidates with the MAGIC
2522 Telescopes”. PhD thesis. Instituto de Astrofísica de Canarias, 2014. doi: <http://dx.doi.org/10.13140/RG.2.1.4140.4969>.
- 2524 [27] Hamamatsu Photonics KK. *Large Photocathode Area Photomultiplier Tubes*. 2019. URL:
2525 https://www.hamamatsu.com/content/dam/hamamatsu-photronics/sites/documents/99_SALES_LIBRARY/etd/LARGE_AREA_PMT TPMH1376E.pdf.
- 2527 [28] A.U. Abeysekara et. al. “The High-Altitude Water Cherenkov (HAWC) observatory in México:
2528 The primary detector”. In: *Nuclear Instruments and Methods in Physics Research*
2529 *Section A: Accelerators, Spectrometers, Detectors and Associated Equipment* 1052 (2023),
2530 p. 168253. ISSN: 0168-9002. doi: <https://doi.org/10.1016/j.nima.2023.168253>.
2531 URL: <https://www.sciencedirect.com/science/article/pii/S0168900223002437>.
- 2533 [29] The HAWC Collaboration. “Data acquisition architecture and online processing system
2534 for the HAWC gamma-ray observatory”. In: *Nuclear Instruments and Methods in Physics*
2535 *Research Section A: Accelerators, Spectrometers, Detectors and Associated Equipment* 888
2536 (2018), pp. 138–146. ISSN: 0168-9002. doi: <https://doi.org/10.1016/j.nima.2018.01.051>. URL: <https://www.sciencedirect.com/science/article/pii/S0168900218300688>.
- 2539 [30] The Milagro Collaboratio. “Milagrito, a TeV air-shower array”. In: *Nuclear Instruments*
2540 *and Methods in Physics Research Section A: Accelerators, Spectrometers, Detectors and*
2541 *Associated Equipment* 449.3 (2000), pp. 478–499. ISSN: 0168-9002. doi: [https://doi.org/10.1016/S0168-9002\(00\)00146-7](https://doi.org/10.1016/S0168-9002(00)00146-7). URL: <https://www.sciencedirect.com/science/article/pii/S0168900200001467>.
- 2544 [31] Ian Gabriel Wisher. “Real-time Transient Monitoring With the HAWC Detector: Design
2545 and Performance”. PhD thesis. The University of Wisconsin - Madison, 2016.

- 2546 [32] The ZeroMQ authors. “ZeroMQ An open-source universal messaging library”. In: (2021).
2547 URL: <https://zeromq.org>.
- 2548 [33] Zigfried Hampel-Archisman. “Cosmic Ray Observations at the TeV Scale with the HAWC
2549 Observatory”. PhD thesis. University of Wisconsin-Madison, 2017.
- 2550 [34] A. U. Abeysekara et al. “Observation of the Crab Nebula with the HAWC Gamma-Ray
2551 Observatory”. In: *The Astrophysical Journal* 843.1 (June 2017), p. 39. doi: [10.3847/1538-4357/aa7555](https://doi.org/10.3847/1538-4357/aa7555). URL: <https://doi.org/10.3847/1538-4357/aa7555>.
- 2553 [35] Kenneth Greisen. “Cosmic Ray Showers”. In: *ANNUAL REVIEW OF NUCLEAR AND
2554 PARTICLE SCIENCE* 10 (1960), pp. 63–108.
- 2555 [36] The HAWC Collabortion. “Sensitivity of the high altitude water Cherenkov detector to
2556 sources of multi-TeV gamma rays”. In: *Astroparticle Physics* 50-52 (2013), pp. 26–32. ISSN:
2557 0927-6505. doi: <https://doi.org/10.1016/j.astropartphys.2013.08.002>. URL:
2558 <https://www.sciencedirect.com/science/article/pii/S0927650513001230>.
- 2559 [37] The HAWC Collaboration. “Measurement of the Crab Nebula Spectrum Past 100 TeV with
2560 HAWC”. in: *The Astrophysical Journal* 881.2 (Aug. 2019), p. 134. doi: [10.3847/1538-4357/ab2f7d](https://doi.org/10.3847/1538-4357/ab2f7d). URL: <https://dx.doi.org/10.3847/1538-4357/ab2f7d>.
- 2562 [38] Samuel Miranelli. “CONSTRAINTS ON LORENTZ-INVARIANCE VIOLATION WITH
2563 THE HAWC OBSERVATORY”. PhD thesis. Michigan State University, 2019.
- 2564 [39] A. A. Abdo et al. “OBSERVATION AND SPECTRAL MEASUREMENTS OF THE
2565 CRAB NEBULA WITH MILAGRO”. in: *The Astrophysical Journal* 750.1 (Apr. 2012),
2566 p. 63. doi: [10.1088/0004-637X/750/1/63](https://doi.org/10.1088/0004-637X/750/1/63). URL: <https://dx.doi.org/10.1088/0004-637X/750/1/63>.
- 2568 [40] Javier Rico. “Gamma-Ray Dark Matter Searches in Milky Way Satellites—A Comparative
2569 Review of Data Analysis Methods and Current Results”. In: *Galaxies* 8.1 (Mar. 2020), p. 25.
2570 doi: [10.3390/galaxies8010025](https://doi.org/10.3390/galaxies8010025). arXiv: [2003.13482 \[astro-ph.HE\]](https://arxiv.org/abs/2003.13482).
- 2571 [41] W. B. Atwood et al. “The Large Area Telescope on the Fermi Gamma-Ray Space Telescope
2572 Mission”. In: *apj* 697.2 (June 2009), pp. 1071–1102. doi: [10.1088/0004-637X/697/2/1071](https://doi.org/10.1088/0004-637X/697/2/1071). arXiv: [0902.1089 \[astro-ph.IM\]](https://arxiv.org/abs/0902.1089).
- 2574 [42] M. Ackermann et al. “Searching for Dark Matter Annihilation from Milky Way Dwarf
2575 Spheroidal Galaxies with Six Years of Fermi Large Area Telescope Data”. In: *prl* 115.23,
2576 231301 (Dec. 2015), p. 231301. doi: [10.1103/PhysRevLett.115.231301](https://doi.org/10.1103/PhysRevLett.115.231301). arXiv:
2577 [1503.02641 \[astro-ph.HE\]](https://arxiv.org/abs/1503.02641).
- 2578 [43] Mattia Di Mauro, Martin Stref, and Francesca Calore. “Investigating the effect of Milky
2579 Way dwarf spheroidal galaxies extension on dark matter searches with Fermi-LAT data”.

- 2580 In: *Phys. Rev. D* 106 (12 Dec. 2022), p. 123032. doi: [10.1103/PhysRevD.106.123032](https://doi.org/10.1103/PhysRevD.106.123032).
2581 URL: <https://link.aps.org/doi/10.1103/PhysRevD.106.123032>.
- 2582 [44] F. et al. Aharonian. “Observations of the Crab Nebula with H.E.S.S.”. In: *Astron. Astrophys.*
2583 457 (2006), pp. 899–915. doi: [10.1051/0004-6361:20065351](https://doi.org/10.1051/0004-6361:20065351). arXiv: [astro-ph/0607333](https://arxiv.org/abs/astro-ph/0607333).
- 2585 [45] J. Albert et al. “VHE γ -Ray Observation of the Crab Nebula and its Pulsar with the MAGIC
2586 Telescope”. In: *The Astrophysical Journal* 674.2 (Feb. 2008), p. 1037. doi: [10.1086/525270](https://doi.org/10.1086/525270). URL: <https://dx.doi.org/10.1086/525270>.
- 2588 [46] N. Park. “Performance of the VERITAS experiment”. In: *Proceedings, 34th International
2589 Cosmic Ray Conference (ICRC2015): The Hague, The Netherlands, July, 30th July - 6th
2590 August*. Vol. 34. 2015, p. 771. arXiv: [1508.07070](https://arxiv.org/abs/1508.07070) [astro-ph.IM].
- 2591 [47] A. Abramowski et al. “H.E.S.S. constraints on Dark Matter annihilations towards the Sculptor
2592 and Carina Dwarf Galaxies”. In: *Astropart. Phys.* 34 (2011), pp. 608–616. doi: [10.1016/j.astropartphys.2010.12.006](https://doi.org/10.1016/j.astropartphys.2010.12.006). arXiv: [1012.5602](https://arxiv.org/abs/1012.5602) [astro-ph.HE].
- 2594 [48] A. Abramowski et al. “Search for dark matter annihilation signatures in H.E.S.S. observations
2595 of Dwarf Spheroidal Galaxies”. In: *Phys. Rev. D* 90 (2014), p. 112012. doi: [10.1103/PhysRevD.90.112012](https://doi.org/10.1103/PhysRevD.90.112012). arXiv: [1410.2589](https://arxiv.org/abs/1410.2589) [astro-ph.HE].
- 2597 [49] H. Abdalla et al. “Searches for gamma-ray lines and ‘pure WIMP’ spectra from Dark
2598 Matter annihilations in dwarf galaxies with H.E.S.S”. in: *JCAP* 11 (2018), p. 037. doi:
2599 [10.1088/1475-7516/2018/11/037](https://doi.org/10.1088/1475-7516/2018/11/037). arXiv: [1810.00995](https://arxiv.org/abs/1810.00995) [astro-ph.HE].
- 2600 [50] J. Aleksić et al. “Optimized dark matter searches in deep observations of Segue 1 with
2601 MAGIC”. in: *JCAP* 1402 (2014), p. 008. doi: [10.1088/1475-7516/2014/02/008](https://doi.org/10.1088/1475-7516/2014/02/008).
2602 arXiv: [1312.1535](https://arxiv.org/abs/1312.1535) [hep-ph].
- 2603 [51] V.A. Acciari et al. “Combined searches for dark matter in dwarf spheroidal galaxies observed
2604 with the MAGIC telescopes, including new data from Coma Berenices and Draco”. In: *Physics of the Dark Universe* (2021), p. 100912. ISSN: 2212-6864. doi: <https://doi.org/10.1016/j.dark.2021.100912>. URL: <https://www.sciencedirect.com/science/article/pii/S2212686421001370>.
- 2608 [52] M. L. Ahnen et al. “Indirect dark matter searches in the dwarf satellite galaxy Ursa Major II
2609 with the MAGIC Telescopes”. In: *JCAP* 1803.03 (2018), p. 009. doi: [10.1088/1475-7516/2018/03/009](https://doi.org/10.1088/1475-7516/2018/03/009). arXiv: [1712.03095](https://arxiv.org/abs/1712.03095) [astro-ph.HE].
- 2611 [53] S. et al. Archambault. “Dark matter constraints from a joint analysis of dwarf Spheroidal
2612 galaxy observations with VERITAS”. in: *prd* 95.8 (Apr. 2017). doi: [10.1103/PhysRevD.95.082001](https://doi.org/10.1103/PhysRevD.95.082001). arXiv: [1703.04937](https://arxiv.org/abs/1703.04937) [astro-ph.HE].

- 2614 [54] Louise Oakes et al. “Combined Dark Matter searches towards dwarf spheroidal galaxies with
2615 Fermi-LAT, HAWC, HESS, MAGIC and VERITAS”. in: *Proceedings of Science*. 2019.
- 2616 [55] Celine Armand et al. on behalf of the Fermi-LAT, HAWC, HESS, MAGIC, VERITAS.
2617 “Combined Dark Matter searches towards dwarf spheroidal galaxies with Fermi-LAT,
2618 HAWC, HESS, MAGIC and VERITAS”. in: *Proceedings of Science*. 2021.
- 2619 [56] Daniel Kerszberg et al. on behalf of the Fermi-LAT, HAWC, HESS, MAGIC, and VER-
2620 TIAS collaborations. “Search for dark matter annihilation with a combined analysis of
2621 dwarf spheroidal galaxies from Fermi-LAT, HAWC, H.E.S.S., MAGIC and VERITAS”. in:
2622 *Proceedings of Science*. 2023.
- 2623 [57] Giacomo Vianello et al. *The Multi-Mission Maximum Likelihood framework (3ML)*. 2015.
2624 arXiv: [1507.08343 \[astro-ph.HE\]](https://arxiv.org/abs/1507.08343).
- 2625 [58] Marco Cirelli et al. “PPPC 4 DM ID: a poor particle physicist cookbook for dark matter
2626 indirect detection”. In: *Journal of Cosmology and Astroparticle Physics* 2011.03 (Mar.
2627 2011). ISSN: 1475-7516. doi: [10.1088/1475-7516/2011/03/051](https://doi.org/10.1088/1475-7516/2011/03/051). URL: <http://dx.doi.org/10.1088/1475-7516/2011/03/051>.
- 2629 [59] Alex Geringer-Sameth, Savvas M. Koushiappas, and Matthew Walker. “DWARF GALAXY
2630 ANNIHILATION AND DECAY EMISSION PROFILES FOR DARK MATTER EXPERI-
2631 MENTS”. in: *The Astrophysical Journal* 801.2 (Mar. 2015), p. 74. ISSN: 1538-4357. doi:
2632 [10.1088/0004-637x/801/2/74](https://doi.org/10.1088/0004-637x/801/2/74). URL: <http://dx.doi.org/10.1088/0004-637X/801/2/74>.
- 2634 [60] A. Albert et al. “Dark Matter Limits from Dwarf Spheroidal Galaxies with the HAWC
2635 Gamma-Ray Observatory”. In: *The Astrophysical Journal* 853.2 (Feb. 2018), p. 154. ISSN:
2636 1538-4357. doi: [10.3847/1538-4357/aaa6d8](https://doi.org/10.3847/1538-4357/aaa6d8). URL: <http://dx.doi.org/10.3847/1538-4357/aaa6d8>.
- 2638 [61] HongSheng Zhao. “Analytical models for galactic nuclei”. In: *Mon. Not. Roy. Astron. Soc.*
2639 278 (1996), pp. 488–496. doi: [10.1093/mnras/278.2.488](https://doi.org/10.1093/mnras/278.2.488). arXiv: [astro-ph/9509122](https://arxiv.org/abs/astro-ph/9509122)
2640 [[astro-ph](https://arxiv.org/abs/astro-ph/9509122)].
- 2641 [62] Julio F. Navarro, Carlos S. Frenk, and Simon D. M. White. “The Structure of Cold Dark
2642 Matter Halos”. In: *ApJ* 462 (May 1996), p. 563. doi: [10.1086/177173](https://doi.org/10.1086/177173). eprint:
2643 [astro-ph/9508025](https://arxiv.org/abs/astro-ph/9508025) ([astro-ph](#)).
- 2644 [63] V. Bonnivard et al. “Spherical Jeans analysis for dark matter indirect detection in dwarf
2645 spheroidal galaxies - Impact of physical parameters and triaxiality”. In: *Mon. Not. Roy.
2646 Astron. Soc.* 446 (2015), pp. 3002–3021. doi: [10.1093/mnras/stu2296](https://doi.org/10.1093/mnras/stu2296). arXiv:
2647 [1407.7822 \[astro-ph.HE\]](https://arxiv.org/abs/1407.7822).
- 2648 [64] M. Ackermann et al. “Searching for Dark Matter Annihilation from Milky Way Dwarf

- 2649 Spheroidal Galaxies with Six Years of Fermi Large Area Telescope Data”. In: *prl* 115.23,
 2650 231301 (Dec. 2015), p. 231301. doi: [10.1103/PhysRevLett.115.231301](https://doi.org/10.1103/PhysRevLett.115.231301). arXiv:
 2651 [1503.02641 \[astro-ph.HE\]](https://arxiv.org/abs/1503.02641).
- 2652 [65] M. L. Ahnen et al. “Limits to Dark Matter Annihilation Cross-Section from a Combined
 2653 Analysis of MAGIC and Fermi-LAT Observations of Dwarf Satellite Galaxies”. In: *JCAP*
 2654 1602.02 (2016), p. 039. doi: [10.1088/1475-7516/2016/02/039](https://doi.org/10.1088/1475-7516/2016/02/039). arXiv: [1601.06590](https://arxiv.org/abs/1601.06590)
 2655 [astro-ph.HE].
- 2656 [66] Javier Rico et al. *gLike: numerical maximization of heterogeneous joint
 2657 likelihood functions of a common free parameter plus nuisance parameters.*
 2658 <https://doi.org/10.5281/zenodo.4601451>. Version v00.09.03. Mar. 2021. doi: [10.5281/zenodo.4601451](https://doi.org/10.5281/zenodo.4601451). URL: <https://doi.org/10.5281/zenodo.4601451>.
- 2660 [67] Tjark Miener and Daniel Nieto. *LklCom: Combining likelihoods from different experiments*.
 2661 <https://doi.org/10.5281/zenodo.4597500>. Version v0.5.3. Mar. 2021. doi: [10.5281/zenodo.4597500](https://doi.org/10.5281/zenodo.4597500). URL: <https://doi.org/10.5281/zenodo.4597500>.
- 2663 [68] T. Miener et al. “Open-source Analysis Tools for Multi-instrument Dark Matter Searches”.
 2664 In: *arXiv e-prints*, arXiv:2112.01818 (Dec. 2021), arXiv:2112.01818. arXiv: [2112.01818](https://arxiv.org/abs/2112.01818)
 2665 [astro-ph.IM].
- 2666 [69] Alex Geringer-Sameth and Matthew Koushiappas Savvas M. and Walker. “Dwarf galaxy
 2667 annihilation and decay emission profiles for dark matter experiments”. In: *Astrophys.
 2668 J.* 801.2 (2015), p. 74. doi: [10.1088/0004-637X/801/2/74](https://doi.org/10.1088/0004-637X/801/2/74). arXiv: [1408.0002](https://arxiv.org/abs/1408.0002)
 2669 [astro-ph.CO].
- 2670 [70] Gianfranco Bertone, Dan Hooper, and Joseph Silk. “Particle dark matter: evidence, can-
 2671 didates and constraints”. In: *Physics Reports* 405.5-6 (Jan. 2005), pp. 279–390. ISSN:
 2672 0370-1573. doi: [10.1016/j.physrep.2004.08.031](https://doi.org/10.1016/j.physrep.2004.08.031). URL: <http://dx.doi.org/10.1016/j.physrep.2004.08.031>.
- 2674 [71] V. Bonnivard et al. “Dark matter annihilation and decay in dwarf spheroidal galaxies: The
 2675 classical and ultrafaint dSphs”. In: *Mon. Not. Roy. Astron. Soc.* 453.1 (2015), pp. 849–867.
 2676 doi: [10.1093/mnras/stv1601](https://doi.org/10.1093/mnras/stv1601). arXiv: [1504.02048 \[astro-ph.HE\]](https://arxiv.org/abs/1504.02048).
- 2677 [72] A. et al. Albert. “Searching for Dark Matter Annihilation in Recently Discovered Milky Way
 2678 Satellites with Fermi-LAT”. in: *Astrophys. J.* 834.2 (2017), p. 110. doi: [10.3847/1538-4357/834/2/110](https://doi.org/10.3847/1538-4357/834/2/110). arXiv: [1611.03184 \[astro-ph.HE\]](https://arxiv.org/abs/1611.03184).
- 2680 [73] Mattia Di Mauro and Martin Wolfgang Winkler. “Multimessenger constraints on the dark
 2681 matter interpretation of the Fermi-LAT Galactic Center excess”. In: *prd* 103.12, 123005
 2682 (June 2021), p. 123005. doi: [10.1103/PhysRevD.103.123005](https://doi.org/10.1103/PhysRevD.103.123005). arXiv: [2101.11027](https://arxiv.org/abs/2101.11027)
 2683 [astro-ph.HE].

- 2684 [74] H. C. Plummer. “On the Problem of Distribution in Globular Star Clusters: (Plate 8.)”
 2685 In: *Monthly Notices of the Royal Astronomical Society* 71.5 (Mar. 1911), pp. 460–470.
 2686 ISSN: 0035-8711. doi: [10.1093/mnras/71.5.460](https://doi.org/10.1093/mnras/71.5.460). eprint: <https://academic.oup.com/mnras/article-pdf/71/5/460/2937497/mnras71-0460.pdf>. URL:
 2688 <https://doi.org/10.1093/mnras/71.5.460>.
- 2689 [75] Daniel R. Hunter. “Derivation of the anisotropy profile, constraints on the local velocity
 2690 dispersion, and implications for direct detection”. In: *JCAP* 02 (2014), p. 023. doi:
 2691 [10.1088/1475-7516/2014/02/023](https://doi.org/10.1088/1475-7516/2014/02/023). arXiv: [1311.0256 \[astro-ph.CO\]](https://arxiv.org/abs/1311.0256).
- 2692 [76] Barun Kumar Dhar and Liliya L. R. Williams. “Surface mass density of the Einasto family
 2693 of dark matter haloes: are they Sersic-like?” In: *Mon. Not. Roy. Astron. Soc.* (2010). doi:
 2694 [10.1111/j.1365-2966.2010.16446.x](https://doi.org/10.1111/j.1365-2966.2010.16446.x).
- 2695 [77] M. Baes and E. Van Hese. “Dynamical models with a general anisotropy profile”. In: *Astron. Astrophys.* 471 (2007), p. 419. doi: [10.1051/0004-6361:20077672](https://doi.org/10.1051/0004-6361:20077672). arXiv:
 2696 [0705.4109 \[astro-ph\]](https://arxiv.org/abs/0705.4109).
- 2698 [78] Matthew G. Walker, Edward W. Olszewski, and Mario Mateo. “Bayesian analysis of re-
 2699 solved stellar spectra: application to MMT/Hectochelle observations of the Draco dwarf
 2700 spheroidal”. In: *mnras* 448.3 (Apr. 2015), pp. 2717–2732. doi: [10.1093/mnras/stv099](https://doi.org/10.1093/mnras/stv099).
 2701 arXiv: [1503.02589 \[astro-ph.GA\]](https://arxiv.org/abs/1503.02589).
- 2702 [79] Nicholas L. Rodd et al. “Dark matter spectra from the electroweak to the Planck scale”. In:
 2703 *J. High Energy Physics* 121.10.1007 (June 2021).
- 2704 [80] Pace, Andrew B and Strigari, Louis E. “Scaling relations for dark matter annihilation and
 2705 decay profiles in dwarf spheroidal galaxies”. In: *Monthly Notices of the Royal Astronomical
 2706 Society* 482.3 (Oct. 2018), pp. 3480–3496. ISSN: 0035-8711. doi: [10.1093/mnras/sty2839](https://doi.org/10.1093/mnras/sty2839).
- 2708 [81] Albert, A. et al. “Search for gamma-ray spectral lines from dark matter annihilation in
 2709 dwarf galaxies with the High-Altitude Water Cherenkov observatory”. In: *Phys. Rev. D* 101 (10 May 2020), p. 103001. doi: [10.1103/PhysRevD.101.103001](https://doi.org/10.1103/PhysRevD.101.103001). URL:
 2710 <https://link.aps.org/doi/10.1103/PhysRevD.101.103001>.
- 2712 [82] Victor Eijkhout and Edmund Show and Robert van de Geijn. *The Science of Computing. The Art of High Performance Computing*. Vol. 3. Open Copy published under CC-BY 4.0
 2713 license, 2023, pp. 63–66.
- 2715 [83] Aartsen, M. et al. “IceCube search for dark matter annihilation in nearby galaxies and galaxy
 2716 clusters”. In: *Phys. Rev. D* 88 (12 Dec. 2013), p. 122001. doi: [10.1103/PhysRevD.88.122001](https://doi.org/10.1103/PhysRevD.88.122001). URL: <https://link.aps.org/doi/10.1103/PhysRevD.88.122001>.
- 2718 [84] Pearl Sandick et al. “Sensitivity of the IceCube neutrino detector to dark matter annihilating

- 2719 in dwarf galaxies”. In: *Phys. Rev. D* 81 (8 Apr. 2010), p. 083506. doi: [10.1103/PhysRevD.81.083506](https://doi.org/10.1103/PhysRevD.81.083506). URL: <https://link.aps.org/doi/10.1103/PhysRevD.81.083506>.
- 2720
- 2721 [85] Qinrui Liu and Jeffrey Lazar and Carlos A. Argüelles and Ali Kheirandish. “ χ aro: a tool
2722 for neutrino flux generation from WIMPs”. In: *Journal of Cosmology and Astroparticle
2723 Physics* 2020.10 (Oct. 2020), p. 043. doi: [10.1088/1475-7516/2020/10/043](https://doi.org/10.1088/1475-7516/2020/10/043). URL:
2724 <https://dx.doi.org/10.1088/1475-7516/2020/10/043>.
- 2725 [86] Tessa Cerver. “Time Integrated searches for Astrophysical Neutrino Sources using the
2726 IceCube Detector and Gender in Physics studies for the Genera Project”. PhD thesis.
2727 UNIVERSITE DE GEN ´ EVE, 2019, pp. 57–64.
- 2728 [87] Minjin Jeong on behalf of the IceCube Collaboration. “Search for Dark Matter Decay in
2729 Nearby Galaxy Clusters and Galaxies with IceCube”. In: *Proceedings of Science* 444.38
2730 (2023).
- 2731 [88] IceCube Collaboration. “Evidence for neutrino emission from the nearby active galaxy NGC
2732 1068”. In: *Science* 378.6619 (2022).
- 2733 [89] Nathan Whitehorn and Jakob van Santen. *Photospline*. IceCube: GitHub.
- 2734 [90] Paul H. C. Eilers and Brian D. Marx. “Flexible smoothing with B-splines and penalties”.
2735 In: *Statistical Science* 11.2 (1996), pp. 89–121. doi: [10.1214/ss/1038425655](https://doi.org/10.1214/ss/1038425655). URL:
2736 <https://doi.org/10.1214/ss/1038425655>.
- 2737 [91] The IceCube Collaboration. *Search for neutrino lines from dark matter annihilation and
2738 decay with IceCube*. 2023. arXiv: [2303.13663 \[astro-ph.HE\]](https://arxiv.org/abs/2303.13663).
- 2739 [92] The IceCube Collaboration. “Measurement of the multi-TeV neutrino interaction cross-
2740 section with IceCube using Earth absorption”. In: *Nature* 551 (2017).